Summer 8-17-2018

# Modeling Coastal Flooding and Sand Transport in the Gulf of Maine during Severe Storms in a Changing Climate

Dongmei Xie
*University of Maine*, dongmei.xie@maine.edu

# MODELING COASTAL FLOODING AND SAND TRANSPORT IN THE GULF OF MAINE DURING SEVERE STORMS IN A CHANGING CLIMATE

By

Dongmei Xie

B.A. Hohai University, 2010

M.A. Hohai University, 2013

A DISSERTATION

Submitted in Partial Fulfillment of the

Requirements for the Degree of

Doctor of Philosophy

(in Civil and Environmental Engineering)

The Graduate School

The University of Maine

August 2018

Advisory Committee:

Jean D. MacRae, Associate Professor of Civil and Environmental Engineering, Advisor

Bryan Pearce, Professor of Civil and Environmental Engineering

Chris Massey, Research Mathematician

Huijie Xue, Professor of Marine Sciences

Damian C. Brady, Professor of Marine Sciences

**MODELING COASTAL FLOODING AND SAND TRANSPORT IN THE GULF OF MAINE DURING SEVERE STORMS IN A CHANGING**

By Dongmei Xie

Dissertation Advisor: Dr. Jean D. MacRae

An Abstract of the Dissertation Presented
in Partial Fulfillment of the Requirements for the
Degree of Doctor of Philosophy
(in Civil and Environmental Engineering)

August 2018

Elevated water level and large waves cause extensive damage and economic loss to coastal communities. An integrated atmosphere-ocean-coast modeling system that links physical processes with scales ranging from the open ocean to the surf zone has been developed for the Gulf of Maine. The modeling system includes a hydrodynamic model, a wave overtopping model and a sediment transport model. It is then applied to investigate and gain a comprehensive understanding of the following coastal processes: (1) the interaction between tide-surge, waves and bathymetry, (2) coastal flooding due to wave overtopping, and (3) sand transport.

Both coastal flooding and sand transport rely on the accurate prediction of water level, waves, and currents at the coast. This work has demonstrated that the interactions between tide-surge, waves and bathymetry have a significant impact on coastal waves, circulation and water level; and the interactions exhibit strong temporal and spatial variability along the coast. The inclusion and appropriate representation of the interaction processes in numerical modeling is important for coastlines with complex configurations.

The integrated modeling system has been applied to predict coastal flooding due to wave overtopping at the seawall in Scituate, Massachusetts. The capacity of the seawalls to protect coastal communities against flooding as sea level rises is investigated. It has been shown that seawalls will have to be elevated much more than the projected sea level rise to cope with future storms due to the presence of larger waves approaching the coast as depth increases.

Sand transport and its response to different storm characteristics are closely linked to waves and currents. Local bathymetry and winds are the two most important factors determining waves, currents and sand transport. The role of wind-driven and wave-induced current for sand transport varies depending on water depth and coastline geometry. The wind-driven current dominates in shallow water, while the wave-induced current is more significant at headlands and around coastal structures and islands. Differences in net sand transport mainly result from different flow patterns due to the counterbalance between wind-driven and wave-induced currents.

**ACKNOWLEDGEMENTS**

When I first started this journey to work on my PhD degree at the University of Maine, I expected ups and downs ahead of me which would give me a balanced life. I was lucky to have good advice and support from dedicated families, advisors and friends.

I would like to express gratitude to my former advisor Qingping Zou for her guidance and discussion. Her pursuit of science inspired me and made me think deeply while working on my research project. I also want to thank my advisor Jean D. MacRae for her encouragement, discussion and dedication. She is a role model for me to work in academia. In addition, I would like to thank my committee members: Chris Massey of U.S. Army Corps of Engineers, Huijie Xue and Damian C. Brady of University of Maine, and Bryan Pearce, formerly of University of Maine, for their insight and comments on my work. I also thank Anthony Mignone of National Weather Service for sharing water level measurements in Scituate for model validation. Many thanks to John Cannon of National Weather Service for his feedback on the work.

Funding for this research mainly came from the Maine Sea Grant of the University of Maine. The grant also provided travel money for presentations of the research results. Additional support in the form of research assistantship and fellowship was provided by the Graduate School of University of Maine.

Finally, I offer my thanks to my families for their dedication and support throughout the duration of my research. Though far away in distance, their unconditional love was the backbone I built upon. I am also grateful that my daughter, Amelia, joined me with the final part of this journey. She is so precious and more than what I could ask for.

## TABLE OF CONTENTS

ACKNOWLEDGEMENTS ..... ii

LIST OF TABLES ..... viii

LIST OF FIGURES ..... ix

LIST OF EQUATIONS ..... xiii

Chapter

1. INTRODUCTION ..... 1

2. APPLICATION OF SWAN+ADCIRC TO TIDE-SURGE AND WAVE SIMULATION IN THE GULF OF MAINE DURING THE APRIL 2007 NOR'EASTER ..... 5

    2.1. Background ..... 5

    2.2. Gulf of Maine ..... 6

    2.3. April 2007 nor'easter ..... 7

    2.4. Methods ..... 8

        2.4.1. Advanced circulation model ..... 8

        2.4.2. Simulating waves nearshore model ..... 9

        2.4.3. SWAN+ADCIRC coupled model ..... 9

    2.5. Model setup ..... 10

        2.5.1. Model domain ..... 10

        2.5.2. Surface wind and air pressure forcing ..... 11

        2.5.3. Model parameters ..... 11

2.6. Results and discussion ..... 13
2.6.1. Tide and surge validation ..... 13
2.6.2. Wave validation ..... 15
2.6.3. Evolution of waves ..... 16
2.6.4. Depth-averaged currents ..... 17
2.6.5. Residual currents ..... 19
2.7. Conclusions ..... 20
3. TIDE-SURGE AND WAVE INTERACTION IN THE GULF OF MAINE DURING AN EXTRATROPICAL STORM ..... 21
3.1. Background ..... 21
3.2. SWAN+ADCIRC model ..... 26
3.2.1. Model description ..... 26
3.2.2. Model domain ..... 27
3.2.3. Surface wind and pressure forcing ..... 29
3.2.4. Model set-up and implementation ..... 30
3.3. Model validation ..... 32
3.3.1. Tide and surge ..... 32
3.3.2. Currents ..... 35
3.3.3. Waves ..... 37
3.4. Model results ..... 39
3.4.1. Wave effects on circulation ..... 39
3.4.2. The impact of tide-surge on waves ..... 45
3.5. Conclusions and discussions ..... 49
4. AN INTEGRATED MODELING SYSTEM TO PREDICT COSATAL FLOODING FROM WAVE OVERTOPPING IN THE NORTHEASTERN USA ..... 51

4.1. Background ..... 51
4.2. Site description and field measurement ..... 55
4.2.1. Site description ..... 55
4.2.2. Storm event description ..... 56
4.2.3. Field measurement ..... 57
4.3. Methodology ..... 60
4.3.1. Tide, surge and wave models ..... 61
4.3.2. Surf zone model ..... 62
4.3.3. Wave overtopping model ..... 63
4.3.4. Drainage model ..... 64
4.4. Model setup ..... 65
4.4.1. Model domain and bathymetry ..... 65
4.4.2. Surface wind and pressure forcing ..... 68
4.4.3. Boundary conditions ..... 69
4.4.4. Model parameters ..... 70
4.5. Tide-surge and wave interaction ..... 71
4.5.1. Model validation ..... 71
4.5.2. Impact of waves on tide-surge ..... 74
4.5.3. Impact of tide-surge on waves ..... 76
4.6. Wave overtopping in Scituate, Massachusetts ..... 78
4.6.1. Drainage parameterization ..... 78
4.6.2. Wave overtopping validation ..... 79
4.6.3. The impact of tide-surge and wave interaction on wave overtopping ..... 82
4.6.4. The impact of sea level rise and increased seawall crest on wave overtopping ..... 84
4.7. Summary and conclusion ..... 86
5. HYDRODYNAMIC AND SAND TRANSPORT SIMULATION IN THE SACO BAY ..... 88

5.1. Background ..... 88
5.2. Site description ..... 91
5.3. Description of storms ..... 93
5.4. Methodology ..... 95
5.4.1. Wave, tide-surge and circulation models ..... 96
5.4.2. Bottom stress and sediment transport models beneath combined waves and currents ..... 96
5.4.2.1. Bed shear-stresses model ..... 97
5.4.2.2. Total load sediment transport model ..... 98
5.4.3. Model setup ..... 100
5.5. Hydrodynamic model results and discussions ..... 102
5.5.1. April 2007 nor'easter ..... 102
5.5.2.1991 Perfect Storm ..... 107
5.5.3. January 2015 North American blizzard ..... 110
5.6. Sand transport model results ..... 115
5.6.1. Peak sand transport ..... 115
5.6.1.1. April 2007 Nor'easter ..... 115
5.6.1.2. 1991 Perfect Storm ..... 119
5.6.1.3. January 2015 North American blizzard ..... 124
5.6.2. Averaged flow field and sand transport flux ..... 127
5.6.2.1. April 2007 Nor'easter ..... 128
5.6.2.2. 1991 Perfect Storm ..... 132
5.6.2.3. January 2015 North American blizzard ..... 135
5.7. Hydrodynamics and sand transport during different storms ..... 138
5.7.1. Hydrodynamics features ..... 138
5.7.2. Sand transport features ..... 141

5.8. Conclusions ..... 143
6. CONCLUSIONS AND DISCUSSIONS ..... 146
6.1. Contribution to knowledge ..... 146
6.2. Conclusions ..... 147
6.3. Future work ..... 148
BIBLIOGRAPHY ..... 150
APPENDIX A: THE FLOW CHART FOR WAVE OVERTOPPING PREDICTION ..... 163
APPENDIX B: RELEVANT PUBLICATIONS ..... 164
BIOGRAPHY OF THE AUTHOR ..... 165

## LIST OF TABLES

Table 3.1. Wave buoys in the Gulf of Maine ..... 28

Table 3.2. Tide gauges in the Gulf of Maine ..... 29

Table 3.3. Error in model predictions of observed tidal level by tide gauges ..... 33

Table 3.4. Error in model prediction of observed surge level by tide gauges ..... 35

Table 3.5. Error in model prediction of observed current by ADCP ..... 37

Table 3.6. Errors in model prediction of observed significant wave height by wave buoys ..... 39

Table 4.1. Detailed information of the seawalls along the Avenues Basin in Scituate, MA (All elevations are referred to local mean sea level in Scituate, MA) ..... 59

Table 4.2. Wave buoys in the Gulf of Maine ..... 67

Table 4.3. Tide gauges in the Gulf of Maine ..... 68

## LIST OF FIGURES

Figure 2.1. Map of Gulf of Maine and its adjacent shelf/slope region. ..... 7

Figure 2.2. Finite element grids, wave buoys, and tide gauges in model domain. ..... 10

Figure 2.3. Comparison of NARR wind outputs with wave buoy observations during April 2007 Nor'easter. ..... 11

Figure 2.4. Comparison of simulated tide level with astronomic tide level during April 2007 Nor'easter at different tide gauges. ..... 14

Figure 2.5. Comparison of computed storm surge with observed data during April 2007 Nor'easter at different tide gauges ..... 14

Figure 2.6. Comparison of simulated wave parameters with buoy data during April 2007 Nor'easter at different wave buoys. ..... 15

Figure 2.7. Snapshots of wind and wave fields at 1400 UTC April 16, 2007. ..... 16

Figure 2.8 Snapshots of circulation in Gulf of Maine at 1400 UTC April 16, 2007. ..... 17

Figure 2.9. Snapshots of meteorological and wave-driven residual currents at 1400 UTC, April 16, 2007. ..... 19

Figure 3.1. Storm track of the April 2007 Nor'easter created by NCEP North American Regional Reanalysis meteorological data. ..... 23

Figure 3.2. Time evolution of pressure and wind fields during the April 2007 Nor'easter by NCEP North American Regional Reanalysis meteorological data from April 16 to April 18, 2007. ..... 25

Figure 3.3. Model domain covering the Gulf of Maine. ..... 28

Figure 3.4. Comparison of NARR winds with buoy measurements at buoy 44005, 44008, 44017 and 44033. ..... 30

Figure 3.5. Comparison of predicted astronomical tides with measurements. ..... 33

Figure 3.6. Predicted storm surge in comparison with measurements. ..... 35

Figure 3.7. The predicted water level (upper) and the comparisons of the predicted depth-averaged current velocity in the east, U, (middle) and north direction, V, (lower) with the ADCP measurements. ..... 36
Figure 3.8. Comparison of predicted wave parameters with buoy measurements. ..... 38
Figure 3.9. Depth-averaged velocity at the peak of the storm (1400UTC April 16, 2007) ..... 40
Figure 3.10. Bathymetry of the Saco Bay. ..... 41
Figure 3.11. Snapshot of circulation and wave field in Saco Bay at 1400UTC April 16, 2007. ..... 43
Figure 3.12. Time series of modeled elevation, significant wave height and wave setup at point A in Saco Bay indicated in Figure 3.7 ..... 44
Figure 3.13. The wave fields (top panel), the tide-surge level and associated current (the second panel), the wave setup (the third panel) and wave-induced current (the bottom panel) in Saco Bay at the four tidal phases marked in Figure 3.10 ..... 45
Figure 3.14. Wave fields at 1400UTC April 16, 2007. ..... 46
Figure 3.15. Directional wave variance density spectra at four wave buoys 44005, 44008, 44011 and 44018 ..... 47
Figure 3.16. Wave field in Saco Bay at 1400UTC April 16, 2007. ..... 48
Figure 4.1. Location of Scituate, MA and the Avenues Basin in Scituate. ..... 56
Figure 4.2. The January 2015 North American blizzard. ..... 57
Figure 4.3. Water level, basin area and water volume measured in the Avenues Basin during January 2015 North American blizzard. ..... 58
Figure 4.4. The sketch of the cross-shore profile from the seawall to the end of foreshore at S2 (Figure 4.1b) ..... 59
Figure 4.5. Integrated modeling system for coastal flooding arising from wave overtopping at a seawall. ..... 61
Figure 4.6. Comparison of model domains for wave and surge modeling. ..... 66
Figure 4.7. The bathymetry within the model domain. ..... 67

Figure 4.8. Comparison of predicted wave level with tide gauge data during the 2015 North American blizzard. 72
Figure 4.9. Comparison of predicted wave parameters with wave buoy data during the 2015 North American blizzard. 73
Figure 4.10. Water level and circulation fields at four tidal phases during the January 2015 North American blizzard. 76
Figure 4.11. Wave fields during the January 2015 North American blizzard. 77
Figure 4.12. Water level and wave overtopping discharge at the survey locations 80
Figure 4.13. Wave overtopping discharge, water level and significant wave height at 10 m water depth and S2 in Avenues Basin, Scituate, MA. 81
Figure 4.14. Comparison of predicted and measured volume of water in the Avenues Basin during the January 2015 North American blizzard. 82
Figure 4.15. Comparison of wave overtopping at S2 with and without the inclusion of tide-surge and wave interaction at the boundary of surf zone model. 84
Figure 4.16. Impact of sea level rise and seawall crest level on wave overtopping discharge at S2 85
Figure 5.1. Location and bathymetry of the Saco Bay 92
Figure 5.2. Surficial geological map of Saco Bay (from Barber, 1995) 93
Figure 5.3. The storm tracks of the three nor'easter storms 94
Figure 5.4. Modeling framework for sediment transport in the Saco Bay 95
Figure 5.5. Model domain and unstructured mesh for hydrodynamical and sand transport simulation 101
Figure 5.6. The water level and wave parameters at the nearest tide gauge 8418150 and wave buoy 44007 around the April 2007 nor'easter. 103
Figure 5.7. Current at storm peak at 14:30UTC on 4/16/2007 105
Figure 5.8. Waves at storm peak at 14:30UTC on 4/16/2007. 106

Figure 5.9. The water level and wave parameters at the nearest tide gauge 8418150 and wave buoy 44007 around the 1991 Perfect Storm. ..... 107
Figure 5.10. Current at storm peak at 23:30UTC on 10/30/1991. ..... 109
Figure 5.11. Waves at storm peak at 23:30UTC on 10/30/1991 ..... 110
Figure 5.12. The water level and wave parameters at the nearest tide gauge 8418150 and wave buoy 44007 around the January 2015 North American blizzard ..... 111
Figure 5.13. Current at storm peak at 18:00UTC on 1/27/2015 ..... 113
Figure 5.14. Waves at storm peak at 18:00UTC on 1/27/2015 ..... 114
Figure 5.15. Seabed shear-stresses and sand transport rate ..... 117
Figure 5.16. The time series of water level, wave height, current speed and sand transport rate at point A during the April 2007 nor'easter ..... 119
Figure 5.17. Seabed shear-stresses and sand transport rate ..... 121
Figure 5.18. The time series of water level, wave height, current speed and sand transport rate at point A during the 1991 Perfect Storm. ..... 123
Figure 5.19. Seabed shear-stresses and sand transport rate ..... 125
Figure 5.20. The time series of water level, wave height, current speed and sand transport rate at point A during the January 2015 North American blizzard ..... 127
Figure 5.21. Averaged wind, waves, currents and sand flux over the two tidal cycles between 08:30UTC 4/16/2007 and 09:30UTC 4/17/2007 when the storm was at its peak. ..... 130
Figure 5.22. Averaged wind, waves, currents and sand flux over the two tidal cycles between 14:00UTC 10/30/1991 and 15:00UTC 10/31/1991 when the storm was at its peak ..... 133
Figure 5.23. Averaged wind, waves, currents and sand flux over the two tidal cycles between 06:00UTC 1/27/2015 and 07:00UTC 1/28/2015 when the storm was at its peak ..... 137

## LIST OF EQUATIONS

Equation 2.1 ..... 8
Equation 2.2 ..... 8
Equation 2.3 ..... 8
Equation 2.4 ..... 9
Equation 2.5 ..... 9
Equation 2.6 ..... 9
Equation 2.7 ..... 12
Equation 2.8 ..... 15
Equation 3.1 ..... 31
Equation 4.1 ..... 63
Equation 4.2 ..... 63
Equation 4.3 ..... 63
Equation 4.4 ..... 64
Equation 4.5 ..... 64
Equation 4.6 ..... 64
Equation 4.7 ..... 64
Equation 4.8 ..... 65
Equation 4.9 ..... 70
Equation 4.10 ..... 79
Equation 5.1 ..... 97
Equation 5.2 ..... 97
Equation 5.3 ..... 97
Equation 5.4 ..... 97
Equation 5.5 ..... 98
Equation 5.6 ..... 98

Equation 5.7 ..... 98
Equation 5.8 ..... 98
Equation 5.9 ..... 98
Equation 5.10 ..... 99
Equation 5.11 ..... 99
Equation 5.12 ..... 99
Equation 5.13 ..... 99

# CHAPTER 1

# INTRODUCTION

According to NOAA's US Billion-dollar Weather and Climate Disasters report, the aggregated economic loss due to storm surge and wave damage in US coastal areas reached approximately 700 billion dollars during major storm events between 1980 and 2017 (https://www.ncdc.noaa.gov/billions/). The risk of storm-related damage, especially coastal flooding, will increase with sea level rise and intensification of storminess due to climate change (Nicholls, 2002; Kirshen et al., 2008; Emanuel, 2013; Roberts et al., 2017). Beach erosion and coastline retreat are issues related to storm events that also pose a great threat to coastal communities.

The Gulf of Maine, a large gulf of the Atlantic Ocean on the east coast of the U.S., is frequently swept by nor'easters: intense, extratropical storms that generate large waves, elevated water level, and coastal flooding due to a long wind fetch from the northeast off the Atlantic (Davis and Dolan, 1993). In the past 30 years, more than 20 notable nor'easters swept through the Gulf of Maine and caused extensive infrastructural damage, beach erosion, and sometimes loss of life (Chen et al., 2013). As a notable example, the April 2007 nor'easter generated large waves and a pronounced storm surge along the western periphery of the Gulf of Maine. The combination of high astronomical tides, storm surge and large waves resulted in significant coastal flooding and severe erosion along the vulnerable sandy coastline from southern Maine through Cape Cod, Massachusetts, U.S. Advanced coastal planning and risk management are needed to facilitate coastal adaptation and resilience to the projected sea level rise, increased storm frequency and intensity in the future (Kirshen et al., 2008; National Research Council, 2009).

Coastal flooding may occur under three scenarios: (1) the water level exceeds the crest elevation of natural barriers or coastal defenses, (2) waves rush up the shore and overtop the crest of natural barriers or coastal defenses, and (3) water flows through breaches in natural barriers or coastal defenses. In the Gulf of Maine, many types of coastal defenses (e.g., seawalls, revetments, groins and jetties) exist along the coast to protect buildings and infrastructure from storms and to prevent damage due to flooding and

erosion. Wave overtopping of seawalls occurs frequently during the storm season and seawall breaches resulting in major flooding of coastal communities has been reported during severe storms (MADCR, 2009; MACZM, 2013). The literature on coastal flooding due to wave overtopping at coastal defenses such as seawalls in the Gulf of Maine is limited (Zou et al., 2013). It is critical to develop predictive methods to quantify water level and waves during storms to assess the capacity of seawalls to protect communities against wave overtopping during future storms, and to provide guidance for the adaptation of coastal structures to reduce loss of life and property.

Storm-related sand transport and beach erosion are also problematic along the sandy coastline from southern Maine to Massachusetts in the Gulf of Maine. Large waves and strong currents are generated during storms, which alter the pattern of hydrodynamics and sediment transport both on continental shelves and in coastal bays and inlets (Warner et al., 2008; Warner et al., 2010; Mulligan et al., 2008, 2010; Orescanin et al., 2014; Wargula et al., 2014; Chen et al., 2015; Li et al., 2015; Li et al., 2017). Understanding the patterns of erosion and deposition during severe storms is thus important for coastal resources management and adaptation. However, due to the complex interactions between waves, currents and bathymetry, coastal hydrodynamics and sediment transport can present high variability both in space and time. Different storm conditions may add to the complexity because the magnitude and pattern of the waves and currents depend on storm characteristics (Young, 1988, 2006; Rego and Li, 2009, 2010; Holthuijsen, 2010; Li et al., 2017). The dominant processes driving both hydrodynamics and sand transport need to be clarified along with the impacts of different storm characteristics on coastal hydrodynamics and sand transport.

Coastal flooding, sand transport and beach erosion in the Gulf of Maine can be addressed based on the investigation of coastal hydrodynamics during storm events. The importance of investigating coastal hydrodynamics in the Gulf of Maine can be illustrated by demonstrating the ways that interactions between physical factors at different spatial and temporal scales influence: (1) the accurate prediction of locally elevated water levels and the battering waves that cause coastal flooding; (2) sediment transport in the littoral zone; (3) the delivery of nutrition and flushing of wastes at aquaculture facilities; and (4) the

design and robustness of coastal structures. However, the reliable prediction of storm surge, waves and their interaction in the Gulf of Maine remains a major challenge due to the complex bathymetry and topography, and large tidal range in this region. Prior to this work, there was a lack of comprehensive study of tide-surge and wave interaction throughout the Gulf of Maine.

The goal of this work was to develop an integrated atmosphere-ocean-coast model that links processes ranging from open ocean to surf zone scales and to apply it to the Gulf of Maine to (1) more accurately model the hydrodynamics of the region by including the interaction between tide-surge and waves; (2) model coastal flooding due to wave overtopping the seawall in Scituate, Massachusetts during a notable nor'easter storm and investigate the impact of sea level rise under similar storm conditions; (3) link the hydrodynamic model to sand transport and determine the response of sand transport to different storm characteristics.

The detailed objectives were as follows:

(1) To develop an integrated atmosphere-ocean-coast model that accurately predicts coastal hydrodynamics, flooding and sand transport for the planning and design of coastal adaptation strategies and structures.

(2) To incorporate tide-surge and wave interaction in shallow water areas of the Gulf of Maine, where the impact of currents, waves and surges are closely linked;

(3) To produce a better understanding of the coupling between tide-surge and waves during extratropical storms such as the April 2007 nor'easter in the Gulf of Maine.

(4) To accurately predict coastal flooding due to wave overtopping at a beach-seawall system.

(5) To investigate the impact of sea level rise on flooding behind seawalls due to wave overtopping for the planning and design of coastal defenses.

(6) To compare the hydrodynamic responses to storms with different tracks, intensities and durations in a coastal bay in the Gulf of Maine;

(7) To identify the contributions of waves, wave-induced current and wind-driven current to storm-induced sand transport;

(8) To investigate the spatial and temporal variations of storm-induced sand transport flux in a coastal bay in the Gulf of Maine.

The following chapters of the dissertation are focused on answering the questions raised above. Chapter 2 describes the application of the state-of-the-art two-way coupled SWAN+ADCIRC model on an unstructured grid covering the Gulf of Maine to simulate the hydrodynamic response in the Gulf of Maine during the April 2007 nor'easter. Chapter 3 investigates the tide-surge and wave interaction in shallow water areas in the Gulf of Maine, including in Saco Bay and over Georges Bank. Chapter 4 couples the hydrodynamic model with a surf zone model and a wave overtopping model to predict coastal flooding due to wave overtopping, and the impact of sea level rise at the seawall in Scituate, Massachusetts, to inform planning and design of coastal defenses. Chapter 5 investigates differences in the hydrodynamic responses to storms with different tracks, intensities and durations in Saco Bay and identifies the contributions of different forcing terms on storm-induced sand transport. The hydrodynamic model is also linked with a sand transport model to investigate spatial and temporal variations of sand transport flux in Saco Bay under storm conditions. Chapter 6 brings together the conclusions and includes a discussion of potential work to further improve the current study.

# CHAPTER 2

# APPLICATION OF SWAN+ADCIRC TO TIDE-SURGE AND WAVE SIMULATION IN THE GULF OF MAINE DURING THE APRIL 2007 NOR'EASTER

## 2.1 Background

Coastal flooding along the southern coast surrounding the Gulf of Maine is mainly caused by the combination of elevated water levels and waves during nor'easters. Nor'easters, so named for the direction from which their winds blow over land, are the cyclonic storms battering the northeastern coast of the United States from October through April (Davis and Dolan, 1993). In the past 30 years, more than 20 notable nor'easters swept through the Gulf of Maine and caused extensive infrastructural damage, beach erosion, and sometimes loss of lives (Chen et al., 2013).

The predictions of storm surges, waves, and coastal flooding in the area remains a challenging issue, which can be addressed from two aspects. First, the nonlinear interaction between tides, storm surges, and waves needs to be resolved with the presence of complex bathymetry and configuration of the coastline. Waves and currents interact with each other through the following physical mechanisms: (1) surface shear stress: the surface drag coefficient is modified with the presence of surface waves (Warner et al., 2008); (2) bottom stress: waves enhance turbulent mixing, and, therefore, modify the bottom stress experienced by currents (Grant and Madsen, 1979; Zou, 2004); and (3) radiation stress, which represents the excessive momentum flux within the circulation due to the presence of waves (Longuet-Higgins and Stewart, 1964; Zou et al., 2006 ). It is well understood that waves contribute to the total water level by wave set-up through radiation stress (Longuet-Higgins and Stewart, 1962), while wave transformation and propagation are affected by the water depth and currents. Other interaction processes between waves and currents, including the surface wind stress and bottom friction, require further exploration. The other aspect is the role of wave action in contributing to coastal damage. Large battering waves can cause significant damage by means of wave run-up and overtopping/splash-over despite water levels below the flood stage.

Numerical studies of hydrodynamic processes in the Gulf of Maine during extratropical storm events fall into three categories: (1) wave models (Sucsy et al., 1993; Panchang et al., 2008), (2) tide-surge models (Bernier and Thompson, 2007), and (3) coupled circulation and wave models (Beardsley et al., 2013; Chen et al., 2013). Only recently, fully-coupled circulation and wave models have been used to assess the contribution of wave-current interaction to coastal flooding (Beardsley et al., 2013; Chen et al., 2013). While Beardsley et al. (2013) and Chen et al. (2013) mainly focused on model skill assessment, the contribution of waves to circulation and surface elevation was not examined in detail.

In this study, a state-of-the-art fully-coupled model, the Simulating WAves Nearshore (SWAN) model with an unstructured grid and the ADvanced CIRCulation (ADCIRC) model, was used to investigate tide-surges and waves in the Gulf of Maine during the April 2007 Nor'easter. The chapter is organized as follows: Section 2.2 briefly introduces the Gulf of Maine. In Section 2.3, the April 2007 Nor'easter is described. A brief introduction of the numerical models, the ADCIRC and SWAN models, is presented in Section 2.4. The following two sections describe model setup, results, and discussion. Finally, conclusions are provided.

**2.2 Gulf of Maine**

The Gulf of Maine (Figure 2.1) is a mid-latitude marginal sea located on the North American continental shelf. It is bounded by the New England coastlines of the United States and Atlantic Canada. The seaward flank of the Gulf of Maine is the Georges Bank, a shallow submarine bank that separates the Gulf of Maine from the Northwest Atlantic Ocean, with a minimum water depth of less than 20 m. The geometry of the Gulf of Maine is characterized by several deep basins and shallow submarine banks. It also has the world's largest tidal range in the Bay of Fundy, the northern part of the Gulf of Maine.

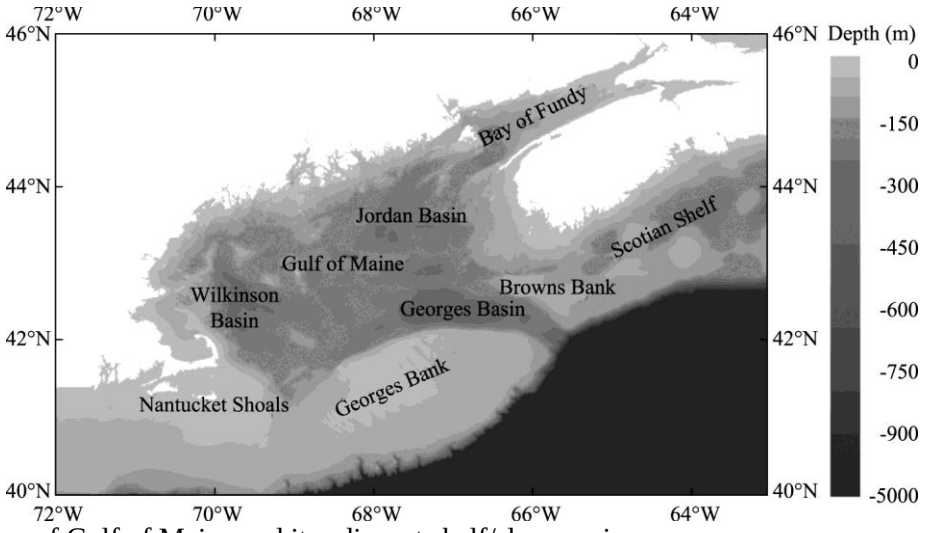

Figure 2.1. Map of Gulf of Maine and its adjacent shelf/slope region.

**2.3 April 2007 nor'easter**

The April 2007 Nor'easter severely impacted the northeastern United States from April 15 to 18, 2007. The surface low pressure system that triggered the development of the nor'easter originated in the southwestern United States. It intensified into a major storm as rapid cyclogenesis occurred well off the Mid-Atlantic Seaboard. A vigorous upper level low briefly retrograded the storm on a dangerous path toward the coastline, eventually allowing the system to become quasi-stationary near New York City on Monday morning, April 16. The lowest central barometric pressure recorded was 968 hPa, with its intensity similar to a moderate category II hurricane. The storm produced intense winds in the Gulf of Maine, with its peak wind gust above 70 m/s (Marrone, 2008).

The storm generated a pronounced storm surge and large waves acting along the western periphery of the Gulf of Maine. The recorded storm tide corresponded to a 10-year return period event in Portland, Maine. The storm tide peaked at Fort Point, New Hampshire, with a return period exceeding 50 years. The highest waves recorded by nearshore buoys were approximately 9 m (Marrone, 2008; Douglas and Fairbank, 2010). The combination of high astronomical tides, storm surges, and large battering waves resulted in significant coastal flooding and severe erosion along the vulnerable sandy coastline from southern Maine through Cape Cod, Massachusetts.

## 2.4 Methods

### 2.4.1 Advanced circulation model

The ADCIRC model, developed by Luettich et al. (1992) and Westerink et al. (1994), was used to simulate the response of water levels and currents to the April 2007 Nor'easter in the Gulf of Maine. The two-dimensional (2D) depth-integrated version, often referred to as ADCIRC-2DDI, was used in this study. It basically solves generalized wave continuity equations on an unstructured triangular mesh with a continuous Galerkin finite-element method. By using an unstructured triangular mesh, the model can resolve complex geometry and bathymetry. The governing equations in spherical coordinates are as follows:

$$\frac{\partial \zeta}{\partial t}+\frac{1}{R\cos\phi}\left[\frac{\partial UH}{\partial \lambda}+\frac{\partial\left(VH\cos\phi\right)}{\partial \phi}\right]=0 \qquad \text{(Equation 2.1)}$$

$$\frac{\partial U}{\partial t}+\frac{1}{R\cos\phi}U\frac{\partial U}{\partial \lambda}+\frac{V}{R}\frac{\partial U}{\partial \phi}-\left(\frac{\tan\phi}{R}U+f\right)V=-\frac{1}{R\cos\phi}\frac{\partial}{\partial \lambda}\left[\frac{p_s}{\rho_0}+g\left(\zeta-\alpha\eta\right)\right]+\frac{\nu_T}{H}\frac{\partial}{\partial \lambda}\left(\frac{\partial UH}{\partial \lambda}+\frac{\partial VH}{\partial \phi}\right)+\frac{\tau_{s\lambda}}{\rho_0 H}-\tau_* U \qquad \text{(Equation 2.2)}$$

$$\frac{\partial V}{\partial t}+\frac{1}{R\cos\phi}U\frac{\partial V}{\partial \lambda}+\frac{V}{R}\frac{\partial V}{\partial \phi}-\left(\frac{\tan\phi}{R}U+f\right)U=-\frac{1}{R}\frac{\partial}{\partial \phi}\left[\frac{p_s}{\rho_0}+g\left(\zeta-\alpha\eta\right)\right]+\frac{\nu_T}{H}\frac{\partial}{\partial \phi}\left(\frac{\partial VH}{\partial \lambda}+\frac{\partial VH}{\partial \phi}\right)+\frac{\tau_{s\phi}}{\rho_0 H}-\tau_* V \qquad \text{(Equation 2.3)}$$

where $t$ is time; $\lambda$ and $\phi$ are longitude and latitude, respectively; $\zeta$ is the free surface elevation relative to the geoid; U and V are depth-integrated velocity components in west-east and south-north directions, respectively; $H=\zeta+h$ is the total water depth and h is the bathymetric water depth relative to the geoid; $f=2\Omega\sin\phi$ is the Coriolis parameter and Ω represents the angular speed of the earth; $p_s$ is the atmospheric pressure at the free surface; η is the Newtonian equilibrium tide potential; α is the effective earth elasticity factor; $\rho_0$ $\rho_0$ is the reference density of water; R is the radius of the earth; g is gravitational acceleration; $\tau_{s\lambda}$ and $\tau_{s\phi}$ are the surface wind stresses in the longitudinal and latitudinal direction, which is computed by a standard quadratic air-sea drag law, and the air-sea drag coefficient is

defined by Garratt's drag formula (Garratt, 1977); $\tau_*$ is the bottom friction term; and $v_T$ is the depth-averaged horizontal eddy viscosity coefficient. The bottom friction term $\tau_*$ is defined as

$$\tau_* = C_f (U^2 + V^2)^{1/2} / H \quad \text{(Equation 2.4)}$$

where $C_f$ is the bottom friction coefficient.

### 2.4.2 Simulating waves nearshore model

A third-generation spectrum wave model, the SWAN model (Booij et al., 1999; Ris et al., 1999), was used for wave simulation in this study. The SWAN model solves the wave action balance equation and obtains wave parameters by integrating a 2D wave energy spectrum in the frequency and direction domain. Its governing equation in spherical coordinates is as follows:

$$\frac{\partial N}{\partial t} + \frac{\partial c_\lambda N}{\partial \lambda} + \cos^{-1}\phi \frac{\partial c_\phi \cos\phi N}{\partial \phi} + \frac{\partial c_\sigma N}{\partial \sigma} + \frac{\partial c_\theta N}{\partial \theta} = \frac{S_{\text{tot}}}{\sigma} \quad \text{(Equation 2.5)}$$

where $\sigma$ is the relative radian or circular frequency; $\theta$ is the wave propagation direction; $c_\lambda$ and $c_\phi$ denotes the speed of wave energy propagation in the longitudinal and latitudinal direction; $c_\sigma$ and $c_\theta$ are the wave energy propagation velocities in spectral space ($\sigma$, $\theta$); $S_{tot}$ is the source/sink term that represents all physical processes which generate, dissipate, or redistribute wave energy; and N is the wave action density, which is defined as:

$$N(\lambda, \phi, \sigma, \theta) = E(\lambda, \phi, \sigma, \theta) / \sigma \quad \text{(Equation 2.6)}$$

in which E represents the wave energy density. The source term on the right side of Equation (2.5) includes input energy from wind, dissipation by the bottom friction, wave breaking, and nonlinear wave-wave interactions.

### 2.4.3 SWAN+ADCIRC coupled model

Dietrich et al. (2011) integrated the unstructured-mesh SWAN model and the ADCIRC model, which is known as the SWAN+ADCIRC model. By sharing the same unstructured finite element mesh, the ADCIRC model and the SWAN model are coupled in the following way: the ADCIRC model first interpolates the input wind spatially and temporally onto the computational vertices and runs to calculate

water levels and currents. The wind field, water level, and currents are then passed to the SWAN model to obtain the wave spectrum by solving the wave action density balance equation. The radiation stress due to the presence of surface gravity waves (Longuet-Higgins and Stewart, 1962) is then passed to the ADCIRC model to predict the water levels and currents.

## 2.5 Model setup

### 2.5.1 Model domain

The model domain for tide-surge and wave simulations covers the Gulf of Maine and waters surrounding Cape Cod, Nantucket Sound, Buzzards Bay, and Nova Scotia (for the sake of simplicity, this area is referred to as the Gulf of Maine) (Figure 2.2). The water depth within the model domain ranges from about 4000 m in the deep ocean to less than 1 m in the coastal area. An unstructured mesh was created in the model domain as shown in Figure 2.2a, with 233939 nodes and 442641 triangular elements. The grid resolution ranges from 25 km along the offshore boundary to 10 m in the coastal area to locally resolve the bathymetry gradient and complicated geometry of coastline. Figure 2.2b shows the bathymetry and locations of wave buoys and tide gauges within the model domain, including wave buoys 44017 (Montauk Point, New York), 44027 (Jonesport, Maine), 44033 (West Penobscot Bay, Maine), and 44034 (Eastern Maine Shelf), and tide gauges 8418150 (Portland, Maine), 8423898 (Fort Point, New Hampshire), and 8452660 (Newport, Rhode Island).

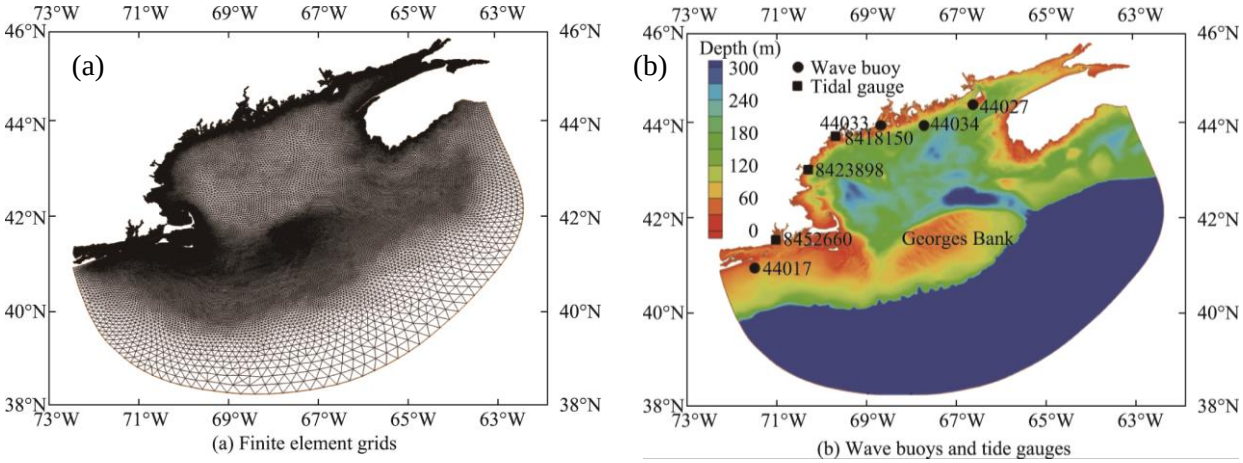

(a) Finite element grids (b) Wave buoys and tide gauges

Figure 2.2. Finite element grids, wave buoys, and tide gauges in model domain.

### 2.5.2 Surface wind and air pressure forcing

The National Centers for Environmental Prediction (NCEP)/North American Regional Reanalysis (NARR) dataset (http://www.esrl.noaa.gov/psd/) was used as the surface wind and pressure forcing for the model. Covering the North American region, the NARR dataset uses the high-resolution NCEP Eta Model (32 km/45 layers) together with the regional data assimilation system (RDAS). With improved modeling and assimilation, the NARR dataset is more accurate than the other reanalysis dataset available in this area. Currently, it contains eight daily outputs (00Z, 03Z, 06Z, 09Z, 12Z, 15Z, 18Z, and 21Z) at 29 levels of temperature, wind, pressure, and precipitation.

The wind outputs at 10 meters above the sea surface were compared with the wave buoy measurements in the Gulf of Maine. Figure 2.3 shows the comparison of wind speed and direction at two wave buoys, in which Obs denotes the wave buoy observations and NARR denotes the NARR outputs. The NARR outputs agree reasonably well with the wave buoy observations, which provides confidence for wave and tide-surge modeling.

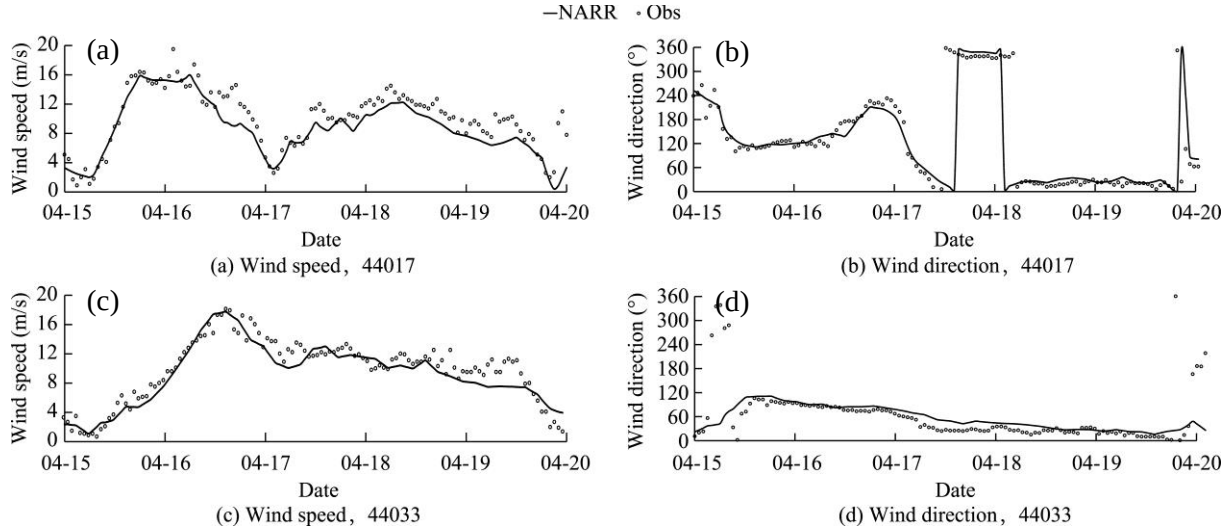


Figure 2.3. Comparison of NARR wind outputs with wave buoy observations during April 2007 Nor'easter.

### 2.5.3 Model parameters

The ADCIRC-2DDI model is used for tide-surge simulation. The finite amplitude and convection terms are activated. Lateral viscosity is set at a constant of 5 $m/s^2$ through the whole domain (Yang and

Myers, 2008). The hybrid bottom friction relationship is used to specify a varying bottom friction coefficient depending on water depth (Luettich and Westerink, 2006):

$$C_{\mathrm{f}} = C_{\mathrm{f\,min}}\left[1+\left(\frac{H_{\mathrm{break}}}{H}\right)^{\theta_{\mathrm{f}}}\right]^{\gamma_{\mathrm{f}}/\theta_{\mathrm{f}}} \quad \text{(Equation 2.7)}$$

where $C_f$ is the bottom friction coefficient, $C_{fmin}$ is the minimum bottom friction coefficient, $H_{break}$ is the break depth, $\theta_f$ is a dimensionless parameter that determines how rapidly the hybrid bottom friction coefficient approaches its deep water and shallow water limits when the water depth is greater than or less than $H_{break}$, and $\gamma_f$ is a dimensionless parameter that determines how the friction factor increases as the water depth decreases. When the water depth is below $H_{break}$, the formulation applies a depth-dependent, Manning-type friction law, while a standard Chezy friction law is used when the depth is greater than $H_{break}$. The parameters in the Equation (2.7) are set to $C_{fmin}$ = 0.03, $H_{break}$ = 2.0 m, $\theta_f$ = 10, and $\gamma_f$ = 1.33333 as recommended by Luettich and Westerink (2006).

For the calculation of surface wind stress, the wind drag coefficient described by Garratt (1977) with a cap of $C_d \leq 0.0035$ is used. The eight most significant astronomical tide constituents (M2, S2, N2, K2, K1, P1, O1, and Q1) are used to drive the model along the open boundary. The corresponding harmonic constants of the eight tidal constituents are interpolated from the OSU TOPEX/Poseidon Global Inverse solution TPXO (Egbert and Erofeeva, 2002). The time step for the ADCIRC model is set to one second to maintain computational stability.

The wave simulation model, i.e., the SWAN model, shares the same unstructured mesh and surface wind forcing with the ADCIRC model. Along the offshore boundary, wave spectra based on National Oceanic and Atmospheric Administration (NOAA) WAVEWATCHIII hindcast reanalysis data in the northwestern Atlantic Ocean (ftp://polar.ncep.noaa.gov/pub/history/waves) are used to allow swells generated outside of the model domain to propagate reasonably into the model domain.

The prescribed spectrum frequencies range from 0.04 to 1.00 Hz and are discretized into 34 bins on a logarithmic scale. The wave spectrum is solved in full circles with the directional resolution being 10

degrees. The Jonswap formulation (Hasselmann et al., 1973) is used for the bottom friction. The friction coefficient of 0.038 $m^2/s^3$ is used for both wind waves and swells (Zijlema et al., 2012). The time step for integration is set to 600 seconds.

The coupling interval of the model is the same as the time step for wave integration. The ADCIRC model passes wind forcing, water levels, and currents to the SWAN model every 600 seconds, while the SWAN model passes radiation stress to the ADCIRC model to update circulation calculations. The model ran for 30 days from April 1, 2007 to April 30, 2007 from a cold start. The elevation-specified boundary condition was first ramped up for five days with a hyperbolic tangent function until an equilibrium state was reached before surface wind and pressure forcing were applied.

Three cases were run in this study: (1) the ADCIRC model run for tide-surge simulation, (2) the SWAN model run for waves, and (3) a fully coupled SWAN+ADCIRC model run considering wave effects on circulation.

### 2.6 Results and discussion

#### 2.6.1 Tide and surge validation

The tide simulated by the ADCIRC model during the April 2007 Nor'easter was first compared with observed data from tide gauge data. This is a prerequisite since coastal flooding often coincides with high tides. The water level recorded by NOAA/CO-OPS tidal stations was analyzed using the MATLAB harmonic analysis toolbox T-Tide (Pawlowicz et al., 2002) to extract tidal components. The extracted tide series was then compared with the model prediction. Figure 2.4 shows the comparison results at three tide gauges along the coast of the Gulf of Maine: tide gauges 8418150, 8423898, and 8452660. In Figure 2.4, astronomic tide denotes the tide level generated by harmonic analysis of the recorded tide gauge data and ADCIRC tide denotes model simulation results. Generally, the simulated tide agrees with the observation both in magnitude and phase. The simulated tide is slightly lower than that of observed data at high tide, which may be due to the overestimated bottom friction coefficient in the model.

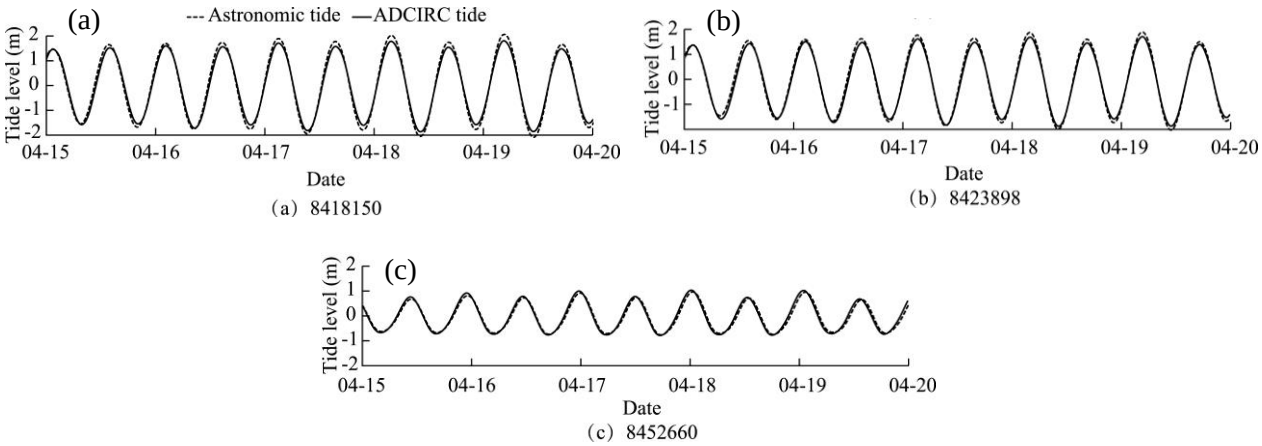


Figure 2.4. Comparison of simulated tide level with astronomic tide level during April 2007 Nor'easter at different tide gauges.

The surface wind and pressure forcing were then added to the model to simulate storm surges during the April 2007 Nor'easter. Figure 2.5 shows the comparison of simulated surge levels with observations. Obs denotes the observed storm surge level and ADCIRC surge denotes modeling results.

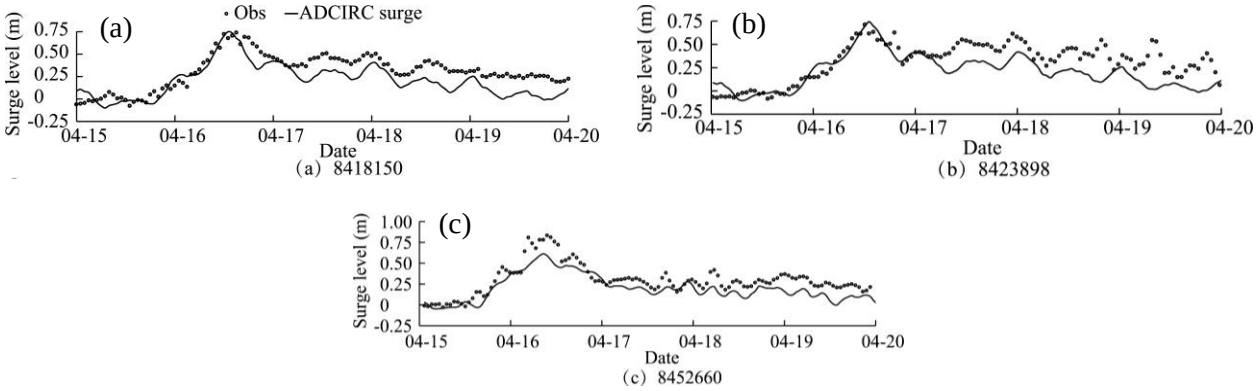


Figure 2.5. Comparison of computed storm surge with observed data during April 2007 Nor'easter at different tide gauges.

At tide gauges 8418150 and 8423898, the predicted peak surge level agrees with the observed data. The oscillation after a surge peak with a similar frequency of tides may be due to strong surge-tide interactions. At tide gauge 8452660, the surge peak is under-predicted by approximately 0.2 m. After the peak of the surge, the surge level is under-predicted, which can be explained by the short fetch from the east boundary of the mode domain to the western periphery of the Gulf of Maine. A simple way to estimate storm surge formation is described by Pugh (1987). For an equilibrium state with a constant

wind field, the sea surface slope can be expressed by a simple linear, steady-state expression so that the surge level at the coast is as follows:

$$\zeta \propto \frac{C_d \rho_A W^2 L}{g \rho D} \qquad \text{(Equation 2.8)}$$

where $\zeta$ is the surge level at the coast, $L$ is the shelf width, $D$ is the averaged water depth, $W$ is the wind speed, $C_d$ is the wind drag coefficient, $\rho_A$ is air density, and $\rho$ is the density of sea water. When offshore wind veers from the southeast to the east as the storm moves to the east, the shelf width L within the model domain is not long enough to predict the observed surge at the coast without proper offshore surge boundary conditions. In this case, it may be more reasonable to specify water level or current velocity instead of tidal constituents to take the surge along the open boundary into consideration.

### 2.6.2 Wave validation

Wave simulations were compared with buoy data in Figure 2.6, in which Obs denotes observed buoy data and SWAN wave denotes simulated results. Figures 2.6a through (d) are the comparisons of significant wave height (SWH) and Figures 2.6e through (h) show the comparisons of dominant wave period (DPD).

Figure 2.6. Comparison of simulated wave parameters with buoy data during April 2007 Nor'easter at different wave buoys.

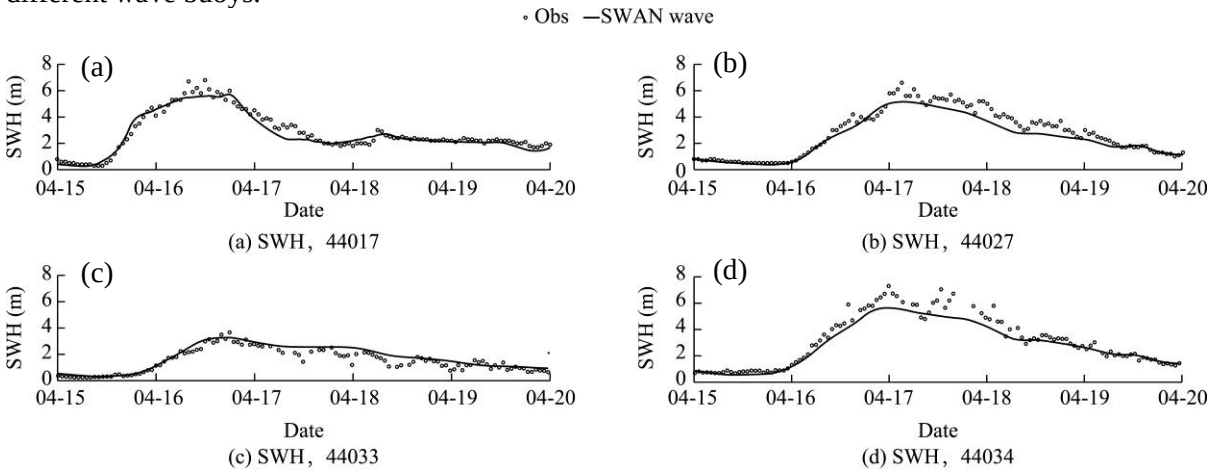

Figure 2.6 Continued

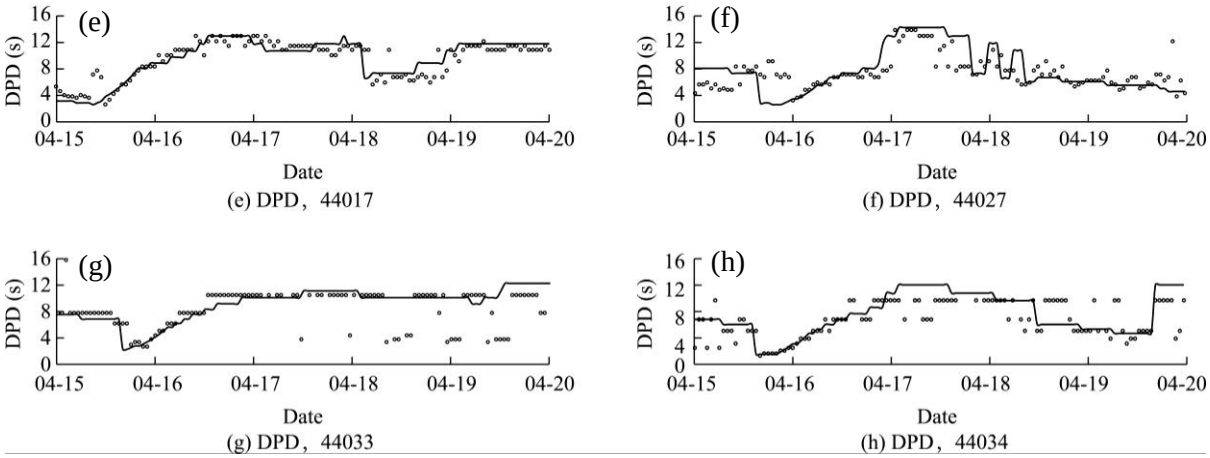


Wave growth and decay can be well reproduced by the model. The peak SWH was underestimated by approximately 1.4 m at buoys 44027, 44034, and 44017, while the DPD was generally in agreement with observations. The underestimation can be largely attributed to the error in surface wind forcing. It is widely accepted that 10 percent error in the input wind speed will result in 20 to 25 percent error in the simulation of SWH (Teixeira et al., 1995). The NARR wind data were measured every three hours, with a grid resolution of 32 km, which can be improved to produce better results.

### 2.6.3 Evolution of waves

Snapshots of wind and wave fields at 1400 coordinated universal time (UTC), April 16, 2007 are presented in this section to describe wave evolution in the modeling domain. The SWH and water level reached their maxima in the southern part of the Gulf of Maine at this moment.

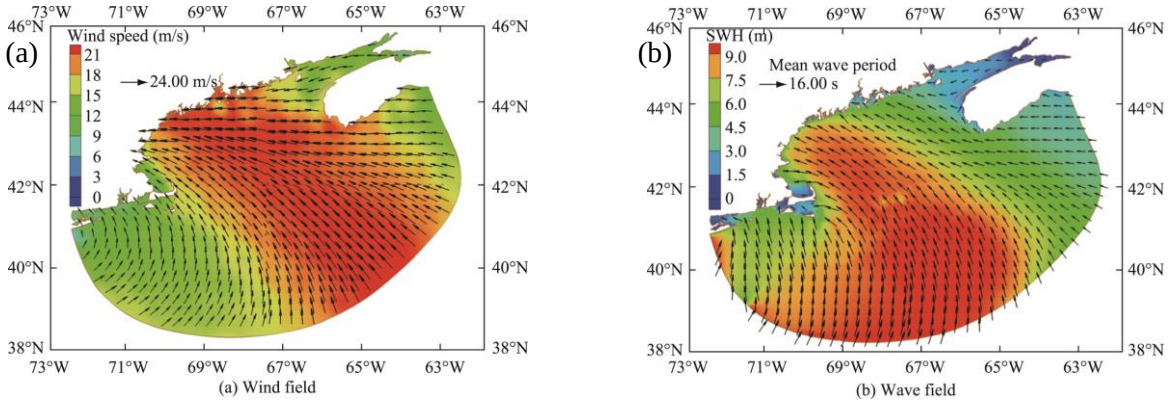


Figure 2.7. Snapshots of wind and wave fields at 1400 UTC April 16, 2007.

As shown in Figure 2.7b, the storm-generated SWH exceeds 5.0 m over most of the model domain, with its maximum being approximately 9.0 m off the Georges Bank. The wave distribution can be approximated by spectral theory depending on whether it is fetch-limited or duration-limited. While SWH will grow in the downwind direction, wave energy will be dissipated by processes including whitecapping, bottom friction, and wave breaking. When waves propagate from deep water into the inner gulf area, wave energy is dissipated over the Georges Bank, as characterized by several troughs and ridges and the minimum water depth of less than 20 m. This phenomenon indicates that the Georges Bank plays an important role in decreasing SWH propagation from offshore into the inner gulf area. Also, SWH further decreases toward the shore due to the bottom friction and wave breaking.

### 2.6.4 Depth-averaged currents

The depth-averaged current fields for the three study cases in the Gulf of Maine at 1400 UTC April 16, 2007 are plotted in Figure 2.8. Figure 2.8a shows tidal circulation only, Figure 2.8b presents the combination of circulations driven by tide and meteorological forcing, and Figure 2.8c considers the effect of waves on circulation by the coupled SWAN+ADCIRC model.

Figure 2.8 Snapshots of circulation in Gulf of Maine at 1400 UTC April 16, 2007.

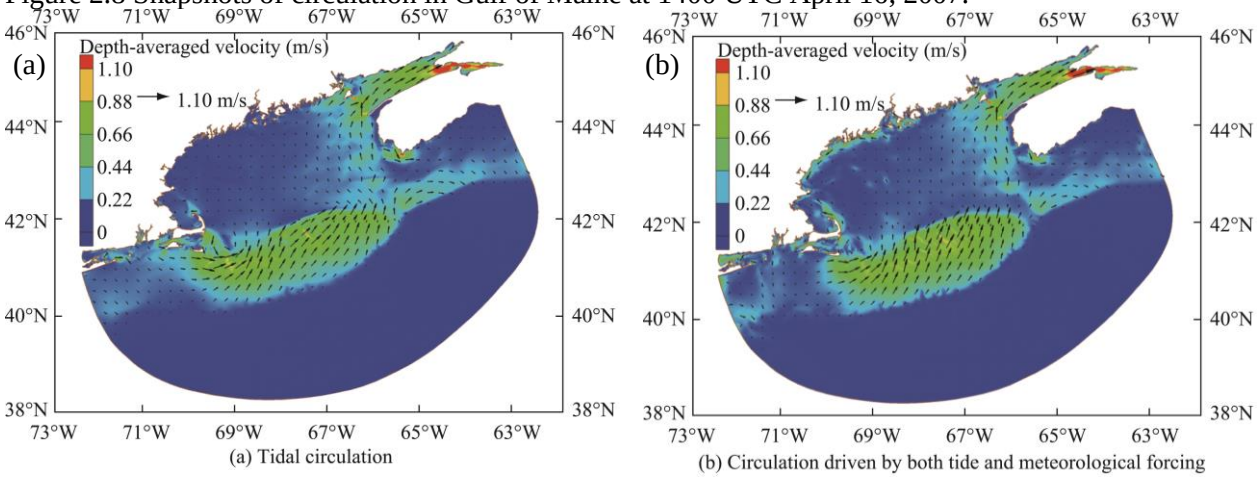

Figure 2.8 Continued

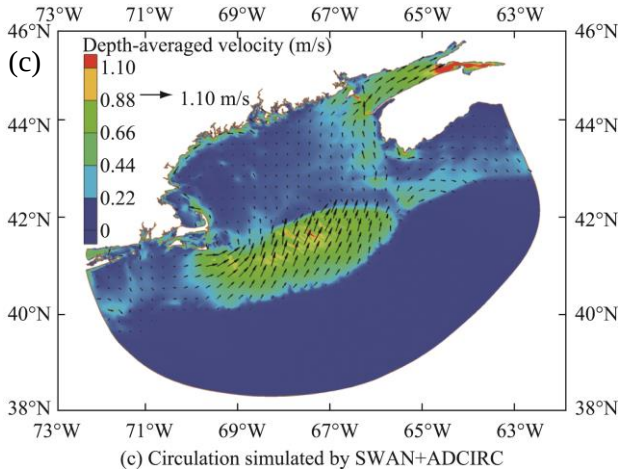

(c) Circulation simulated by SWAN+ADCIRC

The tidal current is dominant over most of the modeling domain, except areas adjacent to the coastline, by comparing Figures 2.8a and 2.8b. The maximum tidal current occurs within the Bay of Fundy and can reach 2.0 m/s. The Georges Bank is another area where large tidal currents are found. At the southern flank of the bank, the depth-averaged tidal current ranges from 0.6 m/s to 0.8 m/s. At the northern flank, the tidal current is slightly larger, between 0.7 m/s and 0.9 m/s. Over the bank with the minimum water depth, the tidal current speed can reach 1.0 m/s.

Figure 2.8b shows the combined depth-averaged velocity driven by both tides and the meteorological forcing. The magnitude of depth-averaged velocity driven by the meteorological forcing significantly increases in the coastal area. Along the west coast of the Gulf of Maine, the current exceeds 0.5 m/s in most areas and is generally in the longshore direction. A simple model can be used to explain this. In the vicinity of the coast, where the condition of no cross-boundary flow can be applied, longshore currents will be generated by the surface wind stress acting parallel to the coastline. The magnitude of the current will generally be inversely proportional to the water depth and eventually be limited by the bottom friction (Pugh, 1987). Meanwhile, in the cross-shore direction, a sea-level gradient normal to the coast will be generated to balance the surface wind stress in the cross-shore direction. Over the Georges Bank, the magnitude of depth-averaged velocity increases and the current direction shifts further north, driven by the meteorological forcing.

Figure 2.8c shows the circulation field considering wave effects on currents through the wave radiation stress, which is mainly significant in shallow water areas where the wave height changes drastically due to wave transformation, e.g., the shoaling effect, wave refraction, bottom friction dissipation, and wave breaking. The depth-averaged velocity mostly increases over the Georges Bank by approximately 0.2 m/s when compared with Figure 2.8b. Since wave energy significantly dissipates over the Georges Bank when it propagates from offshore into the inner gulf (Figure 2.7b), it exerts excess momentum flux on mean circulation, adding net transport into the inner gulf area.

### 2.6.5 Residual currents

The meteorological and wave-driven residual currents are further analyzed at 1400 UTC April 16, 2007 in this section. Figures 2.9a and 2.9b show the residual water level and currents driven by the meteorological forcing and waves, respectively.

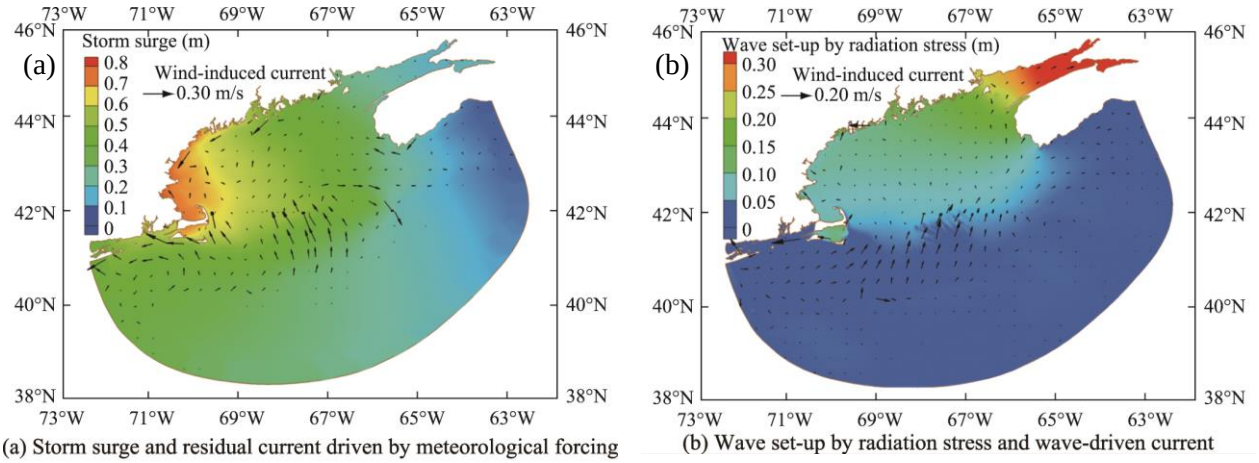


(a) Storm surge and residual current driven by meteorological forcing

(b) Wave set-up by radiation stress and wave-driven current

Figure 2.9. Snapshots of meteorological and wave-driven residual currents at 1400 UTC, April 16, 2007.

The storm surge level driven by the meteorological forcing can reach 0.8 m at the western coast of the Gulf of Maine (Figure 2.9a), which agrees with the results obtained by Marrone (2008). The current driven by the meteorological forcing is mainly significant over the Georges Bank and along the coast, the magnitude of which reaches 0.3 m/s.

The wave-driven residual current shows a different pattern (Figure 2.9b) compared with that driven by the meteorological forcing. The wave set-up by radiation stress reaches its maximum of 0.3 m

in the Bay of Fundy and decreases from north to south, as well as from the coast to offshore. The maximum wave-driven current is over the Georges Bank and along the coast, with its magnitude being 0.2 m/s. Over the Georges Bank, the residual current mainly travels to the north, adding net volume transport into the inner gulf area. Along the coast, the longshore residual current mainly comes from the oblique incidence of waves, introducing longshore wave radiation stress exerted on the mean current. This longshore current will be limited by the bottom friction.

**2.7 Conclusions**

In April of 2007, an intense nor'easter, the April 2007 Nor'easter, swept through the coast of the Gulf of Maine and caused significant coastal flooding and severe beach erosion along the New England coastline. A state-of-the-art fully coupled model, the SWAN+ADCIRC model, was used to study the hydrodynamic response to this notable storm in the Gulf of Maine. The model reasonably reproduced the tides, storm surges, and large waves when compared with tide gauge and wave buoy data. Wave distribution and circulation were analyzed and the following can be concluded:

(1) Wave energy generated by wind well offshore is significantly dissipated over Georges Bank, a region characterized by several deep troughs and shallow ridges, indicating that Georges Bank plays an important role in decreasing SWH when waves propagate from the open northwest Atlantic Ocean toward the inner Gulf of Maine.

(2) The residual currents driven by the meteorological forcing and waves, which reach their maxima of 0.3 m/s and 0.2 m/s, respectively, are enhanced over the Georges Bank and along the western coast of the Gulf of Maine.

(3) Near the coast, where the condition of no normal flow can be applied, the longshore current generated by the wind and wave radiation stress is inversely proportional to the water depth and eventually limited by the bottom friction. The wave set-up due to the radiation stress gradient reaches 0.2 m along the western coast, which has an important implication for coastal flooding.

# CHAPTER 3

# TIDE-SURGE AND WAVE INTERACTION IN THE GULF OF MAINE DURING AN EXTRATROPICAL STORM

## 3.1 Background

The interaction between tide, surge and wave during storm events can be significant in shallow waters where it is enhanced by complicated bathymetric features and geometric configurations (e.g. Wolf, 2009; Nicolle, 2009). Accurate prediction of water level and waves in coastal areas, especially low-lying areas prone to flooding, requires a better understanding of these processes (Zou et al., 2013). Tide, surge and wave interaction have also been found to have significant impacts on sediment transport in the littoral zone (e.g. Warner et al., 2008; Warner et al., 2010).

Tide-surge and waves interact with each other through their influences on the mean water depth/water level and currents. Wave and current in turn is coupled through wave radiation stress (e.g. Longuet-Higgins and Stewart, 1962, 1964; Zou et al., 2006; Ardhuin et al., 2008; Mellor, 2005, 2008), bottom stress (e.g. Grant and Madsen, 1979; Zou, 2004) and surface stress in the presence of waves (e.g. Johnson et al., 1998; Taylor et al., 2001; Moon et al., 2004a, 2004b; Haus, 2007). The mechanisms of tide-surge and wave interaction have been summarized in several papers (e.g. Ozer et al., 2000; Wolf, 2009).

In addition, it is well known that waves give rise to near-surface drift currents known as the Stokes drift. Wind-generated surface currents are modified by wind-wave and wave-current momentum transfer (e.g. Jenkins, 1986, 1987a, 1987b, 1989). The total surface current is the sum of the wave modified current, the Stokes drift and the tidal current (e.g. Perrie et al., 2003; Tang et al., 2007). While 3D wave radiation stress has been derived (e.g. Mellor, 2005, 2008; Ardhuin et al., 2008), the 2D wave radiation stress by Longuet-Higgins and Stewart (1962, 1964) is still widely used (e.g. Dietrich et al., 2012; Bolaños et al., 2014). In shallow water, wave propagation and transformation is strongly dependent on water depth, and therefore on tide and surge level. Currents also cause a Doppler shift of wave frequency and refraction due to horizontal current and current gradients (Komen et al., 1996).

In the coastal area, waves contribute to water level through wave setup and drive longshore and cross-shore current due to the excess momentum flux induced by waves, which is parameterized as wave radiation stress (Longuet-Higgins and Stewart, 1961, 1962, 1964; Xia et al., 2004; Zou et al., 2006; Mellor, 2005, 2008; Ardhuin et al., 2008; Bennis et al., 2011; Sheng et al., 2011). Waves affect surge generation through wave-induced surface roughness and stress (e.g. Janssen, 1989, 1991; Craig and Banner, 1994; Brown and Wolf, 2009). In shallow water, waves enhance the bottom friction experienced by currents (e.g. Grant and Madsen, 1979; Christoffersen and Jonsson, 1985; Xie et al., 2001; Zou, 2004). Many other studies of wave-current interaction have been carried out previously, e.g., Perrie et al. (2003), Tang et al. (2007) and Uchiyama et al. (2009, 2010).

In this paper, we mainly focus on addressing tide-surge and wave interaction in shallow water areas in the Gulf of Maine, where the impacts of currents, waves and surges are closely linked. Since wave radiation stress is only significant where wave height changes drastically due to wave energy dissipation by wave breaking and bottom friction, its impact on mean current in the deep ocean is negligible.

The Gulf of Maine is an area frequently attacked by nor'easters, the intense, extratropical storms with a prolonged northeast fetch off the Atlantic which generate large waves and elevated water level and cause coastal flooding. The April 2007 Nor'easter in April 2007 is a notable example of nor'easter storms. The lowest central barometric pressure recorded was 968 hPa, with its intensity like a moderate category II hurricane. The storm took a dangerous path toward the coastline (Figure 3.1) and swept through the northeastern United States during April 15-18, 2007. It became quasi-stationary near New York City in the morning of April 16, generating persisting strong southeast wind in the Gulf of Maine, with its peak wind gust above 70 m/s (Marrone, 2008). The storm quickly weakened and moved to the east on April 17. It intensified again on April 18 and produced strong northeast wind in the Gulf of Maine (Figure 3.1 and Figure 3.2).

The storm generated a pronounced storm surge and large waves along the western periphery of the Gulf of Maine. The combination of high astronomical tides, storm surge, and large battering waves

resulted in significant coastal flooding and severe erosion along the vulnerable sandy coastline from southern Maine through Cape Cod, Massachusetts. The storm tide near Portland exceeded that of the 1991 “Perfect Storm”. The widespread and severe coastal flooding caused an estimated $22 million in damage to public coastal infrastructure (Marrone, 2008).

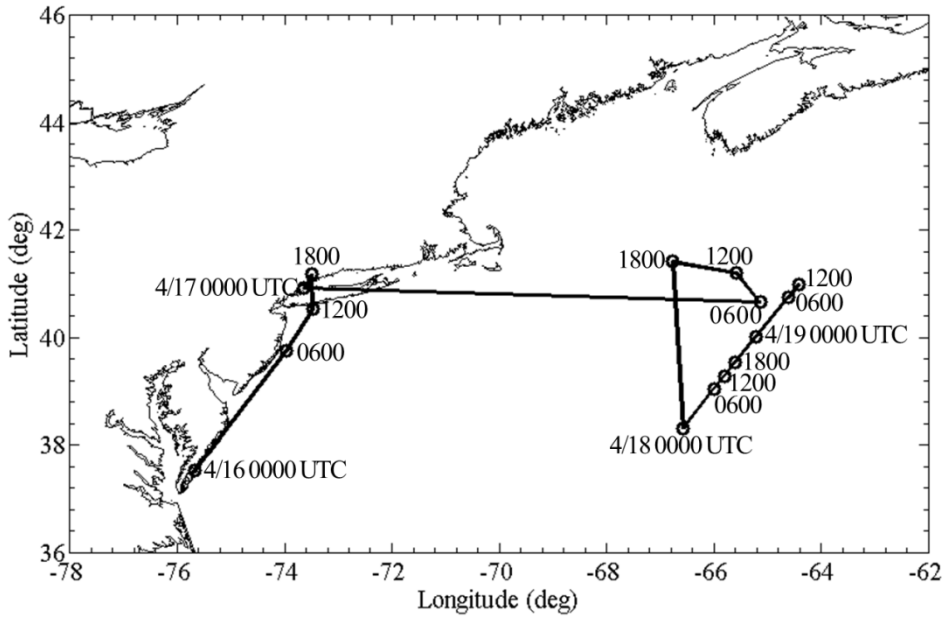


Figure 3.1. Storm track of the April 2007 Nor’easter created by NCEP North American Regional Reanalysis meteorological data. The circles are the locations of the storm center at 6-hourly time interval from 0000UTC 4/16/2007 to 1200 UTC 4/19/2007.

The reliable prediction of storm surge and waves in the Gulf of Maine remains a major challenge due to the complex bathymetry and topography and large tidal range in this region. The accuracy of the wave and surge forecasts is largely dependent on the quality of ocean bathymetry and meteorological forcing that drives the model. Maine has an extremely complex coastline and rapidly changing bathymetry on all scales, so both wind and wave fields are subject to drastic changes along the coast. Wave propagation, growth and dissipation will be heavily influenced by the local wind, bathymetry and surrounding islands (Panchang et al., 2008).

In the past, the numerical studies of tide-surge and waves in the Gulf of Maine have been carried out separately and mainly on nested structured grids. For example, Panchang et al. (2008) conducted

numerical simulation on waves and analyzed wave climate in the Gulf of Maine. In this study, they coupled NOAA's open ocean wave predictions to two coastal, high-resolution, regional and local domain structured grids. Bernier and Thompson (2007) used a modified version of the Princeton Ocean Model to investigate tide-surge interaction in the Gulf of Maine. Only recently, a fully-coupled circulation and wave model, FVCOM-SWAVE on unstructured grids (Sun et al., 2013; Beardsley et al., 2013; Chen et al., 2013) was applied to study waves and circulation in the Gulf of Maine. Sun et al. (2013) investigated the effect of wave-current interaction on storm surge prediction. Chen et al. (2013) evaluated the performance of three fully-coupled current-wave ocean models (ADCIRC/SWAN, FVCOM/SWAVE, SELFE/WWM) for the prediction of coastal inundation at Scituate harbor, Massachusetts during two nor'easters including the April 2007 Nor'easter.

Panchang et al. (2008) pointed out that due to the large tidal range in Maine, the tidal currents are likely to have significant impact on wave propagation. Up to now, however, there is little knowledge of the tide and current effects on waves in the Gulf of Maine. Only very recently, Sun et al. (2013) investigated the wave-current interaction during Hurricane Bob using FVCOM-SWAVE model. But for this storm, they found little tidal effect on surface waves. Xie et al. (2016) applied ADCIRC and SWAN to study tide-surge and waves respectively without considering wave-current interaction at the coast of the Gulf of Maine. In this paper, we examine the tide-surge effect on waves at the coastal areas of Maine during the April 2007 Nor'easter.

The tide-surge model ADCIRC coupled with the nearshore spectral wave model SWAN on the same shared unstructured mesh will be used in this study. ADCIRC's finite element method based approach enables the discrete points to be placed in a highly flexible and unstructured fashion with high resolution in coastal regions and low resolution in deep ocean. The complex bathymetry and topography of the coast of Maine including the nearby mainland, islands, jetties and other structures is best captured in this way. Numerous studies have shown this model to be accurate for computing the variations in water level during extreme events throughout the Western North Atlantic and Gulf of Mexico region (Luettich

et al., 1994; Mukai et al., 2001; Westerink et al., 2008). Zijlema (2010) developed and tested an updated version of SWAN on unstructured grids.

Currently there is a lack of comprehensive study of tide-surge and wave interaction throughout the Gulf of Maine. The objective of this paper is to better understand the coupling between tide-surge and waves during an extratropical storm such as the April 2007 Nor'easter in the Gulf of Maine, with special attention to Georges Bank and Saco Bay. The former is one of the most productive shelf ecosystems in the world (Fry, 1988) and the latter has suffered from severe erosion in the past decades (Hill et al., 2004).

The chapter is organized as follows. A brief description of the fully coupled tide-surge-wave model SWAN+ADCIRC and model setup are given in Section 3.2. In Section 3.3, the model prediction is validated against the measurements. The tide-surge and wave interaction in the Gulf of Maine is evaluated based on model results and discussed in Section 3.4. Finally, conclusions and discussions are presented in Section 3.5.

Figure 3.2. Time evolution of pressure and wind fields during the April 2007 Nor'easter by NCEP North American Regional Reanalysis meteorological data from April 16 to April 18, 2007. The color maps illustrate atmospheric pressure at the sea surface. The vectors represent the wind field at 10 m above the sea surface.

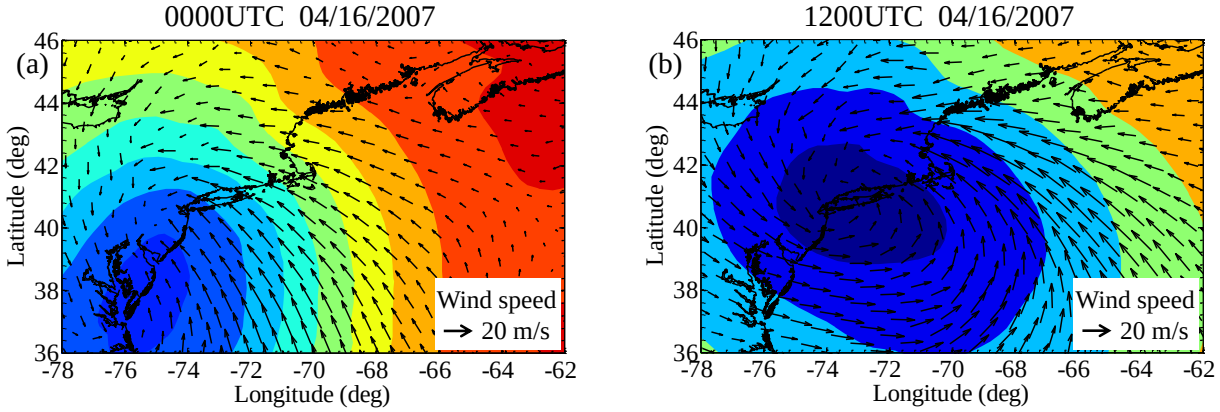

Figure 3.2 Continued

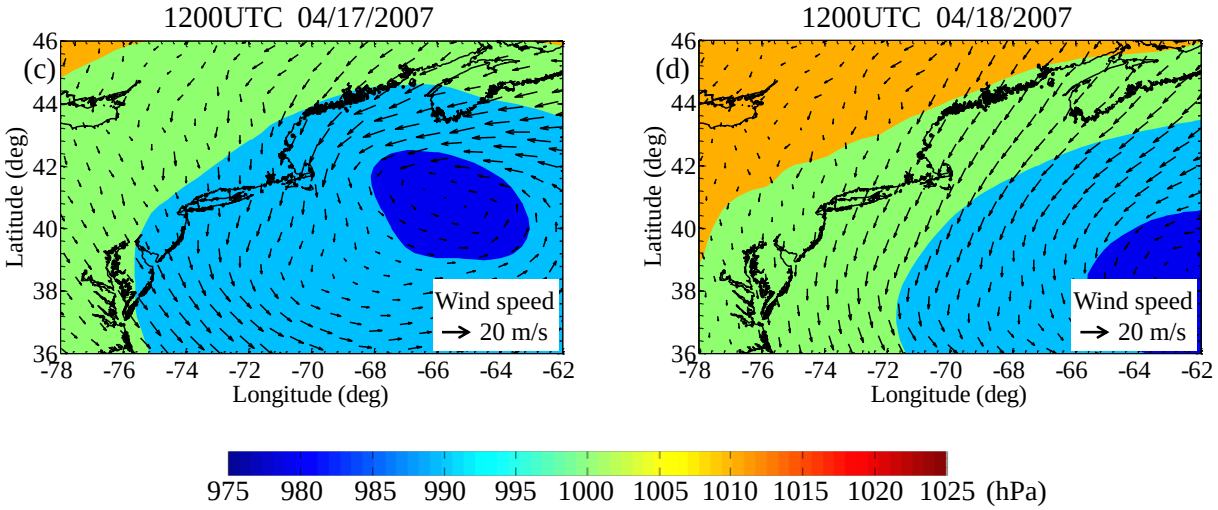


### 3.2 SWAN+ADCIRC model

#### 3.2.1 Model description

The ADvanced CIRCulation (ADCIRC) model was used to simulate the response of water level and currents in the Gulf of Maine during the April 2007 Nor'easter. The model was originally developed by Luettich et al. (1992) and Westerink et al. (1994). The two-dimensional (2-D) depth-integrated version, often referred to as ADCIRC-2DDI, was used in this work. This model solves generalized wave continuity equations on an unstructured finite element mesh with a continuous-Galerkin finite-element formation. By using an unstructured triangular mesh, the model provides considerable flexibility in resolving complex geometry and bathymetry. The ADCIRC-2DDI is particularly suitable for predicting storm surge and coastal inundation with high computing efficiency (Luettich et al., 1992; Westerink et al., 1994; Dietrich et al., 2012). It has been implemented to model coastal circulation by Chen et al. (2008) and Dietrich et al. (2010). In this paper, we mainly focus on wave-current interaction in relatively shallow water areas, i.e., Georges Bank and Saco Bay, where the 2-D model is appropriate.

The third-generation spectrum wave model Simulating WAves Nearshore (SWAN) model is a third-generation phase averaged wave model that computes random, short-crested wind-generated waves in coastal regions and inland water based on wind, bottom topography, currents and tides (Booij et al.,

1999; Ris et al., 1999). The SWAN model accounts for wave triad and quartet interactions, depth-induced wave breaking, bottom friction and whitecapping dissipation. It solves the wave action balance equation and obtains wave parameters by integrating the two-dimensional wave energy spectrum in the frequency and direction domain. Zijlema (2010) developed a new unstructured-grid procedure for the spectral wind-wave model SWAN. The unstructured-grid version of SWAN uses a vertex-based, fully implicit, finite difference method which can accommodate unstructured meshes with a high variability in geographic resolution. Although the unstructured version of SWAN is numerically stable in time integration which adopts the first order implicit Euler scheme, the model results may also be improved by reducing the time step based on our sensitivity tests and previous study by Zijlema (2010).

ADCIRC and SWAN share the same unstructured finite element mesh when they are coupled. ADCIRC interpolates the input wind spatially and temporally onto the computational vertices to calculate water level and currents. The wind field, water level and currents are then passed to the SWAN model. SWAN is run on the same interval, using the average of the ADCIRC variables from the interval in its computations to predict directional wave spectra by solving the wave action density balance equation. After its time step, SWAN computes the radiation stress gradients and passes them to ADCIRC, which then begins the process anew on the next interval (Dietrich et al., 2011). The radiation stress (Longuet-Higgins and Stewart, 1964) is important in predicting water levels and currents especially within the surf zone area (Dietrich et al., 2011).

### 3.2.2 Model domain

The model domain covers the Gulf of Maine and adjacent waters surrounding Cape Cod, Nantucket Sound, Buzzards Bay and Nova Scotia (for simplicity, this area is referred to as the Gulf of Maine). The water depth ranges from about 4,000m in the deep ocean to less than 1m in the coastal area. An unstructured mesh was created with 170,970 nodes and 317,992 triangular elements. The grid resolution ranges from 25,000 m along the offshore boundary to 15 m in the coastal area to locally resolve the bathymetry and complicated geometry of coastline. Figure 3.3 shows the model coverage and the

unstructured mesh. The detailed information of wave buoys and tide gauges within the model domain is listed in Table 3.1 and Table 3.2, respectively.

The model domain was selected based on previous and present domain and grid sensitivity studies of SWAN+ADCIRC for severe storms. For example, the hurricane storm surge study by Blain et al. (1994) indicates that the domain with deep Atlantic Ocean boundaries minimizes the influence of boundary conditions. Chen et al. (2013) and Beardsley et al. (2013) also selected a domain with boundaries well off continental shelf break for coastal inundation simulation in the Gulf of Maine. Nevertheless, the 2-D Depth Integrated (2DDI) model of ADCIRC is likely to not properly resolve the current in deep ocean where the vertical variation of the current becomes important.

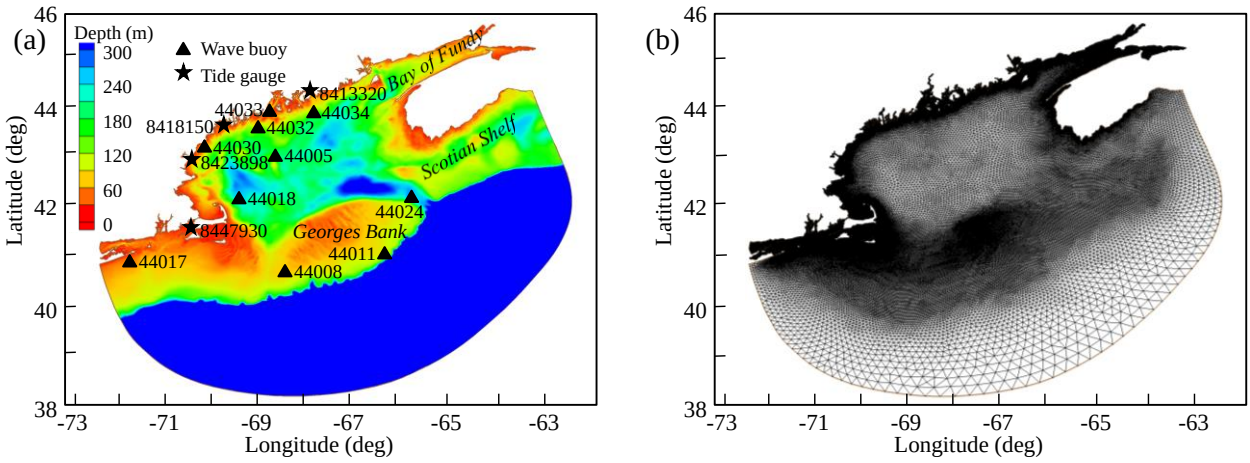


Figure 3.3. Model domain covering the Gulf of Maine. (a) Bathymetry, wave buoys (▲) and tide gauges (★); (b) Finite element mesh.

Table 3.1. Wave buoys in the Gulf of Maine

| Wave buoy | Buoy location | Water depth / m |
|---|---|---|
| 44005 | Gulf of Maine, 78 NM East of Portsmouth, NH | 206.0 |
| 44008 | Nantucket, 54NM Southeast of Nantucket | 66.4 |
| 44011 | Georges Bank, 170 NM East of Hyannis, MA | 82.9 |
| 44017 | Montauk Point, 23 NM SSW of Montauk Point, NY | 52.4 |

Table 3.1 Continued

| | | |
|---|---|---|
| 44018 | Cape Cod, 24 NM East of Provincetown, MA | 217.6 |
| 44024 | Northeast Channel | 225.0 |
| 44030 | Western Maine Shelf | 62.0 |
| 44032 | Central Maine Shelf | 100.0 |
| 44033 | West Penobscot Bay | 110.0 |
| 44034 | Eastern Maine Shelf | 100.0 |

Table 3.2. Tide gauges in the Gulf of Maine

| Tide gauge | Location | Water depth / m |
|---|---|---|
| 8413320 | Bar Harbor, ME | 6.0 |
| 8418150 | Portland, ME | 12.0 |
| 8423898 | Fort Point, NH | 9.0 |
| 8447930 | Woods Hole, MA | 5.0 |

### 3.2.3 Surface wind and pressure forcing

Two sets of wind for wave and surge simulation in the Gulf of Maine, the NASA Cross-Calibrated Multi-Platform (CCMP) ocean surface wind (http://rda.ucar.edu/datasets/ds745.1) and NCEP North American Regional Analysis (NARR) wind data (http://rda.ucar.edu/datasets/ds608.0) were compared. The 6-hourly CCMP wind covers globally with 0.25-degree grid resolution, while the 3-hourly NARR wind covers Continental US with 32 km (approximately 0.30 degree) grid resolution. We found that the NARR wind performed better compared with the CCMP wind in terms of simulation results for the April 2007 Nor'easter. In this paper, simulation results driven by NCEP North American Regional Reanalysis (NARR) database are presented. This database is generated using the high resolution 32 km NCEP Eta Model with 45 vertical layers output together with the Regional Data Assimilation System. By

incorporating regional data assimilation in the North America, the dataset has better accuracy of temperature, winds and precipitation than other datasets available in this area. It outputs wind, air pressure, precipitation and other meteorological parameters 3 hourly at 29 vertical levels.

Wind field at 10 m above sea surface and sea surface pressure were used as meteorological forcing for the ADCIRC and SWAN model. Figure 3.4 shows the comparison of wind vectors at 10 m above sea surface at four wave buoys in the Gulf of Maine. The magnitude and direction of NARR wind output agree reasonably well with buoy measurements, which provides confidence for wave and surge modeling.

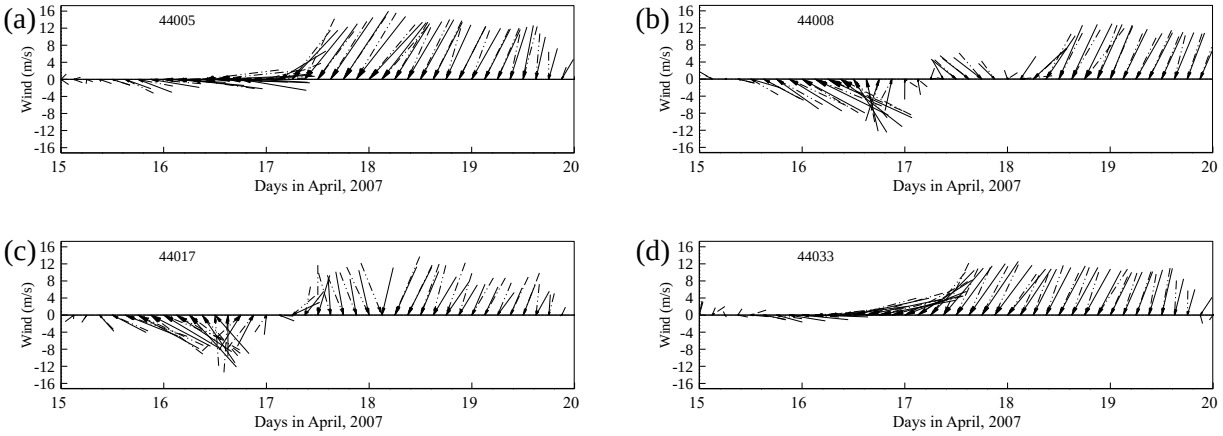


Figure 3.4. Comparison of NARR winds with buoy measurements at buoy 44005, 44008, 44017 and 44033. Measurement data (black dash-dotted vector); NARR reanalysis wind output at buoy stations (black solid vector).

### 3.2.4 Model set-up and implementation

The 2-D depth integrated version of ADCICR (ADCIRC-2DDI) was used for tide and storm surge prediction. The finite amplitude and convection terms were activated. Lateral viscosity was set with a constant of 5 $m^2/s$ following Yang and Myers (2007) and Bunya et al. (2010) through the whole domain. The air-sea drag coefficient defined by Garratt's drag formula (Garratt, 1977) was used with a cap of $C_d \leq 0.0035$. The drag coefficient formula of Garratt (1977) is consistent with the relation proposed by Charnock (1955) between aerodynamic roughness length ($z_0$) and friction velocity ($u_*$), viz, $z_0 = \alpha u_*^2/$ gwhen $\alpha = 0.0144$ over the ocean. Garratt (1977) approximated Charnock's relation (1955) based on

previous observations of wind stress and wind profiles over the ocean using a neutral drag coefficient (referred to 10 m) for 10 m wind speed ranging between 4 m/s and 21 m/s. The drag coefficient of Garratt (1977) is still widely used in recent work on storm surge modeling in the literature, e.g. Westerink et al. (2008), Bunya et al. (2010) and Dietrich et al. (2010).

The hybrid friction relationship is used to specify a spatially varying bottom friction coefficient depending on water-depth (Luettich and Westerink, 2006),

$$C_f = C_{f\min}\left[1+(\frac{H_{break}}{H})^{\theta_f}\right]^{\gamma_f/\theta_f} \quad \text{(Equation 3.1)}$$

When the water depth is larger than $H_{break}$, a constant friction coefficient $C_{fmin}$ based on standard Chezy friction law is applied; when the water depth is less than $H_{break}$, the Manning type friction law is applied where the friction coefficient increases with decreasing water depth, which is more realistic in shallow water areas. The parameters $C_{fmin} = 0.03$, $H_{break} = 2.0\,m$, $\theta_f = 10$ and $\gamma_f = 1.33333$ were used as recommended by Luettich and Westerink (2006).

The eight most significant astronomical tide constituents (M2, S2, N2, K2, K1, P1, O1 and Q1) were used to drive the model along the open boundary. The corresponding harmonic constants of the eight tidal constituents were interpolated from the global model of ocean tides TPXO (http://volkov.oce.orst.edu/tides/global.html). The time step for ADCIRC was set to 1s to maintain computational stability.

The wave model SWAN shares the same unstructured mesh and surface wind forcing with ADCIRC. The 2D wave spectra output by SWAN hindcast in the Western North Atlantic Ocean was used as the offshore boundary conditions, to allow swell generated outside of the model domain to propagate reasonably into the model domain.

The prescribed spectrum frequencies range from 0.031384 to 1.420416 Hz and are discretized into 40 bins on a logarithmic scale. The wave spectrum is solved in full circle with a directional resolution of 10 degrees. The JONSWAP formulation (Hasselmann et al. 1973) was used for bottom friction. The

friction coefficient of 0.038 $m^2s^{-3}$ was used for both wind waves and swell (Zijlema et al., 2012). The time step for integration is set to 600s.

The coupling interval of the ADCIRC and SWAN models is the same as the time step for SWAN. ADCIRC will pass wind forcing, water level and currents to SWAN every 600s, while SWAN passes radiation stress to ADCIRC to update the calculation. The model ran for 30 days from 4/1/2007 to 4/30/2007 from cold start. The elevation specified boundary condition was first ramped up for 5 days with a hyperbolic tangent function until an equilibrium state was reached before surface wind and pressure forcing were applied.

Three cases were run: (1) tide-surge predictions without wave effects; (2) wave prediction without temporal varying water level and currents; (3) a fully coupled SWAN+ADCIRC run to include tide-surge and wave interaction.

### 3.3 Model validation

The model prediction of water level, depth-averaged current and wave parameters were validated hourly during the storm period. The tide and surge levels were validated at four coastal tide gauges. The depth-averaged current was validated by the vertical current profiles measured by Acoustic Doppler Current Profilers (ADCP) at two buoy sites. The significant wave height and dominant wave period were validated at four wave buoys over the continental shelf and within coastal bays. The following statistical parameters are used to quantify model-data comparisons:

i) Mean Bias, the difference between the mean of observed data and model result;

ii) Peak Bias, the difference between the observed data and model result at the storm peak;

iii) RMSE, the root mean square error to evaluate the average accuracy of model prediction over the duration of the storm.

#### 3.3.1 Tide and surge

The predicted astronomical tide during the modeling period was first compared with data from NOAA/CO-OPS tide gauges, which is a prerequisite since coastal flooding often happens at or near high tide especially at high latitudes (Wolf et al., 2009). The water level recorded by NOAA/CO-OPS tide

gauges was analyzed using the MATLAB harmonic analysis toolbox T-Tide (Pawlowicz et al., 2002) to separate tidal components and residuals. The extracted tidal level was then compared with model predictions. Figure 3.5 shows the comparison result at four tide gauges along the coast of the Gulf of Maine, including gauge 8413320 (Bar Harbor, Maine), 8418150 (Portland, Maine), 8423898 (Fort Point, New Hampshire) and 8447930 (Woods Hole, Massachusetts) from north to south. Table 3.3 summarizes the validation metrics. The model prediction agrees well with measurement both in magnitude and phase. The observed tidal level at high tide is slightly under-predicted except at tide gauge 8447930, possibly due to the overestimated bottom dissipation and numerical diffusion accumulated with time.

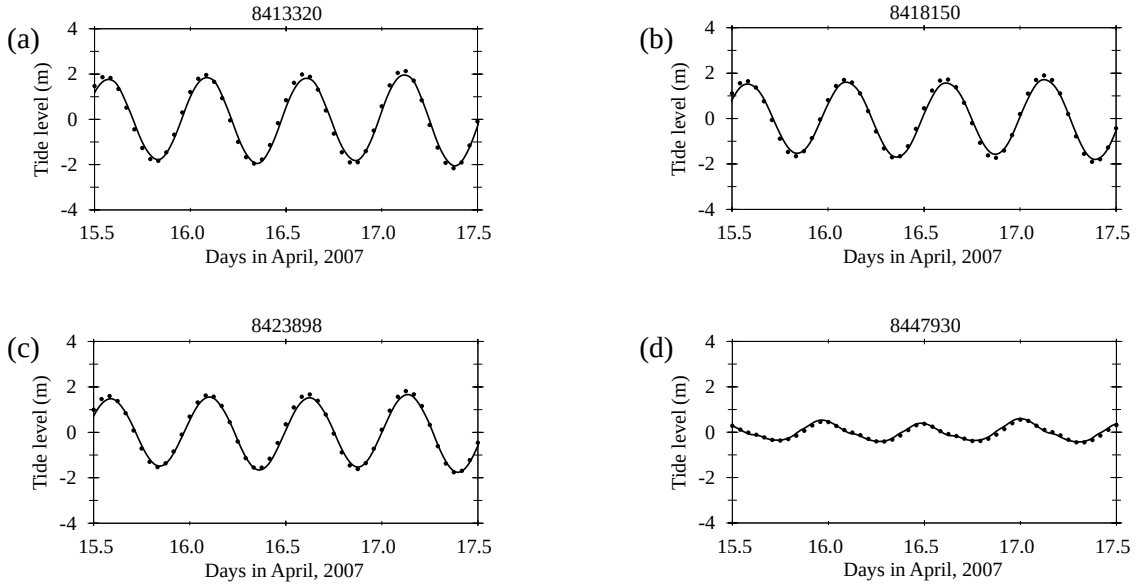


Figure 3.5. Comparison of predicted astronomical tides with measurements. Measurement (black dots); model prediction (black solid line).

Table 3.3. Error in model predictions of observed tidal level by tide gauges

| Tide gauge | Mean Bias (m) | RMSE (m) |
|---|---|---|
| 8413320 | 0.011 | 0.182 |
| 8418150 | 0.018 | 0.148 |
| 8423898 | 0.055 | 0.128 |
| 8447930 | -0.029 | 0.063 |

Figure 3.6 shows the comparison of predicted surge level with measurement at the same four tide gauges. Since the wave effect on surge level is negligible at these four tide gauges, only surge level due to direct meteorological forcing was plotted in Figure 3.6 to compare with recorded residuals by the tide gauges. The wave effect on surge level at these four tide gauges is negligible mainly because these gauges are in estuaries sheltered from offshore storms. However, wave contribution to surge level can be significant in shallow open coast (Brown et al., 2013).

The measured surge by tide gauges was reasonably predicted. Strong tidal modulation of surge can be identified at tide gauge 8413320, 8418150 and 8423898, where tidal range is over 4.0 m. While the first peak of surge level was well reproduced, the second peak was underestimated by approximately 0.2 m. This deficit is due to the following reasons: (1) The Ekman transport (Sverdrup et al. 1942) becomes important as the wind direction changed from southeast to east when the storm gradually moved to the east from April 17 to April 18 (cf. Figure 3.1 and 3.2). When the wind veered to the east, the surface wind stress produced Ekman transport along the offshore boundary of model domain, which contributes to elevated water level along the coastline at the second storm peak; (2) The elevated water level along the lateral boundary at Scotian Shelf (Figure 3.3a) is not negligible. In the present model, only tidal constituents were specified along the ocean boundary, while the effect of elevated water level by surge at the lateral boundary and Ekman transport at the offshore boundary were both neglected. This deficit may be minimized by either extending the model domain so the model results are less sensitive to offshore and lateral boundary conditions or applying more realistic boundary conditions, e.g., current velocity and water level (e.g. Blain et al. 1994). In this study, we will focus on tide-surge and wave interaction during the tidal cycle containing the first storm peak when the model predictions compare well with measurements.

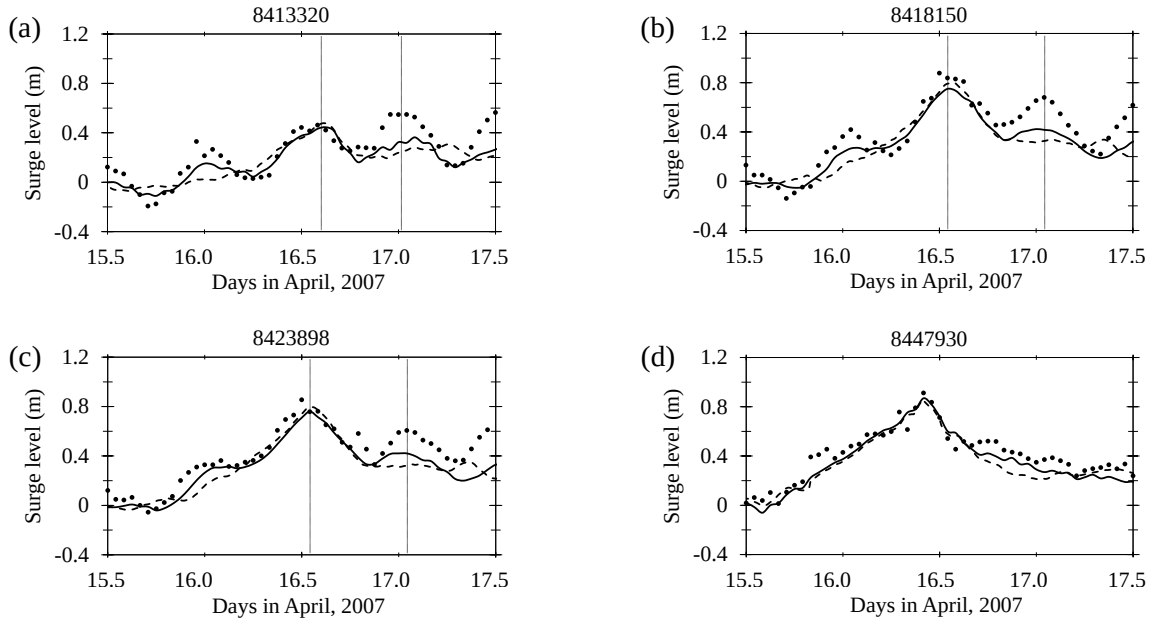


Figure 3.6. Predicted storm surge in comparison with measurements. Measurements (black dots); model prediction with (black solid line) and without (black dash line) tide-surge and wave interaction. The two peaks of storm surge are marked by dash line.

Table 3.4. Error in model prediction of observed surge level by tide gauges

| Tide gauge | Mean bias (m) | Peak Bias (m) | RMSE (m) |
|---|---|---|---|
| 8413320 | 0.066 | 0.029 | 0.116 |
| 8418150 | 0.085 | 0.175 | 0.124 |
| 8423898 | 0.095 | 0.145 | 0.127 |
| 8447930 | 0.051 | 0.020 | 0.080 |

### 3.3.2 Currents

The total current driven by tide, direct meteorological forcing and wave were validated in this section. The vertical current profile by ADCP at two buoy sites, buoy 44024 and buoy 44033, was integrated to obtain depth-averaged current and compare with model prediction.

The ADCP measurements of depth-averaged current at the wave buoys are in good agreement with model prediction. Currents at these two buoys are mainly driven by the tide. The east component of

the current, U, at both buoy sites was slightly overpredicted. The wave effect on the depth-averaged current at the two buoy sites is negligible because the water depth at both locations is in the order of 100 m, where the wave radiation stress is small. However, along the shallow open coast where considerable wave transformation and dissipation take place, wave effect on current can be significant. ADCIRC currently only includes wave radiation stress in the wave current interaction but not Stokes drift. It also neglects the wave-current interaction through surface stress and bottom stress.

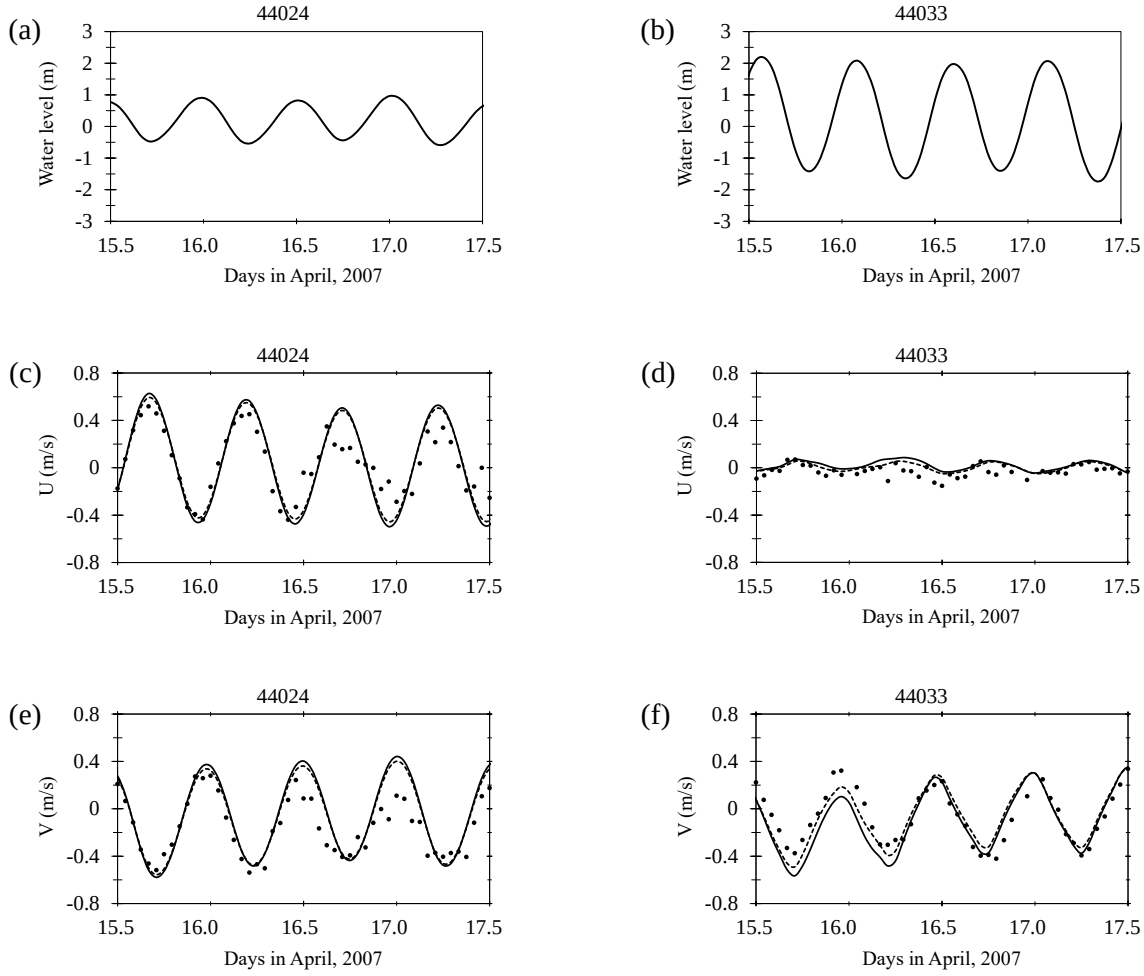


Figure 3.7. The predicted water level (upper) and the comparisons of the predicted depth-averaged current velocity in the east, U, (middle) and north direction, V, (lower) with the ADCP measurements. ADCP measurements (black dots); model prediction with wave-current interaction (black solid line); model prediction without wave-current interaction (black dash line).

Table 3.5. Error in model prediction of observed current by ADCP

| ADCP | Without tide-surge and wave interaction | | | | With tide-surge and wave interaction | | | |
|---|---|---|---|---|---|---|---|---|
| | U component | | V component | | U component | | V component | |
| | Mean Bias (m) | RMSE (m) | Mean Bias (m) | RMSE (m) | Mean Bias (m) | RMSE (m) | Mean Bias (m) | RMSE (m) |
| 44024 | -0.022 | 0.161 | -0.091 | 0.154 | -0.016 | 0.176 | -0.103 | 0.172 |
| 44033 | -0.034 | 0.052 | 0.003 | 0.109 | -0.051 | 0.067 | 0.051 | 0.136 |

### 3.3.3 Waves

Wave predictions with and without tide-surge and wave interactions are compared with measurements in Figure 3.8. Wave growth and decay before and after the storm are well predicted. The prediction with and without wave-current interaction is similar at the four wave buoys, indicating that wave-current interaction at these buoys is negligible. Since these buoys are in relatively deep water where the local current is small (see Table 3.1 for the water depth for all buoys), negligible current effect on waves is expected. This may not be the case at other locations, where the current is large, e.g., over Georges Bank where detailed analysis of current effect on directional wave spectra is carried out in section 4. While the peak of significant wave height was captured well by the model, the wave height after storm peak was underestimated. The rapid evolution of the storm after April 17 (Figure 3.1 and Figure 3.2) generated fast transient wind. The NOAA NARR reanalysis wind with 3-hourly interval cannot capture the rapid variations of wind. In general, it is expected that higher resolution wind at higher sampling rate will likely improve the model prediction (e.g. Zou et al., 2013).

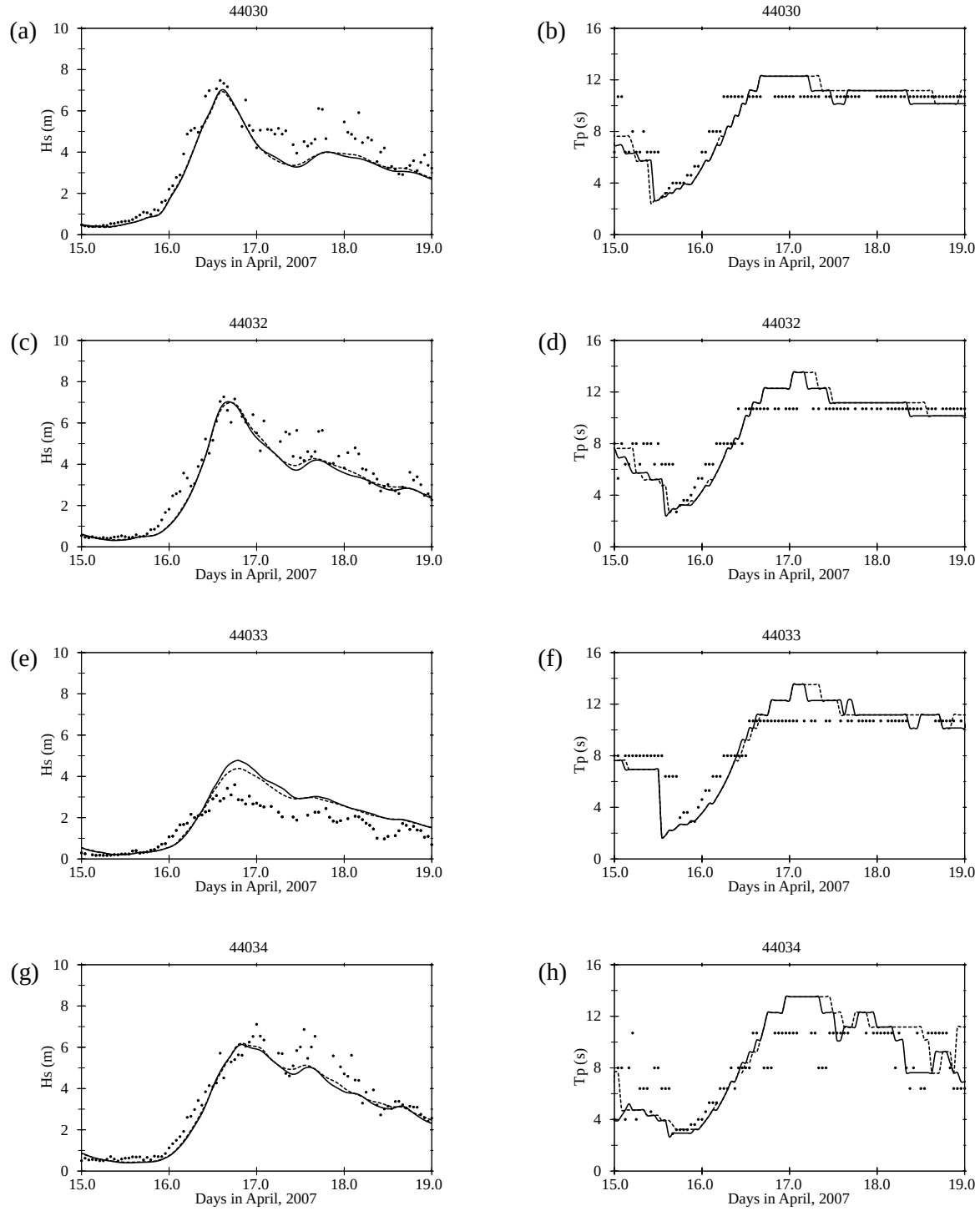


Figure 3.8. Comparison of predicted wave parameters with buoy measurements. Significant wave height (Left) and dominant wave period (Right). Wave buoy data (black dots); model prediction with (black solid line) and without (black dash line) wave-current interaction.

Table 3.6. Errors in model prediction of observed significant wave height by wave buoys

| Wave buoy | Without tide-surge and wave interaction | | | With tide-surge and wave interaction | | |
|---|---|---|---|---|---|---|
| | Mean Bias (m) | Peak Bias (m) | RMSE (m) | Mean Bias (m) | Peak Bias (m) | RMSE (m) |
| 44030 | 0.561 | 0.580 | 0.798 | 0.583 | 0.499 | 0.811 |
| 44032 | 0.314 | 0.425 | 0.609 | 0.369 | 0.319 | 0.655 |
| 44033 | -0.419 | -0.763 | 0.685 | -0.490 | -1.147 | 0.801 |
| 44034 | 0.283 | 1.074 | 0.558 | 0.341 | 1.200 | 0.605 |

### 3.4 Model results

In this section, analysis of tide-surge and wave interaction on circulation and wave was carried out by comparing the wave and circulation at the peak of the storm (1400UTC April 16, 2007) for different scenarios. The wave setup and wave-induced current in Saco Bay over the tidal cycle at the peak of the storm was also analyzed.

#### 3.4.1 Wave effects on circulation

Figure 3.9 shows the depth-averaged velocity in the Gulf of Maine at the storm peak. The depth-averaged velocity is relatively large in the Bay of Fundy and over Georges Bank. The maximum current speed is identified within the Bay of Fundy and reaches 2.0 m/s. At the southern flank of the Georges Bank, the depth-averaged current ranges from 0.6 m/s to 1.0 m/s. At the northern flank, the tidal current speed is slightly larger, between 0.8 m/s and 1.2 m/s. At locations over the Georges Bank with minimum water depth, the depth-averaged current speed reaches 1.4 m/s. The predicted circulation pattern in shallow water region of the Gulf of Maine by the present 2-D model in Figure 3.9 agrees reasonably well with the numerical results by Greenberg (1983) and Xue et al. (2000) and field observations by Pettigrew et al. (2005).

By comparing Figure 3.9a and Figure 3.9b, the effect of wave current interaction on circulation is most significant over Georges Bank. Over the bank, the depth-averaged velocity is increased by approximately 0.2 m/s by the presence of waves through wave radiation stress, which is mainly due to the shallow water depth. The Georges Bank dissipates a significant amount of wave energy through bottom friction and breaking, which leads to decrease in wave height, therefore, wave radiation stress. The wave radiation stress is proportional to the square of wave height. The corresponding excessive momentum flux on the circulation generates the wave-induced circulation in Figure 3.9c.

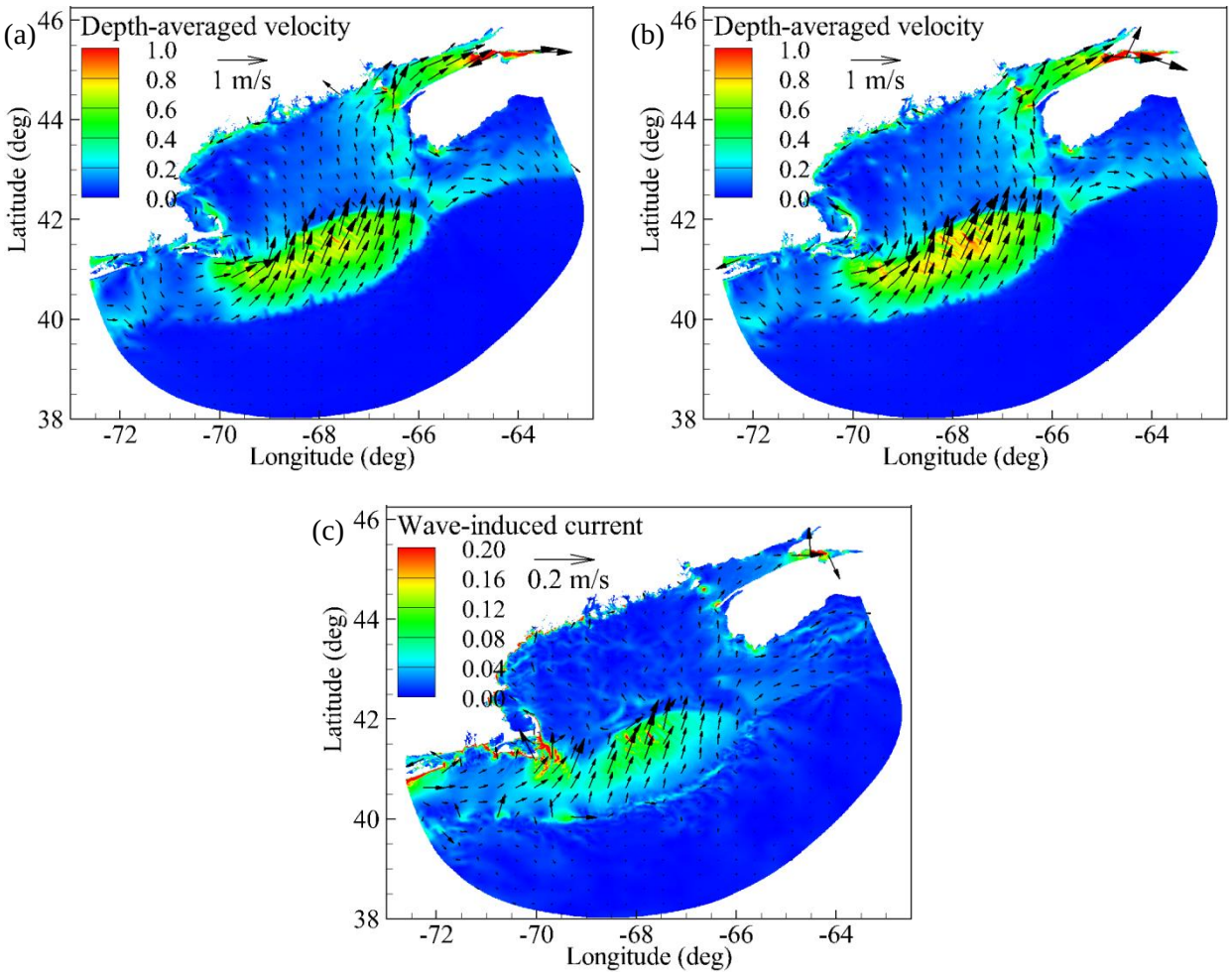


Figure 3.9. Depth-averaged velocity at the peak of the storm (1400UTC April 16, 2007). (a) Without wave effect; (b) with wave effect; (c) wave-induced current.

Since the wave radiation stress gradient becomes significant mainly in coastal areas where wave height changes drastically due to shallow water wave processes such as wave refraction, wave diffraction,

bottom friction effect and wave breaking, its contribution to circulation is more evident in these areas. The Saco Bay was selected to illustrate the wave effect on water level and circulation during the storm. The low-lying coast of this area is prone to flooding due to the combined effect of elevated water level and large waves during storm events. The coastal dynamics and sediment transport in the bay have been examined using observation data in several studies (e.g. Hill et al., 2004; Kelley et al., 2005; Brother et al., 2008; Tilburg et al., 2011), however, no previous study has focused on tide-surge and waves in response to storms in the bay using numerical modeling. Figure 3.10 shows the bathymetry of the Saco Bay. The time series of wave parameters, tidal level, surge level and wave setup was output at point A in Figure 3.10 where the water depth is 3.5 m.

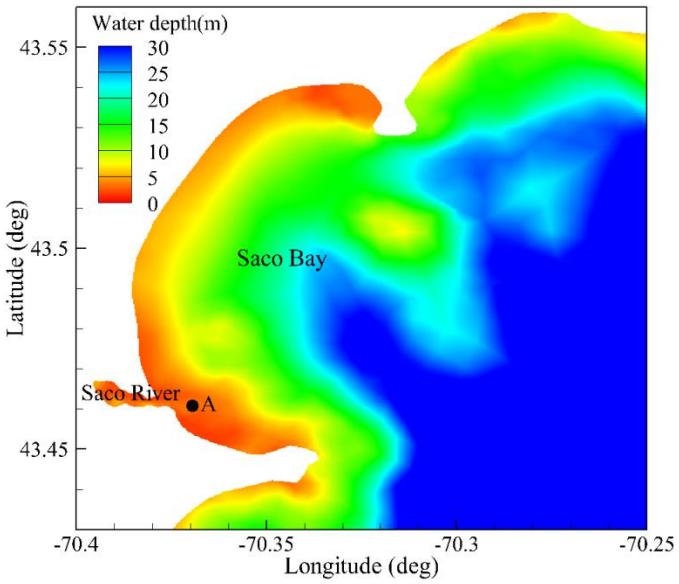


Figure 3.10. Bathymetry of the Saco Bay. Time series of water level and current predicted by the present model in Figure 3.12 is the output at point A denoted by the black circle here.

Figure 3.11c shows the wave field at the peak of the storm in the Saco Bay. The contour of the significant wave height is in parallel with the depth contour in Figure 3.10 due to wave refraction. As the wave propagates toward the shore, wave height increases due to the shoaling effect and decreases due to directional spreading, bottom friction and wave breaking, which generate excess momentum flux, i.e. wave radiation stress. The wave radiation stress exerts on the mean flow and generates wave setup and

wave-induced current. Figure 3.11d shows the radiation stress gradients. The radiation stress gradients are relatively large where bottom topography changes abruptly. Along the central part of the coast in this area, the radiation stress gradients are generally normal toward the coastline and reaches maximum when significant wave height changes most. While at both the northern end and southern end of the coast, the radiation stress gradients are at an oblique angle with the coastline, exerting longshore stress on the circulation. The magnitude of radiation stress gradients ranges from 0.0024 $N/m^2$ to 0.0060 $N/m^2$ along the coastline.

Figure 3.11a and 3.11b shows the surface elevation and depth-averaged velocity with and without wave effect at the peak of the storm. The surface elevation is increased by 0.2 m along the coast due to wave setup, which accounts for 20% of the total surge level. The maximum wave setup is at the river mouth of the Saco River. The depth-averaged velocity is also significantly enhanced by the presence of waves. Wave-induced current is dominant in the bay and reaches over 1.0 m/s, which is in the same order of magnitude as that measured by Hill et al. (2004). A clockwise circulation gyre is identified at the offshore of the Saco River. When tide-surge and wave interaction is considered, the gyre is greatly enhanced and moved further offshore (Figure 3.11b). Along the central part of the coast, the southward and northward longshore current converges and produces a strong current in the offshore direction due to mass conservation in the same fashion as rip current. The offshore current further veers to the south. Part of the southward current continues to the south while the rest merges into the clockwise circulation. The wave-induced circulation in the Saco bay is a major driving force for the sediment transport and beach erosion and accretion in the bay.

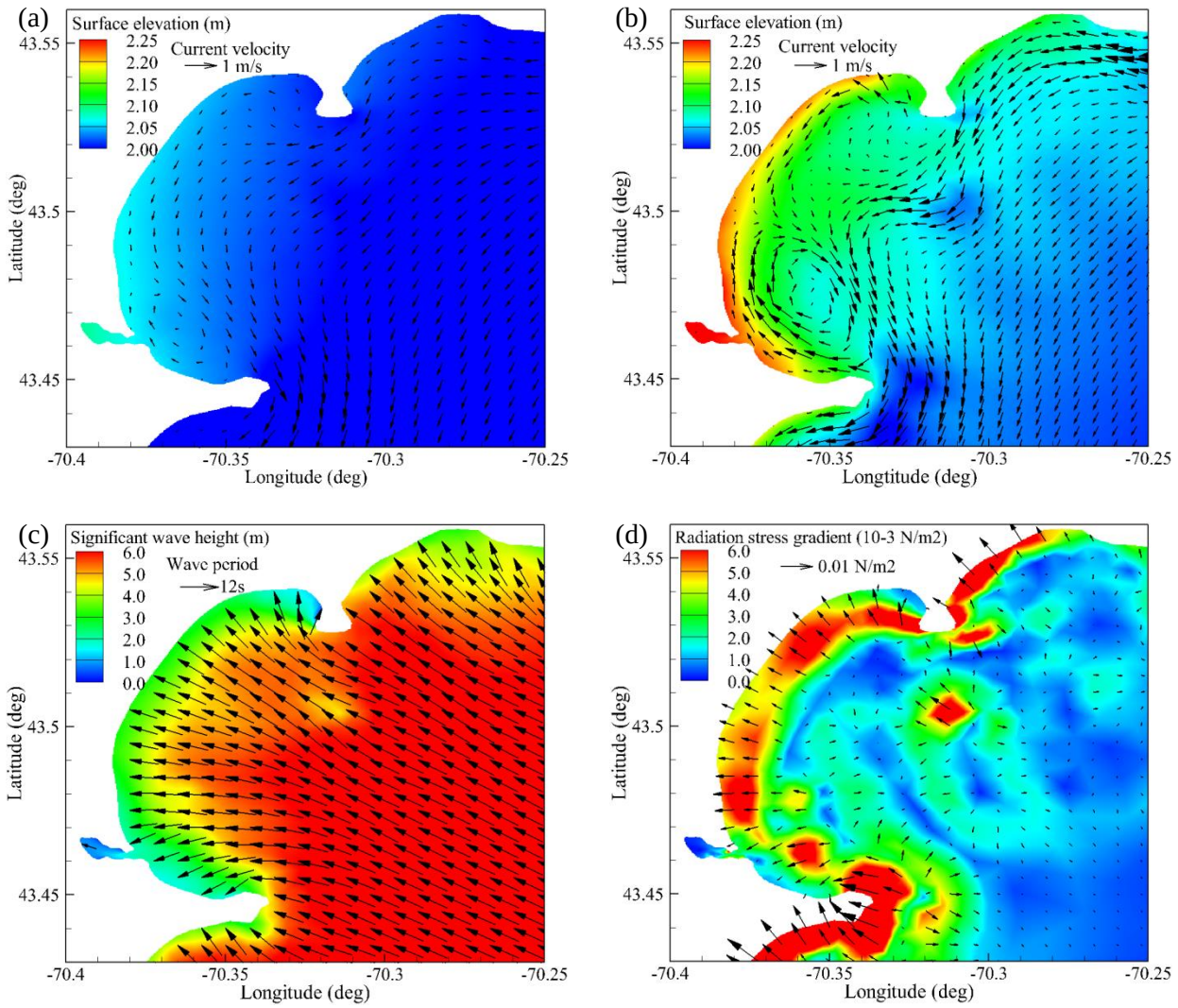


Figure 3.11. Snapshot of circulation and wave field in Saco Bay at 1400UTC April 16, 2007. (a) Circulation without wave effect; (b) circulation with wave effect; (c) wave field; (d) radiation stress gradients.

The time series of predicted tidal level, surge level, significant wave height and wave setup at point A was plotted in Figure 3.12 to further analyze the effect of tide-surge and wave interaction. At point A, while the maximum surge level of 0.9 m occurs two hours before the high tide, the maximum wave setup coincides with high tide as well as maximum significant wave height. Wave setup is mainly related to wave radiation stress gradients in the cross-shore direction. At the coast, tide plays a significant role in modulating wave height (Zou et al., 2013). The wave height is dependent on water depth due to wave shoaling, refraction and breaking. At high tide, excess momentum flux is generated by wave

transformation and breaking in the cross-shore direction and results in elevated water level through wave setup. As tidal level falls, the significant wave height decreases and wave setup decreases correspondingly.

Both wave setup and wave-induced currents in Saco Bay at the four tidal phases illustrated in Figure 3.12 were shown in Figure 3.13. As tidal level increases, significant wave height and wave setup increases and reaches their maxima at high tide. Two clockwise circulation gyres are formed and located close to the headlands to the north and south of Saco Bay. The two gyres sustained for 26 hours during the storm. Wave energy converges at the headlands and diverges in the bay, which generates large momentum fluxes from the headlands to the inner bay and forms the gyres. The two gyres are also intensified as tidal level increases.

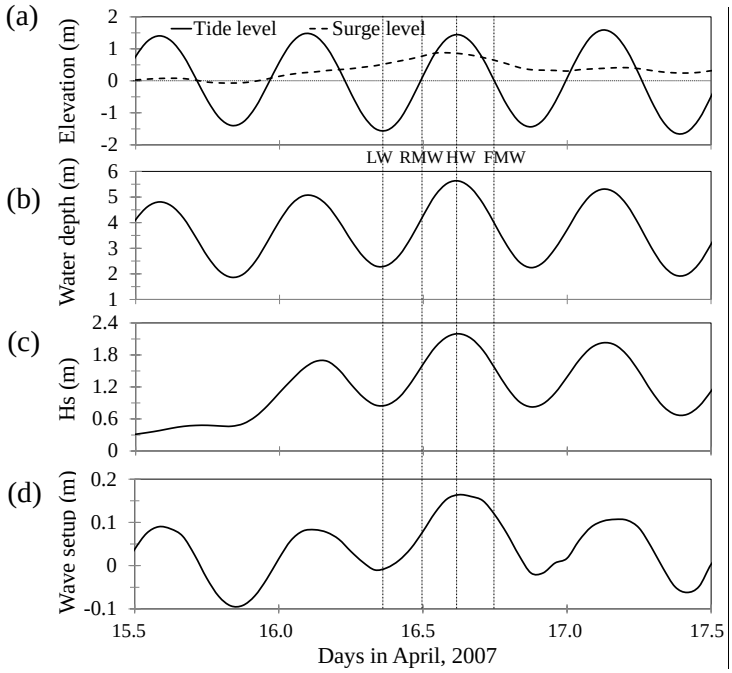


Figure 3.12. Time series of modeled elevation, significant wave height and wave setup at point A in Saco Bay indicated in Figure 3.7. The four vertical dash lines denote the four tidal phases, in which LW is for low water, RMW is for rising mid-water, HW is for high water and FMW is for falling mid-water, respectively.

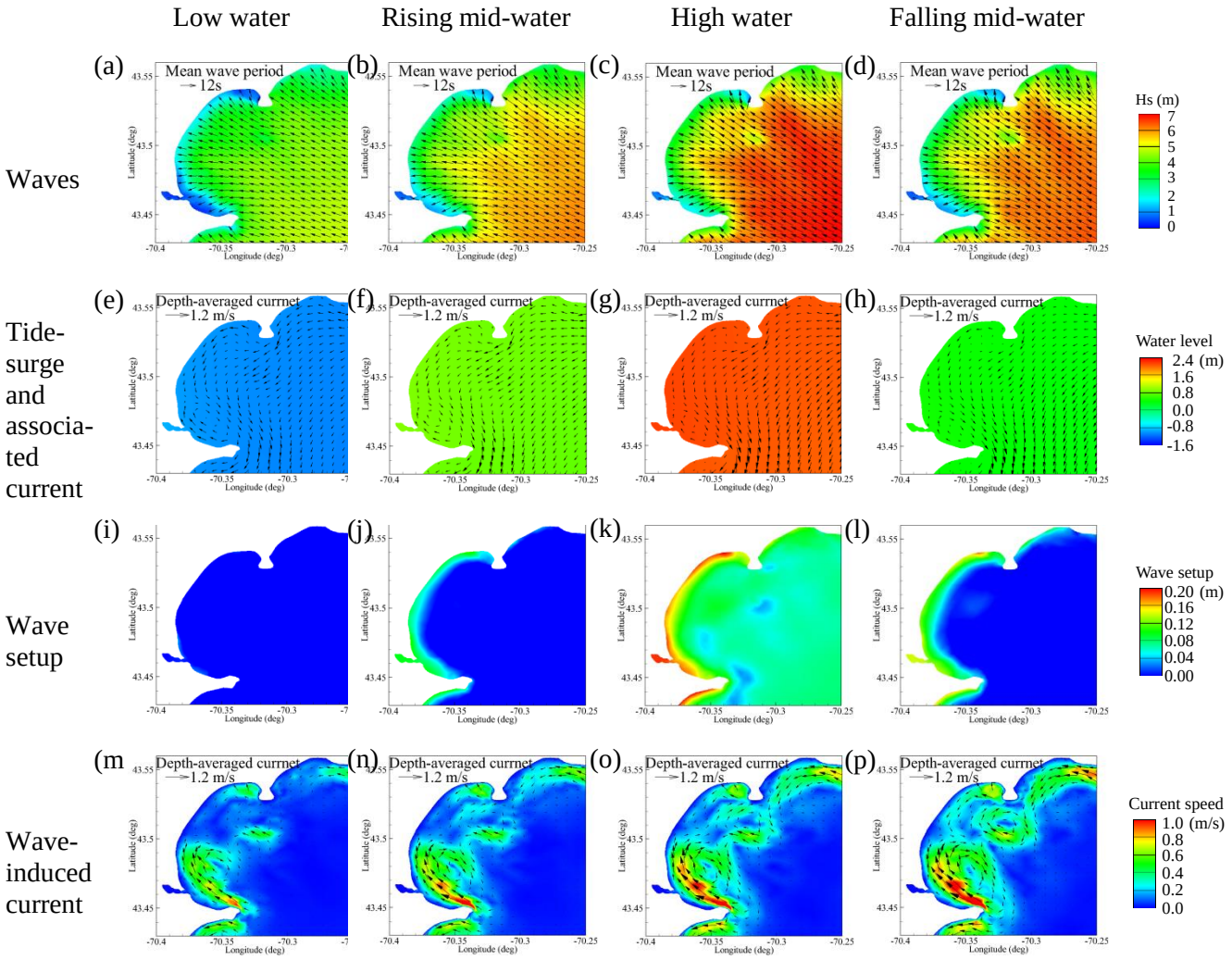


Figure 3.13. The wave fields (top panel), the tide-surge level and associated current (the second panel), the wave setup (the third panel) and wave-induced current (the bottom panel) in Saco Bay at the four tidal phases marked in Figure 3.10.

### 3.4.2 The impact of tide-surge on waves

The analysis of tide-surge and wave interaction on wave prediction is carried out in this section. It is evident from Figure 3.14 that wave distribution within the model domain is similar with and without tide-surge and wave interaction. The storm-generated significant wave height exceeded 7.0 m over most of the model domain at the storm peak. The impact of tide-surge and the associated current on waves is significant over Georges Bank (the square box in Figure 3.14). Over the bank, the significant wave height is decreased by 0.3~0.5 m mainly due to current effect. While the tidal range over the bank is relatively

small compared to the water depth, increasing from 1.0 m at the southern flank to 2.0 m at the northern flank, the current has a magnitude of 1.0 m/s. At the storm peak, the current flows toward the northeast and is normal to the mean wave direction, it slightly refracts waves.

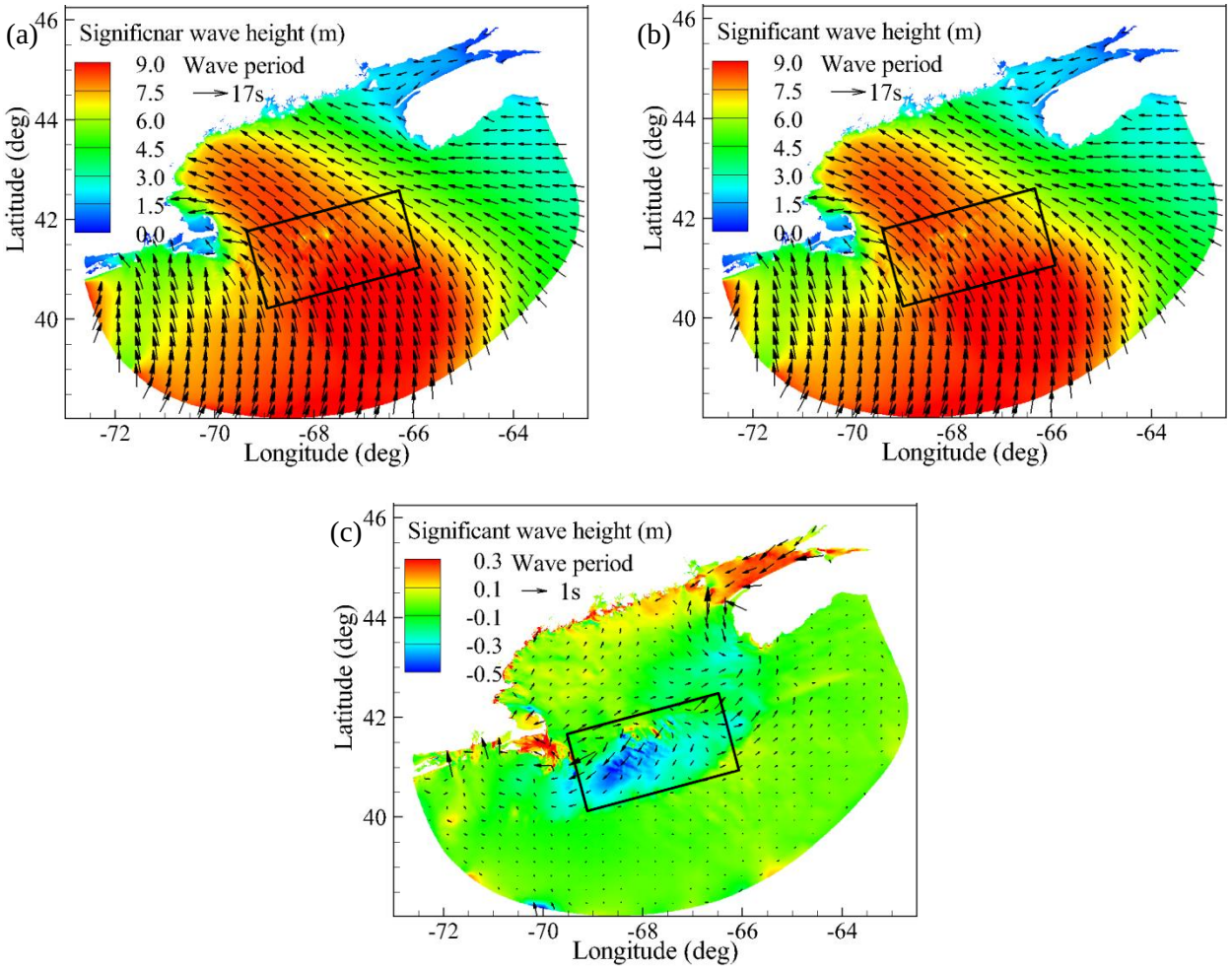


Figure 3.14. Wave fields at 1400UTC April 16, 2007. (a) without tide-surge effect; (b) with tide-surge effect; (c)with minus without tide-surge effect, in which red color indicates the increase of wave height by tide-surge effect while blue color indicates the decrease of wave height.

2D directional wave variance density spectra at four wave buoys (buoy 44005, 44008, 44011 and 44018) were further analyzed to assess the contribution of tide-surge and the associated current to waves. Buoy 44008 and 44011 are located at the southern flank of Georges Bank, and buoy 44005 and 44018 are located at the inner Gulf of Maine (Figure 3.3a). Current has a significant impact on wave energy redistribution over frequency and directional domain. The frequency range of wave spectra is generally

extended to higher frequencies by considering tide-surge and wave interaction, which can be explained by Doppler shift of wave frequency in the presence of current. At buoy 44005, while wave variance density remains the same at peak wave frequency, it decreases from the east and increases from the south with tide-surge effect. The peak wave variance density is significantly reduced by the tide and surge current at buoy 44008, 44011 and 44018. At the two buoys located at the southern flank of the Georges Bank, buoy 44008 and 44011, the reduction of peak wave variance density is largest. Over the Georges Bank, the depth-averaged current speed reaches 1.2 m/s and strong current shear is present, which alters the direction and frequency distribution of wave energy.

Figure 3.15. Directional wave variance density spectra at four wave buoys 44005, 44008, 44011 and 44018. The unit of the variance density is $m^2$/Hz/deg. (a)(d)(g)(j) without tide-surge effect, (b)(e)(h)(k) with tide-surge effect, (c)(f)(i)(l) with minus without tide-surge effect.

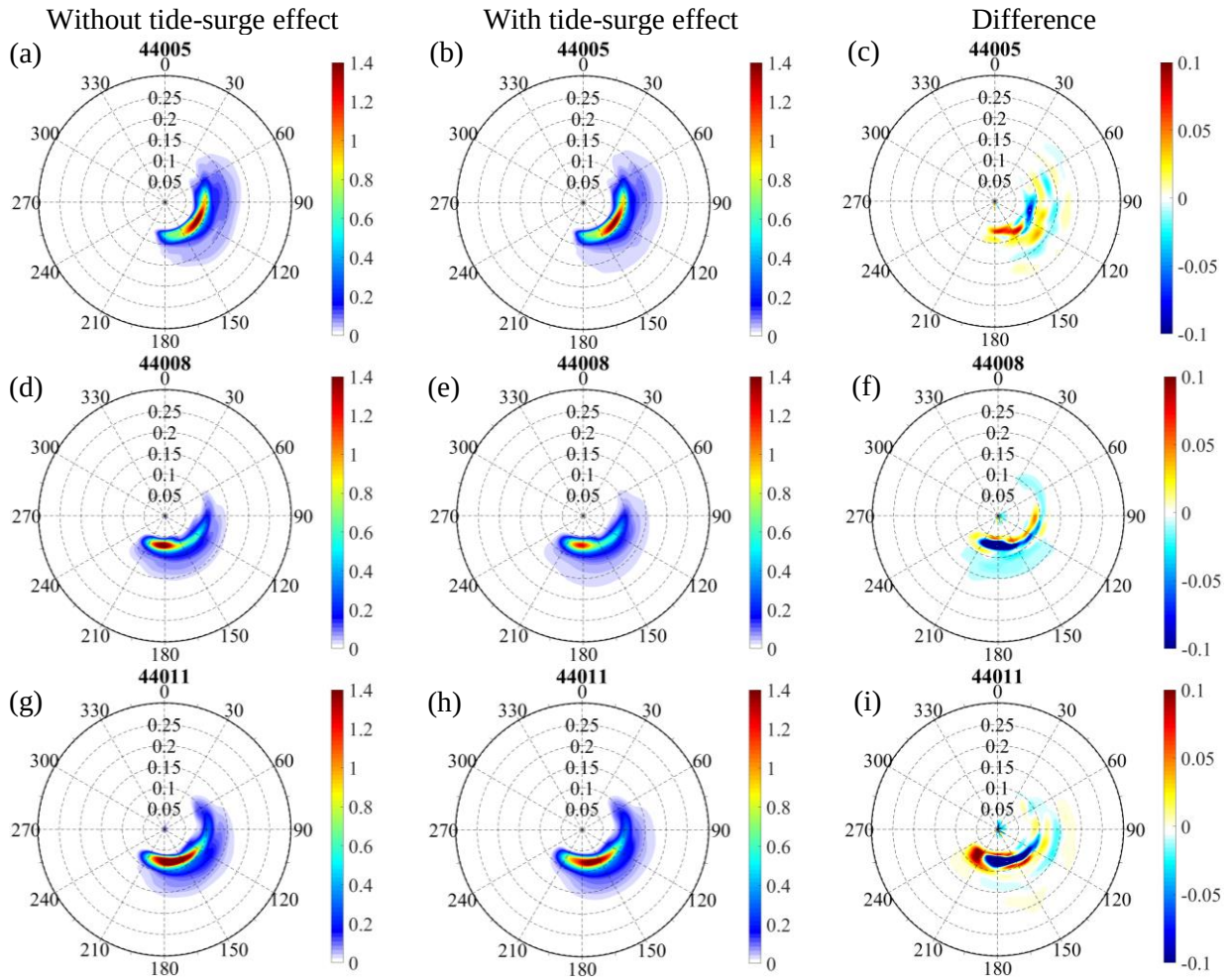

Figure 3.15 Continued

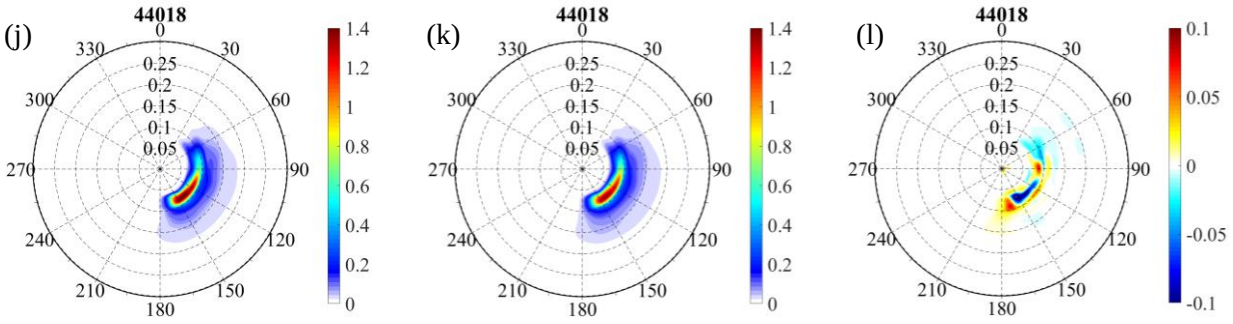


The impact of tide-surge and the associated current on waves at the storm peak in the Saco Bay is shown in Figure 3.16. While wave distribution is similar with and without tide and surge effect, the significant wave height near the coast is increased by 0.8~1.0 m with the presence of the tide-surge. For example, the 5m contour line of significant wave height moves further toward the coastline due to the tide-surge effect. The mean tidal range in Saco Bay is 2.7 m. The peak surge level of 0.8 m occurred 2 hours before high tide. The elevated water level significantly increases water depth in Saco Bay. Toward the coast, wave propagation and transformation is dictated by water depth and wave height contours are parallel with depth contours. Figure 3.16c indicates that waves slightly converge from the northern and southern end of Saco Bay toward its mid-coast due to current refraction.

Figure 3.16. Wave field in Saco Bay at 1400UTC April 16, 2007. (a) Without tide-surge effect; (b) with tide-surge effect; (c) the difference of wave height and wave direction with and without tide-surge effect, in which red color indicates the increase of wave height by tide-surge effect while blue color indicates the decrease of wave height.

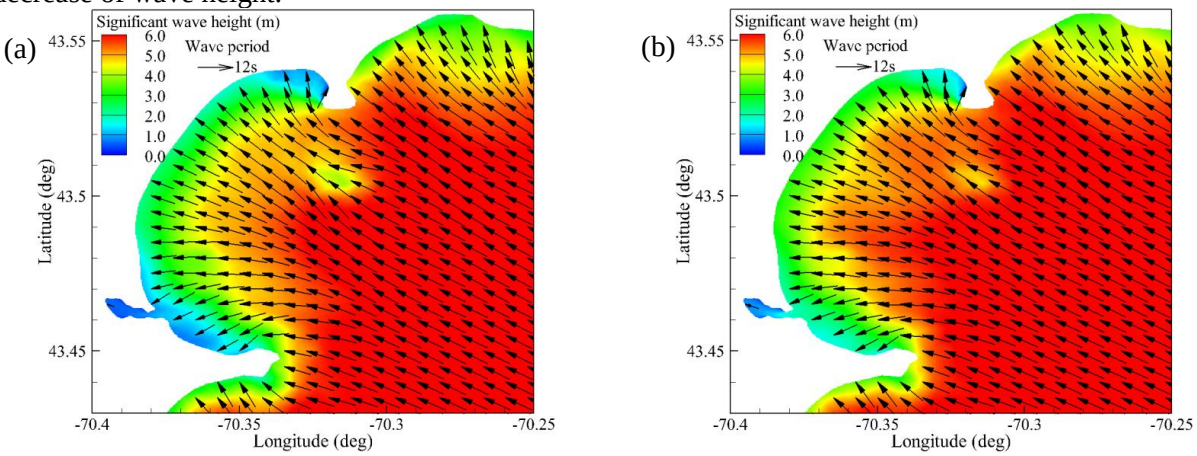

Figure 3.16 Continued

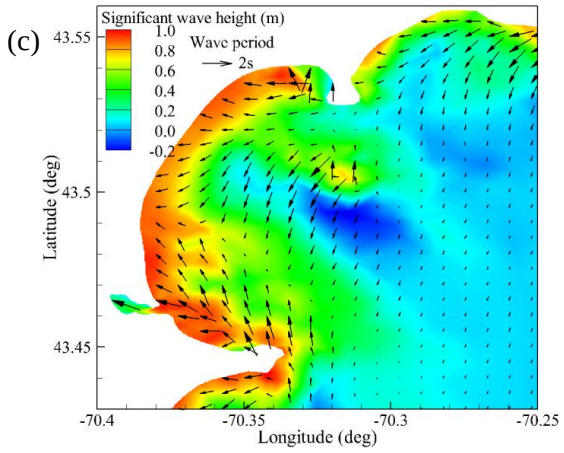


### 3.5 Conclusions and discussions

The fully-coupled spectral wave and circulation model SWAN+ADCIRC was applied to investigate tide-surge and wave interaction in the Gulf of Maine during an extratropical storm, the April 2007 Nor'easter, which retrograded toward the coastline and caused significant coastal flooding and severe beach erosion along the New England coast.

In the Gulf of Maine, tide-surge and wave interaction is significant over Georges Bank and in the coastal areas. During the April 2007 Nor'easter, over Georges Bank, the wind-induced current was approximately 0.2 m/s, accounting for 17% of total current at the storm peak. The wave-induced current mainly occurs at the shallow bathymetry over the Bank, where the wave energy was dissipated significantly by bottom friction and generated momentum flux exerting on the mean flow in the cross-bank direction. Within Saco Bay, the circulation was dominated by wave-induced current during the storm. The magnitude of wave-induced current reached 1.0 m/s, comparable with previous studies. Two clockwise circulation gyres formed in the bay, mainly driven by waves and due to the shallow water bathymetry and configuration of the coastline. When waves entered Saco Bay, wave energy converged at the headlands at the northern and southern ends of the bay and diverged at the inner bay, generating a radiation stress gradient that drives a longshore current from both ends to the inner bay coast. These longshore currents converged and fed into a current directed away from shore at the mid-coast of Saco

Bay. To our knowledge, wave-induced currents over Georges Bank and in the Saco bay have not been studied previously.

Wave setup at the storm peak was 0.2 m along the coast of Saco Bay and reached its maximum at the mouth of the Saco River. Both wave setup and wave-induced current were significantly modulated by the tide in Saco Bay. During the tidal cycle containing the storm peak, wave setup increased with tidal level and the maximum wave setup coincided with the high tide. The clockwise circulation gyres were also intensified at high tide. At the coast, wave transformation is mainly dependent on water depth. At high tide, the wave height gradient reached its maximum, as did the wave radiation stress gradient in the cross-shore direction, producing the maximum wave setup.

The wave prediction was improved significantly by including the tide-surge effect in these two regions. Over Georges Bank, the significant wave height was decreased by 0.3~0.5 m due to wave refraction by current over the bank. Wave height in Saco Bay was modulated by the tide along the coast and it increased with tidal level. The predicted directional wave spectra at the four wave buoy locations in the Gulf of Maine indicate that wave energy is shifted to higher frequencies by the tide-surge interaction, however, the current had a negligible effect on the directional distribution of spectral wave energy at these locations.

In the coupled SWAN+ADCIRC model, ADCIRC calculates water level and depth-averaged currents and passes them to SWAN, SWAN then computes the radiation stress gradients and passes them to ADCIRC (Dietrich et al. 2011). The 2-D depth uniform wave radiation stress formula proposed by Longuet-Higgins and Stewart (1962, 1964) used here is proportional to the square of wave height. The response of the flow to the wave radiation stresses tends to increase with decreasing water depth (Longuet-Higgins 1962). Since wave radiation stress gradient is only significant where wave height changes drastically, its impact on mean current and water level in the deep ocean is negligible. In the deep water, the 2-D model may not be adequate and the 3-D modelling approach including depth-dependent radiation stress such as those proposed by Mellor (2005) and Smith (2006) may be required to resolve the wave current interaction properly.

# CHAPTER 4

# AN INTEGRATED MODELING SYSTEM TO PREDICT COSATAL FLOODING FROM WAVE OVERTOPPING IN THE NORTHEASTERN USA

## 4.1 Background

Low-lying coastal communities are vulnerable to flooding due to elevated water level, large battering waves or the combined effects of both during storm events (Kirshen et al., 2008). Coastal flooding may occur under three scenarios: (1) the water level exceeds the crest elevation of natural barriers or coastal defenses, (2) waves rush up the shore and overtop the crest of natural barriers or coastal defenses, and (3) water flows through breaches in natural barriers or coastal defenses. According to the US Billion-dollar Weather/Climate Disaster report by the National Oceanic and Atmospheric Administration's National Centers for Environmental Information, the aggregated economic loss due to storm surge and wave damage in US coastal areas reached approximately 700 billion dollars during major storm events between 1980 and 2017 (https://www.ncdc.noaa.gov/billions/). The risk of coastal flooding will increase with sea level rise and intensification of storminess due to climate change (Nicholls, 2002; Kirshen et al., 2008; Emanuel, 2013; Roberts et al., 2017). The global mean sea level is predicted to rise on the order of 0.3-1.0 m by 2100 under the presumed low to high greenhouse gas emission scenarios (Church et al., 2013). Nicholls (2002) identified enhanced storm flooding and lowland inundation as one of the four major impacts of sea level rise. Kirshen et al. (2008) concluded that the current 100-year storm surge elevation may be exceeded every 70 years to 30 years by 2050 under low to high greenhouse gas emission scenarios respectively in the northeastern United States. At more exposed locations like Boston, Massachusetts (MA), the recurrence intervals of the current 100-year storm surge elevation may be even reduced to 8-30 years by 2050 (Kirshen et al., 2008).

In the northeastern coast of the United States, many types of coastal defenses, e.g. seawalls, revetments, groins and jetties, exist along the coast to protect buildings and infrastructure from storms and to prevent damage due to flooding and erosion. In Massachusetts, approximately 586 km of the 1770 km of ocean-facing coastline is protected by coastal structures. Of this, approximately 360 km, or 20 percent

of the coastline, is protected by seawalls. Wave overtopping of seawalls occurs frequently during the storm season and seawall breaches resulting in major flooding of coastal communities has been reported during severe storms (MADCR, 2009; MACZM, 2013a). Massachusetts is expecting and planning for 0.25-2.08 m sea level rise along the coast by the year 2100 (MACZM, 2013b). The Town of Scituate, MA, for example, which has experienced its worst flooding in recent years, is planning to elevate the seawall by 0.60 m to help protect against future flooding (MACZM, 2016). It is critical to develop predictive methods to quantify water level and waves during storms to assess the capacity of seawalls to protect communities against wave overtopping during future storms, and provide guidance for the adaptation of coastal structures to reduce loss of life and property.

Advanced coastal planning and risk management are required to facilitate coastal adaptation and resilience to the projected increased flooding risk due to sea level rise and increased storm frequency and intensity in the future (Kirshen et al., 2008; National Research Council, 2009). Coastal inundation models have become popular tools to achieve this objective over the past decade (e.g. Bates et al., 2005; Bunya et al., 2010; Dietrich et al., 2010; Chen et al., 2013; Zou et al., 2013; Gallien et al., 2014; Orton et al., 2015; Gallien, 2016). However, most coastal inundation studies do not consider wave overtopping at coastal defenses (e.g. Bates et al., 2005; Bunya et al., 2010; Dietrich et al., 2010; Chen et al., 2013). Only recently, a few studies have focused on coastal flooding due to wave overtopping using numerical models (Zou et al., 2013; Gallien et al., 2014; Gallien, 2016). Also, there is a lack of field data of wave overtopping at the seawalls in the United States to validate the model predictions.

Currently, the literature on integrated atmosphere-ocean-coast ("clouds-to-coast") modeling of flooding due to wave overtopping at coastal defenses such as seawalls is limited (Zou et al., 2013). This type of coastal flooding modeling requires resolution of processes with different spatial and temporal scales from ocean basin to coast to surf zone, e.g., wave-current interaction and wave breaking. Numerous studies have described the interactions between waves and circulation and their effects on tides, storm surges and waves (e.g. Cavaleri et al., 2007; Wolf, 2009; Dodet et al., 2013; Chen et al., 2015; Xie et al., 2016; Zou and Xie, 2016). At the ocean surface, the presence of waves modifies the wind stress through

ocean surface roughness (Janssen, 1991; Donelan, 1993; Taylor and Yelland, 2001; Drennan et al., 2003; Powell et al., 2003). Several studies on storm surge have incorporated the effect of waves on surface roughness for storm surge simulation (Brown and Wolf, 2009; Bertin et al., 2012). Waves also contribute to mean flow by Stokes Drift due to wave nonlinearity (Jenkins, 1987b) and wave radiation stress (Longuet-Higgins and Stewart, 1962, 1964; Mellor, 2005; Zou, 2006; Ardhuin et al., 2008). The bottom friction experienced by mean current is also modified in the presence of waves (Grant and Madsen, 1979; Zou, 2004).

Current, in turn, affects wind-wave generation (Ardhuin et al., 2012), wave energy dissipation (Ardhuin et al., 2012; van der Westhuysen, 2012) and wave propagation (Komen et al., 1994). In shallow water, wave-current interaction is manifested. Wave radiation stress and its horizontal gradients (Longuet-Higgins and Stewart, 1962, 1964) significantly impact both water level and current through wave setup and set-down, and by generating longshore current when waves approach the coastline at an oblique angle (Bowen, 1969; Longuet-Higgins, 1970). The water level affects wave propagation and refraction because wave propagation is dependent on water depth. The presence of current also results in wave refraction and wave frequency shifts (Komen et al., 1994).

In the surf zone, phase-averaged spectral wave models such as SWAN (Booij et al., 1999; Ris et al., 1999) are unable to resolve the complicated wave breaking processes. Approaches used to model wave propagation and transformation in the surf zone for natural beaches range from energy flux balance models (Goda, 1975; Thornton and Guza, 1983; Battjes and Stive, 1985), Boussinesq-type wave models (Wei and Kirby, 1995; Kennedy et al., 2000; Chen et al., 2000; Shi et al., 2012), and nonlinear shallow water models (Zijlema and Stelling, 2005, 2008; Zijlema et al., 2011; Smit et al., 2013), to sophisticated Reynolds-averaged Navier-Stokes models with free surface capturing techniques (Lin and Liu, 1998, Dalrymple and Rogers, 2006; Wang et al., 2009, Higuera et al., 2013). The energy flux balance models are simple and work well by incorporating some simplifying assumptions (Thornton and Guza, 1983).

Methods used to predict wave overtopping include empirical formulae based on extensive physical model tests (Hedges and Reis, 1998; EurOtop, 2016); Neural Networks (van Gent et al., 2007;

Verhaeghe et al., 2008); and numerical models that are based on nonlinear shallow water equations (Hu et al., 2000), Boussinesq-type models (Lynett et al., 2010; McCabe et al., 2013) and the RANS-VOF model solving the 2-D Reynolds-averaged Navier-Stokes equations (Lara et al., 2006; Losada et al., 2008; Reeve et al., 2008; Peng and Zou, 2011; Zou and Peng, 2011). While sophisticated numerical models like RANS-VOF model can incorporate the effects of complex shoreline geometry including coastal structures, they are computationally demanding and involve a steep learning curve for users. The empirical models have been widely used and provide a robust alternative to predict wave overtopping for the design of coastal structures (EurOtop, 2016).

Currently, there is a lack of study on coastal flooding due to wave overtopping at coastal defenses along the US coasts. Zou et al. (2013) used an integrated meteorological, regional-hydrodynamic and surf-zone-hydrodynamic model to study coastal flood risk due to wave overtopping and found the interlinked ensemble modeling framework provides an efficient way to quantify the uncertainty associated with model predictions. Gallien et al. (2014) and Gallien (2016) integrated a hydrodynamic model based on the shallow-water equations for overland flow simulation with wave overtopping, flood defenses and drainage to investigate the urban coastal flood at Newport and Imperial Beach during two storms in California. Both studies found that the hydrodynamic model provides high accuracy for flood prediction by resolving flood defenses and flow routing in transient conditions. The main objective of this work was to develop an integrated atmosphere-ocean-coast model that accurately predicts coastal flooding due to wave overtopping for the planning and design of coastal defenses while minimizing the complexity of the model. To accomplish this, we used the integrated modeling framework following the approach described in Zou et al. (2013), and validated the model for the Gulf of Maine during a major storm event in Xie et al. (2016) and Zou and Xie (2016). We extended the modeling capability in this work by coupling the spectral wave and circulation model to a surf zone model, a wave overtopping model and a drainage model to predict flooding caused by wave overtopping at seawalls. For model validation, water level data collected during the January 2015 North American blizzard in the Avenues

Basin in Scituate, MA, was combined with USGS LIDAR area relief data to determine the volume of water in the basin.

The chapter is composed of seven sections. Section 4.2 describes the site and field measurement. Section 4.3 focuses on the modeling approach. Model setup and parameters are defined and explained in Section 4.4. Section 4.5 discusses the results from the coupled wave and circulation model. Wave overtopping results are analyzed and discussed in Section 4.6. Conclusions are drawn in the final section.

## 4.2 Site description and field measurement

### 4.2.1 Site description

The town of Scituate, MA, with its 94.5 km coastline, is located approximately 40 km to the southeast of Boston (Figure 4.1a). During winter storms, the coast is frequently subjected to large ocean waves generated by northeasterly winds in the Gulf of Maine. As a defense against waves, an extensive network of hard structures has been constructed, including concrete seawalls, stone masonry seawalls, revetments, dunes, and stone jetties which extend for approximately 32 km. A basin located along Oceanside Drive behind the seawall in the northern part of Scituate (Figure 4.1a), locally known as the Avenues Basin, is periodically flooded due to storm waves overtopping the seawall and overwhelming the drainage system, which results in the flooding of homes and roads during extreme storm events. The basin drainage system consists of a 0.9 m outlet pipe that runs from the Oceanside Drive, under the seawall to discharge to the ocean (Figure 4.1b). The outlet pipe is fitted with a flap gate to prevent ocean water from entering the drainage system during elevated tide levels. Although the Avenues Basin is a closed basin area, once the water level reaches an elevation more than 4.36 m above local mean sea level, water begins to flow out of the basin through a corridor parallel to Ocean Drive at the southeast corner as indicated by the blue arrow in Figure 4.1b. Incoming water can overwhelm the drainage flow rate and water level continues to rise until the top of the seawall is reached at an elevation of 5.00 m above the local mean sea level.

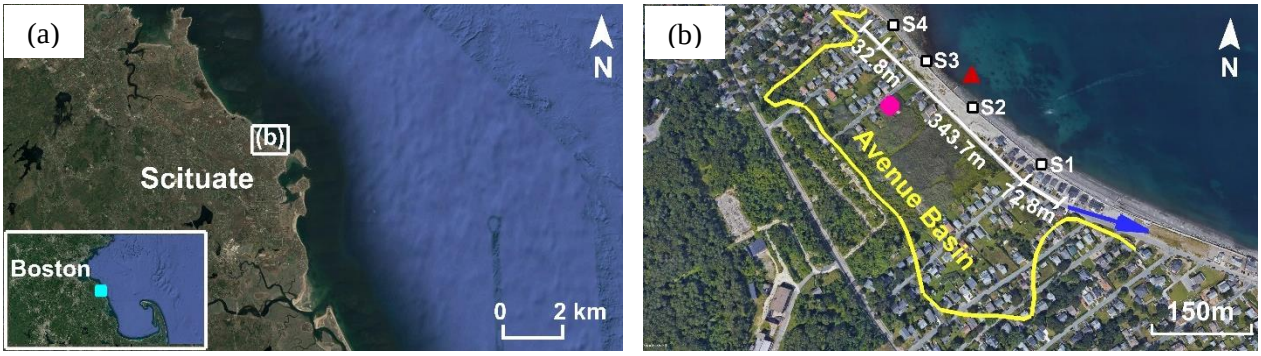


Figure 4.1. Location of Scituate, MA and the Avenues Basin in Scituate. (a) The location of Scituate, MA. (b) The Avenues Basin. The pink circle marks the location of the Solinst LTC Levelogger Edge in the Avenues Basin. The red triangle shows the location of the drainage pipe on the seaside of the basin. The blue arrow represents the corridor through which the water flows out of the Avenues Basin after the water level reaches 4.36m above the local mean sea level in the basin. The corridor is located at the southeast corner of the basin. The four squares denoted by S1 to S4 mark the locations where the site survey of the cross-shore profiles from the seawall to the end of the foreshore was conducted. The length of the seawall contributing to flooded water through wave overtopping is 449.3 m in total.

The Avenues Basin has been extensively flooded during several major storms, e.g., the Northeastern United States blizzard of 1978 (February 7, 1978), the 1991 Perfect Storm (October 31, 1991), the December 2010 North American blizzard (December 27, 2010), the Early February 2013 North American blizzard (February 9-10, 2013), the January 2015 North American blizzard (January 27, 2015) and the January 2016 United States blizzard (January 27, 2016).

### 4.2.2 Storm event description

The January 2015 North American blizzard was a powerful extratropical storm that swept along the coast of the northeastern United States in late January of 2015. The lowest recorded pressure was 970 hPa and the highest wind gust reached 42.5 m/s. From January 27 to 28, the storm moved northeastward off the Mid-Atlantic coast to the east coast of Canada as depicted in Figure 4.2a. The track of the storm maintained the northeasterly wind wave fetch across the Gulf of Maine in the cold air mass for the entire event. When the air temperature stays below the ocean surface temperature, the ocean surface boundary layer becomes much more unstable thus transporting higher winds to the ocean surface. Another important meteorological feature of the storm was the presence of a strong elongated high-pressure system to the north of the region (Figure 4.2b). The interaction of the two pressure systems strengthened

the pressure gradient across the Gulf of Maine, and the east-west elongation of the high-pressure system produced a long fetch distance. The presence of the high-pressure system also impeded the forward movement of the low-pressure system, which resulted in a long duration of winds across the fetch area. The strong northeasterly wind in the fetch area generated a pronounced storm surge and large waves. Significant flooding was reported in Scituate and seawalls were damaged at some other coastal locations in Massachusetts (MACZM, 2016).

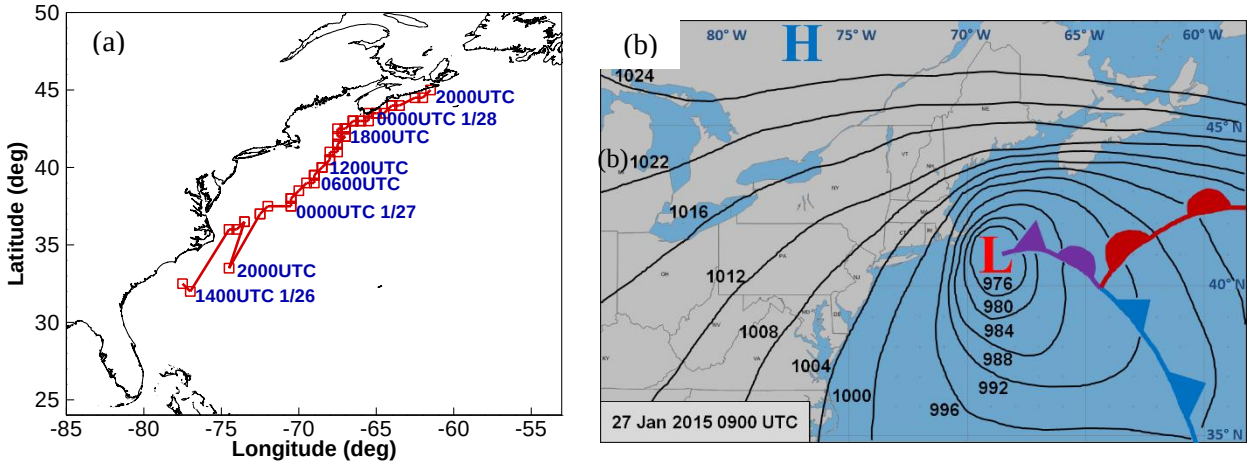


Figure 4.2. The January 2015 North American blizzard. (a) The storm track: the red solid line with squares marks the track; (b) Surface atmospheric pressure analysis at 9:00 UTC, 1/27/2015. Intense low pressure to the southeast of Scituate in conjunction with strong high pressure to the north produces a strong northeasterly wind fetch across the Gulf of Maine. "L" denotes low pressure and "H" denotes high pressure. The solid blue line with triangles marks the cold front. The solid red line with semicircles marks the warm front. The solid purple line with semicircles and triangles marks the occluded front. The Isobars are drawn for every 4 hPa.

### 4.2.3 Field measurement

A Solinst LTC Levelogger Edge, which combines a datalogger, a Hastelloy pressure sensor, a temperature detector and a conductivity sensor, was deployed to measure the water level, temperature and conductivity in the Avenues Basin during storms. Contained in a PVC pipe, the device was secured to a telephone pole next to a staff gauge on the 7th Avenue in the basin prior to several storm events. The datalogger was set to record water level at a 6-minute interval, which was chosen to be the same as the time interval of the data collection at the nearest tide gauge in Boston Harbor. Since the LTC Levelogger Edge measures the absolute pressure, which includes both the water pressure and the atmospheric

pressure to obtain water level, a Solinst Barologger Edge was used to compensate the atmospheric pressure fluctuations. The overtopping water volume was estimated by combining the measured water depth from the bottom of the Avenues Basin with the basin volume determined by the USGS LIDAR data (Heidemann, 2014). The field measurements were used to validate the model prediction of wave overtopping at the seawall.

The water level recorded by the datalogger during the January 2015 North American blizzard is shown in Figure 4.3b. The area of the basin was determined by plotting the USGS LIDAR data of topography in the basin at 0.3048 m elevation contour intervals using ArcGIS. The area in square meters was then calculated for each 0.3048 m slice, from the bottom of the basin at an elevation level of 2.48 m to the seawall crest at 5.00 m above the local mean sea level. To translate the water level recorded by the datalogger to the volume of water in the basin, a 4th order polynomial curve was fit to the basin area data derived using ArcGIS (Figure 4.3a) and the water volume was obtained by integrating the area data over the whole range of water level (Figure 4.3b). During the January 2015 North American blizzard, the maximum water level in the basin reached the crest of the seawall at 10:24 UTC on January 27. The corresponding peak accumulated water volume in the basin was 166,509 $m^3$ (Figure 4.3b).

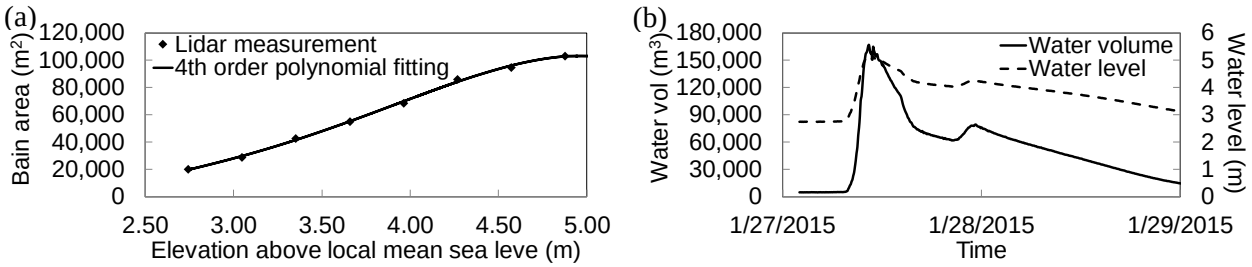


Figure 4.3. Water level, basin area and water volume measured in the Avenues Basin during January 2015 North American blizzard. (a) Basin area; (b) Water level recorded by the datalogger and the corresponding water volume.

About 449.3 m of seawall along the Avenues Basin contributes to the flooding through overtopping. Site survey was conducted at four locations S1-S4 (Figure 4.1b) along the seawall to obtain the crest and toe elevations of the seawall at these locations. The cross-shore profiles from the seawall to the end of the foreshore at these four locations were then determined by combining the site survey data

with USGS LIDAR data. Figure 4.4 shows the sketch of the cross-shore profile at site S2 (Figure 4.1b). The beach profiles consist of two sections: a steep slope adjacent to the seawall and a mild slope further offshore. The steep slope is treated as a sloping structure in this study and the mild slope further offshore is treated as the foreshore in front of the structure. Table 4.1 lists the site survey data necessary for overtopping prediction, including the crest elevation of the vertical wall, the toe elevation of the vertical wall, the steep slope in front of the vertical wall, the toe elevation of the steep slope and the mild slope further offshore.

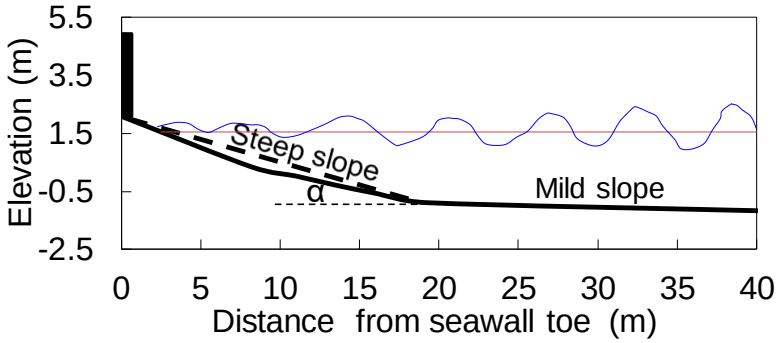


Figure 4.4. The sketch of the cross-shore profile from the seawall to the end of foreshore at S2 (Figure 4.1b).

Table 4.1. Detailed information of the seawalls along the Avenues Basin in Scituate, MA (All elevations are referred to local mean sea level in Scituate, MA)

| Site | Crest elevation of vertical wall (m) | Toe elevation of vertical wall (m) | Steep slope adjacent to seawall α (-) | Toe elevation of the steep slope (m) | Mild slope offshore (-) |
|---|---|---|---|---|---|
| S1 | 5.00 | 2.82 | 0.125 | -0.87 | 0.021 |
| S2 | 5.00 | 2.08 | 0.154 | -0.87 | 0.021 |
| S3 | 5.00 | 1.19 | 0.113 | -0.87 | 0.036 |
| S4 | 5.00 | 2.74 | 0.148 | 0.04 | 0.032 |

## 4.3 Methodology

Coastal flooding prediction presents several challenges: (1) accurate description of processes at various spatial and temporal scales, (2) geometric complexities of the coastal environment (natural barriers, seawalls), (3) nonlinear hydro-morphological interactions, (4) lack of field observation for model validation and (5) the uncertainty propagating from the meteorological forcing to coastal flood risk prediction (Du et al., 2010; Gallien et al., 2014; Zou et al., 2013). In this study, an integrated multiscale model framework was developed to investigate the impacts of tide, surge and waves on coastal flooding in the northeastern United States (Figure 4.5). The integrated model system consists of four components: (i) a tide, surge and wave coupled hydrodynamic model SWAN+ADCIRC (Dietrich et al. (2011, 2012) spanning from the oceanic to nearshore region; (ii) a surf zone model by Goda (1975, 2009), (iii) a wave overtopping model (EurOtop, 2016) and (iv) a drainage model (Henderson, 1966) to estimate the discharge from the basin behind the seawall. The coupled tide, surge and wave model incorporates the meteorological and tidal forcing to obtain nearshore hydrodynamics. The wave overtopping formula requires input of wave height and period at the toe of the seawall for wave overtopping prediction. The finest grid resolution of the unstructured grid along the Scituate coast is 60 m, which is not sufficient to properly resolve the wave parameters at the toe of the seawall. Also, SWAN cannot resolve wave processes in the surf zone properly, so that a surf zone model is required to propagate waves generated by SWAN from nearshore to the toe of coastal structures. The wave parameters and water level at the toe of the structures predicted by the surf zone model are then fed into a wave overtopping model to predict the coastal flooding due to overtopping. The water volume in the basin is then calculated by subtracting the water drained from the total water volume that overtops the seawall.

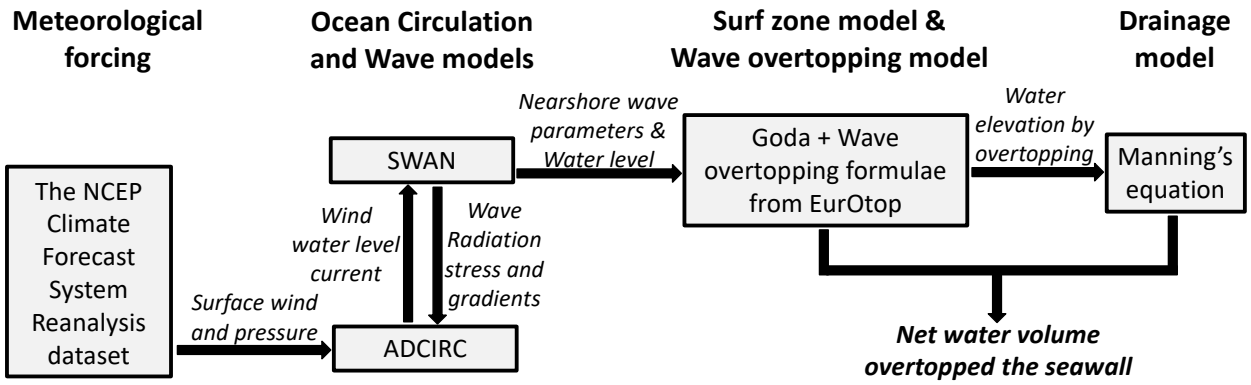


Figure 4.5. Integrated modeling system for coastal flooding arising from wave overtopping at a seawall.

### 4.3.1 Tide, surge and wave models

The northeastern coast of United States is both a geometrically and hydrodynamically complex region due to its intricate coastline and complex bathymetric features. Simulation of the hydrodynamics in this region requires an accurate description of processes at various spatial and temporal scales from the ocean basin to the inlet and estuary. It is therefore advantageous to use the ADvanced CIRCulation (ADCIRC) model on an unstructured grid to capture the hydrodynamic response to both meteorological and tide forcing in this region. Originally developed by Luettich and Westerink (2004), the two-dimensional (2-D) depth-integrated version of ADCIRC, often referred to as ADCIRC-2DDI, was used in this work. The ADCIRC-2DDI (Luettich and Westerink, 2004) solves the depth-integrated shallow water equation on an unstructured triangular mesh using a coupled discontinuous-continuous Galerkin finite element method (Dawson et al., 2006). The depth-integrated shallow water equation couples a hyperbolic continuity equation for water elevation and momentum equations for the horizontal depth-averaged velocities. By adopting an unstructured triangular mesh, the ADCIRC-2DDI model provides considerable flexibility in resolving complex geometry and bathymetry while maintaining computational efficiency when solving multiscale hydrodynamic processes ranging from the deep ocean to the coast. ADCIRC also includes a robust wetting and drying algorithm to predict changes in the location of the water line as the water level rises and falls. In past decades, ADCIRC has gained popularity as a tool to predict coastal inundation.

The third-generation spectral wave model Simulating WAves Nearshore (SWAN) solves the wave action balance equation for wave spectra of random short-crested, wind-generated waves and swell based on winds, bottom topography, tides and currents (Booij et al., 1999; Ris et al., 1999). The model is particularly applicable in coastal waters because it accounts for several shallow water wave processes, i.e., triad-wave interaction, depth-induced wave breaking and bottom friction dissipation. Zijlema (2010) adapted the original SWAN code on structured grid to run on an unstructured grid by using a vertex-based, fully implicit, finite difference algorithm. SWAN on an unstructured grid can simulate multiscale wave hydrodynamic processes ranging from the deep ocean to the coast without the traditional nesting technique. While widely applied for wave simulation in the nearshore, the application of SWAN in surf zone may result in inaccurate prediction of wave parameters.

Dietrich et al. (2011, 2012) integrated SWAN and ADCIRC. The coupled model runs on the same unstructured mesh, which allows seamless information exchange between the two model components. For practical implementation, ADCIRC first interpolates meteorological forcing on each node of the shared unstructured mesh and solves the generalized wave continuity equation for water level and depth-integrated current. It then passes the wind stress, water level and current to SWAN. SWAN solves the wave action balance equation and integrates over the spectral domain for wave radiation stress, which is subsequently passed back to ADCIRC to be included in the vertically-integrated momentum equation for a new calculation of water level and current. ADCIRC is typically run at much shorter time step than SWAN. For two-way coupling between ADCIRC and SWAN, the information exchange between the two model components happens at the same interval as the integration time step of SWAN.

### 4.3.2 Surf zone model

The surf zone model by Goda (1975, 2009) is used to propagate waves from the seaward edge of the surf zone to the toe of coastal defenses in this study. Goda (1975) proposed an empirical formula based on the compilation of laboratory results of wave breaking for random waves. In Goda's model, the breaker index, which is the ratio of limiting breaker height to water depth is dependent on the bottom slope and the relative water depth. The breaker index is expressed as follows,

$$\frac{H_b}{h_b} = \frac{A}{h_b/L_0}\left\{1 - \exp\left[\frac{\pi h_b}{L_0}(1 + 15\tan^{4/3}\theta)\right]\right\} \quad \text{(Equation 4.1)}$$

Where $H_b$ and $h_b$ are wave height and water depth when wave breaks. $L_0$ is the deepwater wave length corresponding to the spectral mean wave period. $\tan\theta$ is the bottom slope. When applied for irregular waves, the empirical constant A is set at 0.18 for the upper limit and 0.12 for the lower limit of the triangular cut of the probability density function of the Rayleigh distribution.

The actual formulae for approximation of significant wave height at the shoreline are as follows.

$$H_{1/3} = \begin{cases} K_s H_0' & : h/L_0 \geq 0.2 \\ \min\{(\beta_0 H_0' + \beta_1 h), \beta_{max} H_0', K_s H_0'\} & : h/L_0 < 0.2 \end{cases} \quad \text{(Equation 4.2)}$$

Where $K_s$ is the shoaling coefficient and is calculated based on linear wave shoaling theory (Dean and Dalrymple, 1984); $H_0'$ is the equivalent deepwater significant wave height with the inclusion of wave refraction; and h is the still water depth. The three coefficients $\beta_0$, $\beta_1$ and $\beta_{max}$ are calculated as below.

$$\left.\begin{aligned} \beta_0 &= 0.028(H_0'/L_0)^{-0.38}\exp[20\tan^{1.5}\theta] \\ \beta_1 &= 0.52\exp[4.2\tan\theta] \\ \beta_{max} &= \max\{0.92, 0.32(H_0'/L_0)^{-0.29}\exp[2.4\tan\theta]\} \end{aligned}\right\} \quad \text{(Equation 4.3)}$$

Goda's model (1975, 2009) is robust and considers the effects of several dynamic processes, e.g. wave setup and surf beats on breaking wave height. However, it is only applicable for unidirectional random waves propagating on a beach of uniform slope, and reasonable results are obtained for bottom slopes ranging from 1/200 to 1/10.

### 4.3.3 Wave overtopping model

The EurOtop (2016) empirical model for wave overtopping was used in this study. The vertical seawall at the Avenues Basin and the relatively steep slope in front of the seawall were treated as an integral structure, with the seawall being a wave wall on top of a slope. The empirical formulae from EurOtop (2016), in which the wave overtopping discharge per unit width is scaled by the relative freeboard, i.e. the height difference between the structural crest and the instantaneous water level, were applied for the corresponding simplified structural configuration. Based on EurOtop (2016), the dimensionless wave overtopping discharge is calculated as follows:

(1) With submerged wave wall toe

$$\frac{q}{\sqrt{g * H_{m0}^3}} = \frac{0.023}{\sqrt{\tan\alpha}} \gamma_b * \xi_{m-1,0} * \exp[-(2.7 * \frac{R_c}{\xi_{m-1,0} * H_{m0} * \gamma_b * \gamma_f * \gamma_\beta * \gamma_v})^{1.3}] \quad \text{(Equation 4.4)}$$

with a maximum of $\frac{q}{\sqrt{g*H_{m0}^3}} = 0.09 * \exp[-(1.5 * \frac{R_c}{H_{m0}*\gamma_f*\gamma_\beta*\gamma^*})^{1.3}]$ (Equation 4.5)

(2) With emerged wave wall toe

$$\frac{q}{\sqrt{g * H_{m0}^3}} = 0.09 * \exp[-(1.5 * \frac{R_c}{H_{m0} * \gamma^*})^{1.3}] \quad \text{(Equation 4.6)}$$

$$\gamma^* = \gamma_v = \exp(-0.56 * \frac{h_{wall}}{R_c}) \quad \text{(Equation 4.7)}$$

Where q is the mean overtopping discharge. $H_{m0}$ is the incident wave height at the toe of the structure. In this study, $H_{m0}$ refers to the significant wave height at the toe of the steep slope in front of the seawall if not described otherwise. $\tan\alpha$ is the characteristic slope of the structure designated "steep slope at the toe of the seawall" in Table 4.1, $\xi_{m-1,0}$ is the breaker parameter, $R_c$ is the crest freeboard, $\gamma_b$ is the influence factor for a berm, $\gamma_f$ is the influence factor for roughness elements on a slope, $\gamma_\beta$ is the influence factor for oblique wave attack, $\gamma_v$ is the influence factor for a wave wall, $h_{wall}$ is the height of the wave wall.

When the toe of the wave wall is submerged, the wave wall is treated as a 1:1 slope while keeping the same relative freeboard. An iterative process is applied to determine the average slope of the integral structure. More details of the procedure for implementing the above overtopping model are given in Appendix A.

**4.3.4 Drainage model**

The water in the flooded Avenues Basin caused by wave overtopping flows out through a drainage pipe and the corridor of the Oceanside Drive at the southeast corner of the basin as described in Section 2.1. During storm events with large wave overtopping discharge, the water mainly flows out

through the Oceanside Drive corridor because the flow rate through the drainage system is limited due to snow, ice and other debris.

Manning's equation (Henderson, 1966) for open channel flow was used to estimate the flow rate through the Oceanside Drive corridor. Manning's equation calculates steady uniform flow velocity in open channels as a function of Manning's roughness coefficient, hydraulic radius and friction slope.

$$V = \frac{1}{n} R^{2/3} S_f^{1/2} \quad \text{(Equation 4.8)}$$

Where V is flow velocity, n is Manning roughness coefficient, R is hydraulic radius of open channels, $S_f$ is friction slope. For uniform flow, the friction slope $S_f$ can be replaced by the bed slope of open channels $S_0$.

## 4.4 Model setup

### 4.4.1 Model domain and bathymetry

Accurate simulation of coastal circulation requires resolving processes ranging from channel-scale to ocean basins (Bunya et al., 2010; Warner et al., 2008; Zhang and Baptista, 2008). To develop a storm surge model at any location, three important factors are considered: (1) the accurate representation of bathymetric and geometric features by model grid, (2) appropriate boundary conditions and (3) the reasonable representation of resonant modes (Blain et al., 1994). While large domains are usually required to reasonably capture the physical responses and simplify the boundary conditions (Blain et al., 1994; Westerink et al., 1994), they can be computationally demanding. The unstructured mesh can accommodate larger domains for coastal ocean circulation and wave models with locally refined grids to resolve shallow bathymetry, steep bathymetric gradients and intricate shorelines (Hagen et al., 2001). Although we mainly focus on surge and wave response along the coast of the northeastern United States, the model grid was set up to cover the entire east coast to minimize the influence of open boundary conditions, while providing high resolution within regions of rapidly varying geometry and flow response (Blain et al., 1994; Westerink et al., 1994; Westerink et al., 2008). The current model domain (Figure 4.6) is an evolution of the Eastcoast domain by Blain and Westerink (1994) and Westerink and Muccino

(1994) and the domain for the Gulf of Maine by Yang and Myers (2007), Xie et al. (2016) and Zou and Xie (2016). The model domain covers the western North Atlantic, the Caribbean Sea, the Gulf of Mexico and the Gulf of Maine. The open boundary of the domain is extended further to the east along the 56°W meridian compared to the Eastcoast domain to allow longer fetch for surge and wave generation. Also, because the open boundary is located primarily in deep-water, the impact of nonlinear processes is limited.

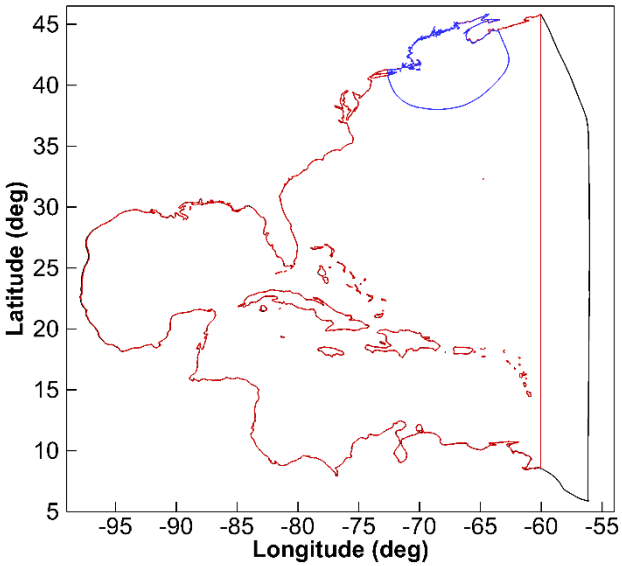


Figure 4.6. Comparison of model domains for wave and surge modeling. The black solid line marks the current model domain. The red solid line marks the Eastcoast model domain used by Blain and Westerink (1994) and Westerink and Muccino (1994). The blue solid line marks the model domain for the Gulf of Maine by Yang and Myers (2007), Xie et al. (2016) and Zou and Xie (2016).

The bathymetric data in the model domain consists of 4 datasets: (1) the ETOPO1 1 arc-minute Global Relief Model by the National Geophysical Data Center (NGDC) of the National Oceanic and Atmospheric Administration (NOAA) (Amante and Eakins, 2009); (2) the 3 arc-second digital elevation model of the Gulf of Maine (Twomey and Signell, 2013); (3) the 1/3 arc-second digital elevation model of Portland, Maine (Lim et al., 2009); (4) the 1/9 arc-second USGS National Elevation Dataset (NED) for southern Maine (https://viewer.nationalmap.gov/viewer/). The NOAA VDatum software was used to convert the dataset elevations to a mean sea level datum when applicable (http://vdatum.noaa.gov). The

bathymetry, and locations of wave buoys and tide gauges are shown in Figure 4.7. The wave buoys and tide gauges in Figure 4.7b are listed in Table 4.2 and 4.3, respectively.

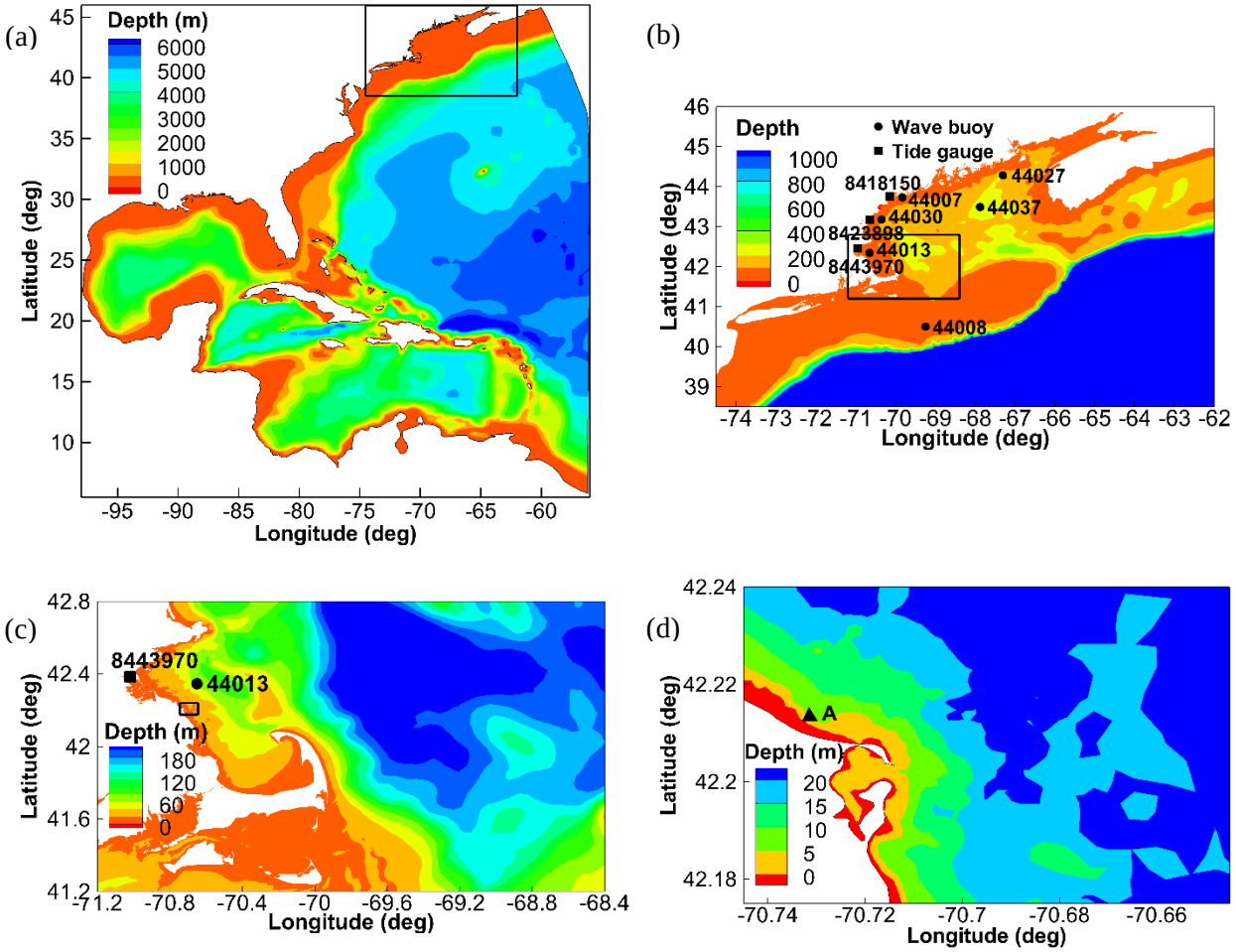


Figure 4.7. The bathymetry within the model domain. (a) The bathymetry for the east coast of United States. (b) Bathymetry for the Gulf of Maine indicated by the black rectangle in (a). (c) Bathymetry for the offshore of Massachusetts, USA indicated by the black rectangle in (b). (d) Bathymetry for the coast of Scituate, MA, USA indicated by the black rectangle in (c) The black triangle indicates the location of the seawall along the Avenues Basin.

Table 4.2. Wave buoys in the Gulf of Maine

| Wave buoy | Buoy location | Water depth / m |
|---|---|---|
| 44007 | Southeast of Portland, Maine | 26.5 |
| 44008 | Southeast of Nantucket, Massachusetts | 66.4 |
| 44013 | East of Boston, Massachusetts | 64.5 |

Table 4.2 Continued

| | | |
|---|---|---|
| 44027 | Southeast of Jonesport, Maine | 178.6 |
| 44030 | Western Maine Shelf | 62.0 |
| 44037 | Jordan Basin | 285.0 |

Table 4.3. Tide gauges in the Gulf of Maine

| Tide gauge | Location | Water depth / m |
|---|---|---|
| 8418150 | Portland, Maine | 11.5 |
| 8423898 | Fort Point, New Hampshire | 3.0 |
| 8443970 | Boston Massachusetts | 5.0 |

The unstructured triangular mesh for the model domain consists of 245,838 nodes and 463,593 elements. The water surface elevation, flow velocity and wave spectra are computed at each node. The grid resolution ranges from 100 km in deep basin to 10 m at the coast, providing sufficient resolution for tide, surge and wave propagation at the coast without compromising computational efficiency. Along the Scituate coast, the grid resolution is 60 to 100 m.

**4.4.2 Surface wind and pressure forcing**

Surface wind and pressure data from two meteorological datasets, the NCEP Climate Forecast System Version 2 (CFSv2) (Saha et al., 2014) and NCEP North American Regional Reanalysis (NARR) (Mesinger et al., 2006), were compared to determine which produced the more accurate storm surge and wave prediction during the January 2015 North American blizzard. The CFSv2 is a quasi-global, fully coupled atmosphere-ocean-land surface-ice model, which incorporates two data assimilation systems and two forecast models. The two assimilation systems provide the atmospheric, land surface and ocean initial conditions for model simulation. The CFSv2 model has a global coverage with 0.5-degree grid resolution and generates atmospheric output at hourly intervals. NARR produces a long-term and high-resolution

atmospheric and land surface hydrology dataset for the North American domain by blending a forecast model, a data assimilation system and a global reanalysis system. Currently, NARR generates 3-hourly wind and pressure data covering the Continental US with 32 km (approximately 0.30 degree) grid resolution.

Both datasets were applied for storm surge and wave prediction during the January 2015 North American blizzard. We found that incorporation of wind and pressure data from the CFSv2 dataset yielded a better prediction of storm surge and wave parameters than the NARR dataset. Even though the NARR model generates higher spatial resolution output than CFSv2, it is optimized to improve prediction of precipitation over land rather than the accuracy of wind and atmospheric pressure over the ocean. Zou et al. (2013) found that increased spatial resolution does not significantly improve the accuracy and reliability of surface wind and pressure values over the open ocean. Also, the hourly output of CFSv2 can more accurately represent the evolution of the storm compared with the 3-hourly output of NARR data.

In this paper, we only show model results with CFSv2 wind and pressure forcing. The ocean surface pressure and wind field at 10 m above ocean surface were used as meteorological forcing for the ADCIRC and SWAN model.

**4.4.3 Boundary conditions**

The choice of boundary conditions can have a significant impact on the modeling results for the area of interest. To accurately predict those conditions, the tide and the storm-induced surge and waves at the open boundaries must be properly included. Since the open boundary for the coupled SWAN+ADCIRC model domain is placed mostly in deep ocean, the effects of shallow water nonlinear processes on the tide are ignored. The storm surge response is mainly an inverted barometer pressure effect at deep water and can be easily calculated. A decrease of 100 Pa in barometric pressure corresponds to a rise in sea level by 0.01 m. In this case, the storm surge due to the inverted barometric pressure effect was negligible. The storm tracked close to the east coast where the storm surge was significant, therefore the lateral boundary condition of storm surge near the Scotian Shelf was neglected. The waves generated

outside of the model domain can propagate into the coupled SWAN+ADCIRC domain to account for the swell impact.

At the open boundary, both tidal response and waves were prescribed for the January 2015 North American blizzard. The eight most significant astronomical tide constituents (M2, S2, N2, K2, K1, P1, O1, Q1) were used. The harmonic constants were interpolated from the global model of ocean tides TPXO (Egbert et al., 1994). A SWAN model covering the North Atlantic was set up to run on a structured grid to generate 2D spectra at the boundary nodes that were subsequently used as the wave boundary condition for the coupled SWAN+ADCIRC model.

**4.4.4 Model parameters**

The two-dimensional depth-integrated version of ADCIRC was used to simulate the water level and circulation during the January 2015 North American blizzard. The wind stress was calculated by a standard quadratic law. The air-sea drag coefficient defined by Garratt's drag formula (Garratt, 1977) was used with a cap of $C_d \leq 0.0035$. Garratt's drag coefficient is widely used for storm surge modeling (e.g., Westerink et al., 2008; Bunya et al., 2010; and Dietrich et al., 2010). The bottom stress was computed by the standard quadratic parameterization. The bottom friction coefficient was calculated using a Manning's n formation.

$$C_f = \frac{gn^2}{\sqrt[3]{H}} \qquad \text{(Equation 4.9)}$$

Where $C_f$ is the bottom friction coefficient, n is the Manning coefficient, H is the total water depth, g is gravitational acceleration. The Manning n was assigned at each node of the unstructured triangular mesh based on the USGS National Land Cover (Bunya et al., 2010). In the open ocean, the Manning n was assigned a value of 0.025.

The finite amplitude and convection terms were activated to include the nonlinear processes. A wetting and drying algorithm was applied as well. The lateral viscosity was set at 5 $m^2/s$ for the ocean following Yang and Myers (2007) and 50 $m^2/s$ for the land. The time step for ADCIRC was set to 0.5 s to maintain computational stability.

The SWAN and ADCIRC models share the same unstructured mesh and surface wind forcing. The SWAN model was run with prescribed spectrum frequencies between 0.031384 and 1.420416 Hz. The range was discretized into 40 bins on a logarithmic scale. The wave spectrum was solved in 360 degrees with a directional resolution of 10 degrees. The JONSWAP formulation (Hasselmann et al., 1973) was used for bottom friction. The friction coefficient of 0.038 $m^2s^{-3}$ was used for both wind waves and swell (Zijlema et al., 2012). The time step for integration was set to 360 s.

The coupling interval at which information is passed between the models was the same as the time step for SWAN. ADCIRC passes wind stress, water level and currents to SWAN every 360 s, while SWAN passes radiation stress to ADCIRC to update the calculation of water level and current. A hyperbolic tangent function was applied for five days until the tidal component reached equilibrium prior to applying surface wind and pressure within the ADCIRC model

Three cases were run: (1) tide-surge simulation without wave effects; (2) wave simulation without tide-surge and the associated current; (3) a fully coupled SWAN+ADCIRC run to include tide-surge and wave interactions.

### 4.5 Tide-surge and wave interaction

#### 4.5.1 Model validation

The model-predicted tides were compared with field measurements at three tide gauges in the Gulf of Maine. Tide gauge 8443970 is the nearest to the area of interest and located approximately 31 km northwest of Scituate, MA. The tidal amplitudes and phases for the five major tidal constituents (M2, S2, N2, K1 and O1) in the Gulf of Maine were obtained using the MATLAB harmonic analysis toolbox T_Tide (Pawlowicz et al., 2002). The time for harmonic analysis spans from 1:00 UTC 12/16/2014 to 0:00 UTC 2/1/2015. For simplicity, 1:00 UTC 12/16/2014 was used as the phase reference. Comparisons of observed and predicted tidal amplitudes and phases for the five major tidal constituents were carried out. The tidal amplitudes and phases are very well reproduced in general. The error of tidal amplitudes was in the range of 0.00-0.09 m. The dominant constituent M2 had an error of 0.07-0.09 m, accounting

for 5-7 percent of the mean tidal amplitude. The error of tidal phases was less than 11°. The dominant constituent M2 had an error of 8°, accounting for 8 percent of the mean tidal phase.

A comparison of the predicted and observed water level at the three tide gauges is shown in Figure 4.8. The model results with and without wave effect compared well with the tide gauge data. The surge level was slightly under-predicted in general. Increased storm surge level was observed at the three tide gauges when the wave effects were included. In shallow water, breaking waves generate radiation stress forcing water onshore. The cross-shore wave radiation stress gradient is balanced in turn by an increased pressure gradient. At the storm peak, the wave setup was 0.14 m at both tide gauge 8423898 and 8443970, accounting for 14 percent and 11 percent of the surge levels respectively. The inclusion of wave effects on surge level significantly increased the accuracy of prediction. After January 28, the surge level was slightly underestimated. A possible cause is that the water level fluctuation generated by the wind and atmospheric pressure anomaly at the open ocean boundary plays a significant role as the storm moves over the boundary, an effect that was not incorporated along the boundary in the current model set.

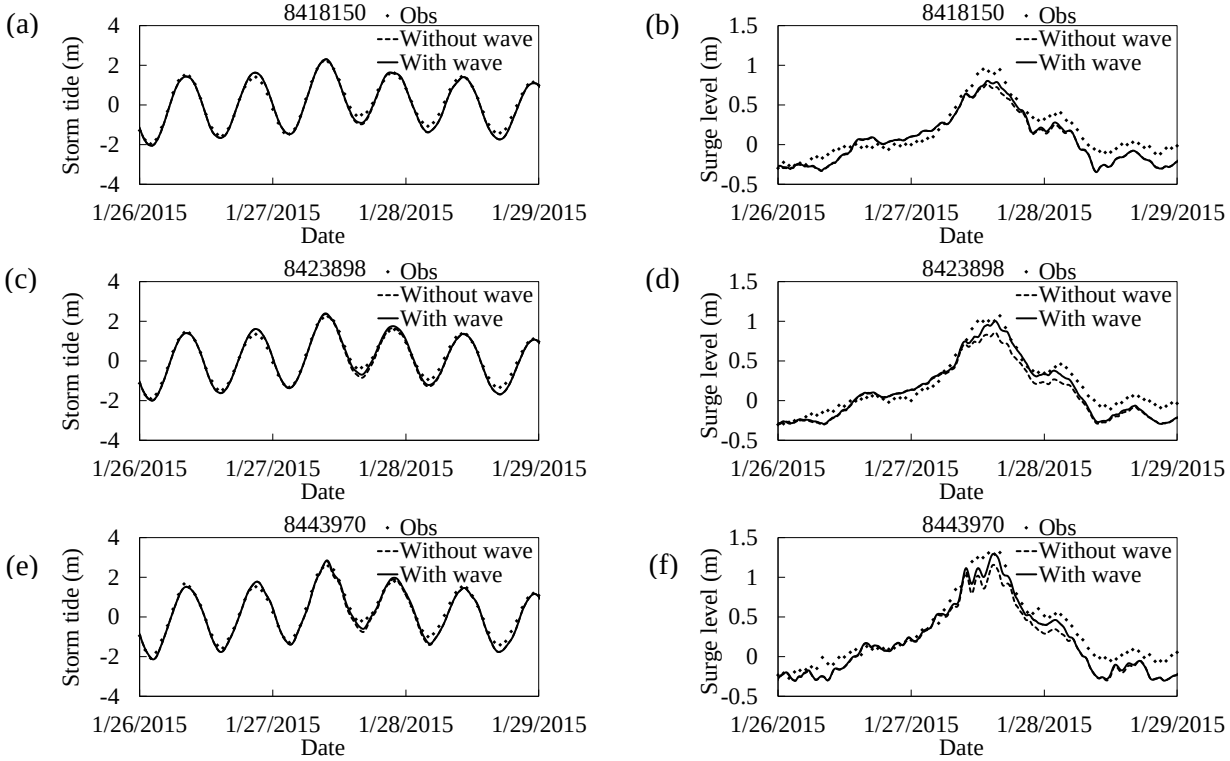


Figure 4.8. Comparison of predicted wave level with tide gauge data during the 2015 North American blizzard.

Wave comparisons are shown in Figure 4.9. Among the five buoys compared, buoy 44013 is located 16 km to the northeast of Scituate. The wave height and period were reasonably well reproduced by model prediction with and without tide-surge effect, however the simulation results were slightly improved when accounting for the tide-surge effect. At buoy 44013, the inclusion of the tide-surge effect increased significant wave height by 0.85 m at the storm peak. The predicted peak wave period was also more accurate when the water level and current effects were considered, indicating more accurate wave spectral distribution. Since the wave buoy in relatively deep water (Table 4.2), the impact of tide-surge on waves is not as significant as that at the coast, where the wave height is significantly modulated by tide-surge through water depth (Zou and Xie, 2016). Current also plays a significant role due to wave refraction and the Doppler effect.

Figure 4.9. Comparison of predicted wave parameters with wave buoy data during the 2015 North American blizzard.

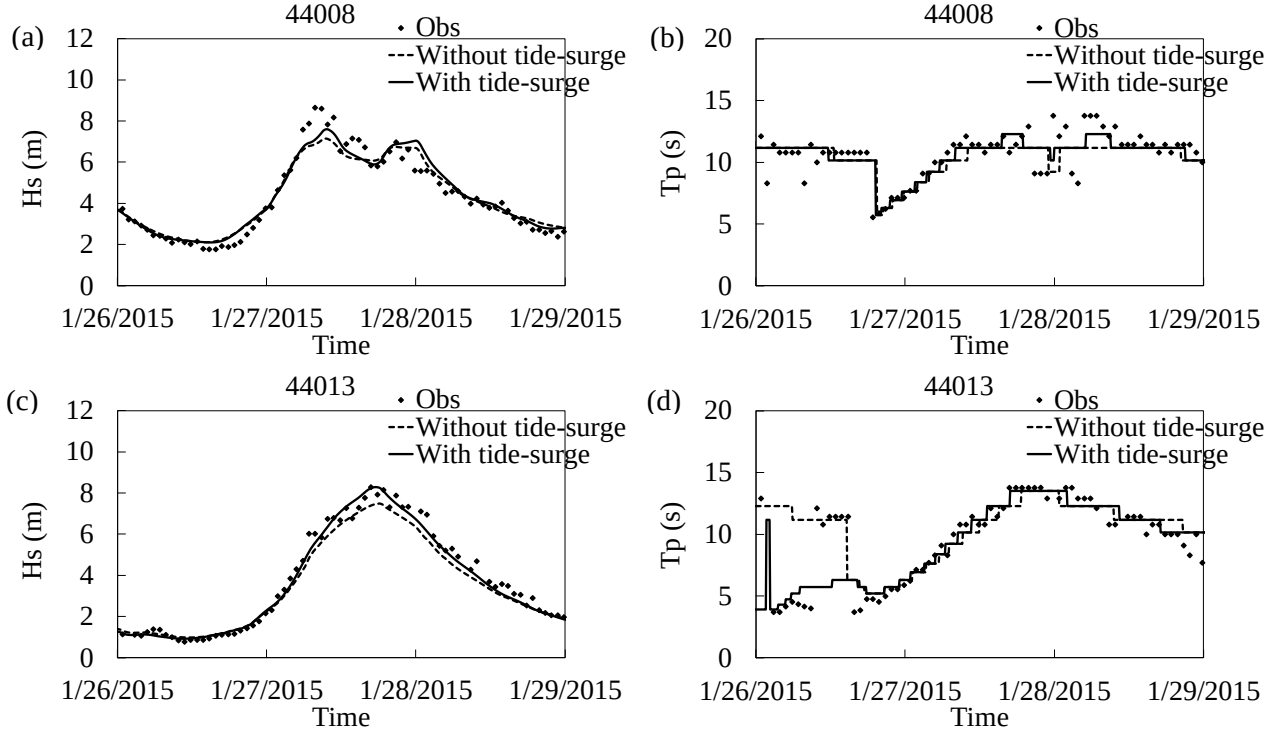

Figure 4.9 Continued

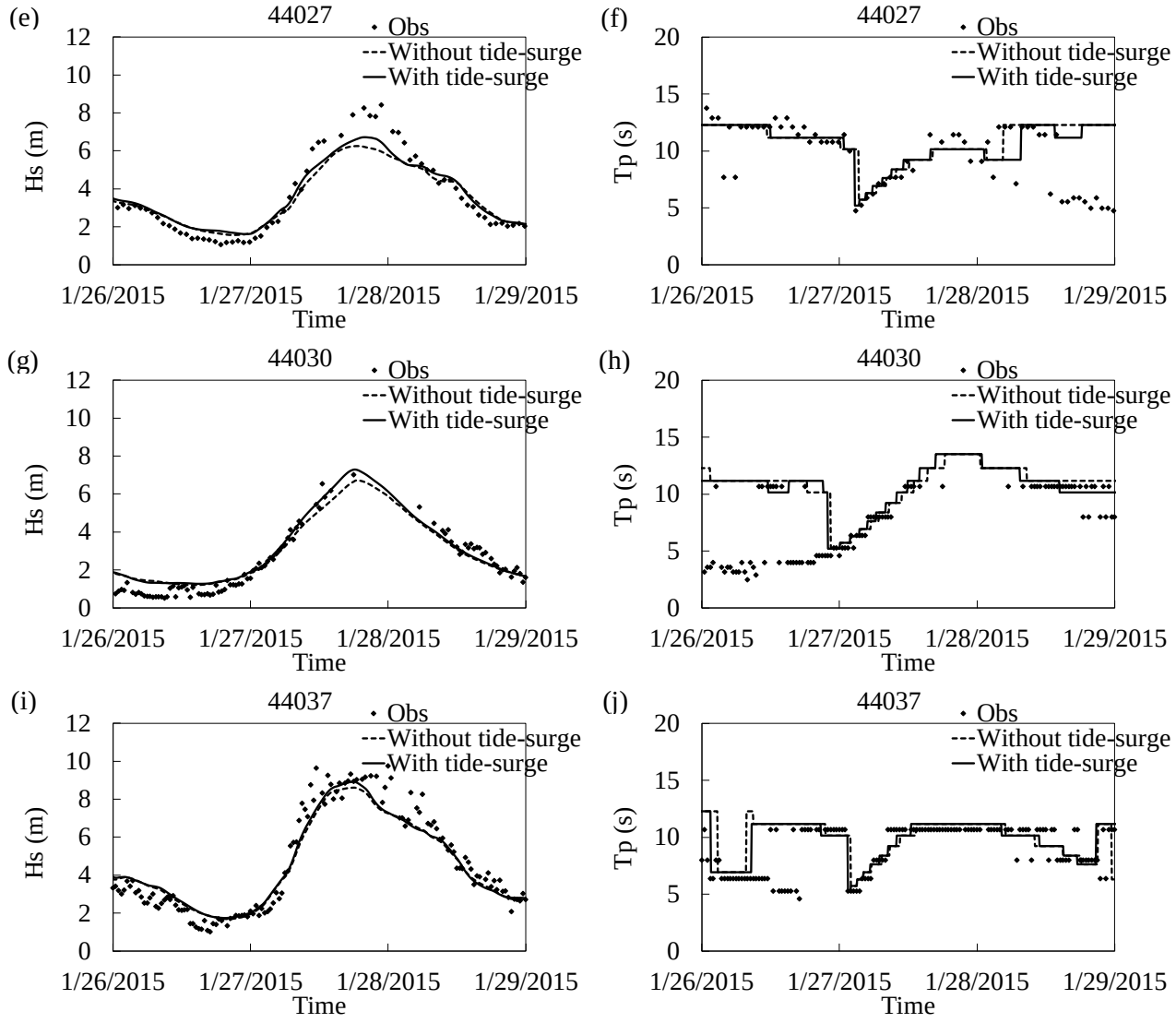


### 4.5.2 Impact of waves on tide-surge

The impact of tide-surge and wave interaction on waves and circulation was analyzed at the Scituate coast. During the January 2015 North American blizzard, the peak wave height offshore of Scituate occurred at 18:00 UTC on January 27th when the total water level was close to mean sea level at the Scituate coast. The peak surge level appeared at 15:00 UTC on January 27th at low tide. The phase lag of peak wave and peak surge was mainly attributed to the modulation of water level on waves and storm surge. While peak surge level usually coincides with low tide, the peak wave appears when less

depth-limited wave breaking happens. The wave and circulation fields were plotted at four tidal phases, i.e. high tide at 10:00 UTC 1/27/2015, falling mid-tide at 13:00 UTC 1/27/2015, low tide at 16:00 UTC 1/27/2015 and rising mid-tide at 19:00 UTC 1/27/2015, to analyze the interaction between tide-surge and waves over one tidal cycle.

The effect of waves on circulation at different tidal phases is shown in Figure 4.10. The waves contribute to increased water level and current through wave radiation stress. The wave setup varied along the coast depending on the geometry of the coastline, as well as the wave-induced current. At high tide, the water depth was increased by 2.5 m at the coast, allowing large waves to propagate toward shore without breaking. The wave setup was thus expected to be smaller, with a magnitude of 0.15 m north of the headland in Scituate. A small clockwise circulation gyre also formed north of the southern headland due to waves, which tend to increase the water level at the south end of the gyre. At the three other tidal phases, the wave setup was more pronounced and reached 0.25 m north of the headland in general. The increased wave setup was mainly caused by: (1) the increased wave height offshore of Scituate; (2) more pronounced depth-limited wave breaking due to smaller water depth at the coast compared to high tide. At low-tide and falling mid-tide, 0.05 m of wave set-down occurred offshore of Scituate, and the wave-induced clockwise circulation gyre gradually disappeared. The onshore current due to waves intensified with increased wave height gradient in the cross-shore direction. Enhanced water level and circulation has been identified due to the wave effect in other open bays as well (Olabarrieta et al., 2014; Zou and Xie, 2016).

At the storm peak, wave setup contributed approximately 0.3 m to the water level along the coast of the Avenues Basin. While the wind-driven current was to the south, the contribution of waves added complexity to the circulation field. A strong wave-induced current flowed in the onshore direction and gradually veered northward to the north of the headland in Scituate, and southward to the south of that point. The wind-driven current ranged from 0.2 to 0.5 m/s. The wave-induced current reached 1.0 m/s and was dominant in the system.

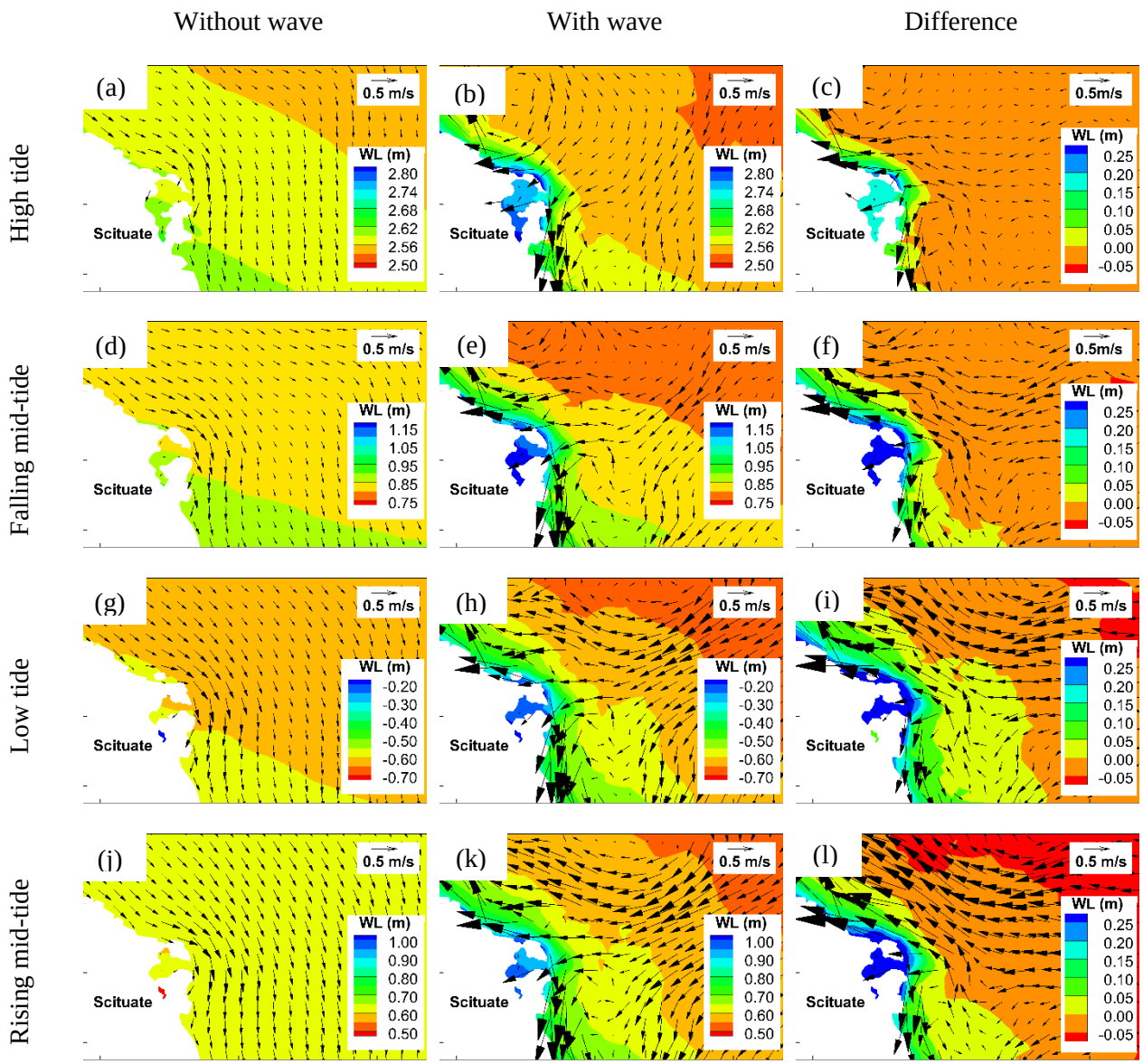


Figure 4.10. Water level and circulation fields at four tidal phases during the January 2015 North American blizzard. (a)(b)(c) show water level and circulation fields at high tide at 10:00 UTC 1/27/2015, (d)(e)(f) show water level and circulation fields at falling mid-tide at 13:00 UTC 1/27/2015, (g)(h)(i) show water level and circulation fields at low tide at 16:00 UTC 1/27/2015, (j)(k)(l) show water level and circulation fields at rising mid-tide at 19:00 UTC 1/27/2015.

### 4.5.3 Impact of tide-surge on waves

The modulation of tidal phases on waves is significant both at the coast and offshore (Figure 4.11). At high tide, the wave height was increased by 0.7-1.0 m at water depth greater than 10 m when the tide-surge effect was included. The tide-surge effect on waves was more pronounced at the coast, with

increased wave heights of 1.3-1.6 m. This is mainly attributed to less wave breaking due to increased water depth. At low tide, the wave height was increased in the offshore region and decreased at the coast. Similarly, at falling and rising mid-water, the wave height increase was greater offshore than that at the coast.

When the significant wave height reached its peak offshore of Scituate at 18:00 UTC 1/27/2015, the impact of tide-surge and its associated current on waves was greater in deeper water than at the coast. In relatively deeper water, the significant wave height increased by 0.5 to 1.5 m with the tide-surge effect. At the coast, the impact of tide-surge was negligible because the wave height reached its peak near rising mid-tide. At this moment, the wave height at the coast was mainly limited by depth-induced wave breaking. The peak wave period increased by 2 to 4 s from offshore to the coast with tide-surge effect, while mean wave direction remained the same because it is mainly determined by wave refraction in shallow water and the wave crests were generally parallel to the depth contour lines.

Figure 4.11. Wave fields during the January 2015 North American blizzard. (a)(b)(c) show wave fields at high tide at 10:00 UTC 1/27/2015, (d)(e)(f) show wave fields at falling mid-tide at 13:00 UTC 1/27/2015, (g)(h)(i) show wave fields at low tide at 16:00 UTC 1/27/2015, (j)(k)(l) show wave fields at rising mid-tide at 19:00 UTC 1/27/2015.

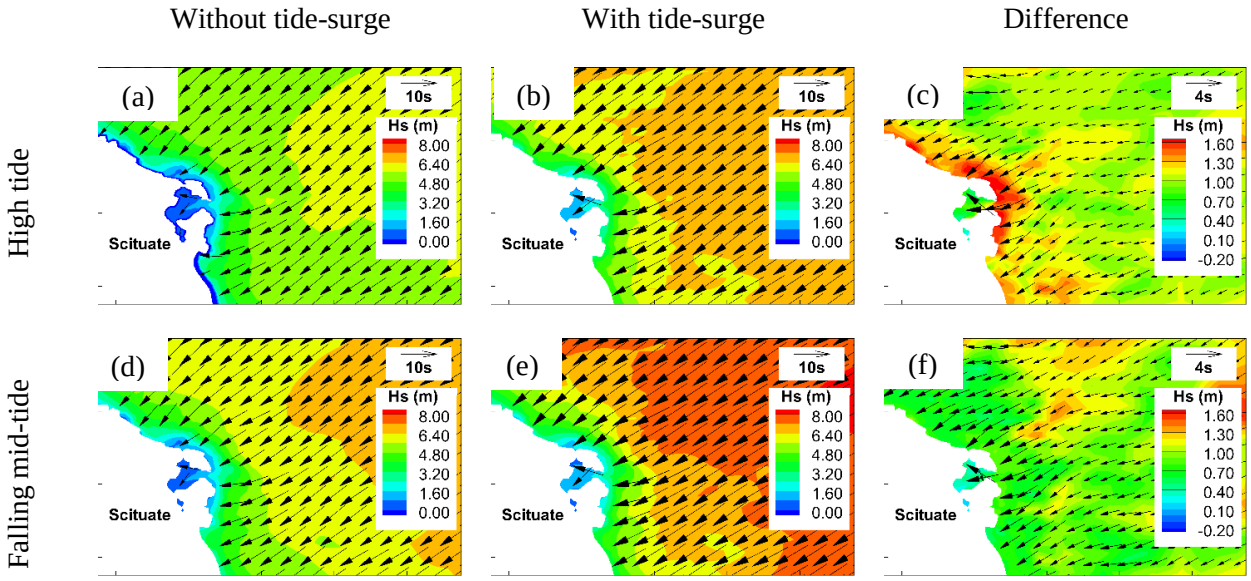

Figure 4.11 Continued

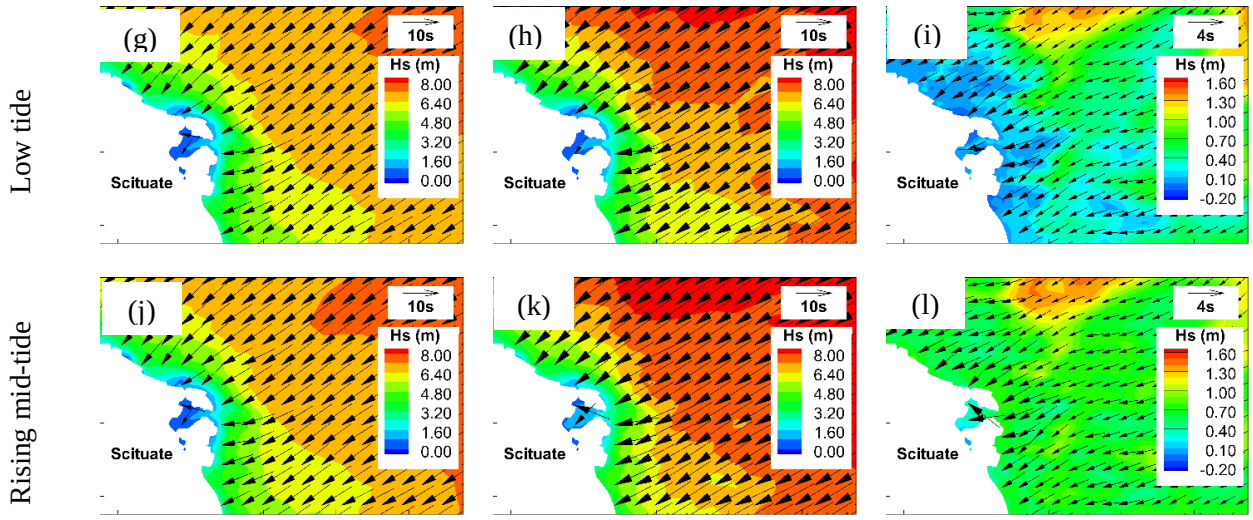


## 4.6 Wave overtopping in Scituate, Massachusetts

### 4.6.1 Drainage parameterization

Drainage of the Avenues Basin in Scituate, MA occurs through a drainage pipe and a flow corridor at the southeast corner of the basin. The drainage rate through the outlet pipe was 0.7 $m^3/s$ during the January 2015 North American blizzard. The cross-section of the flow corridor at the southeast corner of the Avenues Basin was simplified as an isosceles trapezoid. The width of the bottom base of the corridor is 4.60 m at 4.36 m above mean sea level and the base angle is 166 degrees. Flood water flows through this corridor when the water level reaches 4.36 m above mean sea level. The drainage rate was then calculated at 6-minute intervals based on the measured water level in the basin using the drainage model described in Section 3.4. The drainage rate through the corridor increased rapidly after the water level reached 4.36 m above the mean sea level in the basin. When the water level reached its peak in the basin at 10:24 UTC on January 27, the discharge rate through the corridor was 19.0 $m^3/s$. The flow discharge rate through the outlet pipe was significantly lower than via the corridor after the water level in the basin reached 4.36 m above the local mean sea level.

### 4.6.2 Wave overtopping validation

The wave overtopping model computes overtopping discharge per meter length of the seawall. The average wave overtopping discharge for the entire length of the seawall contributing to flooding the basin was calculated as the weighted average of the wave overtopping discharge at the 4 site survey locations as follows:

$$q_{avg} = q_{S1} * 32.8 + (q_{S2} + q_{S3})/2.0 * 343.7 + q_{S4} * 72.8 \quad \text{(Equation 4.10)}$$

Where $q_{avg}$ is the average overtopping discharge along the seawall; $q_{S1}$, $q_{S2}$, $q_{S3}$ and $q_{S4}$ are the wave overtopping discharges at locations S1-S4 respectively; the three constant numbers are the sectional lengths of the seawall marked in Figure 4.1b.

The wave and water level computed by the coupled SWAN+ADCIRC model were subsequently used to drive the surf zone and wave overtopping models to simulate wave overtopping along the coast of Avenues Basin. The predicted water volume in the basin contributed by wave overtopping minus that by drainage was then compared with the volume calculated using the water level data obtained as described in section 4.2.3.

Figure 4.12 shows the wave overtopping discharges at the 4 survey locations during the tidal cycle when the storm surge and waves reached their peaks. At S2 and S3, the wave overtopping discharge reached 0.10 and 0.08 $m^3$/s.m, while the wave overtopping at S1 and S4 was negligible. The wave overtopping discharge was in general in phase with water level at the seawall toe. At the storm peak, the storm tide reached 2.71 m above the mean water level, resulting in a submerged seawall toe at S2 and S3, while the seawall toe at S1 and S4 was still emergent. Even though the waves had broken before they reached the structure, the elevated water level allowed larger waves to propagate further toward shore until they reached the seawall toe because wave height is mainly depth-limited after breaking. Larger waves at the toe of the seawall produced significant overtopping at S2 and S3. The wave overtopping discharge at S2 increased more rapidly than that at S3 due to more vigorous wave breaking caused by the larger slope at S2.

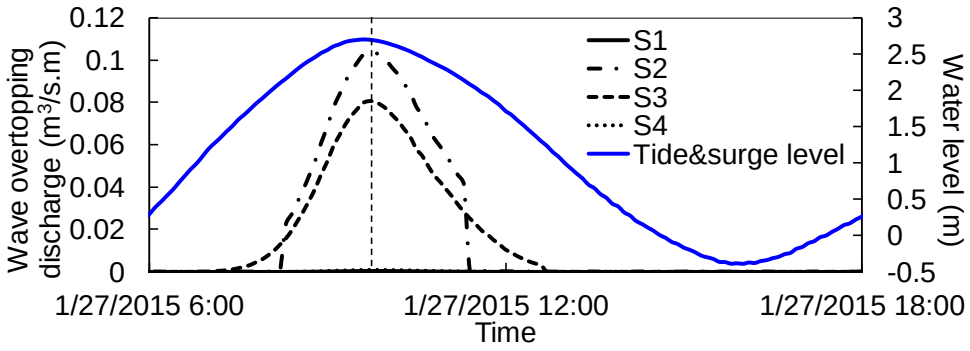


Figure 4.12. Water level and wave overtopping discharge at the four survey locations S1-S4. The tide&surge level were extracted at the toe of the steep slope in front of the seawall at S2 in the Avenues Baisn.

Figure 4.13 further illustrates the relationships between seawall toe elevation, water level, waves and wave overtopping discharge at S2. Due to the phase difference between the peak swell waves offshore and the highest water level at the coast, the peak significant wave height at 10 m water depth lagged slightly behind the highest water level (Figure 4.13a). However, the wave height was in phase with the total water level at the toe of the steep slope in front of the seawall due the modulating effect of water depth on wave height (Figure 4.13b). While the peak surge level reached 1.30 m approximately one hour before low tide, the highest water level coincided with high tide when the surge level was 0.97 m (Figure 4.13b). Between 8:12 UTC and 11:24 UTC on 1/27/2015, the seawall toe at S2 became submerged. With increased water level during this period, the significant wave height at the toe of the integral structure increased accordingly. Large waves rushed up the structure, resulting in significant wave overtopping at this site.

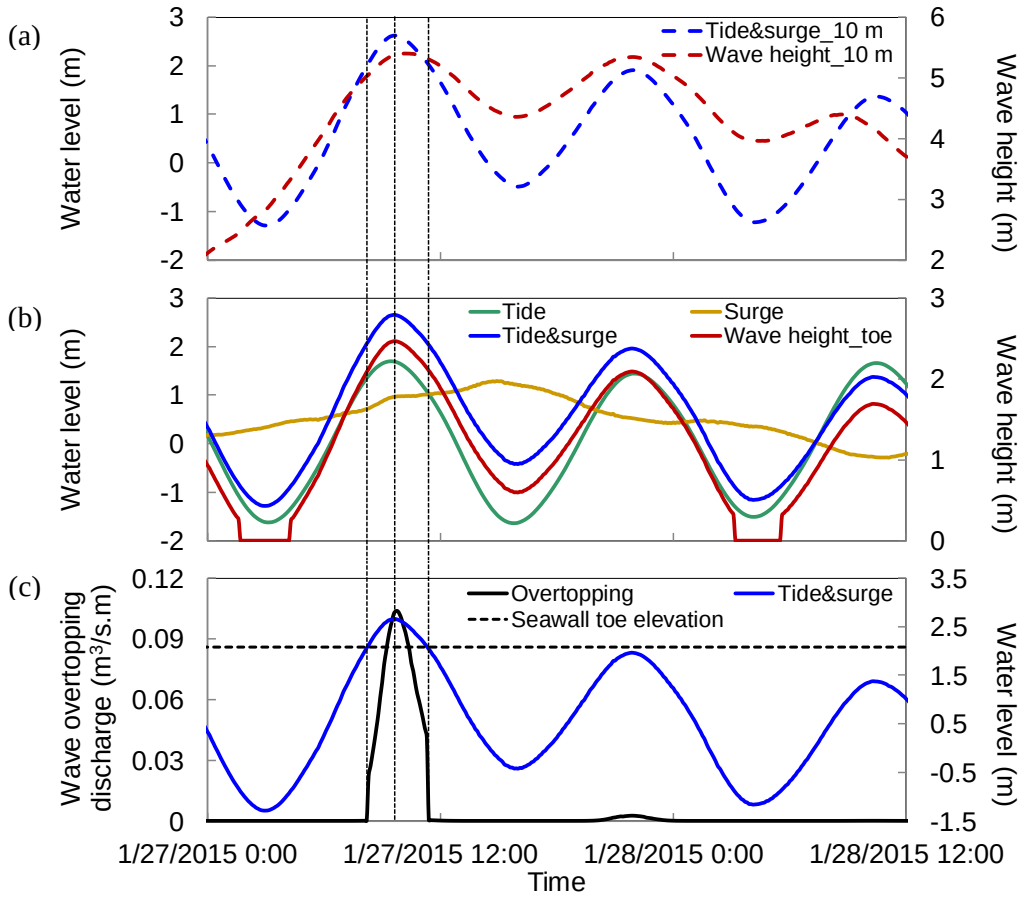


Figure 4.13. Wave overtopping discharge, water level and significant wave height at 10 m water depth and S2 in Avenues Basin, Scituate, MA. (a) Water level and significant wave height at 10 m water depth offshore of the Scituate seawall; (b) Water level and significant wave height at the toe of the steep slope in front of the seawall at S2 in Aveues Basin, Scituate, MA; (c) Tide&surge level at the toe of steep slope, the elevation of the seawall toe and wave overtopping discharge.

Based on the wave overtopping and drainage prediction, the accumulated water volume in the basin was determined. Figure 4.14 shows the comparison between the measured and predicted water volumes in the basin. The prediction agrees reasonably well with the measurement. The measured water volume reached its peak with 166509 $m^3$ at 10:24 UTC on 1/27/2015 and the predicted peak water volume was 166,124 $m^3$ at 11:12 UTC on 1/27/2015. While the magnitude of water volume agrees well, the predicted peak lagged slightly behind the measurement data. Since waves are modulated by water level and wave overtopping mainly occurs during the rising and high water, a slight phase difference between the predicted water level and observed data may result in the shift of the predicted wave

overtopping results. After the water volume reached its peak, the model predicted a rapid decrease of water volume in the basin. This may be partially attributed to the parameterization of flow rate through the corridor. Since the flow rate was calculated based on the water level recorded by the datalogger, there was a slight mismatch in phase with the overtopping prediction. Also, the flow was calculated as a uniform flow at every 6-minute interval based on the water level at the beginning of the interval, which may result in under- or overestimation of flow rate during that interval, depending on whether the water level is rising or falling. The nonlinear hydro-morphological interaction could potentially contribute to the slight mismatch, which was not considered in this study (Du et al., 2010).

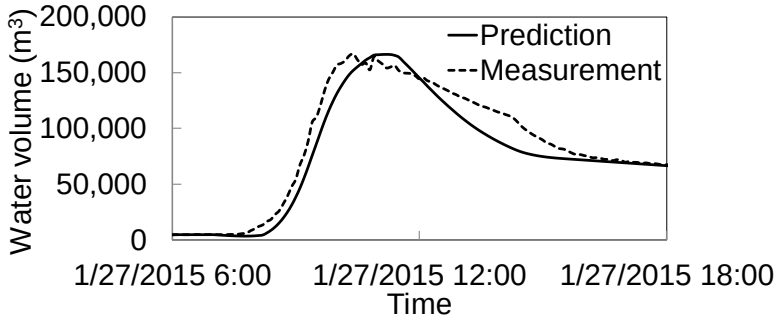


Figure 4.14. Comparison of predicted and measured volume of water in the Avenues Basin during the January 2015 North American blizzard. The solid line represents model prediction, and the dashed line represents field measurement.

### 4.6.3 The impact of tide-surge and wave interaction on wave overtopping

Another numerical simulation was conducted to investigate the effect of the tide-surge and wave interaction on wave overtopping. SWAN and ADCIRC were run independently for wave parameters and water level at the boundary of the surf zone model. The significant wave height, mean wave period and water level were then used as input for the surf zone model and wave overtopping model. The wave overtopping discharges were compared with the overtopping discharges obtained using the coupled SWAN+ADCIRC output as the input for the surf zone and overtopping models. The results from 8:18 UTC to 11:18 UTC on 1/27/2015 are shown in Figure 4.15.

The wave overtopping discharge obtained when the tide-surge and wave interaction at the boundary of the surf zone model was omitted was 20 percent of that obtained with the interaction

included. While the water level at the toe of the steep slope was similar in the two cases, the significant wave height was smaller when the interaction was not included. The wave overtopping discharge is greatly affected by the significant wave height and relative freeboard at the toe of the structure (EurOtop, 2016). On one hand, the decrease of 10 percent in the significant wave height will result in approximately 15 percent decrease in the wave overtopping discharge since the wave overtopping discharge is proportional to 2/3 power of the wave height. On the other hand, the wave overtopping discharge decreases exponentially with increased dimensionless relative freeboard due to the decrease of significant wave height (Figure 4.15c). The decreased significant wave height also reduced the Iribarren number when the tide-surge and wave interaction was not included. The Iribarren number was larger than 2.0 when the interaction was included and smaller than 2.0 without the interaction when wave overtopping occurred. The combined effect of both smaller waves and more wave breaking contributed to a lower estimation of wave overtopping when the tide-surge and wave interaction was not included.

This result mainly arises from the location of the offshore boundary, which was set at the location where the slope of bathymetry changes abruptly for the application of the surf zone model. The water depth relative to mean sea level ranges from 5.5 to 8.5 m, which is shallow enough that the waves are modulated by tide and surge level (Zou et al., 2013). Even though the wave height was adjusted to deepwater wave height by including shoaling effects at these locations, the effect of water level cannot be eliminated. This result justifies the use of a coupled tide, surge, circulation and wave model to simulate water level and wave parameters to provide boundary conditions for wave overtopping prediction.

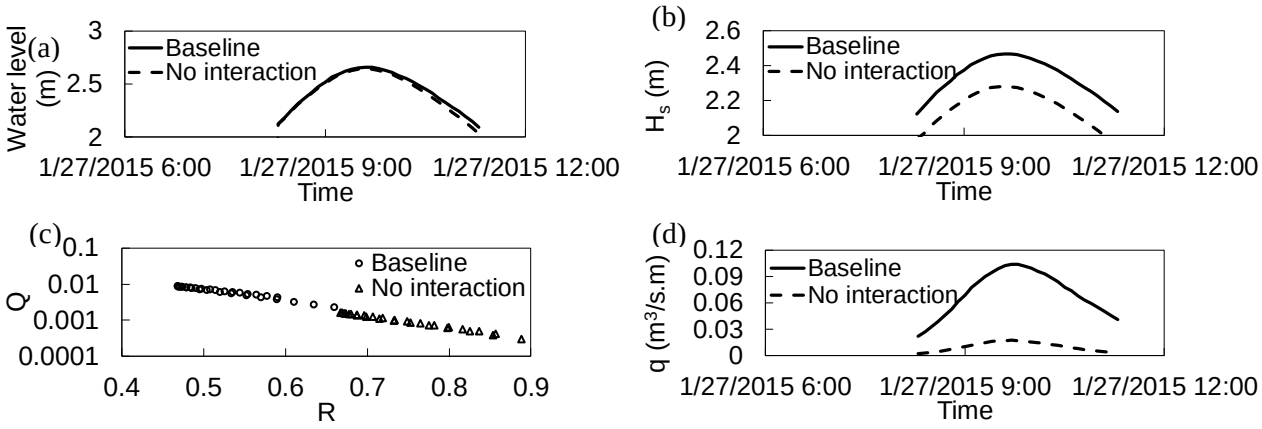


Figure 4.15. Comparison of wave overtopping at S2 with and without the inclusion of tide-surge and wave interaction at the boundary of surf zone model. (a) Water level at the toe of the steep slope, (b) wave height at the toe of the steep slope, (c) dimensionless overtopping discharge $Q = q/\sqrt{gH_{m0}^3}$ against the dimensionless relative freeboard $R = R_c/H_{m0}\xi_{m-1,0}$, (d) wave overtopping discharge. The black solid lines labeled "Baseline" are results obtained using the coupled SWAN+ADCIRC results as the input for surf zone and wave overtopping models. The black dashed lines labeled "No interaction" are results obtained using waves and water level from running SWAN and ADCIRC independently.

### 4.6.4 The impact of sea level rise and increased seawall crest on wave overtopping

As mentioned in the introduction, Massachusetts is planning for a 0.25-2.08 m sea level rise along the coast by the year of 2100. By the year of 2050, the predicted sea level rise is 0.36 m for an intermediate high scenario. In this section, the impacts of 0.36 m rise in the sea level and the seawall crest height on wave overtopping were evaluated for a storm like the January 2015 North American blizzard.

The 0.36 m sea level rise was added to the mean sea level for the coupled SWAN+ADCIRC simulation to generated waves and water level for the surf zone and wave overtopping models. The increased sea level contributes to increased overtopping not only through decreased relative freeboard of the structure, but also due to increased significant wave height at the toe of the structure. While the 0.36 m sea level rise has negligible impact on the water level at the toe of the steep slope, the significant wave height is increased by 0.23 m (Figure 4.16a). As explained in Section 4.6.3, the increase of 10 percent in the significant wave height will result in approximately 15 percent increase in wave overtopping discharge. The dimensionless relative freeboard is also significantly decreased with the 0.36 m sea level rise and the corresponding increase in the wave height. The lowest dimensionless relative freeboard

decreases from 0.47 to 0.38 with the sea level rise (Figure 4.16b). Due to these two effects, the wave overtopping discharge doubled and reached 0.2 $m^3$/s.m with 0.36 m sea level rise at the storm peak (Figure 4.16c).

Increasing the seawall crest elevation is an efficient way to reduce wave overtopping since it increases the relative freeboard. At the current sea level, raising the seawall crest by 0.36 m does not completely protect against flooding during a storm of this magnitude, although it would reduce discharge to about 75 percent of the current level at storm peak. The predicted wave overtopping discharge at the storm peak when both the sea level and the seawall crest elevation were increased by 0.36 m would increase roughly by 50 percent of the baseline case, or account for 75 percent of the overtopping discharge estimated for the case where the seawall crest is not raised. Wave overtopping discharge could be limited to that of the baseline case by raising the seawall crest by 0.9 m in a scenario with a future 0.36 m sea level rise (Figure 4.16c).

Figure 4.16. Impact of sea level rise and seawall crest level on wave overtopping discharge at S2. (a) Water level (WL) and significant wave height (Hs) at the toe of the seawall with and without sea level rise (SLR), (b) dimensionless overtopping discharge against the dimensionless relative freeboard as defined in Figure 4.15, (c) wave overtopping discharge with different combinations of sea level rise and crest eleveation (Crest).

(a)

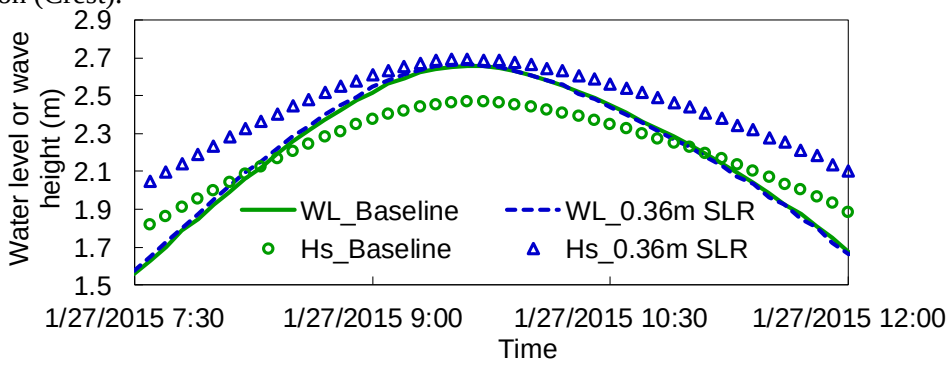


(b)

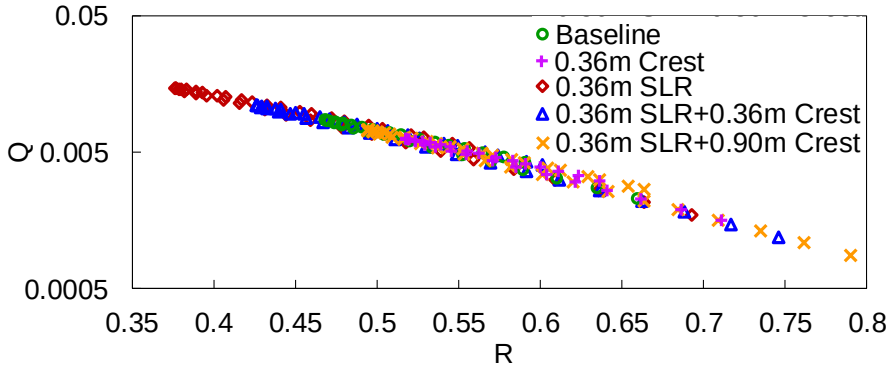

Figure 4.16 Continued

(c)

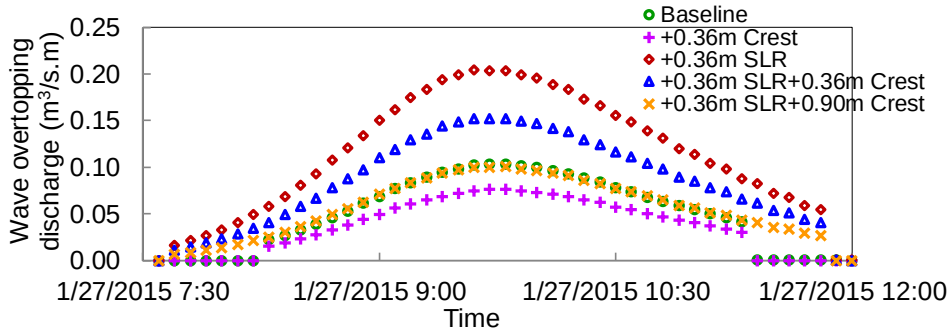


**4.7 Summary and conclusion**

In the present study, the meteorological forcing was used to drive an integrated modelling framework that consists the fully coupled SWAN+ADCIRC model, a surf zone and a wave overtopping model to predict the tide, surge and wave hydrodynamics and wave overtopping in the northeastern USA during the January 2015 North American blizzard.

At the coast, the interaction between tide-surge and waves has an important effect on the water level, waves and overtopping. Strong tidal modulation of wave height is observed at the coast. For example, at a water depth less than 10 m, the wave height was increased by 1.3-1.6 m at high tide and decreased by 0.2 m at low tide. At the storm peak, the wave height was in-creased by 0.7 m at the Scituate coast by tide and surge. The wave setup along the coast varied from 0.1 m to 0.25 m depending on the coastline geometry and tidal phases. The wave setup was larger at the small inlet in Scituate than at the open coastline. Larger wave setup was also observed at low and mid-tide than that at high tide, mainly due to the enhanced wave breaking at low and mid-tide.

The predicted wave and water level by the coupled SWAN+ADCIRC model were then used to drive the surf zone model to obtain the wave height at the toe of the steep beach slope in front of the seawall, which in turn was used to drive the wave overtopping model. Unlike previ-ous studies such as Zou et al (2013), the seawall was treated as a wave wall, i.e. vertical wall on a steep slope embankment, to account for the steep beach slope in front of the Scituate seawall, MA.

Field measurements of water level collected by a Solinst LTC Levelogger Edge in the Ave-nues Basin behind the Scituate seawall in combination with a drainage model was used to esti-mate the measured wave overtopping discharge at the seawall. The model prediction agreed well with the field measurements for the January 2015 North American blizzard but with a slight shift in the timing of peak wave overtopping, which might have arisen from the slight phase shift of the predicted water level at the Scituate coast and the parameterization of drain-age flow. The tide-surge and wave interaction increased the predicted wave overtopping dis-charge by 80 percent, mainly due to larger waves arriving at the seawall without breaking as a result of increased water depth by tide and surge.

The predicted wave overtopping at the Scituate seawall under different sea level rise and raised seawall crest scenarios indicated that a 0.36 m sea level rise in the future would double the peak overtopping discharge during a storm like the January 2015 North American blizzard. Wave overtopping discharge would increase by 50 percent if the seawall crest was raised by the same amount as the sea level rise, due to the increased wave height with the greater depth at the seawall toe. Since the wave overtopping discharge is the product of wave height to the power of 3/2 and the exponential function of wave height, it increases with wave height at a much fast rate than the water level. The model results indicate that increasing the seawall crest elevation by 0.9 m is required to keep the wave overtopping discharge at the current level in the scenario of 0.36 m sea level rise.

The present integrated multi-system modelling framework provides a useful planning tool to guide communities to upgrade their coastal defenses to adapt to the expected sea level rise. The model results show that the increased depth at the coastal structure due to sea level rise would not only decrease the free board but also increase the wave height. The latter causes the wave overtopping to increase at a much faster rate than the former so that coastal defenses will need to be raised much more than the expected rise in sea level. Also, the worst scenario when the high surge coincides with the high tide needs to be considered in the design of the seawall as an adaptation strategy to the future sea level rise.

# CHAPTER 5

# HYDRODYNAMIC AND SAND TRANSPORT SIMULATION IN THE SACO BAY

## 5.1 Background

Both waves and currents may play important roles in sediment transport in coastal settings (Soulsby, 1997). Large waves and strong currents are generated during storm events, which alter the pattern of hydrodynamics and sediment transport both on continental shelves and in coastal bays and inlets (Warner et al., 2008; Warner et al., 2010; Mulligan et al., 2008, 2010; Orescanin et al., 2014; Wargula et al., 2014; Chen et al., 2015; Li et al., 2015; Li et al., 2017). Understanding the response of coastal processes to severe storms is thus important for coastal resources management and adaptation. However, due to the complex interactions between waves, currents and bathymetry, the hydrodynamics and sediment transport can present high variability both in space and time. Different storm conditions may compound the complexity because the magnitude and pattern of the waves and currents depends on storm characteristics (Young, 1988, 2006; Rego and Li, 2009, 2010; Holthuijsen, 2010; Li et al., 2017).

While field measurements provide information on local waves, currents and sediment transport at specific sampling points and time, a comprehensive understanding of these processes over different spatial and temporal scales and under different meteorological conditions still relies on numerical simulation (Elias et al., 2006; Bertin et al., 2009; Warner et al., 2008; Warner et al., 2010). Numerical modeling has been applied to investigate the response of hydrodynamics and sediment transport to wind stress and atmospheric pressure forcing during storms in coastal bays and inlets (Elias et al., 2006; Warner et al., 2008; Warner et al., 2010; Mulligan et al., 2008, 2010; Bertin et al., 2009; Hu et al., 2009; Dodet et al., 2013; Chen et al., 2015; Li et al., 2015; Li et al., 2017; Zou and Xie, 2016; Marsooli et al., 2017). Many prior studies have focused on two aspects: (1) investigating the interaction between waves, currents and bathymetry, and (2) identifying the driving mechanisms influencing hydrodynamics in coastal bays or inlet systems (Signell et al., 1990; Mulligan et al., 2008, 2010; Olabarrieta et al., 2011; Dodet et al., 2013; Marsooli et al., 2017). Recently, numerical modeling has produced more insights into the sediment transport in combination with hydrodynamics (Elias et al., 2006; Warner et al., 2008, 2010;

Hu et al., 2009; Silva et al., 2010; Chen et al., 2015; Li et al., 2017). However, only a limited number of studies have focused on the forcing mechanisms, especially the importance of waves and wave-current interaction on sediment transport (Warner et al., 2008, 2010; Dodet et al., 2013; Chen et al., 2015).

Field observations have demonstrated the importance of waves and wave-current interaction on coastal circulation (e.g. Mulligan et al., 2010; Orescanin et al., 2014; Wargula et al., 2014). Hench and Luettich (2003) concluded that the horizontal pressure gradient and bottom friction are the dominant terms in the momentum balance in coastal areas in the absence of waves, which is corroborated by Olabarrieta et al. (2011). However, this balance is changed when wave forces are present (Olabarrieta et al., 2011). Waves can even dominate coastal processes by generating wave radiation stress due to wave breaking (Mulligan et al., 2008, 2010; Olabarrieta et al., 2011; Orescanin et al., 2014; Wargula et al., 2014). The effect of wave radiation stress and stress gradients on coastal circulation is also well reproduced by numerical modeling (Mulligan et al., 2008, 2010; Olabarrieta et al., 2011; Dodet et al., 2013). Olabarrieta et al. (2011) observed that wave-breaking-induced wave radiation stress gradients were among the leading forcing terms that produced current variations in Willapa Bay. The dominant role of wave radiation stress gradients was also found in Lunenburg Bay by Mulligan et al. (2008, 2010).

The hydrodynamics and sand transport in headland-bay beach systems has been studied at several other locations, which sheds some light on the current work (e.g. Hsu et al., 2008; Silva et al., 2010). Hsu et al. (2008) proposed that the stability of a headland-bay beach is determined by the balance between the incoming and outgoing sediment at the beach, which may be changed by a reduction in sediment supply or the presence of coastal structures. Silva et al. (2010) further added the role of accommodation of the sediment within the embayment in the hydrodynamic equilibrium. The presence of shoals in the headland-bay beach system may result in circulatory current systems due to wave-breaking (Silva et al., 2010).

In this study, the hydrodynamics and sand transport are investigated in Saco Bay, a headland-bay beach system in the northeastern United States (Figure 5.1b). It is home to one of the largest sand beach systems in northern New England and has long been the site of intense sand redistribution. The presence

of two jetties at the Saco River mouth has profoundly changed the flow patterns and sand movement in this area (Kelley et al., 2005). Literature on the dominant processes driving hydrodynamics in the bay is scarce, and there are conflicting theories about sand transport in the bay (Kelley et al., 2005). The few available studies on sand transport and dispersion in Saco Bay are based on field measurements (Hill et al., 2004; Kelley et al., 2005; Brothers et al., 2008). Hill et al. (2004) coupled offshore meteorological data, current meter data and beach profile data to analyze the response of beaches in the cross-shore direction to various storm conditions. Brothers et al. (2008) assembled hydrographic data, local wind observations and drifter data to better understand the nearshore sand transport and dispersion once the sand exits Saco River into the bay. While both studies shed light on sand transport behavior in Saco Bay, the role of waves, currents, and wave-current interaction in sediment transport under different storm conditions is not understood. Recently, Zou and Xie (2016) were able to accurately model hydrodynamics in the bay and identified the importance of waves and wave-current interaction on circulation in the bay during the 2007 Patriots Day storm.

The main objectives of this study were to: (1) investigate differences in hydrodynamic response to storms with different tracks, intensity and durations in the bay; (2) identify the contributions of different forcing terms to storm-induced sand transport; and (3) characterize the spatial and temporal variations of sand transport flux in the bay during storms. The fully two-way coupled spectral wave and circulation modeling system SWAN+ADCIRC, together with a combined-flow sediment transport model were applied to investigate waves, tidal current, wind-driven current, wave-induced current, seabed shear stresses and sand transport in Saco Bay during three notable storms to address these objectives. The numerical modeling approach was used to resolve the spatial variation of wave and current fields and sand transport caused by the complex local bathymetry and coastlines, and to help identify the underlying mechanisms for sand transport and coastal erosion and accretion.

The chapter is organized as follows: a brief site description of Saco Bay is presented in Section 5.2. The three major storms for intercomparison are described in Section 5.3. In Section 5.4, the modeling system and model setup are introduced. Section 5.5 presents and discusses the response of hydrodynamics

to the three storms in the bay. The sand transport rate and tidally averaged sand flux during the storms are discussed in Section 5.6. Conclusions are drawn in the final section.

**5.2 Site description**

Saco Bay is a small arcuate embayment located on the southern coast of Maine in the United States (Figure 5.1a). With a 15 km long stretch of shoreline, it is home to one of the largest sand beach systems in northern New England. The bay is bounded by Fletcher Neck to the south and Prouts Neck to the north (Figure 5.1b). The coast is characterized by three tidal inlets, i.e., the Saco River, Goosefare Brook and the Scarborough River. It is also constrained by two jetties at the Saco River entrance at the southern end of the bay (Figure 5.1b), which were originally constructed for navigation purposes by the United States Army Corps of Engineers (FitzGerald et al., 2002). Beach erosion and accretion have long presented a significant issue in the embayment. At the southern end of the bay, the coastline has suffered from long-term chronic beach erosion, while beach accretion is observed at the northern end of the bay (Kelley et al., 2005). Conflicting theories have been generated regarding: (1) the source of sand to the Saco Bay system, (2) the net sediment transport direction and (3) the influence of the two jetties at the Saco River mouth on sediment transport (Kelley et al., 2005). To resolve these three questions, Kelley et al. (2005) constructed a sand budget in the bay over different time intervals by compiling the data on past and present sand transport pathways, fluxes and reservoir volumes. They concluded that (1) the Saco River is the primary source of sand to the Saco Bay beach system, (2) the net sand movement along the coast has been from south to north, and (3) the construction of the north jetty at the Saco River mouth has profoundly altered the sand movement pattern and resulted in significant erosion at the adjacent Camp Ellis beach over the past century.

The mean tidal range in Saco Bay is 2.7 m, with a spring tidal range of 3.5 m. The mean shallow water wave height is 0.4 m and waves approach the bay predominantly from the south-southeast (Jensen, 1983). The bathymetric contours generally run parallel to the coastline except near the headlands and islands (Figure 5.1b and 5.1c). The bathymetric features have a significant impact on the hydrodynamics and sediment transport in this area.

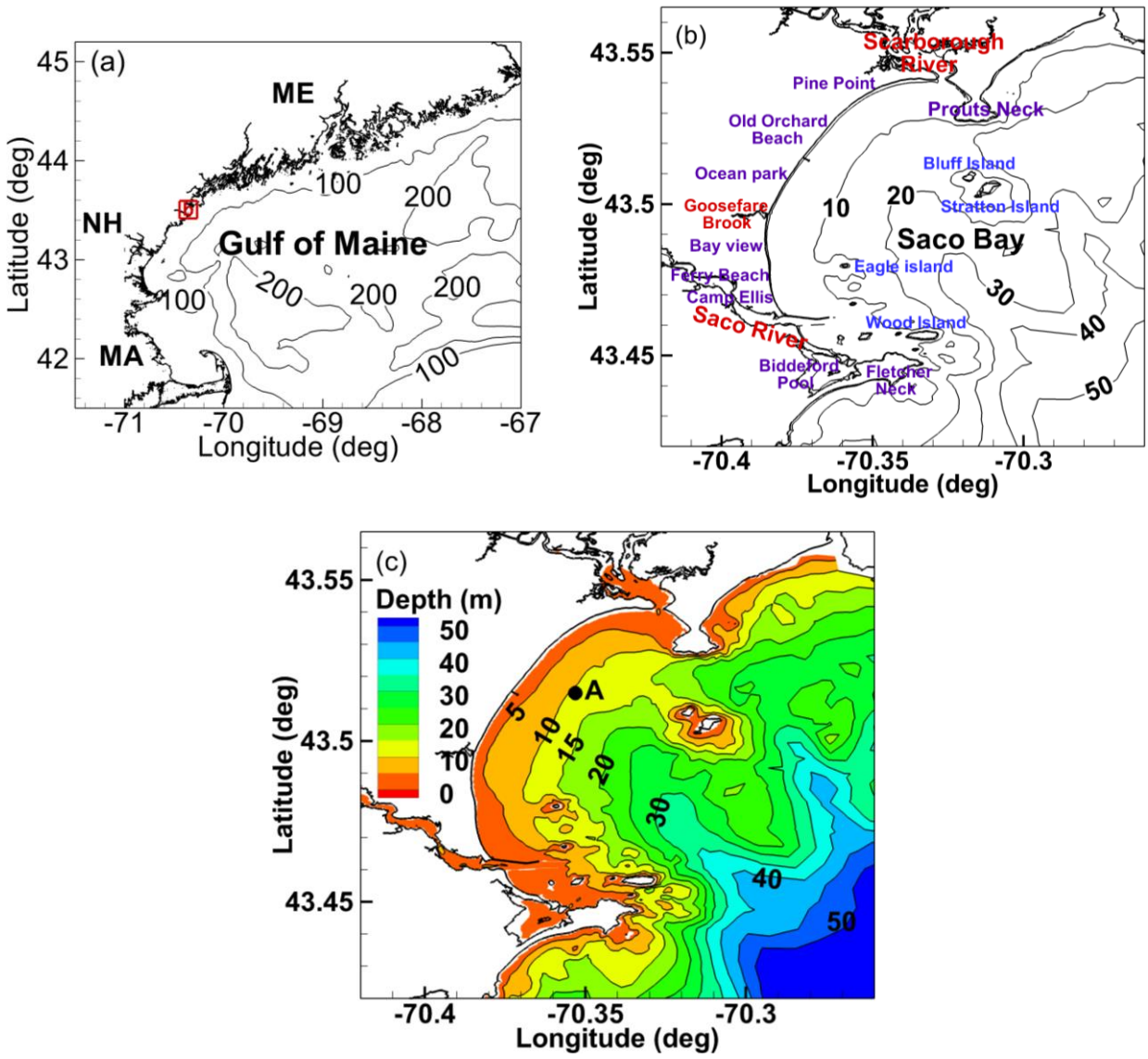


Figure 5.1. Location and bathymetry of the Saco Bay. (a) Location of the Saco Bay in the Gulf of Maine. MA represents Massachusetts, NH represents New Hampshire and ME represents Maine. (b) The Saco Bay system. (c) Bathymetry in the Saco Bay. Point A is located at the 10-m depth contour and is selected for the output of the time series of water level, waves, currents and sand transport rate

On the beaches along the Saco Bay coast, the dominant sediment type is medium-to-coarse grained sand. The mean sand grain size decreases from 700 um in the south to 250 um at the north end of the bay (Farrell, 1972; Kelley et al., 2005). Medium to fine sand dominates water depths less than 15 m. At water depths between 5 and 7 m, a similar fining trend is observed along the depth contours and the sand grain size ranges from 125 um to 250 um (Kelley et al., 1995; Kelley et al.,2005). Barber (1995)

completed a surficial geologic map of Saco Bay, which shows that sand mainly dominates water depth less than 15 m (Figure 5.2). In this study, we mainly focused on sand transport potential without considering morphological change within the bay. The surficial map of Saco Bay by Barber (1995) is thus adopted to delineate the areas with sand.

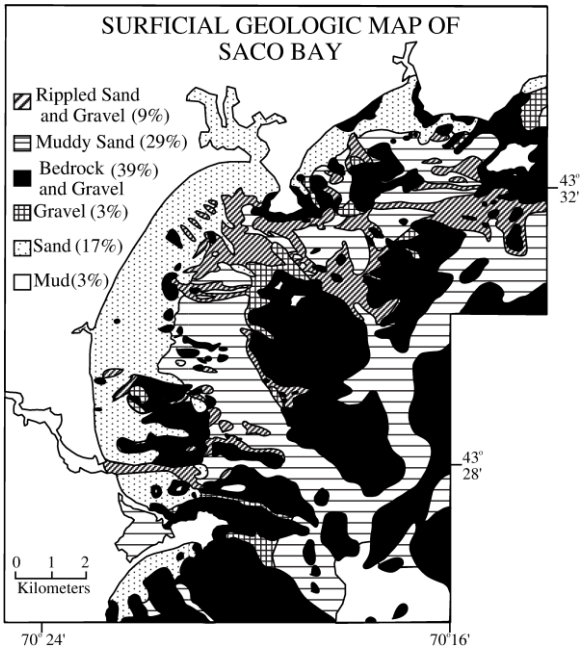


Figure 5.2. Surficial geological map of Saco Bay (from Barber, 1995)

### 5.3 Description of storms

Nor'easters are the primary storms that batter the northeast coast of the United States from October through April with slow forward speeds and diameters reaching thousands of kilometers (Davis and Dolan, 1993). Three notable nor'easters, the 1991 Perfect Storm, April 2007 nor'easter and January 2015 North American blizzard, were selected for this study due to their storm intensity, durations and tracks. While categorized as nor'easters, the three storms had different storm tracks and durations. The 1991 Perfect storm was a very unusual nor'easter that developed off Atlantic Canada on October 29 and evolved back into a small hurricane late in its life cycle. Forced by an elongated high-pressure system to its north, the storm moved southward and then westward when it reached its peak and lashed the east coast of United States with large waves and coastal flooding between October 30 and November 1. In the

Gulf of Maine, the recorded maximum sustained wind reached 90 km/h with gusts to 121 km/h and the significant wave height reached 12.0 m. The storm then turned southwest and transitioned into a subtropical cyclone before executing a loop off the Mid-Atlantic coast and turning toward the northeast (Figure 5.3).

The April 2007 nor'easter took a dangerous path toward the coastline and swept through the northeastern United States between April 15th and 18th (Figure 5.3). It stalled just offshore of New York City on the morning of April 16 and generated persisting strong southeasterly wind in the Gulf of Maine over two tidal cycles. The storm quickly weakened and moved to the east on April 17. It intensified again on April 18 and produced strong northeasterly wind in the Gulf of Maine (Figure 5.3).

The January 2015 North American blizzard swept along the coast of the northeastern United States in late January of 2015. From January 27 to 28, the storm moved northeastward off the Mid-Atlantic coast to the east coast of Canada (Figure 5.3). The track of the storm maintained a long northeasterly wind wave fetch across the Gulf of Maine. The other easterly wind wave fetches responsible for generating large waves were offshore of Nova Scotia, Canada. The presence of a strong elongated high-pressure system to the north of the region impeded the forward movement of the low-pressure system, which resulted in a long duration of winds across the fetch area. The strong northeasterly and easterly wind in the fetch area generated a pronounced storm surge and large waves.

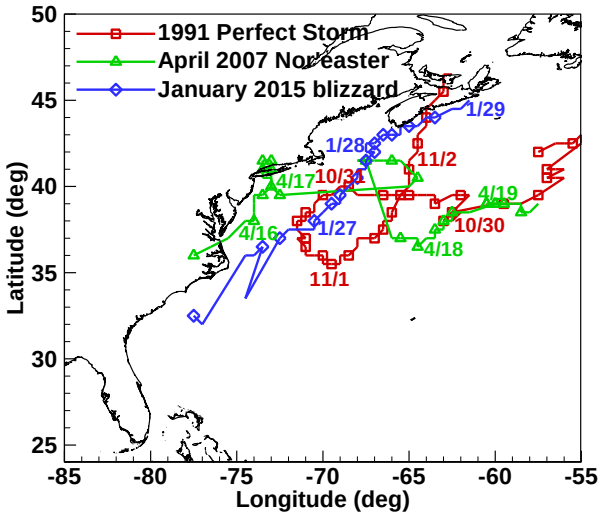


Figure 5.3. The storm tracks of the three nor'easter storms

## 5.4 Methodology

The simulation of coastal hydrodynamics and sediment transport is complicated and computationally demanding because it requires: (1) resolving the processes ranging from oceanic to estuarine scales, (2) accurately representing the geometric and bathymetric complexities, and (3) incorporation of the nonlinear hydro-morphological interactions. In this study, the waves, current and sediment transport processes in Saco Bay during three major storms in the northeastern United States were simulated using a fully coupled wave, tide-surge and circulation model and a combined-flow sediment transport model. Figure 5.4 shows the integrated model framework developed for this study. The fully coupled wave, tide-surge and circulation model SWAN+ADCIRC incorporates meteorological and tidal forcing to obtain coastal hydrodynamics. The simulated wave orbital speed, water level and depth-averaged current are fed into the bed shear-stress model by Soulsby (1997) and the Soulsby-Van Rijn total load sediment transport model (Soulsby, 1997) beneath combined waves and currents for the calculation of enhanced bed shear-stress and total load sediment transport respectively. The features and schemes of the wave and circulation models, bottom shear stress and sediment transport calculations are described in this section.

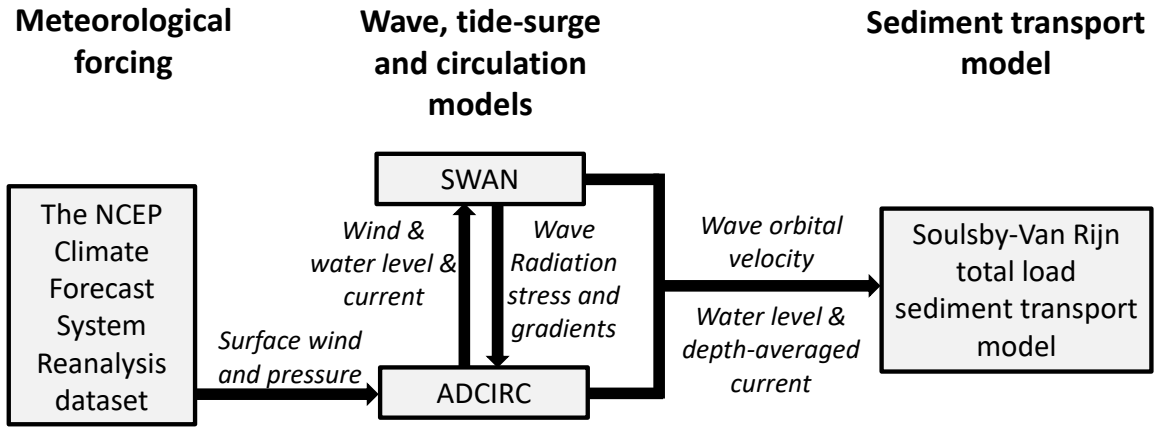


Figure 5.4. Modeling framework for sediment transport in the Saco Bay

### 5.4.1 Wave, tide-surge and circulation models

The fully coupled wave, tide-surge and circulation model SWAN+ADCIRC running on unstructured triangular mesh (Dietrich et al., 2011, 2012) was adopted for the investigation of coastal hydrodynamics in this study. The third-generation spectral wave model SWAN (Booij et al., 1999; Ris et al., 1991) predicts the inhomogeneous wave field due to changes in wind-fetches and seabed. It is sophisticated for wave simulation in the nearshore and coastal areas by considering shallow-water wave processes including wave energy dissipation due to bottom friction and depth-induced breaking, and nonlinear triad-wave interactions.

The vertically-integrated version of the state-of-the-art tide-surge and circulation model ADCIRC (ADCIRC-2DDI) (Luettich and Westerink, 2004) was used to investigate the coastal hydrodynamics. For simplicity, ADCIRC is used to refer to its vertically-integrated version in this study. The model solves the vertically-integrated continuity equation with the Generalized Wave Continuity Equation formulation for water surface elevation and vertically integrated-momentum equations for depth-averaged velocity. SWAN and ADCIRC are coupled by including several important nearshore wave-current interaction processes. The water level and depth-averaged current calculated by ADCIRC are passed to SWAN to include the modulation of water level on waves, as well as the Doppler effect and wave refraction with the presence of current. SWAN then solves the wave action equation for wave parameters and passes wave radiation stress to ADCIRC to address the effect of excess momentum flux exerted on water level and current. The features and schemes of SWAN, ADCIRC and the coupling mechanism were described in detail in Xie et al., (2016), Zou and Xie (2016) and Xie et al. (2018).

### 5.4.2 Bottom stress and sediment transport models beneath combined waves and currents

Both waves and currents may play important roles in sediment dynamics in coastal areas. Due to wave-current interaction, their behavior beneath combined waves and currents is not equivalent to the linear sum of their individual effects. Three interaction processes important for sediment dynamics include: (1) wave refraction due to the presence of current, (2) the enhancement of bed shear-stress due to the interaction between wave and current boundary layers, and (3) wave-generated current exerted on

mean flow. The wave effect on mean flow is included by considering the effect of wave radiation stress on current in the coupled SWAN+ADCIRC model. Wave refraction by current and the enhancement of bed shear-stress are considered here.

#### 5.4.2.1 Bed shear-stresses model

The bed shear-stresses beneath combined waves and currents are enhanced beyond the linear sum of the wave-alone and current-alone stresses (e.g. Grant and Madsen, 1979, Grant et al., 1984; Davies et al., 1988). The enhancement of bed shear-stresses due to the interaction between current and wave boundary layers are important for both circulation and sediment transport (Davies and Lawrence, 1995; Styles and Glenn, 2000; Xie et al., 2001; Warner et al., 2008; Chen et al., 2015; Li et al., 2017). Many theories and models have been proposed to describe the nonlinear interaction between the wave and current boundary layers, for example the analytical models of Grant and Madsen (1979) and Fredsøe (1984), and the numerical models of Davies et al. (1988).

Soulsby et al. (1993) and Soulsby (1995) developed an algebraic approximation for bed shear-stresses beneath combined waves and currents. Their data-based method optimized the parametric coefficients by fitting the model with laboratory and field data. According to Soulsby et al. (1993), the bed shear-stresses beneath combined waves and currents is estimated by

$$\tau_m = y(\tau_c + \tau_w) \quad \text{(Equation 5.1)}$$

$$\tau_{max} = Y(\tau_c + \tau_w) \quad \text{(Equation 5.2)}$$

$$\tau_c = \rho C_D \overline{U}^2 \quad \text{(Equation 5.3)}$$

$$\tau_w = \frac{1}{2}\rho f_w U_w^2 \quad \text{(Equation 5.4)}$$

where $\tau_c$ is the current-alone bottom stress, $\tau_w$ is the maximum wave-only bottom stress, $\tau_m$ and $\tau_{max}$ are the mean and maximum bed shear-stress beneath combined waves and currents. $\tau_{max}$ is calculated to determine the threshold of motion and entrainment rate of sediments, and $\tau_m$ is calculated to determine sediment diffusion. $C_D$ is the drag coefficient for depth-averaged mean current and is obtained from the logarithmic velocity profile with a given bottom roughness length based on the sediment grain

size. $f_w$ is the wave friction factor and is calculated from an explicit formula given by Nielsen (1992) for rough turbulent flow. $\overline{U}$ is the depth-averaged mean current, $U_w$ is the wave orbital speed at seabed. The current-alone bottom stress depends on the drag coefficient and depth-averaged current speed by the quadratic friction law. The drag coefficient increases logarithmically with seabed roughness length and decreases exponentially with water depth. The maximum wave-only bottom stress is a function of wave friction factor and wave orbital speed at seabed. Nielsen (1992) used one expression to relate the wave friction factor with relative roughness of all range. The relative roughness increases the semi-orbital wave excursion and decreases with the Nikuradse equivalent sand grain roughness. The three non-dimensional parameters x, y and Y are expressed as

$$y = x[1 + bx^p(1 - x)^q] \quad \text{(Equation 5.5)}$$

$$Y = 1 + ax^m(1 - x)^n \quad \text{(Equation 5.6)}$$

$$x = \tau_c/(\tau_c + \tau_w) \quad \text{(Equation 5.7)}$$

in which the six fitting coefficients a , b , m , n , p and q are functions of relative angle between wave and current ($\phi$) and the ratio between wave friction factor and drag coefficient for depth-averaged mean current ($f_w/C_D$). Here, we only show the expression for a and the analogous expression for b, m , n , p and q can be found in Soulsby et al. (1993) and Soulsby (1997).

$$a = \left(a_1 + a_2|\cos\phi|^I\right) + (a_3 - a_4|\cos\phi|^I)\log_{10}(f_w/C_D) \quad \text{(Equation 5.8)}$$

The fitting coefficient $a_i$ $(i = 1,4)$ and I can be found in Soulsby et al. (1993) and Soulsby (1997).

**5.4.2.2 Total load sediment transport model**

In coastal areas, both waves and currents are involved in sediment transport calculation. The total load sediment transport model of Soulsby-Van Rijin (Soulsby, 1997) beneath combined waves and currents is used in this study. The sediment transport rate is calculated as follows

$$q_t = A_s\overline{U}\left[\left(\overline{U}^2 + \frac{0.018}{C_D}U_{rms}^2\right)^{\frac{1}{2}} - \overline{U}_{cr}\right]^{2.4}(1 - 1.6\tan\beta) \quad \text{(Equation 5.9)}$$

$$A_s = A_{sb} + A_{ss} = \frac{0.005h(d_{50}/h)^{1.2}}{[(s-1)gd_{50}]^{1.2}} + \frac{0.012d_{50}D_*^{-0.6}}{[(s-1)gd_{50}]^{1.2}} \quad \text{(Equation 5.10)}$$

$$D_* = \left[\frac{g(s-1)}{v^2}\right]^{1/3} d_{50} \quad \text{(Equation 5.11)}$$

$$C_D = \left[\frac{0.40}{\ln\left(\frac{h}{z_0}\right) - 1}\right]^2 \quad \text{(Equation 5.12)}$$

where $\overline{U}$ is the depth-averaged current velocity, $U_{rms}$ is the root-mean-square wave orbital velocity, $A_s$ is an empirical coefficient and calculated based on flow and sediment properties through bedload and suspended load, $C_D$ is the drag coefficient in current-alone condition, $\beta$ is the slope of the bed in the streamwise direction and is positive if the flow runs uphill, h is water depth, $d_{50}$ is the median grain diameter, $z_0$ is the bed roughness length, s is the relative density of sediment, g is the gravitational acceleration, v is the kinematic viscosity of water, $\overline{U}_{cr}$ is the threshold current velocity for sediment motion based on Shield's criterion, which is expressed as

$$\bar{u}_{cr} = \begin{cases} 0.19(d_{50})^{0.1}\log_{10}\left(\frac{4h}{d_{90}}\right) & \text{for } 100 \le d_{50} \le 500 \text{ um} \\ 8.5(d_{50})^{0.6}\log_{10}\left(\frac{4h}{d_{90}}\right) & \text{for } 500 \le d_{50} \le 2{,}000 \text{ um} \end{cases} \quad \text{(Equation 5.13)}$$

where $D_{50}$, $D_{90}$ are the 50$^{th}$ and 90$^{th}$ percentile particle diameters of the bed material (in meters). h is the water depth.

The Soulsby-Van Rijin (1997) sediment transport model applies to total load sediment transport in combined wave and currents on horizontal and sloping beds. Two important assumptions are made during the parameterization. The first is that the sediment transport direction is determined by currents and waves only enhance the magnitude of transport. The magnitude of the wave stirring effect is incorporated as inversely proportional to the bed roughness length through the drag coefficient $C_D$. Based on this assumption, the model is designed for sediment transport in a current-dominant condition and cannot model transport directly associated with surface waves (Chen et al., 2015). The second assumption is that the sediment supply is sufficient, and the vertical structure of the sediment transport is uniform and

steady in time. This indicates that the model is for calculating the equilibrium sediment transport, which is not realistic in most coastal areas with varied hydrodynamic conditions and bathymetry. According to Soulsby (1997), the quasi-equilibrium assumption mainly impacts suspended sediment transport, which responds much more slowly to changes in hydrodynamics or bathymetry compared to bedload transport. However, for a relatively coarse-gridded coastal area model, a quasi-equilibrium model could be adequate depending on the relative value of grid-resolution length scale and the adjustment length scale based on mean current velocity, water depth and settling velocity of sediment grains. In this study, our main goal is to estimate the potential values of sand transport in Saco Bay without considering morphological changes during three major storms, so the adoption of the model was justified.

### 5.4.3 Model setup

The same unstructured mesh covering the East Coast of United States described in Xie et al. (2018) was used for the coupled SWAN+ADCIR model in this study. The unstructured mesh was developed by considering: (1) simplification of the boundary conditions by allowing longer wind and wave fetches along the Scotian Shelf, (2) representation of resonant modes within the model domain, and (3) resolving bathymetric and geometric features with various spatial scales. In Saco Bay, the finest grid resolution is 10 m to accurately represent the geometric and bathymetric complexities in this area. The two jetties at the Saco River mouth were resolved to include their impact on waves, current and sediment transport. The islands with length scales ranging from less than one hundred meters to one kilometer in the bay were also included (Figure 5.5). To more realistically consider the land boundary conditions, part of the dry land adjacent to the bay was included in the mesh to apply the wet-and-dry algorithm in ADCIRC.

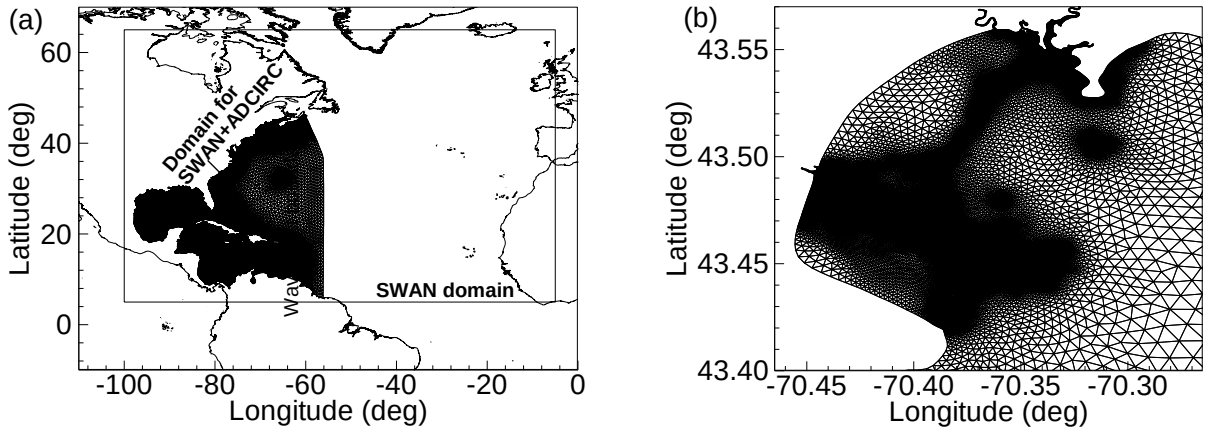


Figure 5.5. Model domain and unstructured mesh for hydrodynamical and sand transport simulation. (a) The nesting model domains, including SWAN model domain covering North Atlantic to provide wave spectra along the ocean boundary for the coupled SWAN+ADCIRC model, and the model domain covering the east coast of US for the coupled SWAN+ADCIRC model. (b) Unstructured grid in the Saco Bay

Wind at 10 m above the sea surface and atmospheric pressure at the sea surface are required as inputs for the coupled SWAN+ADCIRC model. For the 1991 Perfect Storm and April 2007 nor'easter, the National Centers for Environmental Prediction (NCEP) Climate Forecast System Reanalysis (CFSR) (Saha et al., 2010) was adopted. For the January 2015 North American blizzard, the NCEP Climate Forecast System Version 2 (CFSv2) (Saha et al., 2014) was used. Both datasets were produced by the same quasi-global, fully coupled atmosphere-ocean-land surface-ice model, which incorporates two data assimilation systems and two forecast models. While the CFSR dataset spans from 1979 to 2011, the CFSv2 extends the CFSR dataset beyond the year of 2011. The two datasets output wind at 10 m above the sea surface and atmospheric pressure at the sea surface globally with $0.5^{o}$ grid resolution at hourly intervals.

At the ocean boundary of the coupled SWAN+ADCIRC, major tidal constituents and wave spectra were prescribed for the three storm events. The harmonic constants of the eight major astronomical tide constituents (M2, S2, N2, K2, K1, P1, O1, Q1) were obtained from the TPXO global ocean tide model (Egbert et al., 1994). The wave spectra along the ocean boundary were obtained from

SWAN wave simulation covering the North Atlantic as illustrated in Figure 5.5a. The other model parameters for the coupled SWAN+ADCIRC were described in Xie et al. (2018).

Following the study by Farrell (1972), Barber (1995) and Kelley et al. (2005), the median and $90^{th}$ percentile grain sizes of sand were taken as 250 um and 500 um respectively in areas where sand dominates within the bay for the calculation of bottom stress and sand transport rate. Since our study mainly focuses on investigating the mechanism of sand transport and sand transport potential without morphological change during storms, the specification of uniform sand grain size can be justified. We also assumed that sediment transport is not considered in areas dominated by mud, gravel and bedrock as delineated on the surficial map by Barber (1995).

To analyze the impact of tide, wind-driven current, waves and their interactions, four cases were run for each storm: (1) tide simulation only; (2) tide-surge simulation without wave effects; (3) wave simulation without depth variation and current; (4) a fully coupled SWAN+ADCIRC simulation including the nonlinear interactions between waves, current and bathymetry.

## 5.5 Hydrodynamic model results and discussions

In this section, the hydrodynamics at the peak of the three storms were analyzed. The tidal, wind-driven, and wave-induced currents were plotted to compare their magnitudes and distributions in the bay. The wind-driven current was obtained by subtracting tidal current form the combined tide-surge simulation result. The wave-induced current was obtained by subtracting the tide-surge simulation result from the flow field by the coupled SWAN+ADCIRC model. Wave fields were also shown to determine the distribution of wave characteristics. The interactions between waves, tide-surge and bathymetry are then discussed for each of the storms.

### 5.5.1 April 2007 nor'easter

The storm surge and significant wave height reached their peaks at 14:30 UTC on 4/16/2007 around high tide in the bay during the April 2007 nor'easter (Figure 5.6). The two tidal cycles with high storm surge and waves (8:30UTC 4/16/2007 to 9:30UTC 4/17/2007) for averaged circulation and sand transport potential calculation were marked in Figure 5.6 as the shaded area.

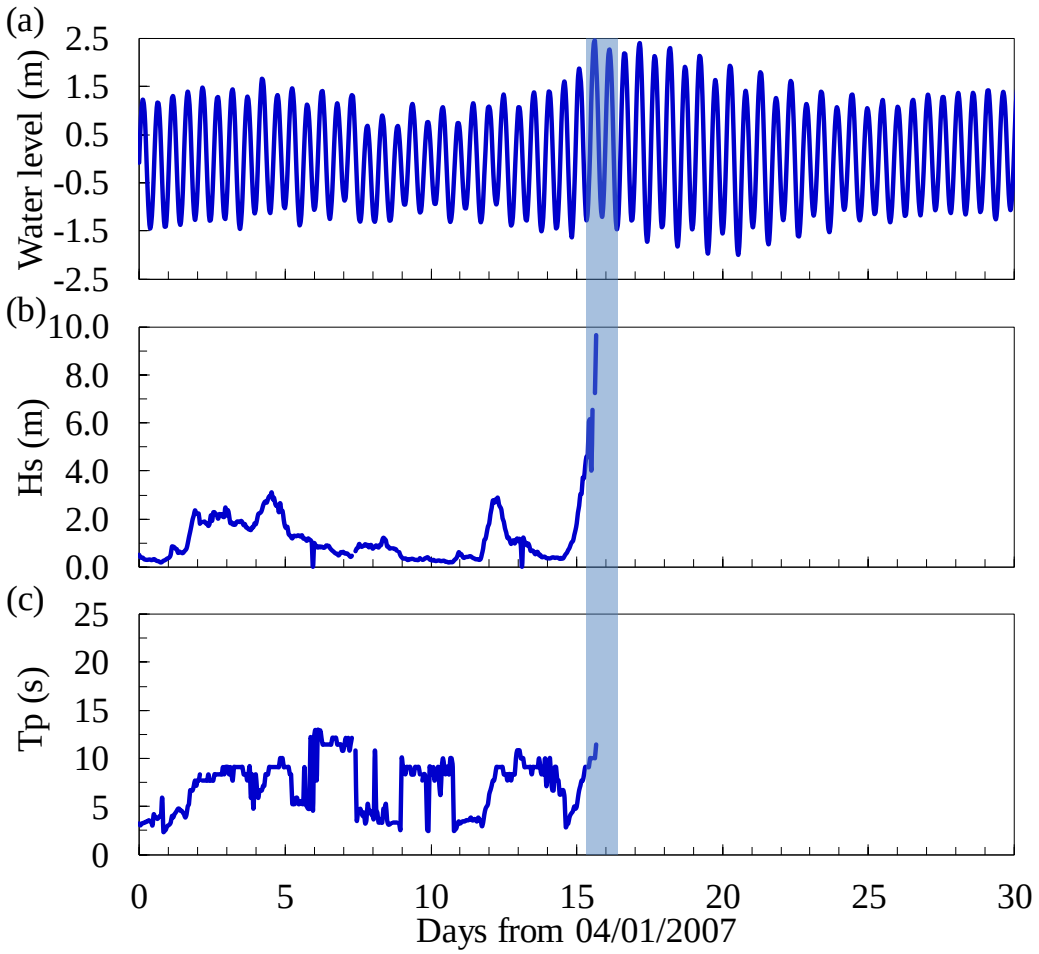


Figure 5.6. The water level and wave parameters at the nearest tide gauge 8418150 and wave buoy 44007 around the April 2007 nor'easter. (a) Water level at tide gauge 8418150; (b) Significant wave height at wave buoy 44007; (c) Peak wave period at wave buoy 44007. The shaded area is the period that contains the storm peak.

The tidal current (Figure 5.7a) was minimum in the bay except at two locations: within the channel between the two jetties at the Saco River mouth into the river, and in the Scarborough River. At these locations, the tidal current reached 0.2 m/s as water funneled into the river mouths. Along the coast between the Scarborough River and the north jetty at the Saco River mouth, the tidal current is less than 0.02 m/s in general.

The wind-driven current (Figure 5.7b) was one order of magnitude higher than tidal current and reached 0.25 m/s at most locations within the bay. The maximum wind-driven current exceeded 1.0 m/s and occurred in the channel between the two jetties at the Saco River mouth and offshore of Eagle Island

and Wood Island. While the enhancement of wind-driven current in the channel is mainly due to the funneling effect, the enhanced current offshore of Eagle Island and Wood Island is mainly caused by the convergence of flows away from the shore and the geometric complexity of the islands. Between the Scarborough River and Bay View, the wind-driven current flowed southward. Beyond Bay View, the southward wind-driven current was diverted offshore before being joined by a small clockwise gyre to the south of Bay view. The wind-driven current rotated clockwise between Bay View and the north jetty at the Saco River mouth. Between the southward wind-driven current and the small clockwise gyre, an area with negligible wind-driven current was present.

The wave-induced current (Figure 5.7c) was closely related to the bathymetry and coastline geometry in the bay. Strong wave-induced current exceeding 1.0 m/s was identified around islands in the bay. At the northern end of the bay, a strong wave-induced current from the headland of Prouts Neck rotated counterclockwise and merged with a small clockwise gyre around Bluff Island and Stratton Island. Part of the northwest wave-induced current that circulated back from offshore of the two islands was diverted southwest and veered offshore before being joined by the wave-induced current from the south of the bay. In the southern part of the bay, the wave-induced current flowed northwards. At the coast between Ferry Beach and Goosefare Brook, the northward wave-induced current reached 0.6 m/s. Enhancement of wave-induced current was identified around islands and the headlands. The pattern of wave-induced current mainly results from the abrupt change of wave height at headlands and islands due to wave breaking, where large wave radiation stress and gradients are generated. The waves also converge at the headlands and diverge in the arcuate bay, which results in wave radiation stress gradients from the headlands into the bay and produces wave-induced current into the bay.

The total depth-averaged current which includes tidal, wind-driven, wave-induced components and their nonlinear interactions was shown in Figure 5.7d. Along the coast, the depth-averaged current was mainly driven by two processes, i.e. wind and waves. The depth-averaged current can be divided into three sections along the coast. In the north of the bay around Pine Point, the southward current from the Prouts Neck split into an offshore component and a southward component mainly due to the wave effect.

The southward component continued moving south until reaching the Goosefare Brook and then diverted offshore. Along the middle part of the shoreline, the depth-averaged current was dominated by the wind-driven current. At the coast south of Goosefare Brook, the depth-averaged current was flowing northward before joining the offshore-diverted current from the north, primarily due to the wave-induced current. This is because large wave radiation stress gradients are generated due to the abrupt change of wave height between the headlands and their adjacent areas. In offshore locations, the depth-induced current followed the pattern of wave-induced current, but the magnitude was larger after combining the wind-driven and wave-induced components.

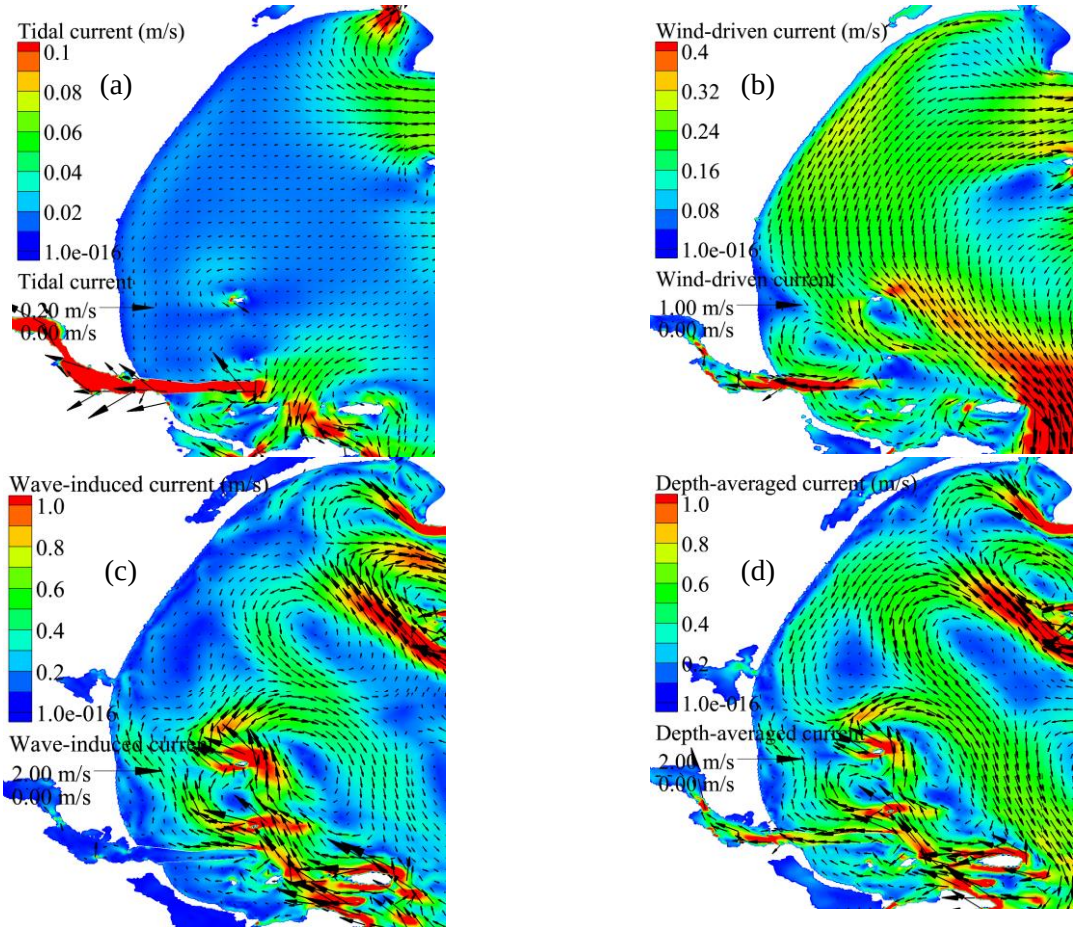


Figure 5.7. Current at storm peak at 14:30UTC on 4/16/2007. (a) Tidal current; (b) Wind-driven current; (c) Wave-induced current; (d) Total current.

The significant wave height and peak wave period are shown in Figure 5.8a. The waves offshore approached Saco Bay from the east to southeast direction. In offshore locations, the significant wave

height reached 7.0 m. Bottom friction and depth-induced wave breaking dissipated wave energy when waves propagated to the coastal regions with shallow bathymetry. Wave shoaling, refraction and diffraction redistributed wave energy due to the bathymetric and geometric features in the bay. In the north of the bay, significant wave height decreased due to wave diffraction and breaking around Bluff Island and Stratton Island. In the south of the bay, the same phenomenon occurred around Eagle Island and Wood Island. In the middle part of the bay with smooth depth contours parallel to the coastline, larger waves propagated closer to shore.

Figure 5.8b shows the wave orbital speed at the seabed. Wave orbital speed at seabed is influenced by wave height, wave period and water depth. While the wave orbital speed at seabed increases linearly with wave height and in the shape of hyperbolic tangent function with wave period, it decreases exponentially with water depth. Large wave orbital speed at seabed of 1.6 m/s occurred around the islands in the bay due to the abrupt change of bathymetry. Medium wave orbital speed was identified in the middle part of the bay. The wave orbital speed at seabed in the middle part of the bay reached 1.4 m/s between water depth of 5.0 m to 10.0 m due the shallow bathymetry. It decreased due to reduced wave height when the water depth was less than 5.0 m. The distribution of wave orbital speed at seabed in the bay has strong implications for sand transport.

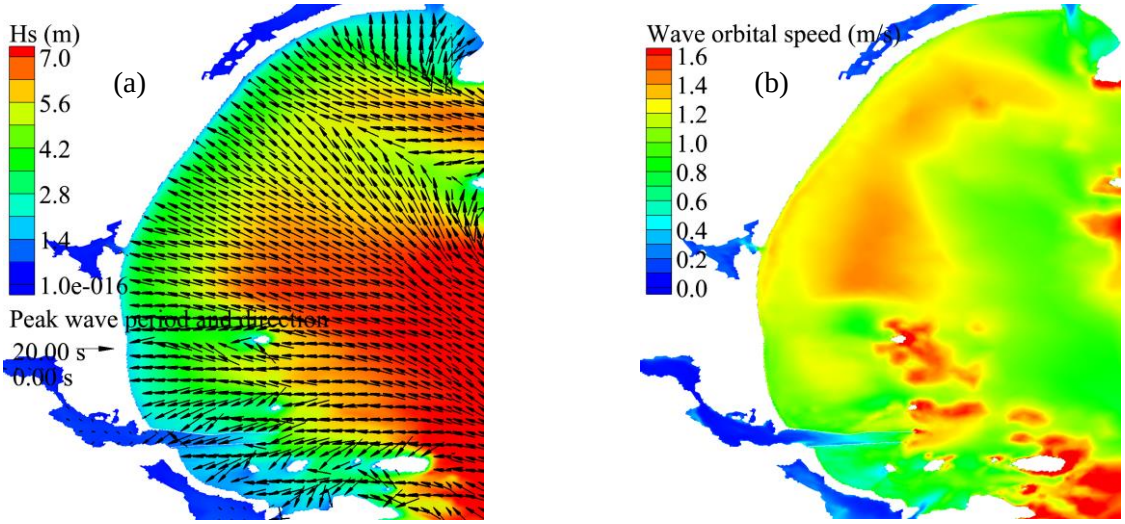


Figure 5.8. Waves at storm peak at 14:30UTC on 4/16/2007. (a) Wave height, period and direction; (b) Wave orbital velocity.

### 5.5.2 1991 Perfect Storm

During the 1991 Perfect Storm, the storm tide and significant wave height reached their peaks at 23:30 UTC on 10/30/1991, which was two hours after the high tide (Figure 5.9). The two tidal cycles with high storm surge and waves (14:00UTC 10/30/1991 to 15:00UTC 10/31/1991) for averaged circulation and sand transport potential calculation were also marked in Figure 5.9.

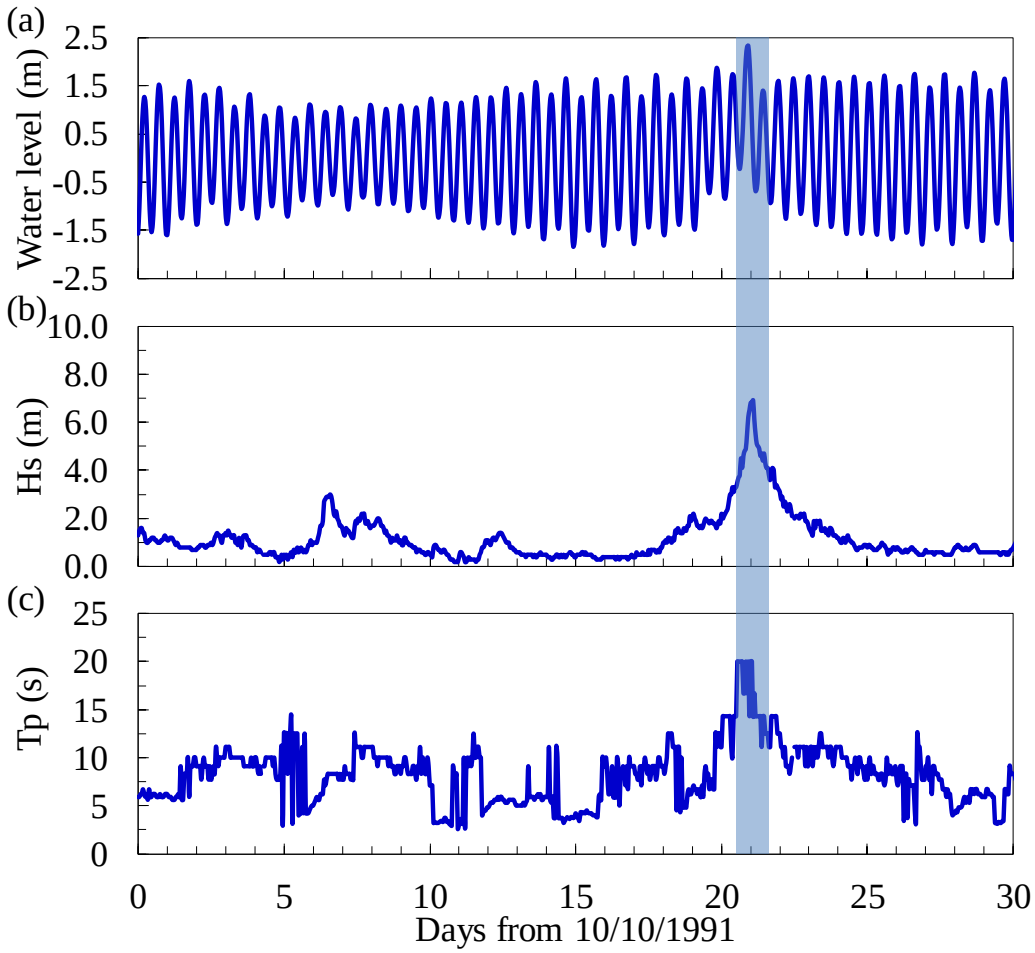


Figure 5.9. The water level and wave parameters at the nearest tide gauge 8418150 and wave buoy 44007 around the 1991 Perfect Storm. (a) Water level at tide gauge 8418150; (b) Significant wave height at wave buoy 44007; (c) Peak wave period at wave buoy 44007. The shaded area is the period that contains the storm peak.

The tidal current at the storm peak (Figure 5.10a) was less than 0.03 m/s at the coast except within the channel at the Saco River mouth and at the mouth of the Scarborough River. The magnitude of

tidal current increased offshore from 0.03 m/s to 0.06 m/s. Around the Wood Island and Fletcher Neck, the tidal current was significantly enhanced and reached 0.2 m/s.

The magnitude and pattern of wind-driven current at the storm peak of the 1991 Perfect Storm was different from that of the April 2007 nor'easter (Figure 5.10b). Except in the lee of Prouts Neck and the south jetty at the Saco River mouth, the wind-driven current was quite uniform at water depth less than 15.0 m and flowed southward with a magnitude of 0.2 m/s in the alongshore direction. At water depth larger than 15.0 m, the wind-driven current gradually decreased to be negligible. No gyre in the bay was identified due to wind effect.

The wave-induced current at the peak of the 1991 Perfect Storm presented a similar pattern as during the April 2007 nor'easter (Figure 5.10c). However, unlike that at the peak of the April 2007 nor'easter, the wave-induced current from Prouts Neck flowed toward the southwest along the shoreline until it turned offshore in the southeast direction. The clockwise gyre around Bluff Island and Stratton Island separated while circulating toward the coast and merged with the southeast offshore flow. From Old Orchard Beach to Goosefare Brook, the wave-induced current was negligible at the coast. In the south of the bay from Fletcher Neck to Goosefare Brook, the wave-induced current flowed northward along the coast. In this part of the bay, the wave-induced current was from Fletcher Neck and was enhanced by the presence of islands. Around Eagle Island, the clockwise wave-induced current circulated toward the east and joined the offshore southeast current from the northern part of the bay.

The total depth-averaged current is shown in Figure 5.10d. The total depth-averaged current followed the distribution of wave-induced current in the bay in general but was enhanced or weakened by the tidal and wind-driven currents. In the northern part of the bay between Prouts Neck and Old Orchard Beach, the total depth-averaged current was enhanced at the coast because the wind-driven and wave-induced currents were in the same direction. Between Goosefare Brook and the Saco River mouth, the total depth-averaged current was weakened due to the counterbalance between the wind-driven and wave-induced currents. Offshore, the total depth-averaged current was mainly enhanced by tidal current.

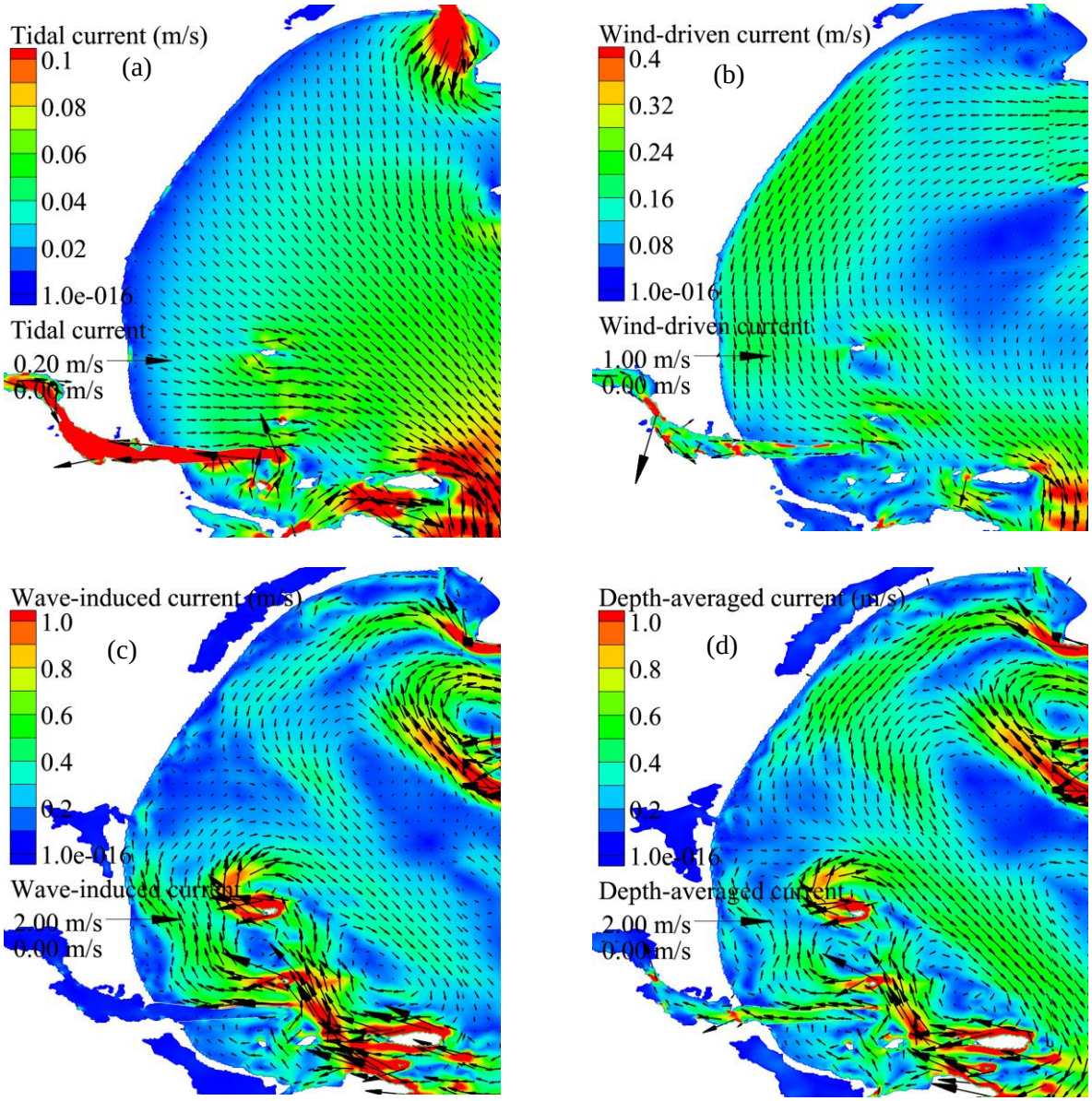


Figure 5.10. Current at storm peak at 23:30UTC on 10/30/1991. (a) Tidal current; (b) Wind-driven current; (c) Wave-induced current; (d) Total current.

The wave fields at the storm peak are shown in Figure 5.11. While the distribution of significant wave height was similar to that at the peak of the April 2007 nor'easter, the wave height at the peak of the 1991 Perfect Storm was smaller. Offshore of Saco Bay, the wave height barely reached 7.0 m and was mainly coming from the southeast direction. Strong wave refraction happened while waves propagated into the bay and the wave direction was perpendicular to the depth contours and coastline. The peak wave

period in the bay was larger in comparison to that during the April 2007 nor'easter, indicating longer waves were present in the bay that could affect the seabed at relatively large water depth.

The wave orbital speed at seabed also presented a similar pattern as was observed during the April 2007 nor'easter. While wave height is smaller in the bay because smaller waves were generated offshore during the 1991 Perfect Storm, the wave period was larger. Because wave orbital speed increases both with wave height and wave period, the reduction of wave orbital speed due to decreased wave height was offset by the increased wave period. The effect of wave period exceeded that of wave height because higher wave orbital speed was found at the coast during the 1991 Perfect storm than during the April 2007 nor'easter.

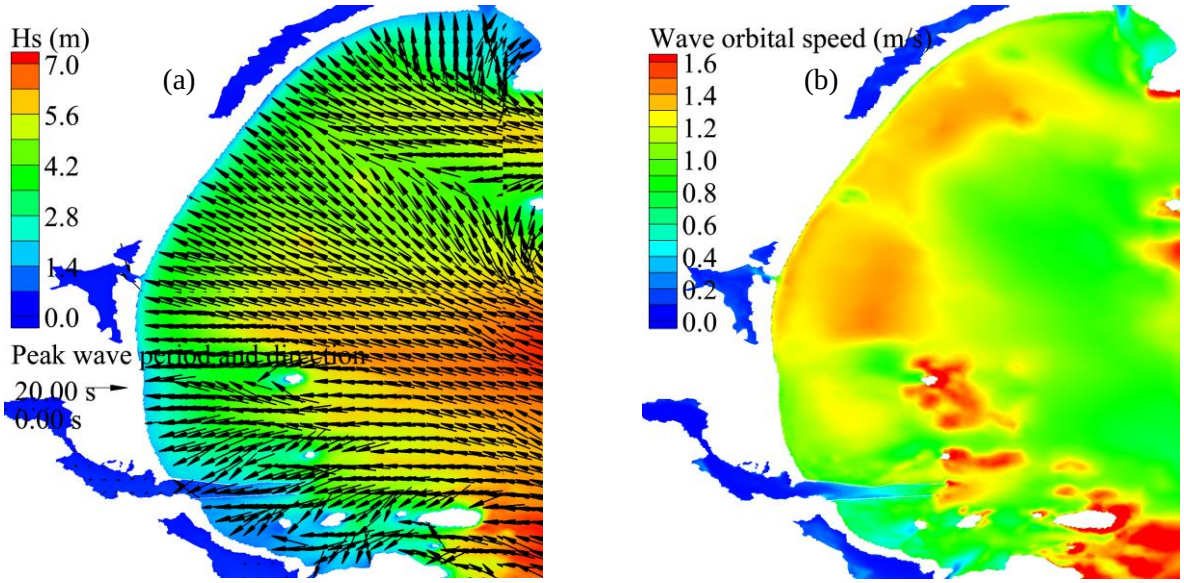


Figure 5.11. Waves at storm peak at 23:30UTC on 10/30/1991. (a) Wave height, period and direction; (b) Wave orbital velocity.

### 5.5.3 January 2015 North American blizzard

The January 2015 North American blizzard storm surge reached its peak an hour after falling mid-tide in Saco Bay at 13:30 UTC on 1/27/2015 and the wave height reached its peak around rising mid-tide at 18:00 UTC on 1/27/2015 (Figure 5.12). The two tidal cycles with high storm surge and waves (6:00UTC 1/27/2015 to 7:00UTC 1/28/2015) for averaged circulation and sand transport potential calculation were marked in Figure 5.12. Unlike the April 2007 nor'easter and the 1991 Perfect Storm,

during which the peak surge and peak wave height happened simultaneously or close in time, the gap between the peak surge and peak wave was 4.5 hours during the January 2015 North American blizzard. As peak sand transport occurred when wave height reached its peak in the bay as described in Section 5.6, the snapshots of current and waves were plotted at 18:00 UTC on 1/27/2015 when the wave height reached its peak.

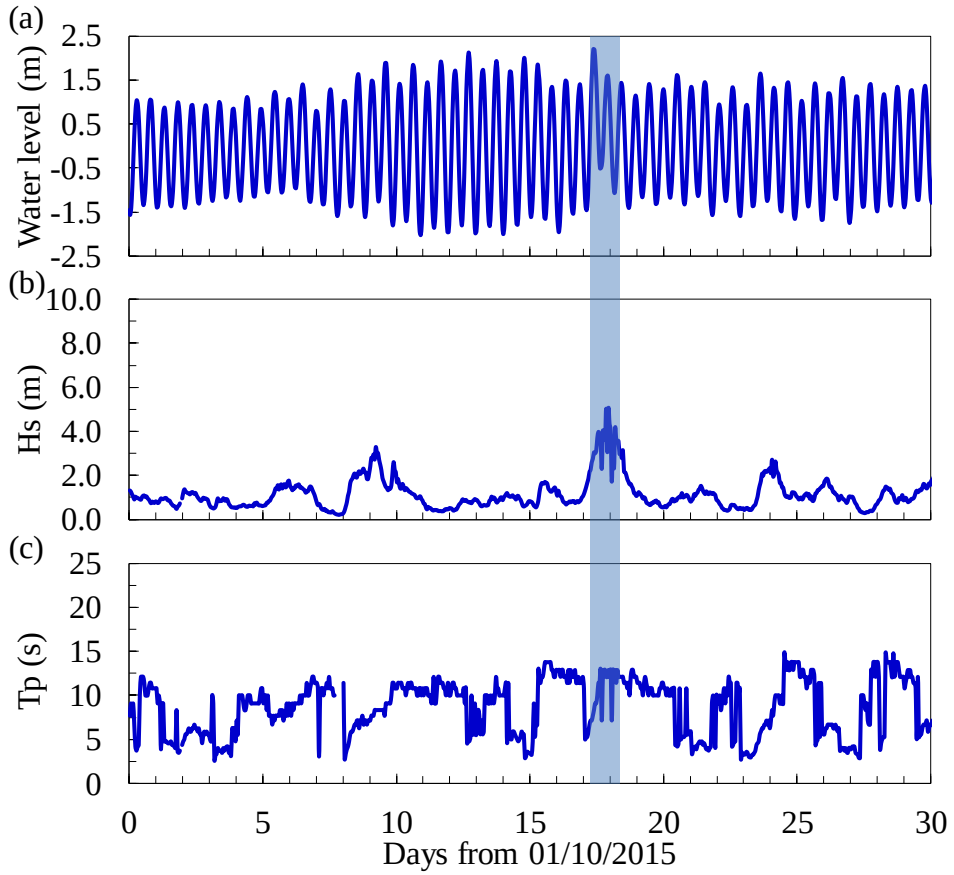


Figure 5.12. The water level and wave parameters at the nearest tide gauge 8418150 and wave buoy 44007 around the January 2015 North American blizzard. (a) Water level at tide gauge 8418150; (b) Significant wave height at wave buoy 44007; (c) Peak wave period at wave buoy 44007. The shaded area is the period that contains the storm peak.

The tidal current in the bay was maximum and water surged into the bay because it was around flood tide (Figure 5.13a). Large tidal current was identified at the northern and southern ends of the bay. To the north, the magnitude of tidal current increased to 0.1 m/s at the mouth of Scarborough River due to the funneling effect. The same phenomenon occurred in the channel bounded by the jetties at the Saco

River mouth. In the middle of bay, the tidal current decreased from 0.06 m/s offshore to less than 0.02 m/s at coast.

The wind-driven current was significant and reached 0.4 m/s in the bay at the peak of the January 2015 North American blizzard (Figure 5.13b). In the lee of Prouts Neck, the main part of the wind-driven current continued in the longshore direction while a small part moved northward before circulating back and joining the longshore current again. Between Pine Point and the Saco River, the longshore wind-driven current decreased from the coast to offshore except around islands where it was enhanced by a channeling effect due to the conservation of mass. At the coast, the wind-driven current reached 0.4 m/s. Between the Bluff Island and Stratton Island in the north of the bay, and Eagle Island in the middle, an area with negligible wind-driven current was found. The reduced magnitude of wind-driven current is mainly due to: (1) the shadowing effect of Bluff and Stratton Islands, and (2) the large local water depth.

The wave-induced current at the peak of the January 2016 North American blizzard presented similar patterns as that during the two other storms in this study (Figure 5.13c). At the coast, the wave-induced current was only significant in the lee of Prouts Neck and north of the Saco River. Around Prouts Neck, wave energy converged at the headland and diverged along the adjacent concave coastline, generating longshore wave radiation stress gradients exerting on mean flow. The wave-induced current flowed from the headland into the bay. The same physical process took place at Fletcher Neck at the southern end of the bay and complicated by the presence of islands. The wave-induced current flowed northward to the north of the Saco River except the clockwise gyre around Eagle Island. The southward wave-induced current from the north met with the northward wave-induced current from the south in the middle of the bay and formed a jet current flowing offshore.

The total depth-averaged current at the peak of the January 2017 North American blizzard was mainly determined by wind-driven and wave-induced currents (Figure 5.13d). However, the two components have disproportionate impact at the coast and in the offshore. At the coast from Prouts Neck to Pine Point, the wave-induced current was dominant due to the large wave radiation stress gradients from the headland to the inner bay. From Pine Point to Bay View, wind-driven current was dominant and

flowed southward. Between Bay View and the Saco River, both wind-driven and wave-induced currents were important and they partially cancelled out their effects because they travelled in opposite directions. However, southward current remained adjacent to the coast between Bay View and the Saco River. A small counterclockwise gyre with 0.3 m/s current speed formed in this area as well. North of Eagle Island, a region with negligible current existed due to the counterbalance between wind-driven and wave-induced currents. A jet was identified offshore of Eagle Island due to mass conservation in the bay.

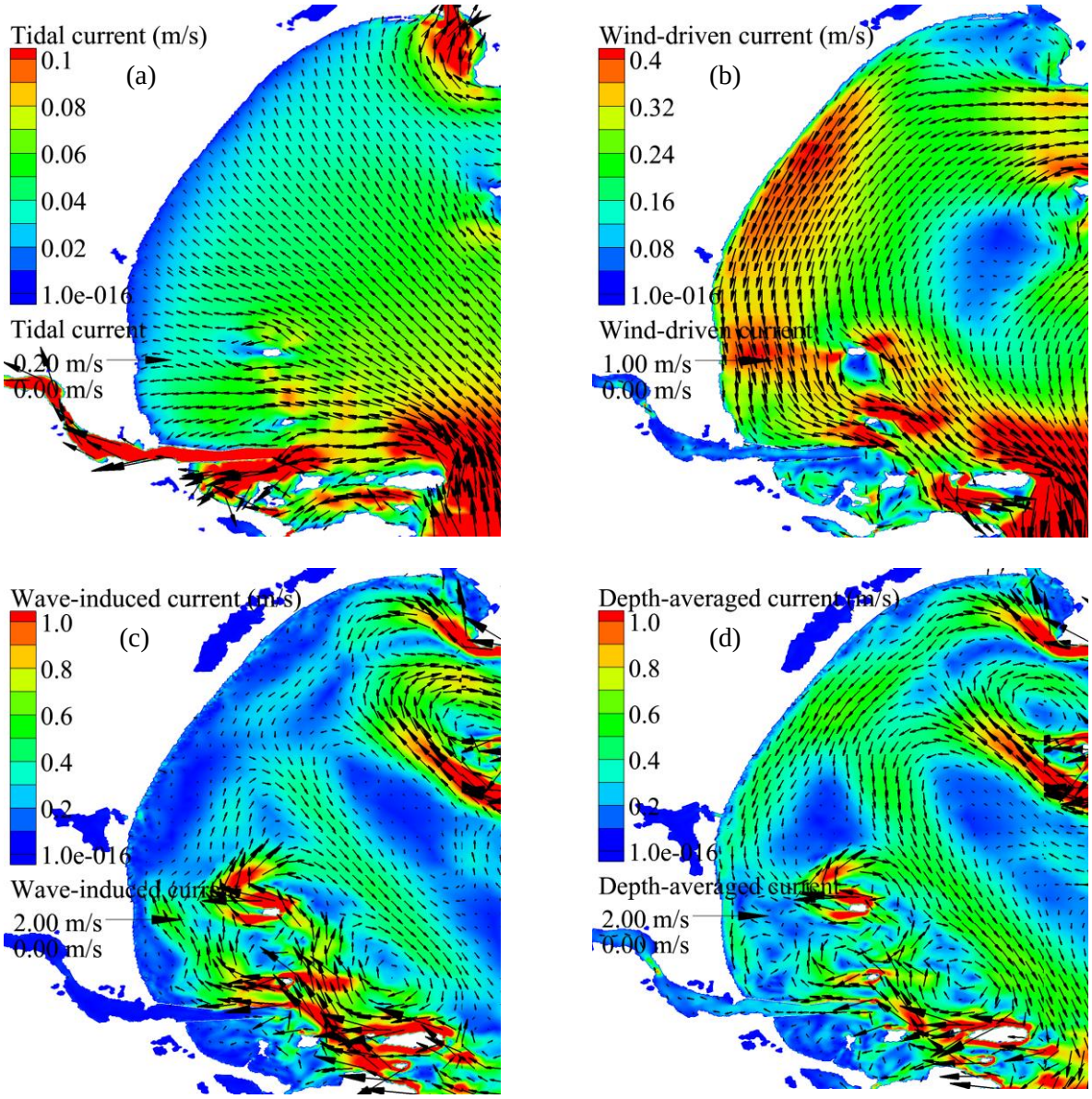


Figure 5.13. Current at storm peak at 18:00UTC on 1/27/2015. (a) Tidal current; (b) Wind-driven current; (c) Wave-induced current; (d) Total current.

The wave distribution in the bay at the peak of the storm was similar to that during the 1991 Perfect Storm (Figure 5.14a). Offshore, the significant wave height reached 7.0 m. Wave energy was dissipated by bottom friction as waves propagated into the bay with shoaling bathymetry. While the incoming significant wave height at the offshore side of the bay was similar during the January 2015 North American blizzard and the 1991 Perfect Storm, the significant wave height was smaller at the coast in comparison to the 1991 Perfect Storm. This was mainly due to the tidal modulation of wave height at coast. For the 1991 Perfect Storm, the wave height reached its peak two hours after high tide while the water level was still above the mean sea level, the peak wave height during the January 2015 North American blizzard happened around rising mid-tide.

The wave orbital speed at seabed during the storm peak is shown in Figure 5.14b. At the coast, the wave orbital speed at seabed is smaller than during the other two storms due to decreased wave height modulated by tide level. Otherwise, the distribution of wave orbital speed at seabed was similar to that during the other two storms.

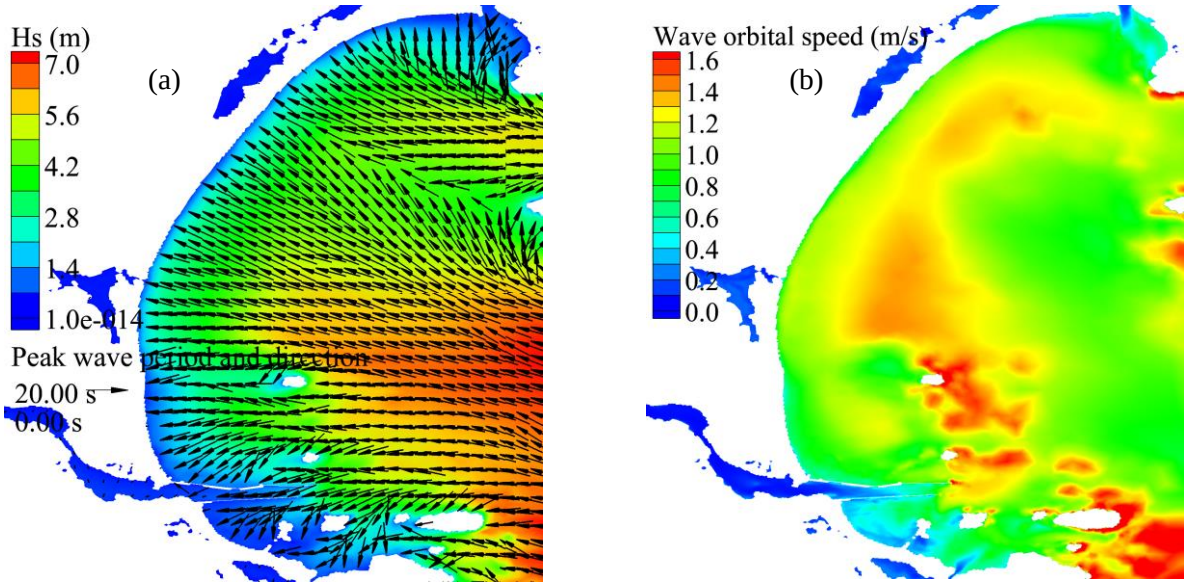


Figure 5.14. Waves at storm peak at 18:00UTC on 1/27/2015. (a) Wave height, period and direction; (b) Wave orbital velocity.

## 5.6 Sand transport model results

In this section, modeling results of sand transport rates at the peak of each storm are described and discussed. The distribution of current-induced bed shear-stress, wave-induced bed shear-stress and bed shear-stresses with the co-existence of waves and currents were calculated to identify the main mechanisms responsible for sand transport in the bay. The maximum and mean combined wave-current shear-stresses were investigated to determine the threshold of motion and sand diffusion respectively. The time series of water level, waves, currents and sand transport rate were also computed to determine the roles of different components of hydrodynamics in sand transport. As stated in Section 5.4.3, we only considered sand transport in areas where sand dominates in the bay.

### 5.6.1 Peak sand transport

#### 5.6.1.1 April 2007 Nor'easter

Sand dominates the seafloor with water depth less than 10 to 15 m in Saco Bay, where the seabed shear-stress and sand transport rate were computed. The distribution of current-alone bottom stress calculated by Equation 5.3 (Figure 5.15a) followed the pattern of depth-averaged current (Figure 5.15a). The current-alone bottom stress was also larger at the coast with shallower water depth than farther offshore. The maximum current-alone bottom stress occurred at locations with maximum depth-averaged current speed. In the lee of Prouts Neck, the current-alone bottom stress reached 0.3 $N/m^2$. Large current-alone bottom stress also occurred north of Eagle Island and the north jetty at the Saco River mouth. At other locations, the current-alone bottom stress was moderate (0.15 $N/ m^2$) or negligible.

The distribution of the wave-alone bottom stress as calculated by Equation 5.4 is well correlated with the wave orbital speed at seabed (Figure 5.15b). At water depths from 10 to 15 m offshore of the coast between Old Orchard Beach and Goosefare Brook, the wave-alone bottom stress reached 5.5 $N/m^2$. The wave-alone bottom stress decreased shoreward between 10 m and 5 m depth contours due to the decreased wave orbital speed at the seabed. At water depth less than 5 m, the wave-alone bottom stress increased mainly due to the shallow water depth, which counterbalanced the effect of decreased wave

height on the wave orbital speed at the seabed. At other locations in the bay, the wave-alone bottom stress was moderate (3.0 $N/m^2$).

The bed shear-stresses beneath combined waves and currents are nonlinearly enhanced beyond the linear summation of the current-alone and wave-alone bed shear-stress. The maximum combined bed shear-stress distribution calculated by Equation 5.2 followed that of the wave-alone bottom stress but was enhanced by current and the nonlinear interaction between waves and current (Figure 5.15c). Between Pine Point and Goosefare Brook, the maximum combined bed shear-stress reached 6.0 $N/m^2$. Large maximum combined bed shear-stress also occurred adjacent to the north side of the north jetty at the Saco River mouth. At other locations, the maximum combined bed shear-stress was moderate with a magnitude less than 4.0 $N/m^2$. The maximum combined bed shear-stress determines the threshold of motion and entrainment rate of sediment. It is reasonable that the distribution of the maximum combined bed shear-stress is well correlated with that of wave-alone bed shear-stress since waves are primarily responsible for setting sediment into motion in coastal environment.

In contrast, the mean combined bed shear-stress over one wave period calculated by Equation 5.1 followed the distribution of current-alone bed shear-stress (Figure 5.15d). The mean combined bed shear-stress reached its maximum value of 1.1 $N/m^2$ in the lee of Prouts Neck, to the north of Eagle Island and the north jetty at the Saco River mouth. Offshore of Old Orchard Beach between 5 m and 10 m water depth, the mean combined bed shear-stress was slightly lower with a magnitude of 0.9 $N/m^2$. The mean combined shear stress was moderate and even negligible for the rest of the bay.

The total load sand transport beneath combined waves and current at the peak of the April 2007 nor'easter is shown in Figure 5.15e. The distribution of total load sand transport was well correlated with that of mean combined bed shear-stress and depth-averaged current speed. Between Prouts Neck and Ocean Park, the total load sand transport was toward the southwest along the shoreline and reached 0.008 $m^3/m.s$ before splitting into a continuing alongshore component and a southward component which brought sand offshore. The alongshore total load sand transport component continued beyond Goosefare Brook and then turned offshore to the north of Eagle Island, where the total load sand transport reached

its maximum in the bay with a magnitude of 0.01 $m^3$/m.s. Between the north jetty at the Saco River mouth and Bay view, the total load sand transport is northward along the shore. It then turned eastwards and merged with the offshore sand transport component from the north of the bay offshore of Bay View.

Figure 5.15. Seabed shear-stresses and sand transport rate. (a) Current-induced bed shear stress; (b) Wave-induced bed shear stress; (c) Maximum combined bed shear stress beneath waves and currents; (d) Mean combined bed shear stress beneath waves and currents; (e) Sand transport at the storm peak at 14:30UTC on 4/16/2007.

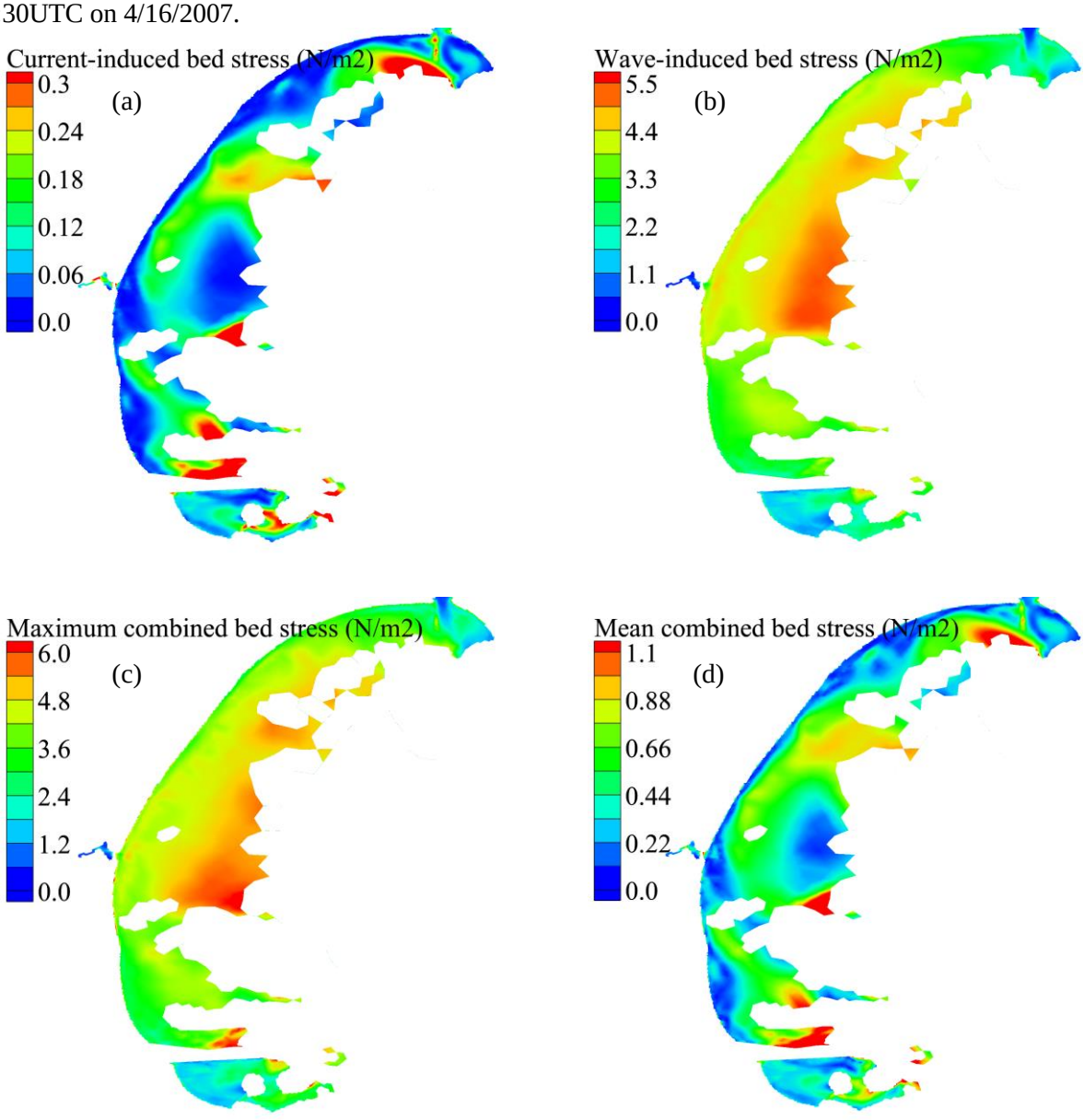

Figure 5.15 Continued

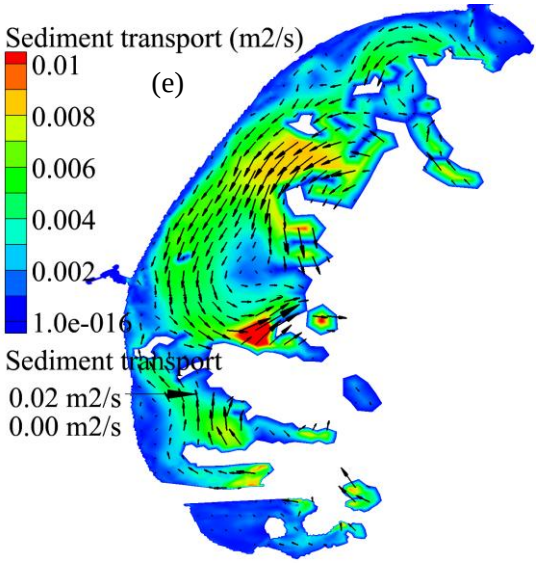


To identify the dominant hydrodynamic processes for total load sand transport in the bay, the time series of tide level, surge level, significant wave height, wave orbital speed at seabed, tidal current, wind-driven current and wave-induced current were plotted at the selected point A (Figure 5.1c). The results are shown in Figure 5.16. During the April 2007 nor'easter, the peak surge occurred around rising mid-tide while peak wave height occurred around high tide. The wave orbital speed at seabed was in phase with the significant wave height. The peak total load sand transport (0.01 $m^3$/m.s) occurred between the time interval of peak wave orbital speed at the seabed and the maximum depth-averaged current speed from 15:00 UTC to 20:00 UTC on April 16$^{th}$. During this time interval, the wave orbital speed decreased gradually from 1.2 m/s to 1.0 m/s, while the depth-averaged current speed increased from 0.4 m/s to 0.6 m/s. This result indicates that both waves and depth-averaged current contributed to total load sand transport at the selected point. The contribution of tidal current to the total depth-averaged current was negligible. The depth-averaged current was mainly attributed to wave and wind effects, with wave-induced current contributing to more than wind-driven current. When the depth-averaged current reached

its peak of 0.6 m/s, the wave-induced component was 0.4 m/s and wind-driven component was slightly less than 0.2 m/s.

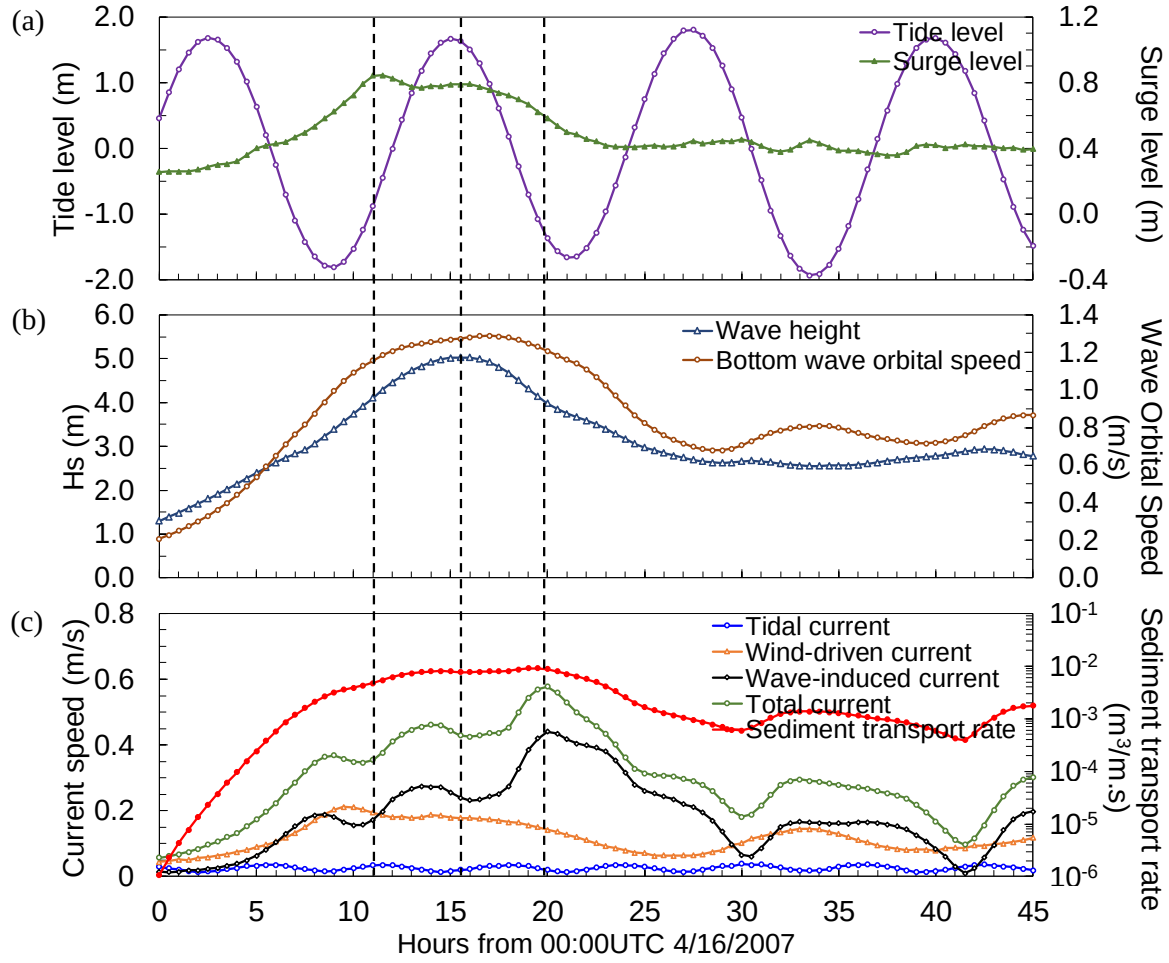


Figure 5.16. The time series of water level, wave height, current speed and sand transport rate at point A during the April 2007 nor'easter. (a) Tide level and surge level, (b) Significant wave height and wave orbital speed at seabed, and (c) Different current components and sand transport rate. The three vertical black dashed lines mark the peak of the surge level, wave orbital speed at seabed and total load sand transport respectively.

#### 5.6.1.2 1991 Perfect Storm

The distribution of current-alone bottom stress (Figure 5.17a) at the peak of the 1991 Perfect Storm was similar to that during the April 2007 nor'easter, however the magnitude throughout most of the bay was lower. The current-alone bottom stress between Prouts Neck and Old Orchard Beach at water depth less than 5.0 m was negligible, mainly due to the negligible depth-averaged current in this area.

Along Old Orchard Beach, the current-alone bottom stress reached 0.27 $N/m^2$ and gradually decreased southwards along the coast. Between Ocean Park and Bay View, the current-alone bottom stress was again negligible with the presence of small depth-averaged current. The maximum current-alone bottom stress of 0.3 $N/m^2$ occurred to the north of Eagle Island and adjacent to the north jetty at the Saco River mouth.

The wave-alone bottom stress in the bay (Figure 5.17b) was one order of magnitude higher than the current-alone bottom stress. High wave-alone bottom stress (4.4 $N/m^2$ to 5.0 $N/m^2$) occurred in the middle section of the bay where large waves approached the shoreline due to the smooth depth contours. In the north and south sections of the bay, the presence of islands and headlands decreased the significant wave height at the coast, which resulted in smaller wave orbital speeds at the seabed and, in turn, lower wave-alone bottom stress (2.2 $N/m^2$ to 3.3 $N/m^2$).

The maximum combined bed shear-stress at the peak of the 1991 Perfect Storm is shown in Figure 5.17c. Significant enhancement of bed shear-stress due to currents and wave-current interaction occurred to the north of Eagle Island and adjacent to the north jetty at the Saco River mouth. To the north of Eagle Island, the maximum combined bed shear-stress reached 6.0 $N/m^2$. In the rest of the bay, the maximum combined bed shear-stress was increased by approximately 0.5 $N/m^2$ in over the wave-alone bottom stress.

The mean combined bed shear-stress (Figure 5.17d) was significantly enhanced relative to current-alone bottom stress due to waves and wave-current interaction in the bay. Between Pine Point and Ocean Park, the mean combined bed shear-stress ranged between 0.5 $N/m^2$ and 1.0 $N/m^2$. South of Ocean Park, the mean combined bed shear-stress first decreased and then increased between Ferry Beach and the Saco River mouth. The maximum value of the mean combined bed shear-stress occurred to the north of Eagle Island and adjacent to the north jetty at the Saco River mouth.

The total load sand transport is shown in Figure 5.17e. In the northern part of the bay between Pine Point and Ocean Park, the total load sand transport was in the southwest direction along the coast. Further south beyond Ocean Park, the magnitude of total load sand transport decreased and gradually

turned eastwards. To the north of Eagle Island, the total load sand transport reached its maximum value of 0.01 $m^3$/m.s. Between the north jetty at the Saco River mouth and Bay View, the total load sand transport was in the northward direction along the coast before being turned offshore and merging with the eastward sand transport from the north of the bay. Unlike the total load sand transport during the April 2007 nor'easter, two small scale sand transport features occurred at the coast that could change the local sand transport pattern. Between Pine Point and Old Orchard Beach, a small part of the total load separated from the main southwest total load sand transport and formed a clockwise sand transport gyre. The magnitude of the small clockwise gyre reached 0.004 $m^3$/m.s. In the south of the bay, a counterclockwise total load sand transport gyre formed between the north jetty at the Saco River mouth and Ferry Beach. Though small in magnitude, the counterclockwise transport gyre may have implication for total load sand transport in this area over the life cycle of the storm due to its cumulative effect over time.

Figure 5.17. Seabed shear-stresses and sand transport rate. (a) Current-induced bed shear stress; (b) Wave-induced bed shear stress; (c) Maximum combined bed shear stress beneath waves and currents; (d) Mean combined bed shear stress beneath waves and currents; (e) Sand transport at the storm peak at 23:30UTC on 10/30/1991.

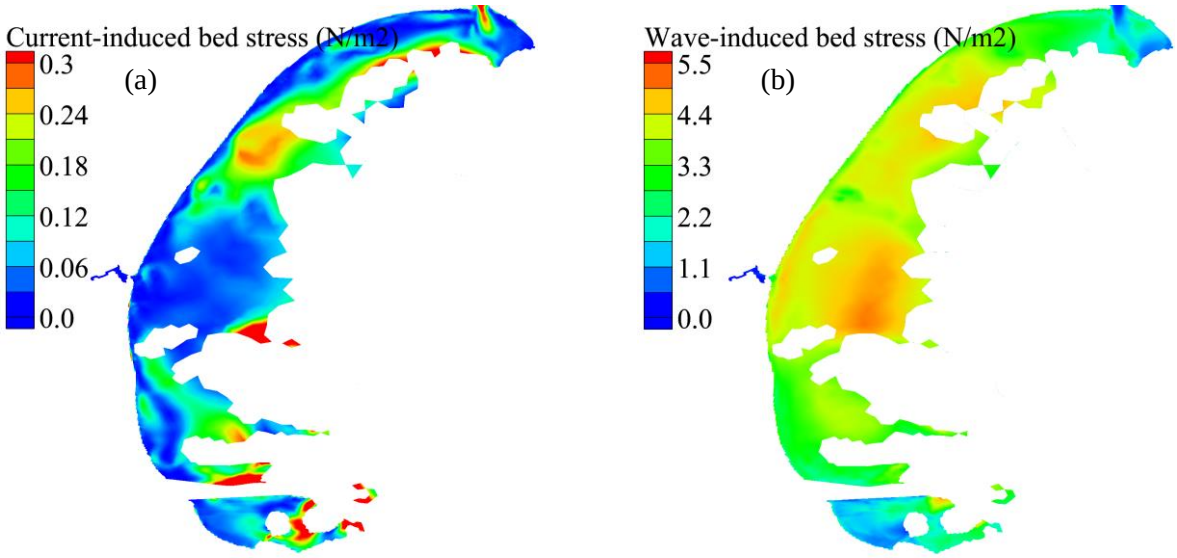

Figure 5.17 Continued

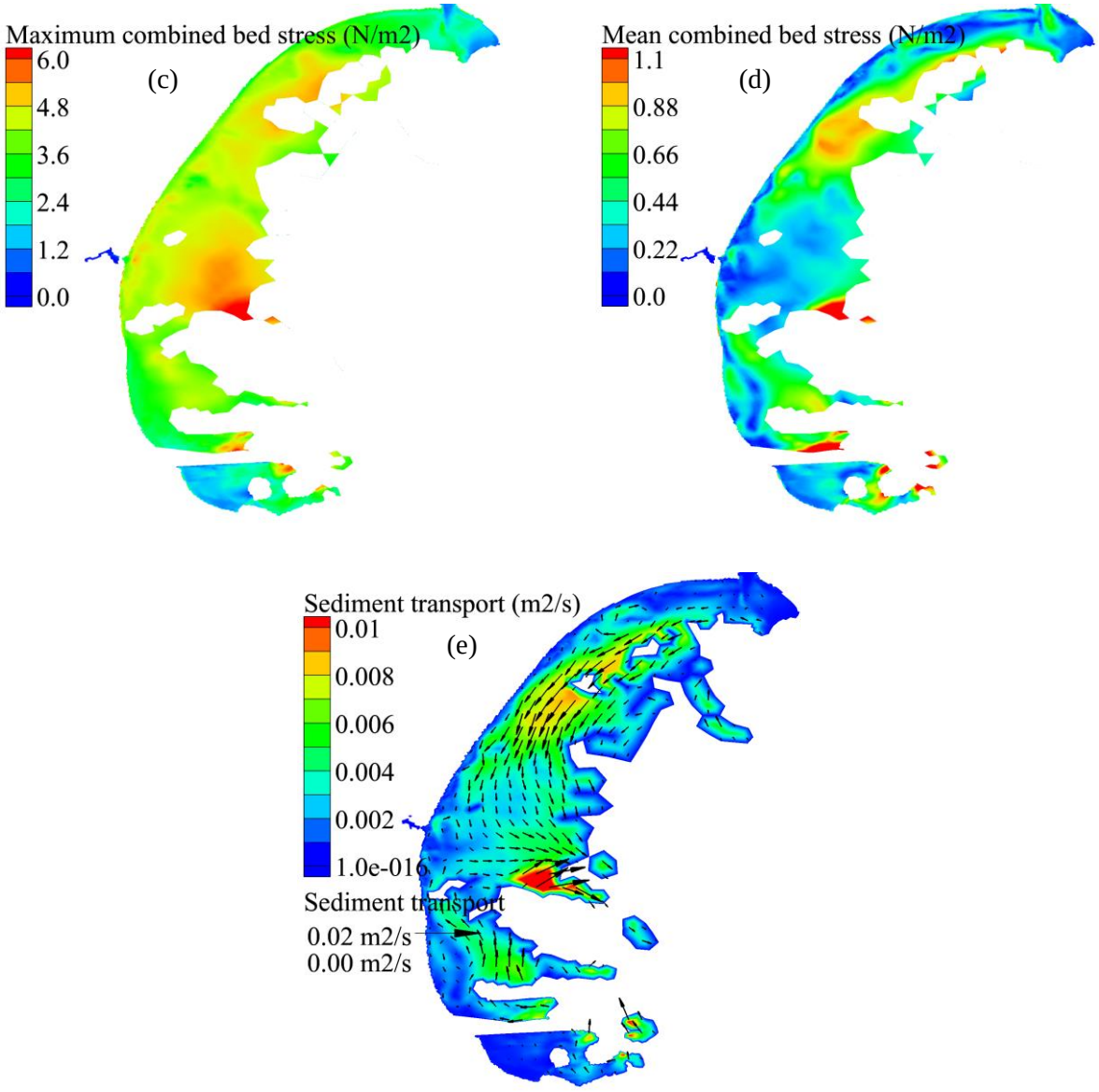


During the 1991 Perfect Storm, the peak of storm surge, significant wave height and total load sand transport happened within 3.5 hours at the selected point A as shown in Figure 5.18. The peak storm surge happened close to the low tide due to the modification of water depth on surge level and the timing of the storm. The peak significant wave height and wave orbital speed at the seabed occurred two hours before the peak surge around falling mid-water. Unlike the total load sand transport during the April 2007 nor'easter, which varied little over 9.0 hours, the sand transport was single-peaked and correlated well

with the depth-averaged current. The wave-induced and wind-driven currents were the main components of the total depth-averaged current. The total depth-averaged current was in phase with the wave-induced current. At the peak of total load sand transport (0.01 $m^3$/m.s), the total depth-averaged current was 0.45 m/s. The wave-induced and wind-driven currents were 0.30 m/s and 0.15 m/s respectively. While the contribution of tidal current on the total depth-averaged current was small, the modulation of tidal level on the wave-induced current, and thus the total load sand transport, was significant. After the total load sand transport reached its peak, it fluctuated inversely with tide level.

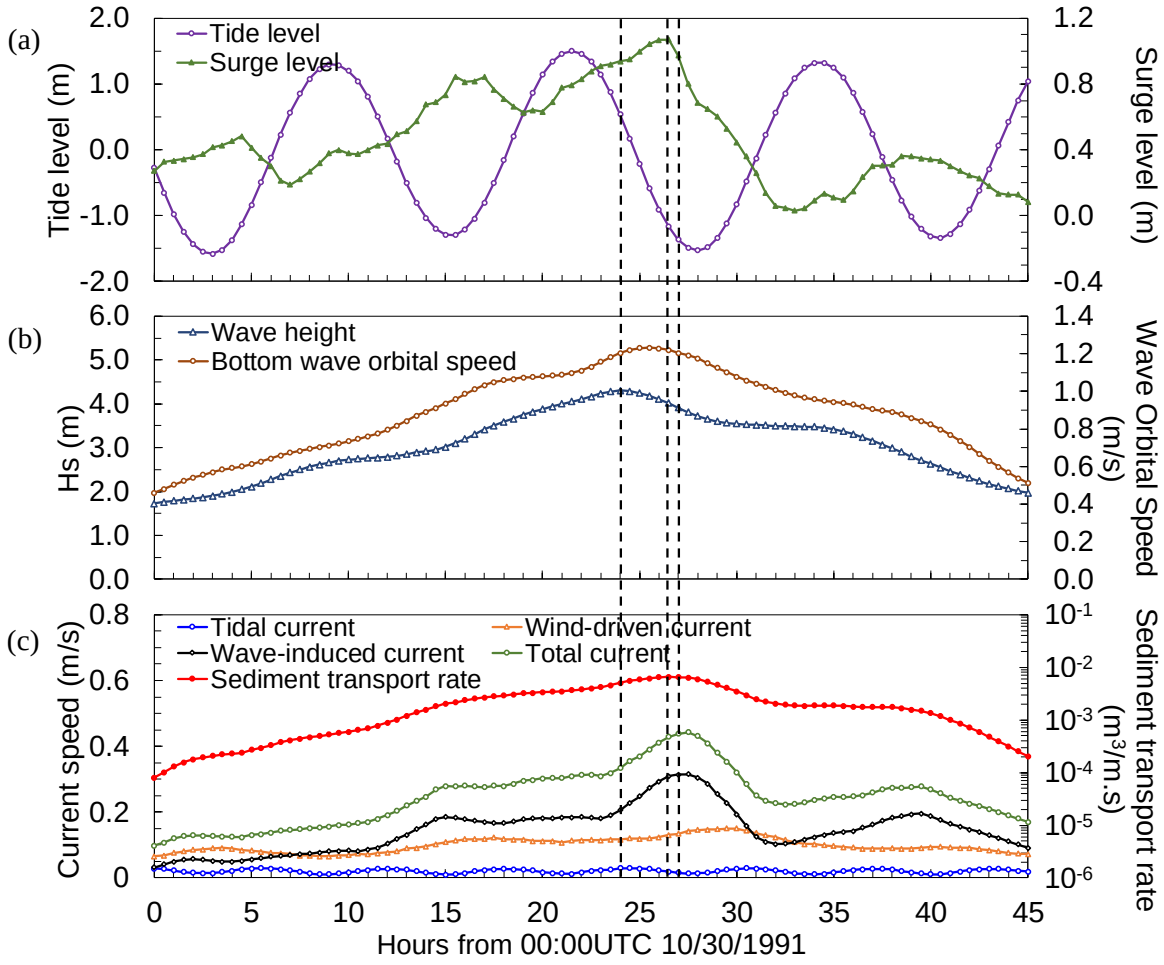


Figure 5.18. The time series of water level, wave height, current speed and sand transport rate at point A during the 1991 Perfect Storm. (a) Tide level and surge level, (b) Significant wave height and wave orbital speed at seabed, and (c) Different current components and sand transport rate. The three vertical black dashed lines mark the peak of the surge level, wave orbital speed at seabed and total load sand transport respectively.

#### 5.6.1.3 January 2015 North American blizzard

The distribution of the current-alone bottom stress (Figure 5.19a) was well correlated with the depth-averaged current at the peak of the storm. The current-alone bottom stress was larger at the coast than in offshore areas except between Pine Point and Old Orchard Beach. The current-alone bottom stress reached its maximum value of 0.3 $N/m^2$ at several locations in the bay, including in the lee of Prouts Neck, between Old Orchard Beach and Ocean Park, to the north of Eagle Island and adjacent to the north jetty at the Saco River mouth. Values were slightly lower at the coast between Ferry Beach and Camp Ellis.

The wave-alone bottom stress at the peak of the January 2015 North American blizzard (Figure 5.19b) was lower than during the 1991 Perfect Storm peak, primarily due to smaller wave height at the coast modulated by tide level during the January 2015 North American blizzard. The wave-alone bottom stress was larger at water depth between 5.0 m and 10.0 m than at water depth less than 5.0 m. Offshore of Goosefare Brook, the wave-alone bottom stress reached its maximum value of 5.0 $N/m^2$. At the coast, the wave-alone bottom stress ranged from 2.5 $N/m^2$ to 4.5 $N/m^2$.

The maximum combined bed shear-stress (Figure 5.19c) followed the pattern of wave-alone bottom stress distribution. The maximum combined bed shear-stress was higher at greater water depth than at smaller water depth. The maximum combined bed shear-stress reached 6.0 $N/m^2$ to the north of Eagle Island. At other locations, the maximum combined bed stress varied between 2.0 $N/m^2$ and 5.0 $N/m^2$.

The distribution of the mean combined bed shear-stress (Figure 5.19d) was similar with that of the current-alone bottom stress, however, its magnitude was significantly enhanced by the combined waves and currents. The mean combined bed shear-stress reached its maximum (1.1 $N/m^2$) at the same locations as those of the current-alone bottom stress.

The total load sand transport is shown in Figure 5.19e. The southward alongshore current from the Prouts Neck to Saco River mouth enabled the southward alongshore total load sand transport from Prouts Neck to Bay View before the total load sand transport turned eastward and merged with the

offshore total load sand transport component from Old Orchard Beach. Between the Saco River and Ferry Beach, the magnitude of total load sand transport is small, however a counterclockwise sand transport gyre was formed.

Figure 5.19. Seabed shear-stresses and sand transport rate. (a) Current-induced bed shear stress; (b) Wave-induced bed shear stress; (c) Maximum combined bed shear stress beneath waves and currents; (d) Mean combined bed shear stress beneath waves and currents; (e) Sand transport at the storm peak at 18:00UTC on 1/27/2015.

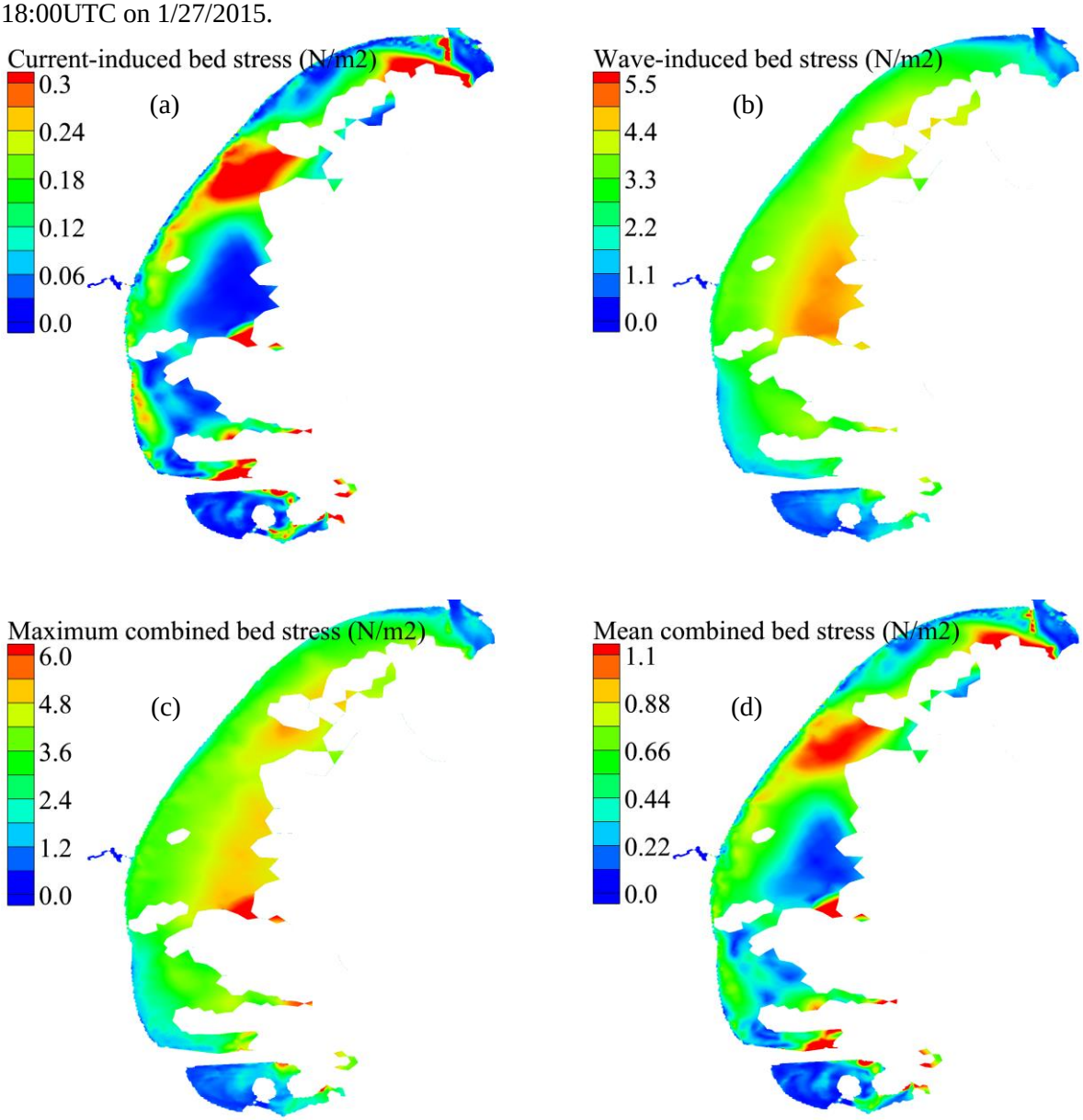

Figure 5.19 Continued

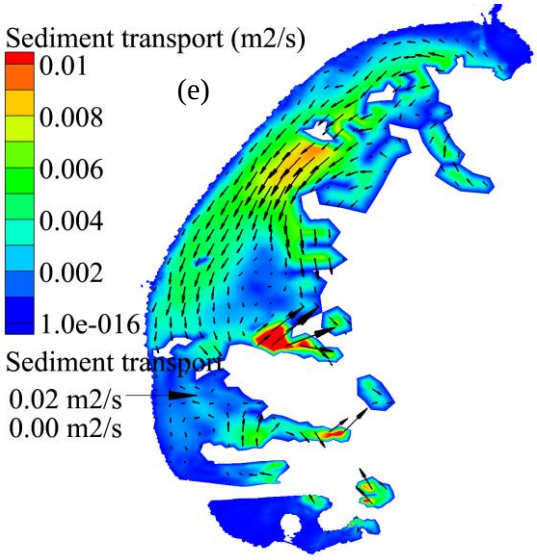


At the selected point A, the peak wave height and peak total load sand transport lagged the peak storm surge due to modulation by the tide. Dual peaks of depth-averaged current speed and total load sand transport occurred during the storm. As during the April 2007 nor'easter, the total load sand transport during the first peak remained steady for 5 hours between 15:00UTC and 20:00UTC on April 27th. During this period, the depth-averaged current decreased gradually, which was complemented by the increased wave orbital speed at seabed. In contrast to the other two storms, the magnitude of wind-driven current was larger than wave-induced current during the first peak of the total load sand transport. At the first peak, the depth-averaged current speed reached 0.4 m/s, in which the wind-driven and wave-induced currents were 0.2 m/s and 0.15 m/s respectively. The total load sand transport decreased sharply with the depth-averaged current speed at 23:00UTC on April 27th. The decrease of the depth-averaged current speed was mainly attributed to the counterbalancing effects of the wind-driven and wave-induced currents. While the wind-driven current consistently flowed southward alongshore at point A, the wave-induced current flowed northward between 21:00UTC and 23:00UTC on April 27th due to the extension of the wave-induced clockwise gyre around Bluff and Stratton Islands toward shore, which countered the

wind-driven current. After 23:00UTC on April 27th, the wave-induced clockwise gyre retreated offshore and the wave-induced current resumed its southward flow alongshore at point A, which enhanced the depth-averaged current and the total load sand transport.

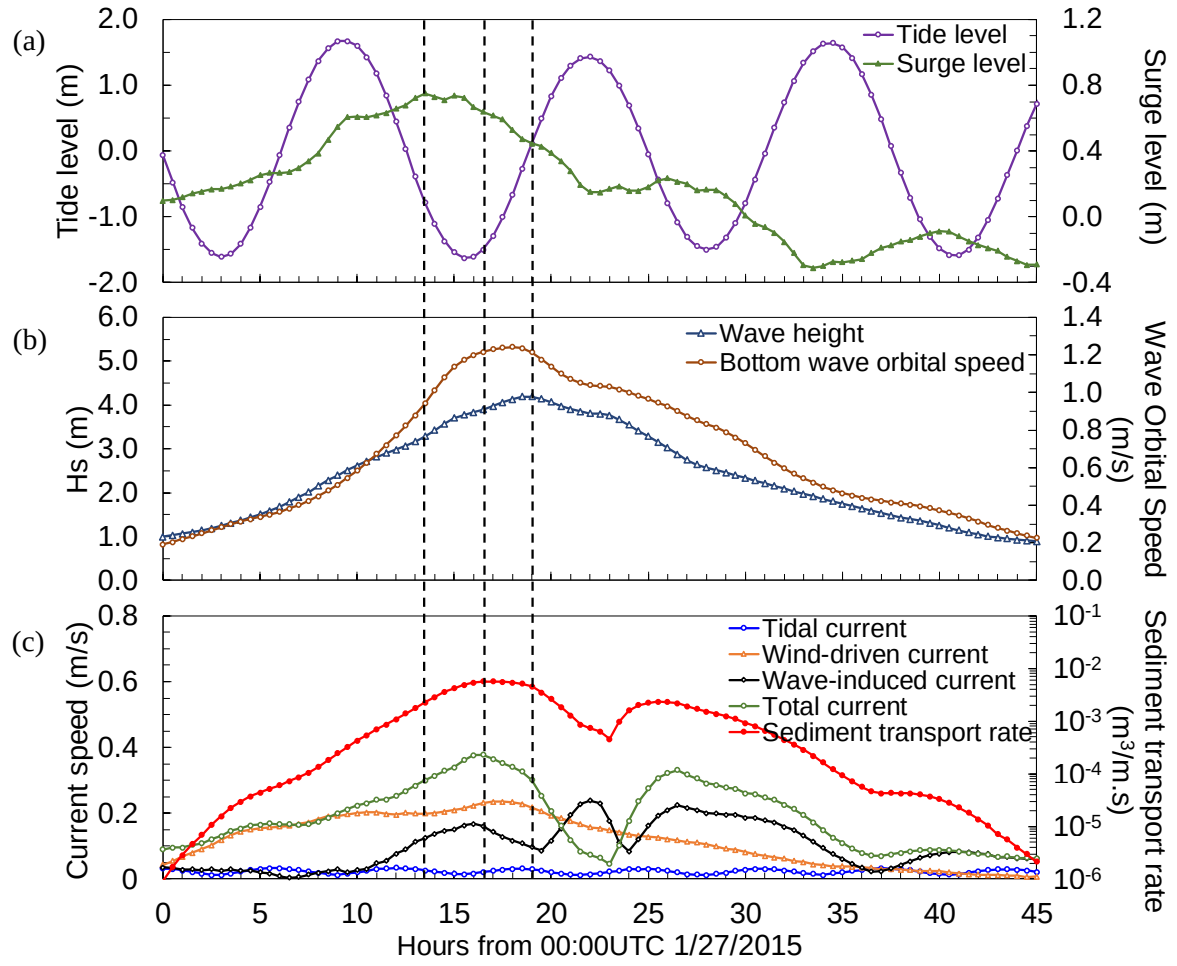


Figure 5.20. The time series of water level, wave height, current speed and sand transport rate at point A during the January 2015 North American blizzard. (a) Tide level and surge level, (b) Significant wave height and wave orbital speed at seabed, and (c) Different current components and sand transport rate. The three vertical black dashed lines mark the peak of the surge level, wave orbital speed at seabed and total load sand transport respectively.

### 5.6.2 Averaged flow field and sand transport flux

The tidally averaged flow fields can be used to identify the main physical processes driving overall sand transport in coastal systems. Because the magnitude and direction of sand transport change over the tidal cycle, this approach was used to account for the net transport of sand caused by the storms.

In this section, the wind, significant wave height, wave orbital speed at seabed, tidal current, wind-driven current, wave-induced current, total depth-averaged current and sand transport rate were averaged over the two tidal cycles spanning the peak of each of the three storms. The averaged flow fields were compared to identify the most important drivers of sand transport.

#### 5.6.2.1 April 2007 Nor'easter

The averaged wind over the two tidal cycles containing the storm peak in Saco Bay (8:30UTC 4/16/2007 to 9:30UTC 4/17/2007) is shown in Figure 5.21a. During the two tidal cycles, the wind speed reached about 13.0 m/s in the entire Saco Bay and was coming from the northeast to east direction. In contrast, waves mainly came from the southeast during the storm (Figure 5.8a) because their generation was dominated by offshore swells. The wave height reached 6.5 m at the offshore and gradually decreased in the bay due to bottom friction. The wave height contours were in parallel with the depth contour in the bay due to wave refraction and depth-induced breaking. Between the 5.0 m and 15.0 m depth contours, the significant wave height ranged from 2.5 m to 5.0 m. The averaged wave orbital speed at seabed was greatest at water depths less than 15.0 m along the coast, where the decreasing wave height was counterbalanced by the decreased water depth. The maximum wave orbital speed at seabed reached 1.5 m/s and occurred around the islands in the bay, where the bathymetry changed abruptly.

The tidal residual current (Figure 5.21d) was negligible compared to the averaged wind-driven and wave-induced currents. At most locations in the bay, the tidal residual current was less than 0.01 m/s. Only at inlets and around islands in the bay, did the tidal residual current reach 0.03 m/s. Around Bluff Island and Stratton Island, the tidal residual current rotated counterclockwise. The same rotary feature was observed in the south of the bay around Eagle Island and between the seaward end of the jetty at the Saco River mouth and Fletcher Neck.

The averaged wind-driven current (Figure 5.21e) during the storm peak flowed southward along the coast before reaching Bay View, where it gradually turned southeast. Between Bay View and the north jetty at the Saco River mouth, the averaged wind-driven current rotated clockwise and merged with

the southeast flow at approximately 5.0 m depth at Camp Ellis. The magnitude of averaged wind-driven current ranged between 0.12 m/s and 0.20 m/s.

The magnitude of the averaged wave-induced current (Figure 5.21f) was small within water depth less than 5.0 m except at the north and south ends of Saco Bay. At both headlands, the significant wave height changed drastically along the coast due to the interaction between waves and bathymetry, resulting in large wave radiation stress gradients that drove the longshore current from the headlands into the bay. The maximum wave-induced current reached 1.0 m/s around islands and at the headlands. One large clockwise wave-induced circulation persisted over the two tidal cycles at the storm peak due to the interaction between waves and bathymetry. The shoreward wave-induced current of the gyre split into two components, one rotated back into the gyre and the other joined the southwest flow before gradually turning to southeast, which formed an offshore jet-shaped flow. Another large wave-induced clockwise gyre occurred between the north jetty at the Saco River mouth and Goosefare Brook. Four secondary gyres existed within the large gyre. The northward wave-induced current originated from Fletcher Neck and separated into a continued northward component and an eastward component due to the interaction between the bathymetry and current. The northward component circulated around Eagle Island and turned eastward to join the jet-shaped flow from the north. The eastward component gradually turned north following the depth contour. Between Camp Ellis and Ferry Beach, a weak secondary counterclockwise gyre was formed.

The averaged total depth-averaged current (Figure 5.21g) was mainly composed of wind-driven and wave-induced current. While the circulation pattern of the total depth-averaged current resembled that of the wave-induced current, the interaction between current, waves and bathymetry produced some differences. At water depth less than 5.0 m along the coast between Prouts Neck and Goosefare Brook, the dominant component of the total depth-averaged current was wind-driven current, which ranged between 0.10 m/s to 0.22 m/s. In the rest of the bay, the wave-induced current was larger than the wind-driven component. The offshore jet-shaped flow was enhanced because the wave-induced and wind-

driven currents were in the same direction. The counterclockwise gyre between Ferry Beach and Camp Ellis was maintained during the peak of the storm.

The pattern of averaged sand transport flux (Figure 5.21h) was similar to that of the averaged total depth-averaged current. The averaged sand transport flux was significant within water depth less than 10.0 m in the bay. To the north of Goosefare Brook, the averaged sand transport was toward the south of the bay along the coast and reached its maximum of 0.005 $m^3$/m.s at approximately 8.0 m depth between Pine Point and Old Orchard Beach. After reaching its maximum, the averaged sand transport split into a continued southwest alongshore component and a southward component. The continued alongshore component turned eastward after reaching Goosefare Brook and merged with the northward averaged sand transport from the south of the bay. At most locations, the averaged sand transport was about 0.0025 $m^3$/m.s. Following the averaged depth-averaged current, a weak counterclockwise averaged sand flux existed between Ferry Beach and Camp Ellis. The magnitude of the corresponding averaged sand flux was 0.0008 $m^3$/m.s.

Figure 5.21. Averaged wind, waves, currents and sand flux over the two tidal cycles between 08:30UTC 4/16/2007 and 09:30UTC 4/17/2007 when the storm was at its peak. (a) Averaged wind, (b) Averaged significant wave height, (c) Averaged wave orbital speed at seabed, (d) Tidal residual current, (e) Averaged wind-driven current, (f) Averaged wave-induced current, (g) Averaged depth-averaged current, (h) Averaged sand flux.

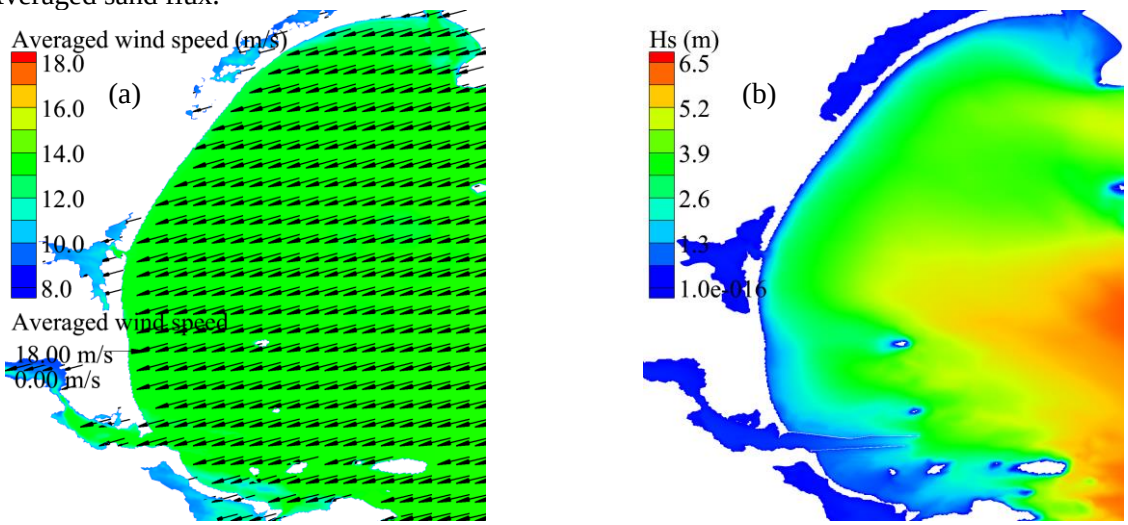

Figure 5.21 Continued

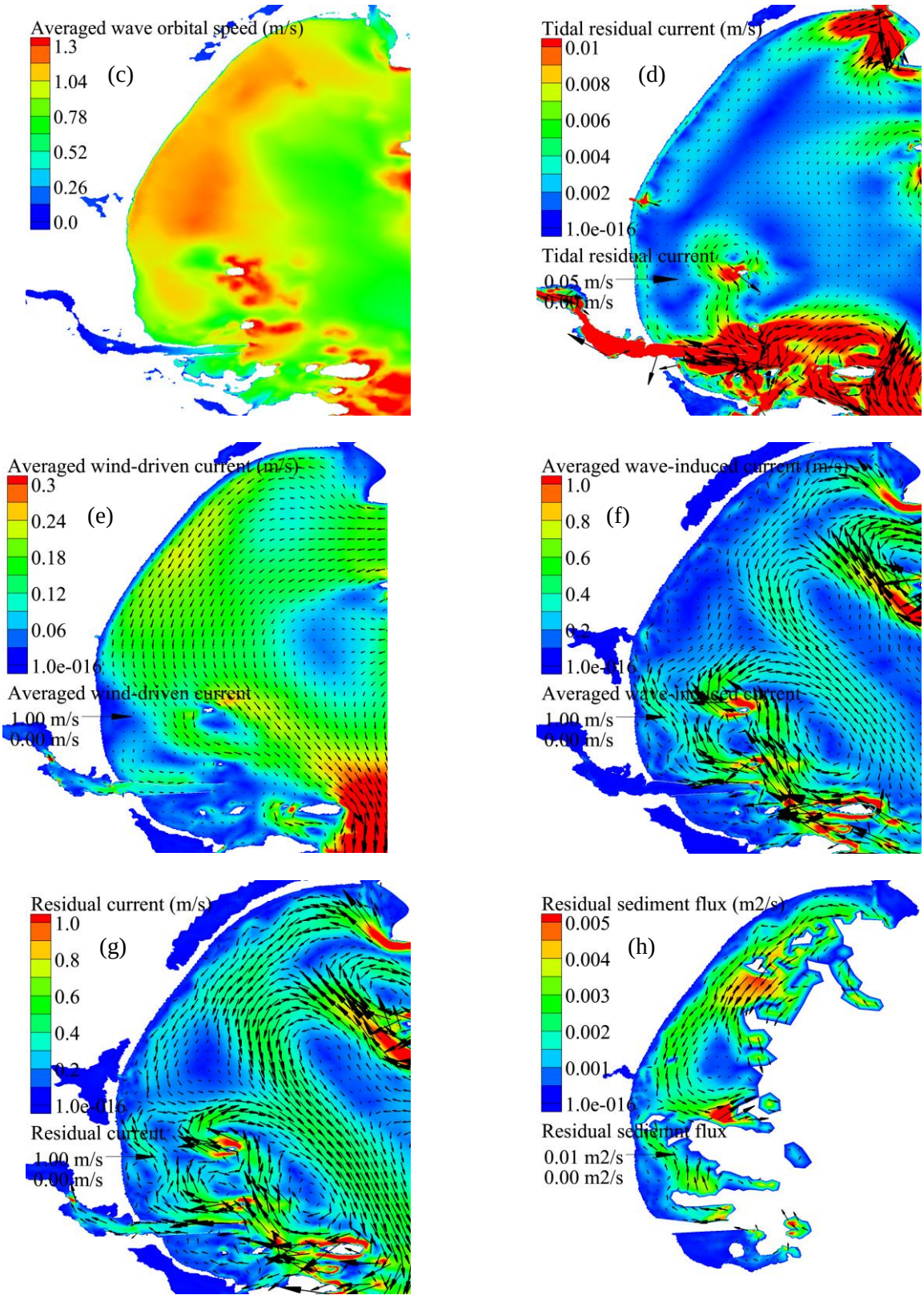

#### 5.6.2.2 1991 Perfect Storm

The wind, waves, currents and sand transport rate were averaged over the two tidal cycles containing the storm peak in Saco Bay (14:00UTC 10/30/1991 to 15:00UTC 10/31/1991). The averaged wind is shown in Figure 5.22a. The averaged wind was from the northeast during the storm peak. Except in the lee of Prouts Neck where the wind speed was approximately 8.0 m/s, the averaged wind speed in the rest of the bay ranged between 12.0 m/s and 13.0 m/s. The averaged wave height (Figure 5.22b) decreased from 6.0 m in offshore areas and gradually decreased while moving shoreward. The wave height distribution was mainly affected by wave refraction due to water depth, as well as bottom friction and wave breaking. The averaged wave orbital speed at seabed (Figure 5.22c) was large and reached 1.3 m/s between Pine Point and Bay View mainly due to shallow water depth at the coast. Other locations with large wave orbital speed at the seabed included at the headlands and around the islands.

Similar with that during the peak of the April 2007 nor'easter, the tidal residual current (Figure 5.22d) was at least one order of magnitude lower than the averaged wind-driven and wave-induced currents. In the middle of the bay with smooth coastline, the tidal residual current was almost zero. The tidal residual current reached 0.05 m/s locally at the Scarborough River, Saco River and around islands due to the modification by local bathymetry.

The averaged wind-driven current (Figure 5.22e) was flowing southward along the coast at water depths less than 15.0 m. The magnitude of the averaged wind-driven current decreased gradually from 0.2 m/s at coast to 0.1 m/s at about 15.0 m water depth. Unlike the averaged wind-driven current pattern during the peak of the April 2007 nor'easter, no rotary wind-driven circulation was found adjacent to the north of the north jetty at Saco River mouth. The averaged wind-driven current reached its maximum of 0.3 m/s around Wood Island and Fletcher Neck.

The averaged wave-induced current is shown in Figure 5.22f. At most locations within water depth less than 30.0 m, the averaged wave-induced current was either larger or comparable to the averaged wind-driven current. The only exception was between Old Orchard Beach and Goosefare Brook when the water depth was less than 10.0 m, where the averaged wind-driven current was approximately

0.2 m/s and the averaged wave-induced current was less than 0.1 m/s. Both the magnitude and distribution of the averaged wave-induced current during the peak of the 1991 Perfect Storm resembled that of the April 2007 nor'easter. The averaged wave-induce current system was featured with the "double-gyre and offshore jet-shaped flow". It reached the maximum value of 1.0 m/s at the headlands and around the islands.

The averaged depth-averaged current is shown in Figure 5.22g. This presented a similar distribution pattern to the averaged wave-induced current. The enhancement of the averaged total depth-averaged current by the combined wind and wave effects was significant. The distribution of averaged sand transport flux during the peak of the 1991 Perfect Storm (Figure 5.22h) was similar to that of the April 2007 nor'easter, however, the maximum averaged sand transport flux was larger. Two locations with large averaged sand flux included 5.0-10.0 m water depth between Old Orchard Beach and Ocean Park and to the north of Eagle Island. Between Old Orchard Beach and Ocean Park, the averaged sand flux reached 0.0056 $m^3$/m.s. North of Eagle Island, the maximum averaged sand flux was 0.009 $m^3$/m.s. Between Ferry Beach and Camp Ellis, the averaged sand flux rotated counterclockwise and the magnitude reached 0.0015 $m^3$/m.s.

Figure 5.22. Averaged wind, waves, currents and sand flux over the two tidal cycles between 14:00UTC 10/30/1991 and 15:00UTC 10/31/1991 when the storm was at its peak. (a) Averaged wind, (b) Averaged significant wave height, (c) Averaged wave orbital speed at seabed, (d) Tidal residual current, (e) Averaged wind-driven current, (f) Averaged wave-induced current, (g) Averaged depth-averaged current, (h) Averaged sand flux.

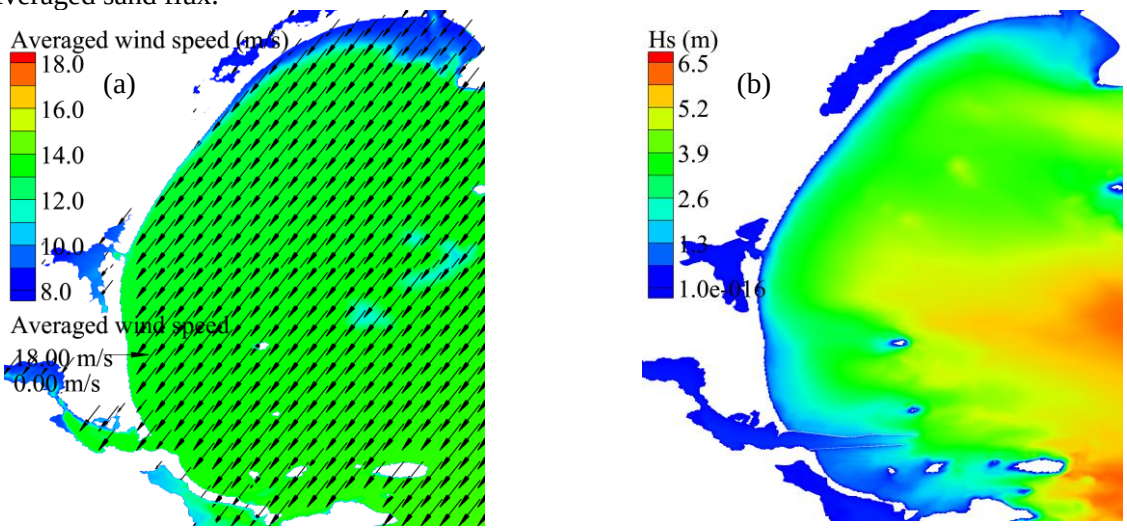

Figure 5.22 Continued

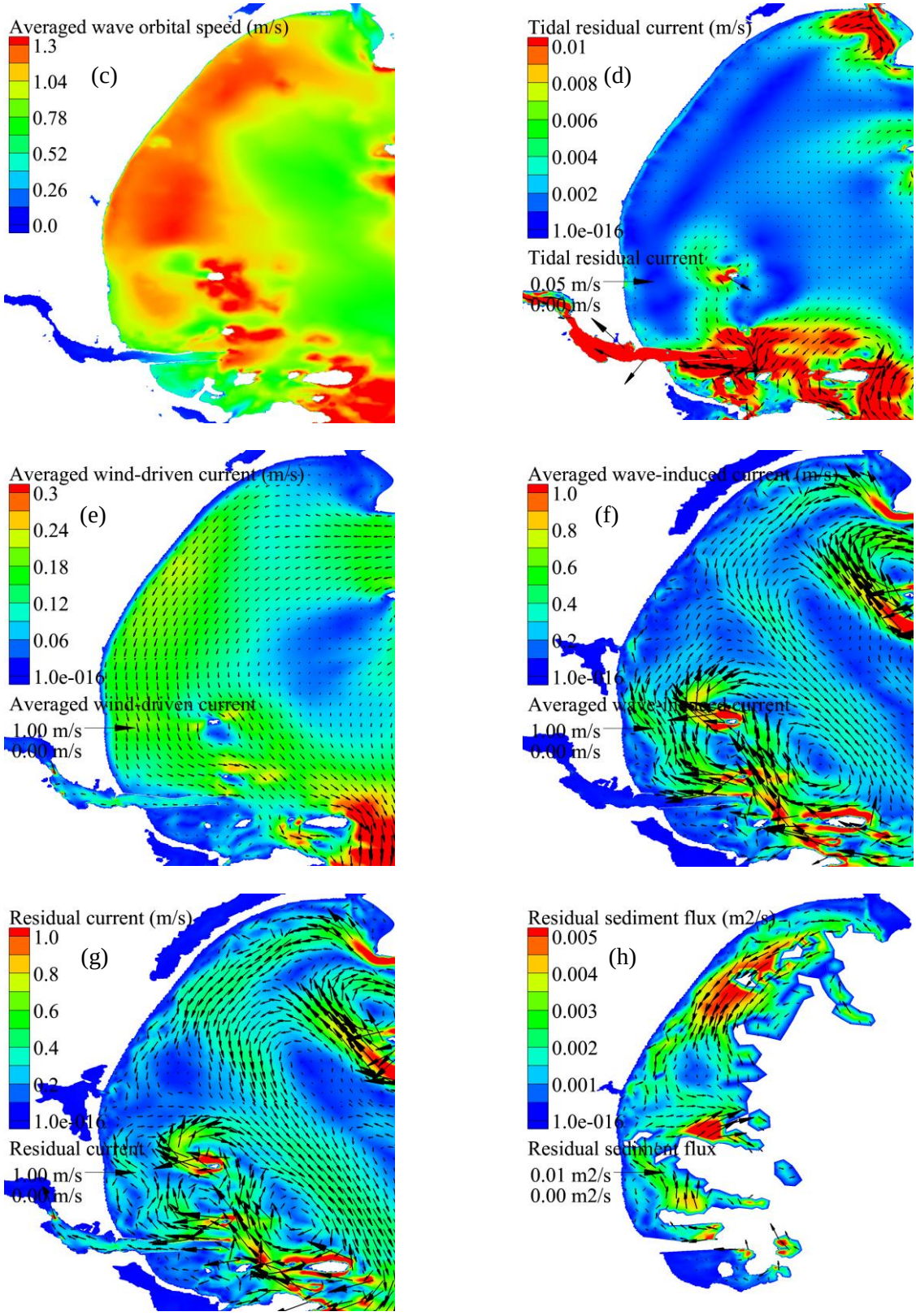

#### 5.6.2.3 January 2015 North American blizzard

The wind, waves, currents and sand transport rate were averaged over the two tidal cycles (6:00UTC 1/27/2015 to 7:00UTC 1/28/2015) containing the storm peak in Saco Bay during the January 2015 North American blizzard.

The averaged wind (Figure 5.23a) during the peak of the January 2015 North American Blizzard was the largest among the three storms within Saco Bay. The wind was from the north to northeast during the storm peak and reached 17.0 m/s throughout most of the bay. However, the averaged significant wave height (Figure 5.23b) was the smallest among the three storms. The dominant waves within the bay were mainly swells generated from offshore in the Gulf of Maine and propagated into the bay from east to southeast. At the offshore of Saco Bay, the averaged significant wave height was 5.0 m. While the peak significant wave height during the January 2015 North American blizzard was comparable to that of the 1991 Perfect Storm, the averaged wave height within the bay was smaller during the January 2015 North American blizzard, which was mainly related to the shorter duration of high winds generating large waves in the Gulf of Maine during the January 2015 North American blizzard. The averaged wave orbital speed at the seabed (Figure 5.23c) followed the same pattern as the other two storms, however the smaller wave height resulted in lower wave orbital speed at the seabed. The wave orbital speed reached its maximum at approximately 9.0 m water depth offshore of Goosefare Brook except at the headlands and around the islands.

The tidal residual current (Figure 5.23d) was small. The tidal residual current reached its maximum of 0.03 m/s in the inlets and around islands in the bay due to the modification by local bathymetry. The magnitude of tidal residual current was small compared to averaged wind-driven and wave-induced currents. The averaged wind driven current (Figure 5.23e) was large in the bay except in the lee of Prouts Neck. It flowed southward within the 25.0 m depth contour in general and the magnitude ranged from 0.1 m/s to 0.5 m/s. Between Old Orchard Beach and Ferry Beach, the averaged wind-driven current was larger than 0.25 m/s with water depth less than 10.0 m. The distribution of the averaged wave-induced current during the peak of the January 2015 North American blizzard (Figure 5.23f) was

similar to that of the two other storms. The averaged wave-induced current was smaller than the averaged wind-driven current from Pine Point to Bay View at water depth less than 15.0 m except around the islands. In the north end of the bay, the wave-induced current ranged between 0.2 m/s to 1.0 m/s between Prouts Neck and Pine Point due to the large wave radiation stress gradients caused by the abrupt change in significant wave height along the coast. A similar process occurred in the south of the bay, where the wave radiation stress gradients produced a large alongshore wave-induced current from Fletcher Neck into the bay. Two wave-induced gyre systems caused by the interaction between waves and bathymetry occurred within the bay. One was located around Bluff and Stratton Islands in the north end of the bay and the other formed between the north jetty at the Saco River mouth and Goosefare Brook. The two gyre systems resulted in an offshore jet-shaped flow. The averaged total depth-averaged current (Figure 5.23g) was the superposition of wind-driven component, wave-induced component and the interaction component among current, waves and bathymetry. Between Pine Point and Goosefare Brook, the wind-driven component was dominant at water depth less than 10.0 m. From Bay View to the north jetty at the Saco River mouth, the northward wave-induced current was partly offset by the non-uniform southward wind-driven current, resulting in counterclockwise total flow with a magnitude of 0.35 m/s. Three small clockwise gyres were presented further offshore adjacent to the counterclockwise gyre between Bay View and the north jetty at the Saco River mouth.

The averaged sand transport flux (Figure 5.23h) was smaller in magnitude than during the April 2007 nor'easter and 1991 Perfect Storm. By comparing the total current and wave field, it mainly resulted from smaller wave height during the peak of the January 2015 North American blizzard. The longshore southward averaged sand transport flux extended further south to Bay View before it turned eastward to the offshore. The maximum averaged sand transport flux of 0.005 $m^3$/m.s occurred adjacent to the north of Eagle Island. Between Bay View and the north jetty at the Saco River mouth, the counterclockwise averaged sand transport flux reached 0.0015 $m^3$/m.s.

Figure 5.23. Averaged wind, waves, currents and sand flux over the two tidal cycles between 06:00UTC 1/27/2015 and 07:00UTC 1/28/2015 when the storm was at its peak. (a) Averaged wind, (b) Averaged significant wave height, (c) Averaged wave orbital speed at seabed, (d) Tidal residual current, (e) Averaged wind-driven current, (f) Averaged wave-induced current, (g) Averaged depth-averaged current, (h) Averaged sand flux.

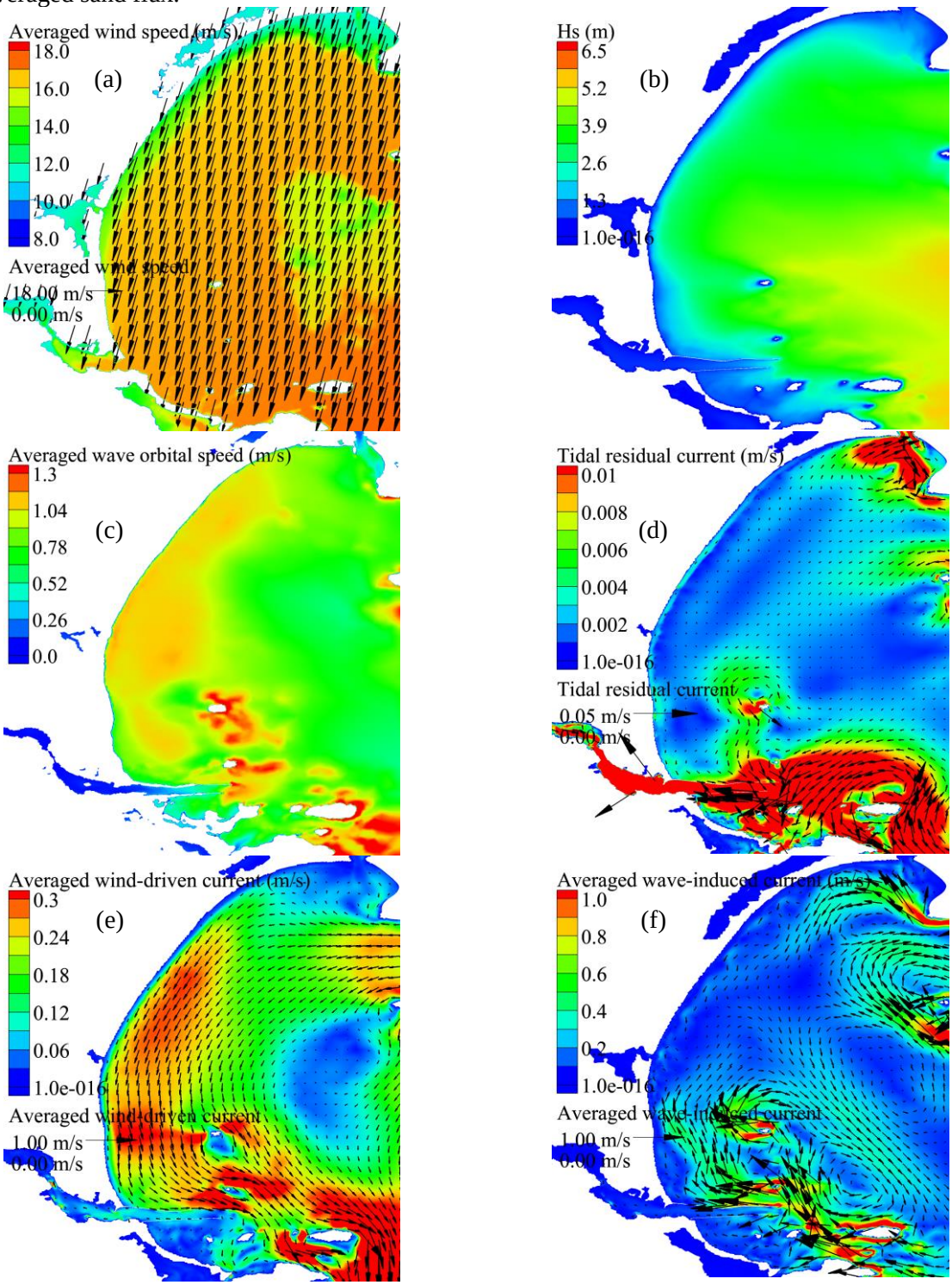

Figure 5.23 Continued

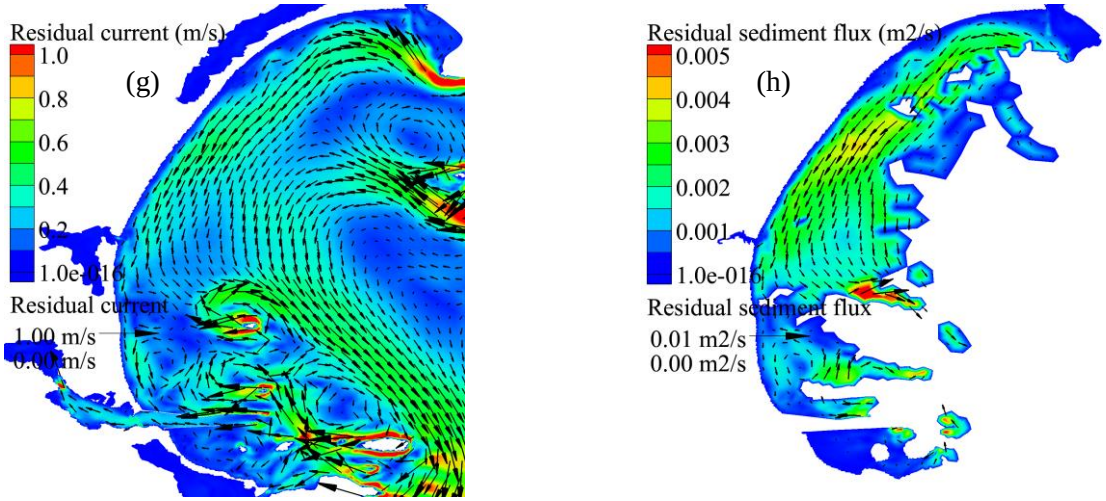


### 5.7 Hydrodynamics and sand transport during different storms

As discussed in Sections 5.5 and 5.6, the spatial and temporal patterns of waves, currents and sand transport presented both similarities and differences during the three storm events studied here. In this section, the detailed features of hydrodynamics and sand transport during the April 2007 nor'easter, the 1991 Perfect Storm and the January 2015 North American blizzard were compared and analyzed.

#### 5.7.1 Hydrodynamics features

Even though the three storms investigated in this study had different storm tracks and durations, the storm wind and waves approached Saco Bay from a similar angle. During the three storms, the waves and currents shared some common features in Saco Bay.

The tidal current in the bay was less than 0.05 m/s and was negligible relative to the wind-driven and wave-induced currents except at the Scarborough and Saco River mouths, where the tidal current reached 0.2 m/s due to the funneling effect.

The wind-driven current flowed southward because winds were blowing from north to east during all three storms. At straight coastlines with no cross-boundary flow, the simplified depth-integrated momentum equation can be applied to estimate the depth-averaged current (Pugh, 1996), where the magnitude of current is proportional to the square of wind speed and inversely proportional to water

depth. The wind-driven current along the coast was highest (0.4 m/s) at the peak of the January 2015 North American blizzard due to the high peak storm wind speed. It was moderate during the April 2007 nor'easter and 1991 Perfect Storm, which had lower peak storm wind speeds. The patterns and distributions of wind-driven current were also correlated with the wind direction relative to the coastline. A clockwise wind-driven circulation was formed between Bay View and the north jetty at the Saco River mouth at the peak of the April 2007 nor'easter, while no such pattern was predicted at the peak of the 1991 Perfect Storm or the January 2015 North American blizzard. The coastline of Saco Bay is concave-shaped, with the apex of the curve between Goosefare Brook and Bay View. During the April 2007 nor'easter, the wind was coming from the east at the storm peak, which resulted in southward wind and wind-driven current components to the north of Bay View and northward wind and wind-driven current components to the south. The clockwise wind-driven circulation merged with the southward wind-driven current from the north of the bay to achieve both mass conservation and momentum balance. In contrast, during the 1991 Perfect Storm and January 2015 North American blizzard, the winds were blowing from the northeast and north respectively, which resulted in consistent southward alongshore wind and wind-driven current components before they were blocked by the north jetty at the Saco River mouth causing the wind-driven current to veer eastward.

The wave-induced current presented strong interaction between waves and bathymetry. During the three storms, large waves propagated from the southeast into the bay. This was consistent with a previous study by Jensen (1983). Wave energy converged at the headlands at both ends of the bay and diverged along the concave-shaped coastline within the bay. Wave radiation stress gradients proportional to the square of wave height produced high mean flows from both ends into the bay due to the larger wave heights at the headlands and smaller wave heights within the bay. The pattern of wave-induced current was complicated by the interaction between waves and bathymetry in the bay. In the north of the bay, the presence of Bluff and Stratton Islands resulted in a clockwise wave-induced circulation around the islands. Part of the gyre was diverted to southwest when it circulated toward the coast. The southwest flow joined the alongshore wave-induced current originating from Prouts Neck and veered southeast. In

the south of the bay, the northward wave-induced current generated around Fletcher Neck was split into several branches by the islands and jetties at the Saco River mouth before they all joined the southeast flow from the north of the bay and formed a jet-shaped offshore current. At least two secondary clockwise wave-induced circulations were also formed in the south of the bay, with one around Eagle Island and the other to the north of Wood Island.

The total depth-averaged current was mainly composed of wind-driven current, wave-induced current and the interaction between currents, waves and bathymetry. The flow pattern and distribution of the total depth-averaged current mimicked that of the wave-induced current but presented local variability due to the presence of wind-driven and interaction components. A transition between the dominant driving mechanisms was predicted in the bay, in which the wind-driven current dominated between 5.0-10.0 m depth, and wave-induced current was more significant around headlands and islands and responsible for the circulation patterns within the bay during the three storms. The local variability of total depth-averaged circulation was mainly caused by the relative intensity of the wind-driven and wave-induced currents. At the peak of the April 2007 nor'easter, the wind-driven clockwise circulation was joined by the northward wave-induced current between Bay View and the north jetty at the Saco River mouth, resulting in northward total flow. The total depth-averaged flow patterns in the same region at the peak of the 1991 Perfect Storm and January 2015 North American blizzard were more complicated. At the peak of the 1991 Perfect Storm, a weak counterclockwise depth-averaged circulation was observed at water depth less than 5.0 m between Bay View and the north jetty at the Saco River mouth. With more intense wind-driven current at the peak of the January 2015 North American blizzard, the northward wave-induced current between Bay View and the north jetty at the Saco River mouth were cancelled out and a counterclockwise gyre with 0.3 m/s was predicted. The local variability of total depth-averaged current strongly influenced sand transport in this area.

The waves in Saco Bay were dominated by large swell waves generated in the Gulf of Maine. The swells approached the bay from the southeast during all the three storm events. Wave refraction redistributed wave energy within the bay and the wave direction gradually became perpendicular to the

depth contour lines. Wave energy was also dissipated by bottom friction and wave-induced breaking as waves approached the shoreline. The significant wave height was larger in the middle of the bay with greater water depth, and smaller to the north and south. While the significant wave height was larger at greater water depth, the wave orbital speed at the seabed was larger at water depth less than 15.0 m. As explained in Section 5.5, the wave orbital speed at seabed is related to both wave height and water depth. Since the wave orbital speed at the seabed increases linearly with wave height and decreases exponentially with water depth, it increases more quickly with decreasing water depth than with increasing wave height. The banded distribution of wave orbital speed at the seabed can thus be explained. The wave orbital speed first increased due to decreased water depth as waves propagated into the bay and then decreased as waves approached the coastline where significant wave height decreased due to depth-induced breaking. Large wave orbital speed at seabed was also observed around islands due to the abrupt change in water depth.

The pattern of averaged wind-driven current, wave-induced current and wave fields over tidal cycles resembled those at the storm peaks. The magnitude of the tidally averaged fields differed from those at the storm peaks mainly due to the storm duration and tidal modulation in the bay. During the April 2007 nor'easter, large waves and high storm surge persisted in Saco Bay for approximately one tidal cycle. While no strong tidal modulation on significant wave height, wave orbital speed, storm surge level and wind-driven current was observed, the wave-induced current fluctuated inversely with tidal level. The wave-induced current was largest around low tide and decreased with increasing tidal level. During the 1991 Perfect Storm and January 2015 North American blizzard, the storm durations were shorter, resulting in lower averaged currents and wave fields.

### 5.7.2 Sand transport features

The storm peak sand transport rates were highly correlated with the flow and wave fields and their associated bed shear-stresses. The distribution of the total load sand transport rate mimicked that of the depth-averaged current, indicating that the sand transport rate was strongly dependent on local bathymetry. The bed shear-stress is also a strong indicator of the capacity of sand transport associated

with a coastal environment. Beneath combined waves and currents, the distribution of bed shear-stress followed that of current-alone bed shear-stress, but the magnitude was enhanced by waves. The total load sand transport at the storm peaks closely followed the distribution of mean combined bed shear-stress.

At the peak of the April 2007 nor'easter in the northern part of the bay, total load sand transport went southward along the coast to Bay View while in the south, sand moved northward. The southward and northward flows merged between Bay View and Goosefare Brook and diverted offshore. Similar sand transport patterns were observed at the peak of the 1991 Perfect Storm and January 2015 North American blizzard to the north of Bay View, however local variability of sand transport occurred due to the distribution of total depth-averaged current. At the peak of the 1991 Perfect Storm, a weak counterclockwise sand transport was formed between Bay View and the north jetty at the Saco River mouth at water depth less than 5.0 m, which was responsible for bringing sand back to this area. Sand transport was insignificant at water depth less than 10.0 m to the south of Bay View during the January 2015 North American blizzard, which was mainly attributed to a failure to exceed the threshold velocity for the sand grain size used in the model beneath the combined waves and currents.

The tidally averaged sand transport flux resembled that at the storm peaks. In Saco Bay, the net sand transport was from southward alongshore between Pine Point and Bay View. Net offshore sand transport was identified at two locations during the April 2007 nor'easter and the 1991 Perfect Storm, (1) at approximately 10.0 m water depth offshore Between Old Orchard Beach and Ocean Park, and (2) at approximately 10.0 m water depth off Bay View. During the January 2015 North American blizzard, net sand transport was only observed at approximately 10.0 m offshore of Bay View. Between Bay View and the north jetty at the Saco River mouth, the net sand transport was different during the three storms. During the April 2007 nor'easter, net sand transport was northward at water depth larger than 5.0 m. Similar northward net sand transport occurred during the 1991 Perfect Storm, however, a counterclockwise net sand transport was observed at water depth less than 5.0 m between Bay View and the north jetty at the Saco River mouth. The counterclockwise net sand transport between Bay View and the north jetty at the Saco River mouth extended to 10.0 m water depth during the January 2015 North

American blizzard. Brothers et al. (2008) found that Saco Bay is not a closed system in terms of sand transport. Sand can bypass the headlands enclosing Saco Bay and escape from the nearshore. Also, downwelling happened at the coast during nor'easters, which results in a net sediment transport away from the beach. The sand transport pattern described by Brothers et al. (2008) was confirmed in this study.

The timing of the peak total load sand transport is dependent on the timing and relative magnitude of the wave orbital speed at seabed and the total depth-averaged current. During the April 2007 nor'easter, large total load sand transport persisted for approximately one tidal cycle, which was mainly due to the combined effect of total depth-averaged current and wave orbital speed at seabed. At least three combinations of depth-averaged current and wave orbital speed at seabed may result in large sand transport: (1) both moderately high depth-averaged current and wave orbital speed at seabed, (2) moderate depth-averaged current and high wave orbital speed at seabed, and (3) high depth-averaged current and moderate wave orbital speed at seabed. While large sand transport rates during the 1991 Perfect Storm and January 2015 North American blizzard did not last over one tidal cycle, the relative importance of total depth-averaged current and wave orbital speed at seabed is still true.

**5.8 Conclusions**

In this study, the fully coupled wave, tide-surge and circulation model SWAN+ADCIRC and the Soulsby-Van Rijn total load sediment transport were applied to investigate the hydrodynamics and sand transport during storms in Saco Bay, Maine. While the durations and tracks of the three storms investigated were different, the hydrodynamics and sand transport shared some common features. The large waves generated in the Gulf of Maine approached Saco Bay from the southeast during the three storms and were strongly affected by local bathymetry while propagating into the bay. Due to wave refraction, the significant wave height contours gradually became parallel to the depth contours. Wave energy was also dissipated by bottom friction and wave-induced breaking as waves propagated at shallow water depths. Unlike the wave height distribution, the wave orbital speed at the seabed was larger at the coast (water depth < 15.0 m) than offshore. While the wave orbital speed at the seabed increases linearly

with wave height, it decreases exponentially with water depth. In shallow water, the increase of wave orbital speed with decreasing water depth was greater than the decrease of wave orbital speed caused by decreasing wave height. The wave orbital speed reached 1.6 m/s at the coast and around islands with abrupt changes in bathymetry.

During all three storms, tidal current was dwarfed by the wind-driven and wave-induced currents except in the Scarborough River and Saco River mouths, where the approaching water was funneled into the river channels. The wind-driven current was strongly affected by the local winds, bathymetry and coastline geometry. In an idealized scenario with a straight coastline and constant water depth, the magnitude of wind-driven current is proportional to the square of wind speed and inversely proportional to the water depth when the equilibrium state is reached. Here, the direction of the wind relative to the coastline resulted in different patterns of wind-driven current. During the 1991 Perfect storm and January 2015 North American blizzard, the winds were from northeast and north respectively, resulting in southward alongshore wind components and thus southward wind-driven current along the whole concave-shaped coastline. However, during the April 2007 nor'easter, the wind was from the east and a southward alongshore wind component was obtained to the north of the apex of the coastline between Goosefare Brook and Bay View, while northward alongshore component to the south of the apex. This generated a clockwise wind-driven circulation between Bay View and the north jetty at the Saco River mouth.

The wave-induced current was the result of strong interactions between waves and bathymetry. From the bay scale, the wave-induced current was generated at both headlands enclosing the bay and flowed into the bay. The local pattern of wave-induced current was complicated by the presence of islands and coastal structures. In the north of the bay, a clockwise wave-induced circulation was generated around Bluff and Stratton Islands. In the south of the bay, the wave-induced current was northward alongshore before veering offshore. At least two secondary clockwise wave-induced gyres were formed between Goosefare Brook and the north jetty at the Saco River mouth. Due to the

convergence of wave-induced current from both ends of the bay, a jet-shaped offshore flow was formed in the middle of the bay.

The total depth-averaged current mimicked that of wave-induced current, however the magnitude varied with both wind and wave effect. At water depth less than 5.0-10.0 m, the wind-driven current was dominant, while wave induced current was more significant at headlands and around coastal structures and islands. The tidally averaged wind-driven current, wave-induced current and wave fields resembled those at storm peaks, however, the magnitude varied due to tidal modulation and storm duration.

Both the instantaneous sand transport at storm peaks and tidally averaged sand transport flux were correlated with waves and flow fields and the associated mean combined bed shear-stress. Beneath combined waves and current, the bed shear stress was enhanced nonlinearly in comparison with current alone and wave alone conditions. The total load sand transport followed the pattern of mean combined bed shear-stress and total depth-averaged current, however the flow field and sand transport may not be the same because the threshold velocity for the sand to move may not be exceeded beneath the combined waves and current. The movement of sand over time is dependent on the timing and relative magnitude of the total depth-averaged current and the wave orbital speed at seabed. The net sand transport was southward between Pine Point and Bay View during all three storms. To the south of Bay View, variability of net sand transport was observed during the three storms. A counterclockwise net sand transport was identified at water depths less than 10.0 m between Bay View and the north jetty at the Saco River mouth during the 1991 Perfect Storm and January 2015 North American blizzard, however no such pattern was observed during the April 2007 nor'easter. Net offshore sand transport occurred between Old Orchard Beach and Bay View at the convergence zone.

# CHAPTER 6

# CONCLUSIONS AND DISCUSSIONS

## 6.1 Contribution to knowledge

Both coastal flooding and sand transport rely on the accurate prediction of water level, waves, and currents at the coast, which can be achieved by (1) resolving bathymetry and coastline geometry with refined grid sizes at the coast; and (2) considering the interactions between tide-surge, current, waves and bathymetry through wave radiation stress and bottom friction. This work has demonstrated that the interactions between tide-surge, waves and bathymetry have a significant impact on coastal waves, circulation and water level in the Gulf of Maine; and the interactions exhibit strong temporal and spatial variability in response to storms along the coast. Wave-induced current has the same order of magnitude as wind-driven current during storms and varies with water level and local water depth. Wave height and period are modulated by water level and are affected by current refraction. The inclusion and appropriate representation of the interaction processes is thus important along coastlines with complex configurations, such as that of the coastline of the Gulf of Maine.

The integrated modeling system has been successfully applied to predict coastal flooding due to wave overtopping at seawalls in Scituate, Massachusetts, by validating the predicted wave overtopping volume with that of field measurements. The inclusion of interaction between tide-surge and waves improved the accuracy of wave overtopping prediction at the study site. The effect of sea level rise and seawall crest level on wave overtopping were investigated. The work has shown that a much larger elevation of seawall height than sea level rise will be required to cope with future storms as the sea level rises, mainly due to the development of larger waves approaching the coast. The integrated atmosphere-ocean-coast modeling framework can thus provide guidance for risk assessment and decision making as communities decide how to prepare and respond to change.

Sand transport and its response to different storm characteristics in an arcuate bay has been carried out using the integrated modeling system. Sand transport is closely linked with waves and currents. This work has shown that the waves, currents and sand transport in the bay share some common

features with different storm durations and tracks because of the dominant influence of local bathymetry on waves, currents and sand transport. Wind is the other important factor influencing hydrodynamics and sediment transport. The direction of wind relative to the coastline results in different patterns of wind-driven current. The wave-induced current demonstrates strong interactions between waves and bathymetry. Generated at both headlands, the wave-induced current flows into the bay and its local pattern is complicated by the presence of islands and coastal structures. A jet-shaped offshore wave-induced current is formed due to the convergence of flow from both ends of the arcuate bay. The role of wind-driven and wave-induced current for sand transport varies depending on water depth and coastline geometry. The wind-driven current dominates in shallow water, while the wave-induced current contributes more at headlands and around coastal structures and islands. Both the instantaneous sand transport at storm peaks and tidally averaged sand transport flux were correlated with waves and flow fields. The sand transport follows the pattern of mean combined bed shear-stress and depth-averaged current; however, the flow field and sand transport may not be the same since the threshold velocity for moving the sand may not be exceeded beneath the combined waves and current. The difference in net sand transport during nor'easters mainly results from different flow patterns due to the counterbalance between wind-driven and wave-induced current.

**6.2 Conclusions**

Coastal resources management relies on the accurate description of coastal hydrodynamics, geomorphological and ecological processes. Numerical modeling provides an efficient and effective tool to investigate and understand these processes. Integrated modeling systems which resolve physical processes with varied spatial and temporal scales are now the state-of-the-art method to help facilitate coastal resilience and adaption in a changing climate.

In this study, an integrated atmosphere-ocean-coast modeling system that links physical processes ranging from open ocean to surf zone scales has been developed for the Gulf of Maine to investigate coastal hydrodynamics, flooding due to wave overtopping, and sand transport during severe storms. The modeling system includes a hydrodynamic model, a wave overtopping model and a sediment transport

model. The modeling system allows a comprehensive understanding of coastal processes by including: (1) the interaction between tide-surge, waves and bathymetry, (2) coastal flooding due to wave overtopping at seawalls, and (3) sand transport in response to different storm characteristics. The modeling system can be applied to provide guidance to steer important decisions and investment, such as: (1) to gain an insight on the potential change in coastal processes, e.g. the frequency and intensity of coastal flooding, beach erosion and accretion in a changing climate; (2) to help with aquaculture siting and (3) to help with future coastal resilience and adaptation.

### 6.3 Future work

Although the current work has developed a useful integrated modeling system and applied it to investigate coastal hydrodynamics, coastal flooding due to wave overtopping, and sand transport in the Gulf of Maine, further work can be done to either improve and generalize the modeling system and to advance the understanding of coastal processes in greater detail in other locations along the coast.

The presence of surface waves modifies the roughness length on the ocean surface, which may affect the generation of storm surge. It is thus important that the effect of wind-generated surface waves be parameterized in the hydrodynamic model for more accurate storm surge prediction. Also, even though empirical formulas for wave overtopping are used in the current work due to their robustness and computational efficiency, they are tested with limited field and experimental data, and are only valid with certain structure configurations. Numerical models like RANS-VOF model are more sophisticated and can incorporate the effects of complex shoreline geometry. In the future, the RANS-VOF model should be linked with the coastal hydrodynamic model to generalize the application of the integrated modeling system for coastal flooding prediction due to wave overtopping. Thirdly, the modelling system in this work simulates total load transport using an empirical sediment transport formula, which assumes an equilibrium state for sediment concentration in the water column and may overestimate the sediment transport flux. The formula also only calculates longshore sediment transport without considering cross-shore transport due to wave effects, which is important for beach erosion during storms. In the future, the suspended sediment transport and bedload transport can be simulated individually with different

algorithms, e.g. the suspended sediment transport can be computed with the advection-diffusion algorithm for passive tracer, and bedload transport can be achieved by resolving the bottom boundary layer with the coexistence of waves and current. Morphological change due to sediment redistribution would have to be incorporated for the long-term prediction of the change of coastlines. Long-term sand transport in the Saco Bay can be simulated to investigate the sand transport pathways and predict long-term coastline change. Last but not the least, field measurements of sediment characteristics need to be carried out to better represent the spatial distribution of sediment, which will provide more detailed information on the sediment grain sizes as a model input. Field measurements of sand transport will also be required for model validation purpose.

## BIBLIOGRAPHY


Amante, C., Eakins, B. W., 2009. ETOPO1 1 arc-minute globe relief model: Procedures, data sources and analysis, NOAA Tech. Memo. NESDIS NGDC-24, 19 pp.

Ardhuin, F., Rascle, N., Belibassakis, K. A., 2008. Explicit wave-averaged primitive equations using a generalized Lagrangian mean. Ocean Modelling, 20(1): 35-60.

Ardhuin, F., Roland, A., Dumas, F., Bennis, A. C., Sentchev, A., Forget, P., Wolf, J., Girard, F., Osuna, P., Benoit, M., 2012. Numerical wave modeling in conditions with strong currents: Dissipation, refraction, and relative wind. Journal of Physical Oceanography, 42(12), 2101-2120.

Bates, P. D., Dawson, R. J., Hall, J. W., Horritt, M. S., Nicholls, R. J., Wicks, J., Hassan, M. A. A. M., 2005. Simplified two-dimensional numerical modelling of coastal flooding and example applications. Coastal Engineering, 52(9), 793-810.

Barber, D.C. 1995. Holocene evolution and modern sand budget of inner Saco Bay, Maine. MS thesis, University of Maine, Orono, Maine. 178 pp.

Battjes, J. A., Stive, M. J. F., 1985. Calibration and verification of a dissipation model for random breaking waves, Journal of Geophysical Research: Oceans, 90(C5), 9159-9167.

Beardsley, R.C., Chen, C.S., Xu, Q.C., 2013. Coastal flooding in Scituate (MA): A FVCOM study of the Dec. 27, 2010 Nor'easter. Journal of Geophysical Research: Oceans, 118(11), 6030-6045.

Bennis, A. C., Ardhuin, F., Dumas, F., 2011. On the coupling of wave and three-dimensional circulation models: choice of theoretical framework, practical implementation and adiabatic tests. Ocean Modelling, 40(3): 260-272.

Bernier, N.B., Thompson, K.R., 2007. Tide-surge interaction of the east coast of Canada and northeastern United States. Journal of Geophysical Research: Oceans, 112(C6), C06008.

Bertin, X., Bruneau, N., Breilh, J. F., Fortunato, A. B., Karpytchev, M., 2012. Importance of wave age and resonance in storm surges: The case Xynthia, Bay of Biscay. Ocean Modelling, 42, 16-30.

Bertin, X., Fortunato, A. B., Oliveira, A., 2009. A modeling-based analysis of processes driving wave-dominated inlets. Continental Shelf Research, 29(5-6), 819-834.

Blain, C. A., Westerink, J. J., Luettich, R. A., 1994. The influence of domain size on the response characteristics of a hurricane storm surge model. Journal of Geophysical Research: Oceans, 99(C9), 18467-18479.

Bolaños, R., Brown, J. M., Souza, A. J., 2014. Wave-current interactions in a tide dominated estuary. Continental Shelf Research, 87: 109-123.

Booij, N., Ris, R. C., Holthuijsen, L. H., 1999. A third-generation wave model for coastal regions. Part 1, Model description and validation. Journal Geophysical Research: Oceans, 104(C4), 7649-7666.

Bowen, A. J., 1969. Rip currents: 1. Theoretical investigations. Journal of Geophysical Research, 74(23), 5467-5478.

Brothers, L. L., Belknap, D. F., Kelley, J. T., Janzen, C. D. (2008). Sediment transport and dispersion in a cool-temperate estuary and embayment, Saco River estuary, Maine, USA. Marine Geology, 251(3-4), 183-194.

Brown, J. M., Wolf, J., 2009. Coupled wave and surge modelling for the eastern Irish Sea and implications for model wind-stress. Continental Shelf Research, 29(10): 1329-1342.

Brown, J. M., Bolaños, R., Wolf, J., 2013. The depth-varying response of coastal circulation and water levels to 2D radiation stress when applied in a coupled wave-tide-surge modelling system during an extreme storm. Coastal Engineering, 82: 102-113.

Bunya, S., Dietrich, J. C., Westerink, J. J., Ebersole, B. A., Smith, J. M., Atkinson, J. H., Jensen, R., Resio, D. T., Luettich, R. A. Jr, Dawson, C., Cardone, V. J., Cox, A. T., Powell, M. D., Westerink, H. J., Roberts, H. J., 2010. A high-resolution coupled riverine flow, tide, wind, wind wave, and storm surge model for southern Louisiana and Mississippi. Part I: Model development and validation. Monthly Weather Review, 138(2): 345-377.

Cavaleri, L., Alves, J. H., Ardhuin, F., Babanin, A., Banner, M., Belibassakis, K., Benoit, M., Donelan, M., Groeneweg, J., Herbers, T.H.C., Hwang, P., Janssen, P.A.E.M., Janssen, T., Lavrenov, I. V., Magne, R., Monbaliu, J., Onorato, M., Polnikov, V., Resio, D., Rogers, W. E., Sheremet, A., McKee Smith, J., Tolman, H. L., van Vledder, G., Wolf, J., Young, I., 2007. Wave modelling-the state of the art. Progress in Oceanography, 75(4), 603-674.

Charnock, H., 1955. Wind stress on a water surface. Quarterly Journal of the Royal Meteorological Society, 81(350): 639-640.

Chen, C., Beardsley, R. C., Luettich, R. A., Westerink, J. J., Wang, H., Perrie, W., Xu, Q., Donahue, A. S., Qi, J., Lin, H., Zhao, L, Kerr, P. C., Meng, Y., Toulany, B., 2013. Extratropical storm inundation testbed: Intermodel comparisons in Scituate, Massachusetts. Journal of Geophysical Research: Oceans, 118(10), 5054-5073.

Chen, J. L., Hsu, T. J., Shi, F., Raubenheimer, B., Elgar, S., 2015. Hydrodynamic and sediment transport modeling of New River Inlet (NC) under the interaction of tides and waves. Journal of Geophysical Research: Oceans, 120(6), 4028-4047.

Chen, Q., Kirby, J. T., Dalrymple, R. A., Kennedy, A. B., Chawla, A., 2000. Boussinesq modeling of wave transformation, breaking, and runup. II: 2D. J. Waterw. Journal of Waterway, Port, Coastal, and Ocean Engineering, 126(1), 48-56.

Chen, Q., Wang, L., Tawes, R., 2008. Hydrodynamic response of northeastern Gulf of Mexico to hurricanes. Estuaries and Coasts, 31(6): 1098-1116.

Christoffersen, J. B., Jonsson, I. G., 1985. Bed friction and dissipation in a combined current and wave motion. Ocean Engineering, 12(5): 387-423.

Church, J. A., Clark, P. U., Cazenave, A., Gregory, J. M., Jevrejeva, S., Levermann, A., Merrifield, M. A., Milne, G. A., Nerem, R. S., Nunn, P. D., Payne, A. J., Pfeffer, W. T., Stammer, D., Unnikrishnan, A. S., 2013. Sea level change. In: Stocker, T. F., Qin, D., Plattner, G.-K., Tignor, M., Allen, S. K., Boschung, J., Nauels, A., Xia, Y., Bex, V., Midgley, P.M. (Eds.), Climate Change 2013: The Physical Science Basis, Contribution of Working Group I to the Fifth Assessment Report of the Intergovernmental

Panel on Climate Change. Cambridge University Press, Cambridge, UK, New York, NY, USA, pp. 1137-1216.

Craig, P. D., Banner, M. L., 1994. Modeling wave-enhanced turbulence in the ocean surface layer. Journal of Physical Oceanography, 24(12): 2546-2559.

Dalrymple, R. A., Rogers, B. D., 2006. Numerical modeling of water waves with the SPH method. Coastal Engineering, 53(2), 141-147.

Davis, R.E., Dolan, R., 1993. Nor'easters. American Scientist, 81(5) 428-439.

Davies, A. G., Soulsby, R. L., & King, H. L. (1988). A numerical model of the combined wave and current bottom boundary layer. Journal of Geophysical Research: Oceans, 93(C1), 491-508.

Davies, A. M., Lawrence, J. (1995). Modeling the effect of wave-current interaction on the three-dimensional wind-driven circulation of the Eastern Irish Sea. Journal of Physical Oceanography, 25(1), 29-45.

Dawson, C., Westerink, J. J., Feyen, J. C., Pothina, D., 2006. Continuous, discontinuous and coupled discontinuous-continuous Galerkin finite element methods for the shallow water equations. International Journal for Numerical Methods in Fluids, 52(1), 63-88.

Dean, R. G., Dalrymple, R. A., 1984. Water Wave Mechanics for Engineers and Scientists. Prentice-Hall, Englewood Cliffs, NJ. 353 pp.

Dietrich, J. C., Zijlema, M., Westerink, J. J., Holthuijsen, L. H., Dawson, C., Luettich, R. A., Jensen, R. E., Smith, J. M., Stelling, G. S., Stone, G. W., 2011. Modeling hurricane waves and storm surge using integrally-coupled, scalable computations. Coastal Engineering, 58(1), 45-65.

Dietrich, J. C., Tanaka, S., Westerink, J. J., Dawson, C. N., Luettich, R. A., Zijlema, M., Hol-thuijsen, J. M., esterink, L. G., Westerink, H. J., 2012. Performance of the unstructured-mesh, SWAN+ ADCIRC model in computing hurricane waves and surge. J. Sci. Com-put. 52(2), 468-497.

Dietrich, J. C., Bunya, S., Westerink, J. J., Ebersole, B. A., Smith, J. M., Atkinson, J. H., Jensen, R., Resio, D. T., Luettich, R. A. Jr, Dawson, C., Cardone, V. J., Cox, A. T., Powell, M. D., Westerink, H. J., Roberts, H. J., 2010. A high-resolution coupled riverine flow, tide, wind, wind wave, and storm surge model for southern Louisiana and Mississippi. Part II: Synoptic description and analysis of Hurricanes Katrina and Rita. Monthly Weather Review, 138(2), 378-404.

Dodet, G., Bertin, X., Bruneau, N., Fortunato, A. B., Nahon, A., Roland, A., 2013. Wave-current interactions in a wave-dominated tidal inlet. Journal of Geophysical Research: Oceans, 118(3), 1587-1605.

Douglas, E. M., Fairbank, C., 2010. Is precipitation in northern New England becoming more extreme? Statistical analysis of extreme rainfiall in Massachusetts, New Hampshire, and Maine and updated estimates of the 100-year storm. Journal of Hydrologic Engineering, 16(3), 203-217.

Donelan, M. A., Dobson, F. W., Smith, S. D., Anderson, R. J., 1993. On the dependence of sea surface roughness on wave development. Journal of Physical Oceanography, 23(9), 2143-2149.

Drennan, W. M., Graber, H. C., Hauser, D., Quentin, C., 2003. On the wave age dependence of wind stress over pure wind seas. Journal of Geophysical Research: Oceans, 108, 8062.

Du, Y., Pan, S., Chen, Y., 2010. Modelling the effect of wave overtopping on nearshore hydrodynamics and morphodynamics around shore-parallel breakwaters. Coastal Engineering, 57(9), 812-826.

Egbert, G. D., Bennett, A. F., Foreman, M. G., 1994. TOPEX/POSEIDON tides estimated using a global inverse model. Journal of Geophysical Research: Oceans, 24, 821-852.

Egbert, G. D., Erofeeva, S.Y., 2002. Efficient inverse modeling of barotropic ocean tides. Journal of Atmospheric and Oceanic Technology, 19(2), 183-204.

Elias, E. P. L., Cleveringa, J., Buijsman, M. C., Roelvink, J. A., & Stive, M. J. F. (2006). Field and model data analysis of sand transport patterns in Texel Tidal inlet (the Netherlands). Coastal Engineering, 53(5-6), 505-529.

Emanuel, K. A., 2013. Downscaling CMIP5 climate models shows increased tropical cyclone activity over the 21st century. Proc. Natl. Acad. Sci. U.S.A. 110(30), 12219-12224.Garratt, J. R., 1977. Review of drag coefficients over oceans and continents. Monthly Weather Review, 105(7): 915-929.

Farrell, S.C., 1972. Present coastal processes, recorded changes, and the post-Pleistocene geologic record of Saco Bay, Maine. PhD dissertation, University of Massachusetts, Amherst, MA. 296 pp.

FitzGerald, D. M., Buynevich, I. V., Davis Jr, R. A., Fenster, M. S. (2002). New England tidal inlets with special reference to riverine-associated inlet systems. Geomorphology, 48(1-3), 179-208.

Fredsøe, J. (1984). Turbulent boundary layer in wave-current motion. Journal of Hydraulic Engineering, 110(8), 1103-1120.

Fry, B., 1988. Food web structure on Georges Bank from stable C, N, and S isotopic compositions. Limnology and Oceanography, 33(5): 1182-1190.

Gallien, T. W., Sanders, B. F., Flick, R. E., 2014. Urban coastal flood prediction: Integrating wave overtopping, flood defenses and drainage. Coastal Engineering, 91, 18-28.

Gallien, T. W., 2016. Validated coastal flood modeling at Imperial Beach, California: Comparing total water level, empirical and numerical overtopping methodologies. Coastal Engineering, 111, 95-104.

Garratt, J. R., 1977. Review of drag coefficients over oceans and continents. Monthly Weather Review, 105(7), 915-929.

Goda, Y., 1975. Irregular wave deformation in the surf zone. Coastal Engineering, Japan, 18, 13-26.

Goda, Y., 2009. A performance test of nearshore wave height prediction with CLASH datasets. Coastal Engineering, 56(3), 220-229.

Grant, W. D., Madsen, O. S., 1979. Combined wave and current interaction with a rough bottom. Journal of Geophysical Research: Oceans, 84(C4), 1797-1808.

Grant, W. D., Williams III, A. J., Glenn, S. M., 1984. Bottom stress estimates and their prediction on the northern California continental shelf during CODE-1: the importance of wave-current interaction. Journal of Physical Oceanography, 14(3), 506-527.

Greenberg, D. A., 1983. Modelling the mean barotropic circulation in the Bay of Fundy and Gulf of Maine. Journal of Physical Oceanography, 13(5): 886-904.

Hagen, S., Westerink, J., Kolar, R., Horstmann, O., 2001. Two-dimensional, unstructured mesh generation for tidal models. International Journal for Numerical Methods in Fluids, 35(6), 669-686.

Hasselmann, K., Barnett, T. P., Bouws. E., Carlson, H., Cartwright, D. E., Enke, K., Ewing, J. A., Gienapp, H., Hasselmann, D. E., Kruseman, P., Meerburg, A., Müller, P., Olbers, D. J., Richter, K., Sell, W., Walden, H.,1973. Measurements of wind-wave growth and swell decay during the Joint North Sea Wave Project (JONSWAP). Dtsch. Hydrogr. Z. Suppl., 8A (12), 95 pp.

Haus, B. K., 2007. Surface current effects on the fetch-limited growth of wave energy. Journal of Geophysical Research: Oceans, 112: C03003.

Hedges, T.S., Reis,M.T., 1998. Randomwave overtopping of simple seawalls a new regression model. Proceedings of the Institution of Civil Engineers. Water, maritime and energy, 157, 113-122.

Heidemann, H. K., 2014, Lidar base specification version 1.2 (November 2014), Chapter 4 of Section B, U.S. Geological Survey Standards, Book 11, Collection and Delineation of Spatial Data. U.S. Geological Survey Techniques and Methods, 67 pp. Available online at http://pubs.usgs.gov/tm/11b4/.

Hench, J. L., Luettich Jr, R. A. (2003). Transient tidal circulation and momentum balances at a shallow inlet. Journal of Physical Oceanography, 33(4), 913-932.

Henderson, F.M., 1966. Open channel flow. Macmillan Publ. Co., New York, N.Y., 522 pp.

Higuera, P., Lara, J. L., Losada, I. J., 2013. Simulating coastal engineering processes with OpenFOAM®. Coastal Engineering, 71, 119-134.

Hill, H. W., Kelley, J. T., Belknap, D. F., Dickson, S. M., 2004. The effects of storms and storm-generated currents on sand beaches in Southern Maine, USA. Marine Geology, 210(1-4), 149-168.

Holthuijsen, L. H. (2010). Waves in oceanic and coastal waters. Cambridge university press.

Hsu, J. R., Benedet, L., Klein, A. H., Raabe, A. L., Tsai, C. P., Hsu, T. W. (2008). Appreciation of static bay beach concept for coastal management and protection. Journal of Coastal Research, 198-215.

Hu, K., Ding, P., Wang, Z., Yang, S. (2009). A 2D/3D hydrodynamic and sediment transport model for the Yangtze Estuary, China. Journal of Marine Systems, 77(1-2), 114-136.

Hu, K., Mingham, C. G., Causon, D. M., 2000. Numerical simulation of wave overtopping of coastal structures using the non-linear shallow water equations. Coastal Engineering, 41(4), 433-465.

Janssen, P. A., 1989. Wave-induced stress and the drag of air flow over sea waves. Journal of Physical Oceanography, 19(6): 745-754.

Janssen, P.A.E.M., 1991. Quasi-linear theory of wind-wave generation applied to wave forecasting. Journal of Physical Oceanography, 21(11), 1631-1642.

Jenkins, A. D., 1986. A theory for steady and variable wind-and wave-induced currents. Journal of Physical Oceanography, 16(8): 1370-1377.

Jenkins, A. D., 1987a. Wind and wave induced currents in a rotating sea with depth-varying eddy viscosity. Journal of Physical Oceanography, 17(7): 938-951.

Jenkins, A. D., 1987b. A Lagrangian model for wind-and wave-induced near-surface currents. Coastal Engineering, 11(5): 513-526.

Jenkins, A. D., 1989. The use of a wave prediction model for driving a near-surface current model. Deutsche Hydrografische Zeitschrift, 42(3-6): 133-149.

Jensen, R. E., 1983. Atlantic Coast Hindcast, Shallow-Water, Significant Wave. WIS Report 9: Vicksburg, MS. 711 pp.

Johnson, H. K., Højstrup, J., Vested, H. J., Larsen, S. E., 1998. On the dependence of sea surface roughness on wind waves. Journal of Physical Oceanography, 28(9): 1702-1716.

Kelley, J. T., Barber, D. C., Belknap, D. F., FitzGerald, D. M., van Heteren, S., Dickson, S. M., 2005. Sand budgets at geological, historical and contemporary time scales for a developed beach system, Saco Bay, Maine, USA. Marine Geology, 214(1): 117-142.

Kelley, J. T., Barber, D. C., Belknap, D. F., FitzGerald, D. M., van Heteren, S., Dickson, S. M. (2005). Sand budgets at geological, historical and contemporary time scales for a developed beach system, Saco Bay, Maine, USA. Marine Geology, 214(1-3), 117-142.

Kennedy, A. B., Chen, Q., Kirby, J. T., Dalrymple, R. A., 2000. Boussinesq modeling of wave transformation, breaking, and runup. I: 1D. J. Waterw. Journal of Waterway, Port, Coastal, and Ocean Engineering, 126(1), 39-47.

Kirshen, P., Watson, C., Douglas, E., Gontz, A., Lee, J., Tian, Y., 2008. Coastal flooding in the Northeastern United States due to climate change. Mitigation and Adaptation Strategies for Global Change, 13(5-6), 437-451.

Komen, G. J., Cavaleri, L., Donelan, M., Hasselmann, K., Hasselmann, S., Janssen, P.A.E.M., 1994. Dynamics and modelling of ocean waves. Cambridge University Press, Cambridge. 532 pp.

Lara, J. L., Garcia, N., Losada, I. J., 2006. RANS modelling applied to random wave interaction with submerged permeable structures. Coastal Engineering, 53(5), 395-417.

Li, M. Z., Wu, Y., Han, G., Prescott, R. H., Tang, C. C. (2017). A modeling study of the impact of major storms on seabed shear stress and sediment transport on the Grand Banks of Newfoundland. Journal of Geophysical Research: Oceans, 122(5), 4183-4216.

Li, M. Z., Hannah, C. G., Perrie, W. A., Tang, C. C., Prescott, R. H., & Greenberg, D. A. (2015). Modelling seabed shear stress, sediment mobility, and sediment transport in the Bay of Fundy. Canadian Journal of Earth Sciences, 52(9), 757-775.

Lim, E., Taylor, L.A., Eakins, B.W., Carignan, K.S., Warnken, R. R., Medley, P. R., 2009. Digital elevation model of Portland, Maine: Procedures, data sources and analysis. National Oceanic and Atmospheric Administration Technical Memorandum NESDIS NGDC-30, U.S. 29 pp.

Lin, P., Liu, P. L. F., 1998. A numerical study of breaking waves in the surf zone. Journal of Fluid Mechanics, 359(1), 239-264.

Longuet-Higgins, M. S., 1970. Longshore currents generated by obliquely incident sea waves: 1. Journal of Geophysical Research, 75(33), 6778-6789.

Longuet-Higgins, M. S., Stewart, R. W., 1961. The changes in amplitude of short gravity waves on steady non-uniform currents. Journal of Fluid Mechanics, 10: 529-549.

Longuet-Higgins, M. S., Stewart, R. W., 1962. Radiation stress and mass transport in gravity waves, with application to 'surf beats'. Journal of Fluid Mechanics, 13(04), 481-504.

Longuet-Higgins M. S., Stewart, R. W., 1964. Radiation stresses in water waves; a physical discussion, with applications. Deep-Sea Research, 11(4): 529-562.

Losada, I. J., Lara, J. L., Guanche, R., Gonzalez-Ondina, J. M., 2008. Numerical analysis of wave overtopping of rubble mound breakwaters. Coastal Engineering, 55(1), 47-62.

Luettich, R. A. Jr, Westerink, J. J., Scheffner, N. W., 1992. ADCIRC: an advanced three-dimensional circulation model for shelves, coasts and estuaries. Report 1. Theory and methodology of ADCIRC-2DDI and ADCIRC-3DL. U.S. Army Corps of Engineers Technical Report DRP-92-6. http://oai.dtic.mil/oai/oai?verb=getRecord&metadataPrefix=html&identifier=ADA261608

Luettich, R. A. Jr, Hu, S., Westerink, J. J., 1994. Development of the direct stress solution technique for three-dimensional hydrodynamic models using finite elements. International Journal for Numerical Methods in Fluids, 19(4): 295-319.

Luettich, R. A., Westerink, J. J., 2004. Formulation and numerical implementation of the 2D/3D ADCIRC finite element model version 44.XX. 74 pp. Available online at http:// adcirc.org/adcirc_theory_2004_12_08.pdf.

Luettich, R. A. Jr, Westerink, J. J., 2006. ADCIRC: A (parallel) advanced circulation model for oceanic, coastal and estuarine waters; users manual for version 51. http://adcirc.org/home/documentation/users-manual-v51

Lynett, P. J., Melby, J. A., Kim, D. H., 2010. An application of Boussinesq modeling to Hurricane wave overtopping and inundation. Ocean Engineering, 37(1), 135-153.

Marrone, J. F., 2008. Evaluation of impacts of the Patriots' Day storm (April 15-18, 2007) on the New England coastline. Solutions to Coastal Disasters: 507-517.

Marsooli, R., Orton, P. M., Mellor, G., Georgas, N., Blumberg, A. F. (2017). A coupled circulation-wave model for numerical simulation of storm tides and waves. Journal of Atmospheric and Oceanic Technology, 34(7), 1449-1467.

McCabe, M. V., Stansby, P. K., Apsley, D. D., 2013. Random wave runup and overtopping a steep sea wall: Shallow-water and Boussinesq modelling with generalised breaking and wall impact algorithms validated against laboratory and field measurements. Coastal Engineering, 74, 33-49.

Massachusetts Office of Coastal Zone Management (MACZM), 2013a. Mapping and analysis of privately-owned coastal structures along the Massachusetts shoreline. 76 pp. Available online at http://www.mass.gov/eea/docs/czm/stormsmart/seawalls/private-coastal-structures-2013.pdf.

Massachusetts Department of Conservation and Recreation (MADCR), 2009. Massachusetts coastal infrastructure inventory and assessment project. 76 pp. Available online at http://www.mass.gov/eea/docs/czm/stormsmart/seawalls/public-inventory-report-2009.pdf.

Massachusetts Office of Coastal Zone Management (MACZM), 2013b. Sea level rise: understanding and applying trends and future scenarios for analysis and planning. 22 pp. Available online at http://www.mass.gov/eea/docs/czm/stormsmart/slr-guidance-2013.pdf.

Massachusetts Office of Coastal Zone Management (MACZM), 2016. Coastal erosion, sediment transport, and prioritation management strategy assessment for shoreline protection: Scituate, Massachusetts. 199 pp. Available online at https://www.scituatema.gov/sites/scituatema/files/file/file/scituateprioritization_finalreport_august2016_compress_main.pdf.

Mellor, G., 2005. Some consequences of the three-dimensional current and surface wave equations. Journal of Physical Oceanography, 35(11): 2291-2298.

Mellor, G., 2008. The depth-dependent current and wave interaction equations: a revision. Journal of Physical Oceanography, 38(11): 2587-2596.

Mesinger, F., DiMego, G., Kalnay, E., Mitchell, K., Shafran, P. C., Ebisuzaki, W., Jovic, D., Woollen, J., Rogers., E., Berbery, E., Ek, M. B., 2006. North American regional reanalysis. Bulletin of the American Meteorological Society, 87(3), 343-360.

Moon IJ, Hara T, Ginis I, Belcher SE, Tolman HL (2004a) Effect of surface waves on air-sea momentum exchange. Part I: Effect of mature and growing seas. J Atmos Sci 61(19): 2321-2333.

Moon IJ, Ginis I, Hara T (2004b) Effect of surface waves on air-sea momentum exchange. Part II: Behavior of drag coefficient under tropical cyclones. J Atmos Sci 61(19): 2334-2348.

Mukai AY, Westerink JJ, Luettich RA Jr, Mark D (2001) Eastcoast2001, a tidal constituent database for the Western North Atlantic Ocean, Gulf of Mexico and Caribbean Sea. Technical Report ERDC/CHL TR-02-24, U.S. Army Corps of Engineers. http://oai.dtic.mil/oai/oai?verb=getRecord&metadataPrefix=html&identifier=ADA408733

Mulligan, R. P., Hay, A. E., Bowen, A. J. (2008). Wave-driven circulation in a coastal bay during the landfall of a hurricane. Journal of Geophysical Research: Oceans, 113(C5).

Mulligan, R. P., Hay, A. E., & Bowen, A. J. (2010). A wave-driven jet over a rocky shoal. Journal of Geophysical Research: Oceans, 115(C10).

National Research Council, 2009. Mapping the Zone: Improving Flood Map Accuracy. The National Academies Press, Washington, DC.

Nicholls, R. J., 2002. Analysis of global impacts of sea-level rise: a case study of flooding. Physics and Chemistry of the Earth, Parts A/B/C, 27(32), 1455-1466.

Nicolle, A., Karpytchev, M., Benoit, M., 2009. Amplification of the storm surges in shallow waters of the Pertuis Charentais (Bay of Biscay, France). Ocean Dynamics, 59(6): 921-935.

Nielsen, P., 1992. Coastal bottom boundary layers and sediment transport. World Scientific Publishing Company, Singapore, Advanced Series on Ocean Engineering, vol. 4.

Olabarrieta, M., Geyer, W. R., Kumar, N., 2014. The role of morphology and wave-current interaction at tidal inlets: an idealized modeling analysis. Journal of Geophysical Research: Oceans, 119, 8818-8837.

Orescanin, M., Raubenheimer, B., Elgar, S., 2014. Observations of wave effects on inlet circulation. Continental Shelf Research, 82, 37-42.

Orton, P. M., Talke, S. A., Jay, D. A., Yin, L., Blumberg, A. F., Georgas, N., Zhao, H., Roberts, H. J., MacManus, K., 2015. Channel shallowing as mitigation of coastal flooding. Journal of Marine Science and Engineering, 3 (3), 654-673.

Ozer, P., Padilla-Hernández, R., Monbaliu, J., Fanjul, E. A., Albiach, J. C. C., Osuna, P., Yu, J. C. S., Wolf, J., 2000. A coupling module for tides, surges and waves. Coastal Engineering, 41: 1-3,95-124.

Panchang, V. G., Jeong, C., Li, D., 2008. Wave climatology in coastal Maine for aquaculture and other applications. Estuaries and Coasts, 31(2), 289-299.

Pawlowicz, R., Beardsley, B., Lentz, S., 2002. Classical tidal harmonic analysis including error estimates in MATLAB using T_TIDE. Computers and Geosciences, 28(8), 929-937.

Peng, Z., Zou, Q. -P., 2011. Spatial distribution of wave overtopping water behind coastal structures. Coastal Engineering, 58: 489-498.

Perrie W, Tang CL, Hu Y, DeTracy BM (2003) The impact of waves on surface currents. Journal of Physical Oceanography, 33(10): 2126-2140.

Pettigrew NR, Churchill JH, Janzen CD, Mangum LJ, Signell RP, Thomas AC, Townsend DW, Wallinga JP, Xue H (2005). The kinematic and hydrographic structure of the Gulf of Maine Coastal Current. Deep-Sea Research Part II: Topical Studies in Oceanography, 52(19): 2369-2391.

Powell, M. D., Vickery, P. J., Reinhold, T. A., 2003. Reduced drag coefficient for high wind speeds in tropical cyclones. Nature, 422(6929), 279-283.

Pugh, D. T., 1987. Tides, Surges and Mean Sea-level: A Handbook for Engineers and Scientists. John Wiley and Sons, New York.

Pugh, D. T., 1996. Tides, surges and mean sea-level (reprinted with corrections). John Wiley & Sons Ltd.

Reeve, D. E., Soliman, A., Lin, P. Z., 2008. Numerical study of combined overflow and wave overtopping over a smooth impermeable seawall. Coastal Engineering, 55(2), 155-166.

Rego, J. L., Li, C., 2009. On the importance of the forward speed of hurricanes in storm surge forecasting: A numerical study. Geophysical Research Letters, 36(7).

Rego, J. L., Li, C., 2010. Nonlinear terms in storm surge predictions: Effect of tide and shelf geometry with case study from Hurricane Rita. Journal of Geophysical Research: Oceans, 115(C6).

Ris, R. C., Holthuijsen, L. H., Booij, N., 1999. A third-generation wave model for coastal regions. Part 2, Model description and validation. Journal of Geophysical Research: Oceans, 104(C4), 7649-7666.

Roberts, K. J., Colle, B. A., Korfe, N., 2017. Impact of simulated twenty-first-century changes in extratropical cyclones on coastal flooding at the Battery, New York City. Journal of Applied Meteorology and Climatology, 56(2), 415-432.

Saha, S., Moorthi, S., Pan, H. L., Wu, X., Wang, J., Nadiga, S., Tripp, P., Kistler, R., Woollen, J., Behringer, D., Liu, H., Stokes, D., Grumbine, R., Gayno, G., Wang, J., Hou, Y. T., Chuang, H., Juang H. M. H., Sela, J., Iredell, M., Treadon, R., Kleist, D., Delst, P. V., Keyser, D., Derber, J., Ek, M., Meng, J., Wei, H., Yang, R., Lord, S., Dool H., Kumar, A., Wand, W., Long, C., Chelliah, M., Xue, Y., Huang, B., Schemm, J. K., Ebisuzaki, W., Lin, R., Xie, P., Chen, M., Zhou, S., Higgins, W., Zou, C. Z., Liu, Q., Chen, Y., Han, Y., Cucurull, L., Reynolds, R. W., Rutledge, G., Goldberg, M., 2010. The NCEP climate forecast system reanalysis. Bulletin of the American Meteorological Society, 91(8), 1015-1058.

Saha, S., Moorthi, S., Wu, X., Wang, J., Nadiga, S., Tripp, P., Behringer, D., Hou, Y., Chuang, H., Iredell, M., Ek, M., Meng, J., Yang, R., Mendez, M. P., van den Dool, H., Zhang, Q., Wang, W., Chen, M., Becker, E., 2014. The NCEP climate forecast system version 2. J. Climate 27(6), 2185-2208.

Sheng, Y. P., Liu, T., 2011. Three-dimensional simulation of wave-induced circulation: Comparison of three radiation stress formulations. Journal of Geophysical Research: Oceans, 116: C05021.

Shi, F., Kirby, J. T., Harris, J. C., Geiman, J. D., Grilli, S. T., 2012. A high-order adaptive time-stepping TVD solver for Boussinesq modeling of breaking waves and coastal inundation. Ocean Modelling, 43, 36-51.

Signell, R. P., Beardsley, R. C., Graber, H. C., Capotondi, A., 1990. Effect of wave-current interaction on wind-driven circulation in narrow, shallow embayments. Journal of Geophysical Research: Oceans, 95(C6), 9671-9678.

Silva, R., Baquerizo, A., Losada, M. Á., Mendoza, E., 2010. Hydrodynamics of a headland-bay beach—nearshore current circulation. Coastal Engineering, 57(2), 160-175.

Smit, P., Zijlema, M., Stelling, G., 2013. Depth-induced wave breaking in a non-hydrostatic, near-shore wave model. Coastal Engineering, 76, 1-16.

Soulsby, R. L., Hamm, L., Klopman, G., Myrhaug, D., Simons, R. R., Thomas, G. P., 1993. Wave-current interaction within and outside the bottom boundary layer. Coastal engineering, 21(1-3), 41-69.

Soulsby, R. L., Davies, A. G., 1995. Bed shear-stresses due to combined waves and currents. In Advances in coastal morphodynamics (Vol. 4, pp. 4-23). Delft Hydraulics Delft, The Netherlands.

Soulsby, R., 1997. Dynamics of marine sands: a manual for practical applications. Thomas Telford.

Styles, R., Glenn, S. M., 2000. Modeling stratified wave and current bottom boundary layers on the continental shelf. Journal of Geophysical Research: Oceans, 105(C10), 24119-24139.

Sucsy, P. V., Pearce, B. R., Panchang, V.G., 1993. Comparison of two-and three-dimensional model simulation of the effect of a tidal barrier on the Gulf of Maine tides. Journal of Physical Oceanography, 23(6), 1231-1248.

Sun Y, Chen C, Beardsley RC, Xu Q, Qi J, Lin H (2013) Impact of current-wave interaction on storm surge simulation: A case study for Hurricane Bob. Journal of Geophysical Research: Oceans, 118(5): 2685-2701.

Sverdrup HU, Johnson MW, Fleming RH (1942) The Oceans: Their physics, chemistry, and general biology. Prentice-Hall, New York.

Tang, C. L., Perrie, W., Jenkins, A. D., DeTracey, B. M., Hu, Y., Toulany, B., Smith, P. C., 2007. Observation and modeling of surface currents on the Grand Banks: A study of the wave effects on surface currents. Journal of Geophysical Research: Oceans, 112: C10025.

Taylor, P. K., and Yelland, M. J., 2001. The dependence of sea surface roughness on the height and steepness of the waves. Journal of Physical Oceanography, 31(2), 572-590.

Teixeira, J. C., Abreu, M. P., Soares, C. G., 1995. Uncertainty of ocean wave hindcasts due to wind modeling. Journal of Offshore Mechanics and Arctic Engineering, 117(4), 294-297.

Thornton, E. B., Guza, R. T., 1983. Transformation of wave height distribution. Journal of Geophysical Research: Oceans, 88(C10), 5925-5938.

Tilburg, C. E., Gill, S. M., Zeeman, S. I., Carlson, A. E., Arienti, T. W., Eickhorst, J. A., Yund, P. O., 2011. Characteristics of a shallow river plume: observations from the Saco River Coastal Observing System. Estuaries and Coasts, 34(4): 785-799.

Twomey, E. R., Signell, R. P., 2013. Construction of a 3-arcsecond digital elevation model for the Gulf of Maine. Open-File Report 2011-1127, 24 pp, US Geological Survey. Available online at https://pubs.usgs.gov/of/2011/1127/.

Uchiyama, Y., McWilliams, J. C., Restrepo, J. M., 2009. Wave-current interaction in nearshore shear instability analyzed with a vortex force formalism. Journal of Geophysical Research: Oceans, 114: C06021.

Uchiyama, Y., McWilliams, J. C., Shchepetkin, A. F., 2010. Wave-current interaction in an oceanic circulation model with a vortex-force formalism: Application to the surf zone. Ocean Modelling, 34(1): 16-35.

Van der Meer, J. W., Allsop, N. W. H., Bruce, T., De Rouck, J., Kortenhaus, A., Pullen, T., Schüttrumpf, H., Troch, P. and Zanuttigh, B. (EurOtop), 2016. Manual on wave overtopping of sea defences and related structures. An overtopping manual largely based on European research, but for worldwide application. Available online at www.overtopping-manual.com.

van der Westhuysen, A. J., 2012. Spectral modeling of wave dissipation on negative current gradients. Coastal Engineering, 68, 17-30.

van Gent, M. R., van den Boogaard, H. F., Pozueta, B., Medina, J. R., 2007. Neural network modelling of wave overtopping at coastal structures. Coastal Engineering, 54(8), 586-593.

Verhaeghe, H., De Rouck, J., van der Meer, J., 2008. Combined classifier-quantifier model: a 2-phases neural model for prediction of wave overtopping at coastal structures. Coastal Engineering, 55(5), 357-374.

Wang, Z., Zou, Q., Reeve, D., 2009. Simulation of spilling breaking waves using a two-phase flow CFD model. Computers & Fluids, 38(10), 1995-2005.

Wargula, A., Raubenheimer, B., Elgar, S. (2014). Wave-driven along-channel subtidal flows in a well-mixed ocean inlet. Journal of Geophysical Research: Oceans, 119(5), 2987-3001.

Warner, J. C., Butman, B., Dalyander, P. S., 2008. Storm-driven sediment transport in Massachusetts Bay. Continental Shelf Research, 28(2): 257-282.

Warner, J. C., Sherwood, C. R., Signell, R. P., Harris, C. K., Arango, H. G., 2008. Development of a three-dimensional, regional, coupled wave, current, and sediment-transport model. Computers & Geosciences, 34(10), 1284-1306.

Warner, J. C., Armstrong, B., He, R., Zambon, J. B., 2010. Development of a coupled ocean-atmosphere-wave-sediment transport (COAWST) modeling system. Ocean Modelling, 35(3): 230-244.

Wei, G., Kirby, J. T., Grilli, S. T., Subramanya, R., 1995. A fully nonlinear Boussinesq model for surface waves. Part 1. Highly nonlinear unsteady waves. Journal of Fluid Mechanics, 294(13), 71-92.

Westerink, J. J., Luettich, R. A., Muccino, J. C., 1994. Modelling tides in the western north atlantic using unstructured graded grids. Tellus A, 46(2), 178-199.

Westerink, J. J., Luettich, R. A., Blain, C. A., Scheffner, N. W., 1994. ADCIRC: an advanced three-dimensional circulation model for shelves, coasts and estuaries. Report 2: users' manual for ADCIRC-2DDI. Technical Report DRP-92-6, U.S. Army Corps of Engineers. http://www.unc.edu/ims/adcirc/publications/1994/1994_Westerink01.pdf

Westerink, J. J., Luettich, R. A., Feyen, J. C., Atkinson, J. H., Dawson, C., Roberts, H. J., Powell, M. D., Dunion, J. P., Kubatko, E. J., Pourtaheri, H., 2008. A basin- to channel-scale unstructured grid hurricane storm surge model applied to southern Louisiana. Monthly Weather Review, 136(3), 833-864.

Wolf, J., 2009. Coastal flooding: impacts of coupled wave-surge-tide models. Natural Hazards, 49(2), 241-260.

Xia, H., Xia, Z., Zhu, L., 2004. Vertical variation in radiation stress and wave-induced current. Coastal Engineering, 51(4): 309-321.

Xie, L., Wu, K., Pietrafesa, L., Zhang, C., 2001. A numerical study of wave-current interaction through surface and bottom stresses: Wind-driven circulation in the South Atlantic Bight under uniform winds. Journal of Geophysical Research: Oceans, 106(C8): 16841-16855.

Xie, D., Zou, Q., Cannon, J. W., 2016. Application of SWAN+ADCIRC to tide-surge and wave simulation in Gulf of Maine during Patriot's Day storm. Water Science and Engineering, 9(1): 33-41.

Xie, D., Zou, Q., Mignone, A., MacRae, J. D., 2018. An integrated modeling system to predict coastal flooding from wave overtopping in the northeastern USA. Submitted to Coastal Engineering.

Xie, L., Wu, K., Pietrafesa, L., Zhang, C. (2001). A numerical study of wave-current interaction through surface and bottom stresses: Wind-driven circulation in the South Atlantic Bight under uniform winds. Journal of Geophysical Research: Oceans, 106(C8), 16841-16855.

Xue, H. J., Chai, F., Pettigrew, N. R., 2000. A Model study of the seasonal circulation in the Gulf of Maine, Journal of Physical Oceanography, 30(5):1111-1135.

Yang, Z., Myers, E. P., 2008. Barotropic tidal energetics and tidal datums in the Gulf of Maine and Georges Bank region. In Estuarine and Coastal Modeling 2007. p. 74-94. ASCE.

Young, I. R., 1988. Parametric hurricane wave prediction model. Journal of Waterway, Port, Coastal, and Ocean Engineering, 114(5), 637-652.

Young, I. R., 2006. Directional spectra of hurricane wind waves. Journal of Geophysical Research: Oceans, 111(C8).

Zijlema, M., 2010. Computation of wind-wave spectra in coastal waters with SWAN on unstructured grids. Coastal Engineering, 57(3): 267-277.

Zijlema, M., Stelling, G. S., 2005. Further experiences with computing non-hydrostatic free-surface flows involving water waves. International Journal for Numerical Methods in Fluids, 48(2), 169-197.

Zijlema, M., Stelling, G. S., 2008. Efficient computation of surf zone waves using the nonlinear shallow water equations with non-hydrostatic pressure. Coastal Engineering, 55(10), 780-790.

Zijlema, M., Stelling, G., Smit, P., 2011. SWASH: An operational public domain code for simulating wave fields and rapidly varied flows in coastal waters. Coastal Engineering, 58(10), 992-1012.

Zijlema, M., van Vledder, G. P., Holthuijsen, L. H., 2012. Bottom friction and wind drag for wave models. Coastal Engineering, 65, 19-26.

Zou, Q. P., 2004. A simple model for random wave bottom friction and dissipation. Journal of Physical Oceanography, 34(6), 1459-1467.

Zou, Q. P., Bowen, A. J., Hay, A. E., 2006. Vertical distribution of wave shear stress in variable water depth: Theory and field observations. Journal of Geophysical Research: Oceans, 111(C9), C09032.

Zou, Q., Chen, Y., Cluckie, I., Hewston, R., Pan, S., Peng, Z., Reeve, D., 2013. Ensemble prediction of coastal flood risk arising from overtopping by linking meteorological, ocean, coastal and surf zone models. Quarterly Journal of the Royal Meteorological Society, 139(671): 298-313.

Zou, Q., Xie, D., 2016. Tide-surge and wave interaction in the Gulf of Maine during an extratropical storm. Ocean Dynamics, 66(12), 1715-1732.

Zou, Q. P., Peng, Z., 2011. Evolution of wave shape over a low-crested structure. Coastal Engineering, 58: 478-488.

## APPENDIX A: THE FLOW CHART FOR WAVE OVERTOPPING PREDICTION

The following flowchart illustrates the procedure to use the wave overtopping model for overtopping predictions for seawalls with the submerged or emerged foot. All the equations refer to the equations in Section 4.3.3 of the main context.

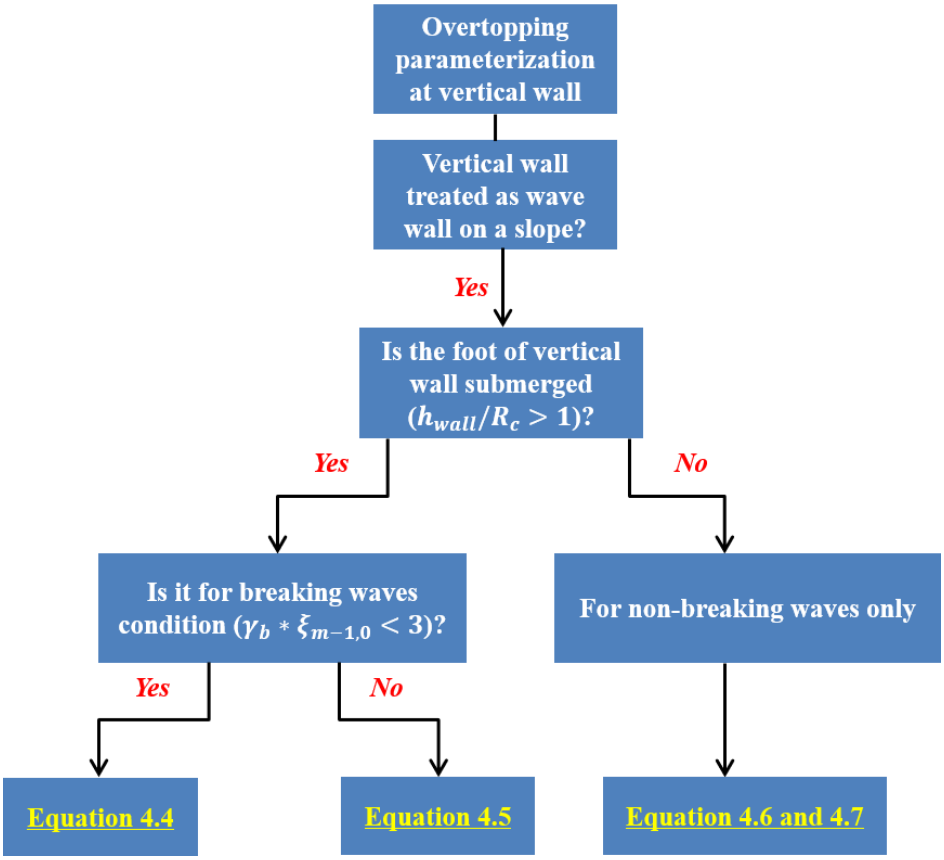


Where $h_{wall}$ is the height of the wave wall, $R_c$ is the crest freeboard, $\gamma_b$ is the influence factor for a berm, $\xi_{m-1,0}$ is the breaker parameter.

## APPENDIX B: RELEVANT PUBLICATIONS

### JOURNAL PAPERS:

Xie, D. M., Zou, Q. P., Cannon, J. W., 2016. Application of SWAN+ADCIRC to tide-surge and wave simulation in Gulf of Maine during Patriot's Day storm. Water Science and Engineering, 9(1), 33-41. **(Chapter 2)**

Zou, Q. P., Xie, D. M., 2016. Tide-surge and wave interaction in the Gulf of Maine during the Patriot's Day storm. Ocean Dynamics, 66(12), 1715-1732. **(Chapter 3)**

Xie, D. M., Zou, Q. P., Mignone, A. R., MacRae, J. D., 2017. An integrated modeling system to predict coastal flooding from wave overtopping in the northeastern USA. (Submitted to Coastal Engineering and in revision). **(Chapter 4)**

Xie, D. M., Zou, Q. P., MacRae, J. D., 2018. Hydrodynamic and sediment transport simulation in Saco Bay, Maine. (In preparation). **(Chapter 5)**

### CONFERENCE PAPERS:

Xie, D.M., Zou, Q.P., Cannon, J.W., 2015. Tide-surge and wave modeling in the Gulf of Maine during the Patriot's Day storm. 3rd IMA International Conference on Flood Risk, Swansea, Wales, UK.

Xie, D. M., Zou, Q. P., Cannon, J. W., 2015. Coastal flooding at the Gulf of Maine during the Patriot's Day storm. Coastal Structures & Solutions to Coastal Disasters, Boston, MA, USA.

Xie, D. M., Zou, Q. P., 2016. Effect of wave-current interaction on waves and circulation over Georges Bank during storm events. International Conference on Coastal Engineering, Istanbul, Turkey.

Zou, Q.P., Xie, D. M., MacRae, J. D., Mignone, A., Coastal flooding and sediment transport during extreme storms in the Northeastern USA in a changing climate. Proceedings of the 21st IAHR-APD Congress 2018, Yogyakarta, Indonesia.

## BIOGRAPHY OF THE AUTHOR

Dongmei Xie was born in Sichuan, China on January 5, 1988. She attended Hohai University in China and graduated with a bachelor's degree in Civil Engineering in 2010. She entered the Civil Engineering graduate program in 2010 and got her master's degree in 2013. She is a candidate for the Doctor of Philosophy degree in Civil and Environmental Engineering from the University of Maine in August 2018.